DOCTOR OF PHILOSOPHY

# Disordered ionic conductors insights from atomistic modelling

Kordatos, Apostolos

*Award date:*
2019

*Awarding institution:*
Coventry University

# Disordered Ionic Conductors: Insights from Atomistic Modelling

By

**Apostolos Kordatos**

**September 2018**

Coventry University

***A thesis submitted in partial fulfilment of the University's requirements for the Degree of Doctor of Philosophy***

# Certificate of Ethical Approval

Applicant:

Apostolos Kordatos

Project Title:

DISORDERED IONIC CONDUCTORS

This is to certify that the above named applicant has completed the Coventry University Ethical Approval process and their project has been confirmed and approved as Low Risk

Date of approval:

23 July 2018

Project Reference Number:

P72983

# AKNOWLEDGEMENTS

I would like to express my thanks to my Director of Studies Prof. Alexander Chroneos and my supervisors Prof. Elena Gaura and Dr James Brusey for the constant motivation, encouragement, patience and inspiration.  Financial support was provided by the Faculty of Engineering, Environment and Computing. Computing resources were provided by the High – Performance Computing facilities in Coventry University. I would also like to express my gratitude to the atomistic simulations group Dr Nikolaos Kelaidis, Dr Stavros – Richard Christopoulos and Dr David Parfitt for their valuable advice and discussions as well as their continuous help and support. Dr Navaratnarajah Kuganathan is acknowledged for stimulating discussions and collaboration in battery materials projects.

# ABSTRACT

The increasing demand for efficient energy storage and conversion in a low-cost, safe and sustainable manner has attracted considerable research efforts. In particular, the research community investigates candidate materials suitable for energy applications such as Li – ion batteries and solid oxide fuel cells. As many key factors of energy systems depend on the properties of their constituent materials, the relation between the materials properties and their applicability in devices is important. The aim of the present thesis is to examine promising systems and provide a deeper understanding on their atomic-scale mechanisms with respect to their potential performance. Density Functional Theory (DFT) calculations are employed to investigate the defect chemistry, doping processes, electronic structure and ionic diffusion in $Li_2ZrO_3$, $Li_2CuO_2$, $Li_2SnO_3$, $Li_2RuO_3$, $Li_3SbO_4$, $Li_3NbO_4$ and anatase $TiO_2$. Theoretical modelling provides advanced insights on the intrinsic processes and relative energetics, governed by point defects. Overall the dominant mechanisms are identified as well as the structural modifications under doping and / or mechanical strain. The presented results are expected to motivate further research through both theoretical and experimental techniques.

# CONTENTS

# LIST OF FIGURES

**5.8** Densities of states of substitutional dopants-oxygen vacancy pairs in $Li_2ZrO_3$ (a)-(c) divalent dopants (d)-(e) trivalent dopants.

**6.1** Crystallographic structure of $Li_2CuO_2$ (space group *Immm*).

**6.2** The possible lithium ion migration paths considered. $Li^+$, $Cu^{2+}$, and $O^{2-}$ atoms are shown as green, blue and red spheres respectively.

**6.3** The chemical bonding of the substitutional dopant with nearest oxygen atoms in $Li_2CuO_2$.

**6.4** The densities of states for $Li_2CuO_2$ (a) perfect cell (b) $V_{Li}'$ (c) $Al_{Cu}^{\bullet}$ (d) $\{Al_{Cu}^{\bullet}:V_{Li}'\}^X$.

**6.5** The contribution of the atomic orbitals to the partial densities of states of the perfect $Li_2CuO_2$ supercell shown in Figure 4(a).

**6.6** The densities of states for (a) $Al_{Cu}^{\bullet}$ (b) $\{Al_{\boldsymbol{Cu}}^{\bullet}:V_{\boldsymbol{Li}}'\}^X$ (c) $In_{Cu}^{\bullet}$ (d) $\{In_{\boldsymbol{Cu}}^{\bullet}:V_{\boldsymbol{Li}}'\}^X$ (e) $La_{Cu}^{\bullet}$ (f) $\{La_{\boldsymbol{Cu}}^{\bullet}:V_{\boldsymbol{Li}}'\}^X$ (g) $Sc_{Cu}^{\bullet}$ (h) $\{Sc_{\boldsymbol{Cu}}^{\bullet}:V_{\boldsymbol{Li}}'\}^X$ (i) $Y_{Cu}^{\bullet}$ (j) $\{Y_{\boldsymbol{Cu}}^{\bullet}:V_{\boldsymbol{Li}}'\}^X$.

**7.1** The crystal structure (space group C2/c), atomic configuration and chemical environment of (a) $Li_2SnO_3$ and (b) $Li_2RuO_3$.

**7.2** Possible long-range lithium vacancy migration paths considered. Green, blue and red colors correspond to $Li^+$, $Sn^{4+}$, and $O^{2-}$ atoms respectively.

**7.3** Possible long range lithium vacancy migration paths considered. Green, grey and red colors correspond to Li, Ru, and O atoms respectively.

**7.4** Octahedral $SnO_6$ unit in the relaxed structure of doped $Li_2SnO_3$ and the coordination formed by the dopants on the Sn site with neighbor oxygen atoms.

**7.5** Octahedral $RuO_6$ units of the relaxed structure in undoped $Li_2RuO_3$ and the coordination formed by dopants on the Ru site with neighbor oxygen atoms.

**7.6** The PDOS calculated using DFT for the (a) $Li_2SnO_3$ perfect cell (b) $Li_2SnO_3$ with Li interstitial (c) Al – Doped $Li_2SnO_3$ and (d) Al-Doped $Li_2SnO_3$ with Li interstitial.

**7.7** (a) The complete contribution of the atomic orbitals in the Densities of States for the undoped Li2SnO3 (b) The contribution of Li orbitals (c) The contribution of O orbitals and (d) The contribution of Sn orbitals.

**7.8** The $Li_2SnO_3$ Densities of States for (a) Sc – doped supercell (b) Sc – doped supercell with one Li interstitial (c) In – doped supercell (d) In – doped supercell with one Li interstitial (e) Y – doped supercell (f) Y – doped supercell with one Li interstitial (g) Gd – doped supercell (h) Gd – doped supercell with one Li interstitial (i) La – doped supercell (j) La – doped supercell with one Li interstitial.

**7.9** $Li_2RuO_3$ PDOS for (a) The non – defective cell (d) The Li interstitial (c) The Al – doped cell (d) The Al – doped cell with one Li interstitial (e) The Co – doped cell (f) The Co – doped cell with one Li interstitial.
**7.10** $Li_2RuO_3$ PDOS for (a) The total contribution of orbitals in the non – defective cell (b) The contribution of $Li^+$ orbitals (c) The contribution of $O^{2-}$ orbitals (d) The contribution of Ru orbitals.

**7.11** The Co – doped $Li_2RuO_3$ PDOS for (a) The contribution of elements in the doped cell (b) The total contribution of orbitals (c) The contribution of $Li^+$ orbitals (d) The contribution of $O^{2-}$ orbitals (e) The contribution of $Co^{3+}$ orbitals (f) The contribution of $Ru^{4+}$ orbitals.

**7.12** The $Li_2RuO_3$ PDOS for (a) The Sc - doped supercell (d) The Sc - doped supercell with a Li interstitial (c) The In - doped supercell (d) The In - doped supercell with a Li interstitial (e) The Y - doped supercell (f) The Y - doped supercell with a Li interstitial (g) The Gd - doped supercell (h) The Gd - doped supercell with a Li interstitial (i) The La - doped supercell (j) The La - doped supercell with a Li interstitial.

**8.1** The crystallographic structure for the **(a)** Monoclinic (P2/c) $Li_3SbO_4$ **(b)** Cubic ($I\bar{4}3m$) $Li_3NbO_4$.

**8.2** Possible long-range lithium vacancy migration paths considered. Green, blue and red colors correspond to Li, Sb, and O atoms respectively.

**8.3** Possible long-range lithium vacancy migration paths considered. Green, yellow and red colors correspond to Li, Nb, and O atoms respectively. Long range paths are labelled as L, M, N and O.

**8.4** Octahedral $SbO_6$ unit in the relaxed structure of undoped $Li_3SbO_4$ and the coordination formed by the dopants on the Sb site with neighbor oxygen.

**8.5** Octahedral $NbO_6$ unit in the relaxed structure of undoped $Li_3NbO_4$ and the coordination formed by the dopants on the Nb site with neighbor oxygen.

**8.6** The PDOS for the (a) $Li_3SbO_4$ perfect cell (b) $Li_3SbO_4$ with a $Li^+$ vacancy (c) Si – Doped $Li_3SbO_4$ and (d) Si- Doped $Li_3SbO_4$ with $Li^+$ vacancy.

**8.7** The Density of States for the undoped $Li_3SbO_4$ with respect to (a) The total contribution of orbitals (b) The $Li^+$ orbitals (c) The $O^{2-}$ orbitals (d) The $Sb^{5+}$ orbitals

**8.8** The Density of States for the doped Li3SbO4 with respect to (a) Ge doping (b) Ge doping with a Li vacancy (c) Ti doping (d) Ti doping with a Li vacancy (e) Zr doping (f) Zr doping with a Li vacancy (g) Ce doping (h) Ce doping with a Li vacancy

**8.9** The $Li_3NbO_4$ PDOS for the (a) Perfect cell (b) The $Li^+$ Interstitial defect (c) The $Si^{4+}$ - doped cell (d) The $Si^{4+}$ - doped with a $Li^+$ interstitial defect.

**8.10** The PDOS for the non-defective $Li_3NbO_4$ structure with respect to (a) The complete contribution of orbitals (b) The $Li^+$ orbitals only (c) The $O^{2+}$ orbitals only (d) The $Nb^{5+}$ orbitals only.

**8.11** The PDOS for the doped supercell with respect to (a) $Ge^{4+}$ doping (b) $Ge^{4+}$ doping with one $Li^+$ interstitial (c) $Ti^{4+}$ doping (d) $Ti^{4+}$ doping with one $Li^+$ interstitial (e) $Zr^{4+}$ doping (e) $Zr^{4+}$ doping with one $Li^+$ interstitial (g) $Ce^{4+}$ doping (h) $Ce^{4+}$ doping with one $Li^+$ interstitial.

**9.1** The crystallographic structure of anatase $TiO_2$.

**9.2** The $Li^+$ and $Na^+$ interstitial sites in $TiO_2$.

**9.3 (a)–(d)** The diffusion mechanisms of $Li_i$ and $Na_i$ in anatase.

**9.4** The electronic structure of the (a) non – defective perfect supercell (b) defective supercell containing $Li_i$ and (c) defective supercell containing $Na_i$.

**9.5** The minimum energy fluorine-nitrogen defects in anatase $TiO_2$ (a) $F_i$ (b) $N_i$ (c) $F_iN_i$ (d) $F_ON_i$ (e) $F_iN_{Ti}$ (f) $F_iN_i$_away and (g) $F_iF_i$.

**9.6** Densities of States of the defective supercells containing (a) $F_i$ (b) $N_i$.

**9.7** Densities of States of the defective supercells containing (c) $F_iN_i$ (d) $F_ON_i$ (c) $F_iN_{Ti}$.

**9.8** Volume of primitive cell with respect to stress.

**9.9** Band gap with respect to stress for undoped anatase for hydrostatic, biaxial and uniaxial stress.

# CHAPTER 1

# Introduction

Among the most challenging fields in the modern research is the generation and storage of energy in a cleaner and environmentally friendly approach. Research in $Li^+$- ion batteries and solid oxide fuel cells (SOFCs) aims to address future energy demand by achieving higher energy efficiency at a lower cost[1, 2]. Chemically stable materials able to undergo high rates of charge / discharge cycles in a fast and efficient way will boost the advanced technologies of portable electronics and electric vehicles[3, 4] as promising alternative power sources to burning fuel and internal combustion engines. Vehicle electrification is considered as the main key-enabling technology to the decarbonization of long range road based transportations[5] and the required reduction of oil usage due to limited resources globally[6]. Optimizing energy materials is of crucial importance from both a scientific and technological perspective[7]. Furthermore, the demand for the rapid reduction of the greenhouse gas emissions with the has been officially confirmed through the Paris agreement in 2016[8]. Technical requirements such as high power and energy density are necessary and under investigation presenting considerable progress, whereas recent advances in electrode performance enhancement through nanosized and nanostructured materials are constantly updated[9]. In addition, battery technology has to overcome limitations[10] such as low thermal stability, capacity reduction at high current and cycling rates as well as safety issues such as flammability. The motivation of this work is to investigate advanced materials as potential candidates for efficient energy applications. In this Chapter, the scientific background as well as the research orientation is described.

## 1.1 The evolution in materials science

The key factors of energy systems depend on the properties of their constituent materials[11]. Therefore, the growing field of nanoscience and nanotechnology revealed numerous attractive possibilities. Design, discovery and industrial exploitation of high-performance materials as well as tuning their properties according to the potential application has been among the primary ambitions of the research community[12]. Efficient synthesis methods (sol-gel, sputtering, and plasma) as well as characterization techniques provide a toolbox to build nanostructured phases that lead technology in new horizons[13]. However, the investigation of energy materials demands a fundamental understanding of their properties in the atomic scale, to provide a predictive role synergetically with experiment. Most of the materials properties are strongly connected with the crystallography in conjunction with the electronic configuration of atoms as well as bonding. In addition, many processes occur concurrently that should be investigated separately and in conjunction with each other. Thus, the relation between the materials properties and their potential applicability in energy devices is crucial and has intrigued the scientific community.

## 1.2 Energy challenges

To overcome the limitations in energy applications, one should consider what type of properties the component materials should exhibit. This is in direct connection with the atomic scale mechanisms and intrinsic processes. Diffusion of atoms is a fundamental process of significance in solids[14] and atomic scale modelling investigations can be used to derive the diffusion mechanisms and dynamics. Electrochemical cells / devices are able to convert chemical energy to electrical in terms of differential potential between the electrodes. For efficient operation, the atoms should have a low activation energy of migration through the electrolyte during charge / discharge and thus, diffusion is of crucial significance affecting the storing of energy, capacity, power density and cyclability. Additionally, being able to predict the mechanisms such as electronic and ionic conduction can complement interpretation of experimental results including surface structures and doping effects. The electrode components in batteries are considered as limiting factors, as the cyclability is strongly connected with the overall capacity, whereas the electronic properties affect the cell voltage of the device. Among the fundamental criteria for a candidate material must be fast ion migration and structural stability that undergoes the repeated charge / discharge cycles. In essence, these mechanisms involve the movement of atoms in the material and it is unsurprising that atomic parameters influence diffusion. The atomic configuration and oxidation state for every element as well as its position in a lattice are strongly connected with the redox reactions and transition mechanisms. Additionally, the cation diffusivities within the cathode and electrode corresponds to the maximum rates for charge and discharge, the determining factor of power density. Furthermore, the cell tolerance of charging cycles is essential to the longevity of the cathode – electrode – anode coupling. $Li^+$ exhibits an attractive set of properties. First, it presents the lowest reduction potential among other elements enabling $Li^+$ batteries to operate at the highest possible cell potential. In addition, it is the third lightest element with a small ionic radius (0.76 Å)[15]. Formulas based on $Li^+$ allow the electrochemical cells to have high gravimetric and volumetric capacities. States of structural disorder in the anion sublattice can impact the material properties and the diffusion of intrinsic point defects. This is a common perspective in energy related materials, where intrinsic disorder and doping effects can influence the formation (e.g.

concentration of point defects mediating diffusion) and the migration (e.g. the energy barriers for diffusion) processes.

## 1.3 Tailoring in the nanoscale

The aim of this thesis is to investigate the intrinsic defect processes of specific promising systems, suitable as candidates in energy storage applications such as $Li^+$-ion batteries. A greater insight into the defect properties of energy materials is crucial to gain a better understanding of their electrochemical behaviour. The principles and models of condensed matter physics provide the ability to get advanced insights on the atomistic phenomena[16]. In particular, with the continuous growth in computer power during the last decades, computational methods gained a major role, with successful applications in solid structures and dynamics[17]. The theoretical background of quantum mechanics as well as the point defects in solids are some of the powerful tools for atomic scale structures. In the present thesis, atomistic modelling is employed to predict and characterize structures and properties of complex materials while acting synergetically with experimental studies. Investigation of the intrinsic defect processes provide insights on the physical phenomena and the energetics of point defects in order to identify the dominant mechanisms that influence the materials performance. Notably, this approach has to be in accordance with experimental results and based on a vast knowledge of previous studies and relevant literature.

### 1.4 Outline of thesis

Atomistic modelling methods are used as a predictive approach of the defect processes in energy materials. In this regard, properties such as structural parameters, defect chemistry and doping as well as their connection with the diffusion mechanisms is discussed.

In Chapter 2, the research challenges, issues and concerns are described in conjunction with previous works and literature.

Chapter 3 presents the theoretical background of point defects. The Kröger-Vink notation is introduced to describe point defects as it is applied in the following chapters. Additionally, the different types of intrinsic defects in a crystal is explained in conjunction with the required principles of condensed matter physics. Furthermore, the defect concentrations and thermodynamics as well as the mechanism of diffusion and doping processes are discussed.

Density Functional Theory is described in Chapter 4. At first, an introduction to the quantum mechanical formulation is provided as well as the two fundamental mathematical theorems by Kohn and Honenberg. Then, the exchange – correlation functional with respect to the different approximations (LDA / GGA), plane wave basis and K-Points are described as they are methodologically important. Furthermore, the Density of States (DOS) as a valuable tool for the description of the electronic structure characterization of materials is introduced. Finally, the CASTEP code is described and comments on the calculations are provided.

Chapter 5 presents the intrinsic processes in $Li_2ZrO_3$. Overall, the defect chemistry, doping effects and electronic structure of the material is investigated. Initially, the energies for the Frenkel, antisite and Schottky defects are calculated in order to identify the dominant mechanism. Then, doping with divalent, trivalent and tetravalent elements on the $Zr^{4+}$ site is investigated with respect to the association with $O^{2-}$ vacancies and their binding energies are discussed. Additionally, the effect of the doping processes is analysed in terms of the partial density of states (DOS) of the material.

In Chapter 6, the defect chemistry, $Li^+$ diffusion and trivalent doping in $Li_2CuO_2$ is reported. In essence, the system is investigated as a potential cathode material based on the dominant mechanism of the defect processes and the $Li^+$ activation energy of migration. The introduction of dopants in the host lattice provide further insights on the materials behaviour.

Chapter 7 reports on the intrinsic defects in $Li_2SnO_3$ and $Li_2RuO_3$. The doping processes as well as the $Li^+$ diffusion pathways are investigated in both materials. Furthermore, their electronic structure is analysed and discussed.

Chapter 8 considers trivalent doping, electronic properties in intrinsic defects in $Li_3SbO_4$ and $Li_3NbO_4$. Here, the energies of the dominant mechanisms are calculated, and trivalent doping is investigated as a promising technique to enhance the materials' performance. An extended analysis and discussion on the PDOS are provided for completeness.

In Chapter 9, anatase $TiO_2$ is considered as a potential candidate material for photocatalytic and battery applications. The investigation of $Li^+$ and $Na^+$ doping in interstitial sites and their migration mechanisms in $TiO_2$ is reported. Additionally, the intrinsic $F^-$ / $N^+$ defect cluster formation through various configurations is discussed. Furthermore, the investigation of strain applied in the crystal and their association with the band gap of the material is considered.

Concluding remarks and future work are discussed in Chapter 10. Here, the outcomes of the research included in the present thesis are summarized and the potential for further investigation of energy materials is provided.

# REFERENCES

---

[1] E. Kendrick and P. R. Slater, Battery and solid oxide fuel cell materials. *Annual Reports on the Progress of Chemistry, Section A: General Physical and Inorganic Chemistry*, **109**, 396, (2013).

[2] S. Chu and A. Majumdar, Opportunities and challenges for a sustainable energy future. *Nature*, **488**, 294, (2012).

[3] J. Tollefson, Car industry: Charging up the future. *Natur*e, **456**, 436, (2008).

[4] Y. Ding, Z. P. Cano, A. Yu, J. Lu and Z. Chen, Automotive Li-Ion Batteries: Current Status and Future Perspectives. *Electrochemical Energy Reviews*, **2**, 1, (2019).

[5] Z. P. Cano, D. Banham, S. Ye, A. Hintennach, J. Lu, M. Fowler and Z. Chen, Batteries and fuel cells for emerging electric vehicle markets. *Nature Energy*, **3**, 279, (2018).

[6] V. Etacheri, R. Marom, R. Elazari, G. Salitra and D. Aurbach, Challenges in the Development of Advanced Li-Ion Batteries: A Review. *Energy & Environmental Science*, **4**, (2011).

[7] Z. Lin, T. Liu, X. Ai and C. Liang, Aligning academia and industry for unified battery performance metrics. *Nature Communications*, **9**, 5262, (2018).

[8] J. Rogelj, M. d. Elzen, N. Höhne, T. Fransen, H. Fekete, H. Winkler, R. Schaeffer, F. Sha, K. Riahi and M. Meinshausen, Paris Agreement climate proposals need a boost to keep warming well below 2 °C. *Nature*, **534**, 631, (2016).

[9] H. Zhang, C. Mao, J. Li and R. Chen, Advances in electrode materials for Li-based rechargeable batteries. *RSC Advances*, **7**, 33789, (2017).

[10] M. Armand and J.-M. Tarascon, Building better batteries. *Nature*, **451**, 652, (2001).

[11] M. S. Islam and P. R. Slater Solid State Materials for Clean Energy: Insights from Atomic-scale Modelling. *MRS Bulletin*, **34**, 12, (2009).

[12] R. Marom, S. F. Amalraj, N. Leifer, D. Jacob and D. Aurbach, A review of advanced and practical lithium battery materials. *Journal of Materials Chemistry*, **21**, 9938, (2011).

[13] T.V.S.L. Satyavani, A. Srinivas Kumar and P.S.V. Subba Rao, Methods of synthesis and performance improvement of lithium iron phosphate for high rate Li-ion batteries: A review. *Engineering Science and Technology, an International Journal*, **19,** 178, (2016).

[14] X., He, Y. Zhu, and Y. Mo, Origin of fast ion diffusion in super-ionic conductors. *Nature Communications*, **8**, 15893, (2017).

[15] R. D. Shannon, Revised Effective Ionic Radii and Systematic Studies of Interatomic Distances in Halides and Chalcogenides. *Acta Crystallographica*, **32**, 751, (1976).

---

[16] J. Lee, A. Urban, X. Li, D. Su, G. Hautier and G. Seder, Unlocking the Potential of Cation-Disordered Oxides for Rechargeable Lithium Batteries. *Science,* **343,** 519, (2014).

[17] D. Parfitt, A. Kordatos, P.P. Filippatos and A. Chroneos, Diffusion in energy materials: Governing dynamics from atomistic modelling, *Applied Physics Reviews*, **4**, 031305, (2017).

# CHAPTER 2

# Literature Review

## 2.1. Introduction

The research community has been engaged in considerable efforts to face the challenges of future perspectives in energy storage applications. The global interest in sustainable energy has addressed the crucial significance of the discovery, design and exploitation of new materials that will ensure high performance in a clean environmental friendly and low-cost agenda[1, 2]. Suitable candidate materials should exhibit excellent cycling charge / discharge rates, high capacity and chemical stability[3, 4]. So far, a variety of experimental and theoretical studies have focused in the synthesis and characterisation of new and promising compositions whilst the connection of specific properties with the defect chemistry and intrinsic mechanisms is gaining a continuous attention and interest. In this section the limiting factors and challenges in energy applications such as $Li^+$ ion batteries technology are addressed while providing the background based on previous studies and recent trends. The technological developments as well as the scientific strategies to improve performance characteristics[5, 6, 7, 8] are considered. Well established compounds and new promising materials are presented whilst the associated terminology of conduction mechanisms and electrochemical reactions is also provided.

## 2.2. Pioneering materials

The requirements for solid-state lithium batteries with better capacity, safety, cycle performance, and durability have generated interest in materials with high lithium ion conductivity [9, 10, 11, 12, 13, 14]. Different types of materials are being considered for energy applications[15] while there is an increasing research interest in improving their properties and performance[16, 17]. Since the early '1990s, Sony $Li^+$-ion battery manufacturing and the recently employed Panasonic batteries for Tesla electric vehicles have made Li-ion batteries of particular interest to the industry and research communities[18, 19, 20]. The interest in this field has increased rapidly. The design principles for super-ionic conductors are continuously updated when it comes to both electrodes and electrolytes[21, 22]. As $Li^+$ exhibits a very low reduction potential, $Li^+$ based batteries present a very high cell potential. This scheme obtains, a high-power density and gravimetric / volumetric capacity. The positive (cathode) and negative (anode) are host structures where the guest $Li^+$ ions are accommodated. **Table 2.1** includes the electrochemical performance properties for potential candidate materials in energy storage applications.

**Table 2. 1** Electrochemical potential parameters and units of candidate materials for energy storage applications

| **Property** | **Units** |
|---|---|
| Gravimetric Capacity | $mA \cdot h\ g^{-1}$ |
| Volumetric Capacity | $mA \cdot h\ cm^{-1}$ |
| Gravimetric Energy Density | $W \cdot h\ kg^{-1}$ |
| Volumetric energy Density | $W \cdot h\ L^{-1}$ |
| Ionic / Electronic conductivity | $\Omega^{-1}\ m^{-1}$ |
| Diffusion coefficient | $m^2\ s^{-1}$ |

The intercalation compounds are categorised into several groups depending on their crystallography such as layered, spinel, olivine, borate and tavorite. $Li^+$- rich materials include compositions where more than one $Li^+$ – ion per formula can be extracted during charging. Furthermore, the point defect formation and migration enthalpies are strongly connected with the cationic vacancies to become the most important charge carriers in these structures[23]. Several selection criteria for electrode materials should be taken into consideration such as electrochemical potential, particle size (ionic radius) and electronegativity.

Among the most commercially successful cathode materials are **$Li_xCoO_2$** layered crystal structures[24], whose formula is described as $ABO_2$ where A is an alkali metal ion and B corresponds to a transition metal. The crystallographic structure is illustrated in **Figure 2.1**. Both of the A and B species are surrounded by octahedral configurations of oxygen atoms occurring to alternate layers within the structure. Notably, these structures often exhibit transformation and coexistence of different phases, affecting the overall performance in conditions of inclusion and removal of the alkali cations.

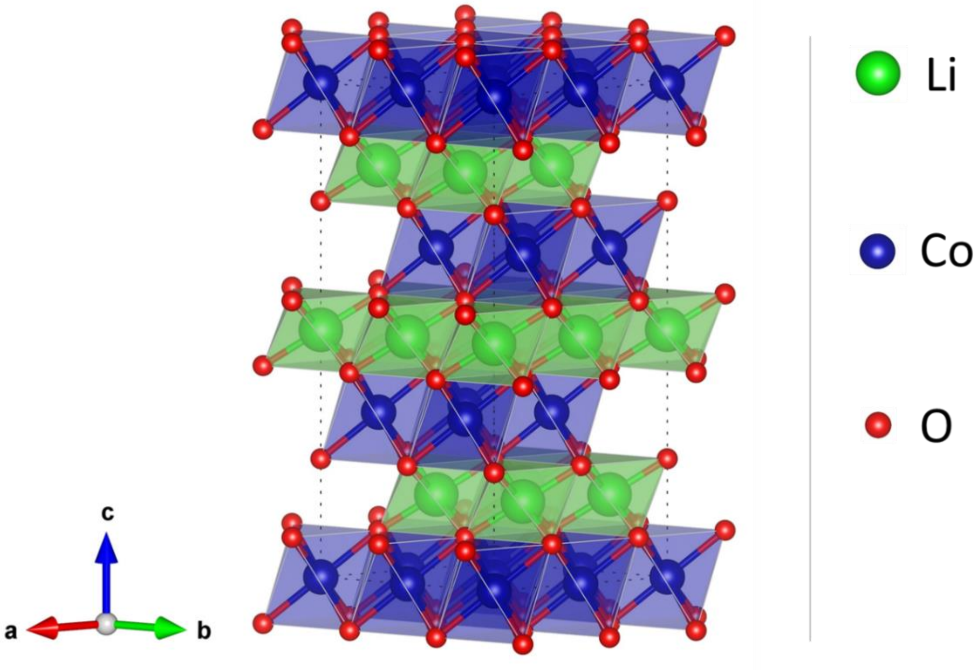

**Figure 2.1**. The crystallographic structure of $Li_xCoO_2$.

So far, the most applicable cathode compound used in electrochemical cells has been $LiCoO_2$ (LCO)[25]. However, despite LCO's theoretical capacity, a structural instability is reported at high rates of delithiation (above 50%), a major issue already being addressed when designing new materials. Furthermore, the high cost of Co ($33.000 / Kg), poor thermal stability (Melting point is 1768 K) and toxicity (The immediately dangerous to life and health - IDLH value is 20 $mg/m^3$)[26] required alternatives based on similar structures[27]. The substitution of Ni and Mn at the transition metal site offers promising possibilities if this overcomes the transition of the layered structure to spinel. Computational studies[28] have reported on the $LiCoO_2$ electronic and transport properties where the barrier for Li mobility is estimated at 0.44 eV. $LiNiO_2$ (LNO) is proposed as an attractive alternative due to its similar theoretical capacity to LCO and high energy density, however the $Li^+$ /$Ni^{4+}$ antisite formation (cation exchange) is reported as the main factor justifying its poor rate performance, as $Li^+$ migration pathways are blocked during synthesis and delithiation[29]. Furthermore, $LiMnO_2$ (LMO) has attracted significant interest as Mn is much cheaper and less toxic than Co or Ni. The limited cycling performance however is attributed to the structural transition from layered to spinel during $Li^+$ ion extraction where a considerable leak of $Mn^{3+}$ during cycling is under investigation.

Despite the majority of commercialised $Li^+$ - ion electrochemical cells using $LiMO_2$ (M=Co, Ni, Mn, Al, Co) layered oxides as cathode materials, high voltage spinel oxides ($AB_2O_4$ cubic) have been also extensively investigated[30]. The most famous commercialised spinel oxide is $LiMn_2O_4$, whose structure is represented in **Figure 2.2** and with its general composition being $LiMn_{2-x}M_xO_4$, where M corresponds to the transition metal element. The material shows a 3D Li – ion transport and recent studies in doped $Mn^{3+}$ spinels (including elements such as Ti, Cr, V, Cu, Co, Fe and Ni) report on the reduced $Li^+$ migration energy barrier for Co and Cu doping processes. Investigation into the defect chemistry of spinels suggests that cation antisite formation is the most favourable intrinsic defect.

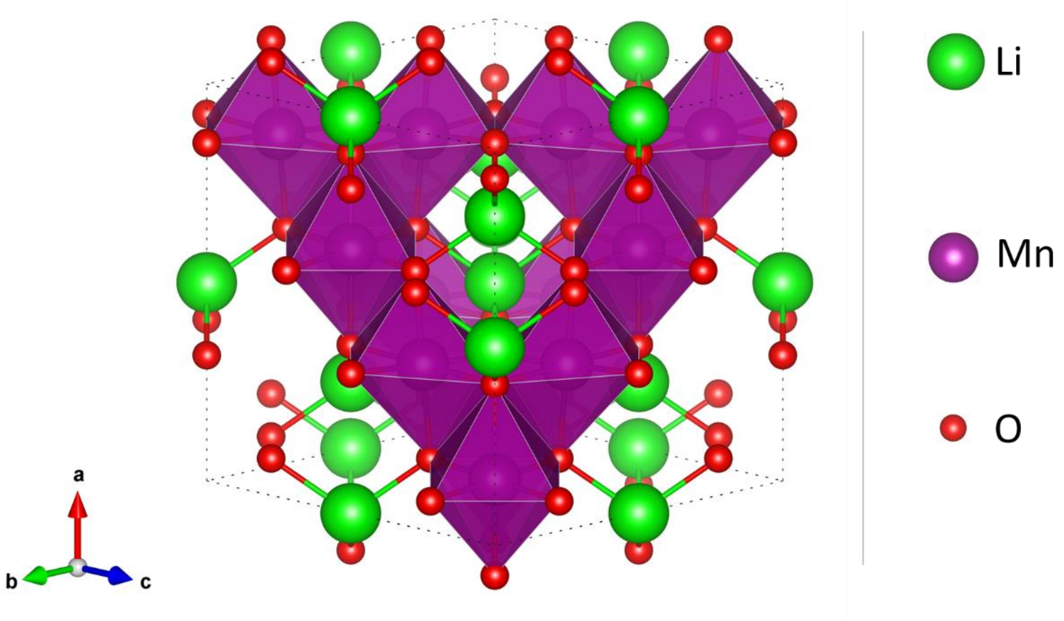

**Figure 2.2** The crystallographic structure of $LiMn_2O_4$ spinel.

Polyanion compounds are a new class of potential cathode materials. Phosphate structures of the $Li_xMPO_4$ formula such as olivine-type $LiFePO_4$[31] ($A_2BO_4$ based on magnesium iron silicate - Orthorhombic lattice) present relatively high rates of ionic diffusion through 1D pathways with a very low activation energy of migration (0.1 – 0.2 eV). **Figure 2.3** illustrates the $LiFePO_4$ crystallographic structure. System whose lattice positions are occupied by $(XO_4)^{3-}$ (X=W, S, P, Mo, As and Si) polyanion frameworks correspond to an increased redox potential and high phase stability[32]. Despite the high-power capability and thermal stability of $LiFePO_4$, the low electrical and ionic conductivity limit its applicability for commercial exploitation. Thus, particle size reduction, carbon coating and cationic doping are considered as promising strategies to improve the materials properties. The most favourable intrinsic defect is the Li / Fe antisite effect[33, 34], also reported for other olivine structures $LiMPO_4$ (M=Mn, Co, Ni) as well[11].

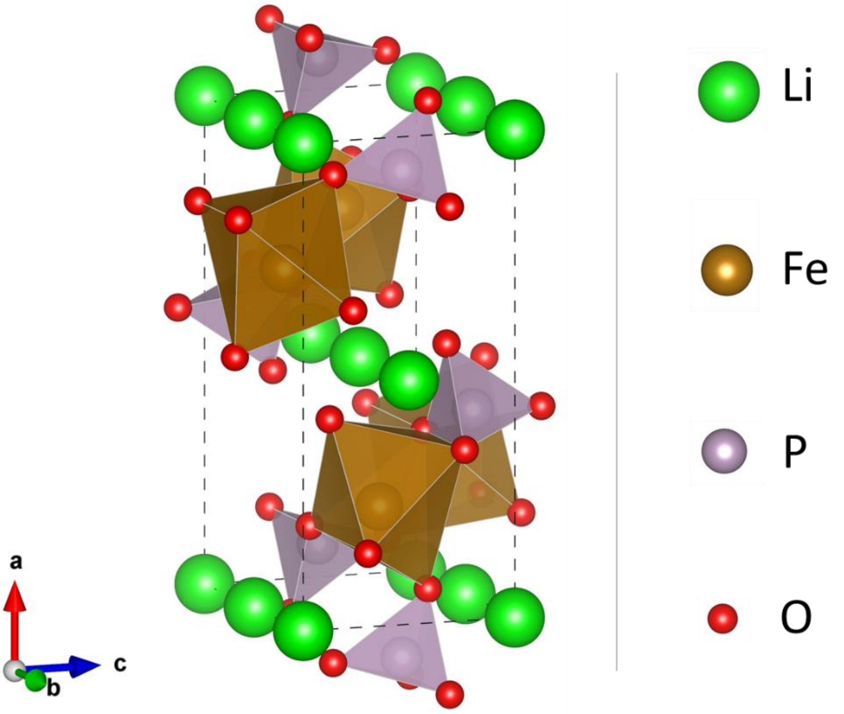

**Figure 2.3** The crystallographic structure of $LiFePO_4$ olivine-type phosphate.

Notably, $LiCoO_2$ exhibits the highest electronic and ionic conductivity compared to $LiFePO_4$ and $LiMn_2O_4$. A comparable study[35] on the kinetics of $Li^+$- ion transport at $LiCoO_2$, $LiMn_2O_4$ and $LiFePO_4$ cathodes (with layered, spinel and polyanion structures respectively) reports on the lithiation / delithiation processes, whereas the compatibility of those structures with the $LiC_6$ anode is also discussed. Specifically, electrochemical impedance spectroscopy (EIS) has been applied to estimate the charge transfer resistance. $LiFePO_4$ corresponds to the lowest value of 6.0 Ω followed by 55.4 Ω and 88.5 Ω for $LiCoO_2$ and $LiMn_2O_4$ respectively. The trend is also followed by the charge transfer activation energies, however the current density for the three cathodes is reported to exhibit comparable values ($0.55 \cdot 10^{-2}$ – $1 \cdot 10^{-2}$ mA $cm^{-2}$ at T = 298 K). Notably, in this study the theoretical capacities correspond to 120 mA·h $g^{-1}$ for $LiMn_2O_4$, 140 mA·h $g^{-1}$ for $LiCoO_2$ and 170 mA·h $g^{-1}$ for $LiFePO_4$.

Anode materials have been also investigated with respect to their electrochemical reaction with $Li^+$ - ions[36]. As the main duty of the anode material is to carry on the delithiation process during charging, the cell will reach a fully charged state when the cell voltage is at its maximum value[37]. The most commercially exploited anode has been conventional graphite in conjunction with $LiCoO_2$, $LiMn_2O_4$ and $LiFePO_4$ as positive electrodes. Optimising the graphite structural modification would be beneficial for the battery's performance. The introduction of fluorine is proposed to improve the Li-ion diffusion through the graphene layers and lead to a capacity increase. Furthermore, this doping process is questionable as the delithiation process is not affected. The anode and cathode in the electrochemical cell are separated through an electrolyte material. Solid-state inorganic electrolytes are extensively investigated with respect to their material properties as well as the potential tuning of specific features such as diffusivity[22]. The ionic size and lattice volume are strongly connected with the ionic transport while controlling the anion packing is considered to optimize the systems behaviour[21]. Electrolytes should exhibit good lithium diffusion rates but low electronic conduction in order to avoid short-circuit formation. Polymers and glasses are among the most famous electrolytes, however ceramic materials are also considered to be advantageous due to safety issues[38, 39]. Liquid electrolytes have presented incidents of flammability increasing the risks for their applicability. This is due to the mixture of lithium salt ($LiPF_6$) with solvents such as ethylene carbonate (EC), dimethyl carbonate (DMC), diethyl carbonate (DEC) as well as ethyl methyl carbonate (EMC), which are considered as highly flammable compounds[40,

[41]. The safety issues in lithium-ion batteries mainly refer to overcharge, dendritic lithium formation, thermal runaway and current-collector dissolution.

Overcharge state occurs when electricity flows through the cell in conditions of already full capacity, whereas thermal runaway corresponds to an exothermic reaction that is not under control.  Specifically, the case of thermal runaway that is related to both overcharge and overheating and will ultimately result to fire or battery explosion especially for large packs. Dendritic lithium formation grown on the surface of the anode is one the most important factors when considering risks of safety as it leads to internal short-circuits in lithium-ion batteries due to the connection of the positive and negative electrodes. Thus, investigation of new electrolyte materials of all-solid-state batteries as well as the improvement of electrode compounds through coating[42] is among the key challenges of Li-ion battery research in order to achieve high energy density and safety against flammability.

## 2.3. Novel structures and perspectives

Monoclinic $Li_3V_2(PO_4)_3$ has also been considered as a cathode material in an effort to overcome the LCO limitations, due to its structural stability and high rate of cycling performance[43]. It exhibits the highest theoretical capacity of 197 $mA{\cdot}h\ g^{-1}$ when compared to a variety of olivine-type phosphates like $LiMnPO_4$ (171 $mA{\cdot}h\ g^{-1}$), $LiCoPO_4$ (167 $mA{\cdot}h\ g^{-1}$) or $LiNiPO_4$ (169 $mA{\cdot}h\ g^{-1}$)[44]. This is due to the $Li^+$ excess in the unit cell formula where three $Li^+$-ion are available for the lithiation / delithiation process. However, low reversibility is reported as only 2 $Li^+$-ions are extracted in conditions of operation, delivering a discharge capacity of 173.2 $mA{\cdot}h\ g^{-1}$ [45] or even lower (132 $mA{\cdot}h\ g^{-1}$)[46]. Furthermore, it is characterised by low intrinsic electronic conductivity while the activation energy of $Li^+$-ion migration is calculated to be 0.4 eV along the a-axis through atomistic simulations[47], with a rapid diffusion of ions[48] corresponding to the diffusion coefficient calculated to be approximately $D_{Li+} = 10^{-11}$ $cm^2$ $s^{-1}$ at room temperature (298 K)[43]. The capacity fading issue has been investigated[49] and it is proposed that an effective technique to preserve the charge / discharge rates is the material's orthorhombic phase stabilization at room temperature[50]. Notably, the structural modifications from monoclinic to orthorhombic are reported to be fully reversible by cooling down to the room temperature.

Promising new compositions such as $Li_{1.211}Mo_{0.467}Cr_{0.3}O_2$ (LMCO) have been extensively investigated[51] demonstrating high levels of diffusion and good cycling tolerance, whereas the structures exhibit various states of disorder. $Li^+$ – ion migration in LMCO involves hopping based on the arrangement of the transition metal ions around $Li^+$. Notably, the migration energies are driven by the associated forces of electrostatic repulsion in the crystal. Silicate structures $Li_2MSiO_4$ (M=Fe, Mn, Co) have also attracted significant interest due to their high abundancy of silicon and iron[52] as well as the potential extraction of two $Li^+$ ions per formula[53]. The first material to be investigated was $Li_2FeSiO_4$[54]. Recently, orthorhombic $Li_2MnSiO_4$ has been investigated[55] as a potential cathode material mainly due to its high reversible capacity wherein the $Li^+$ - ions per formula can be completely extracted / reinserted. This is an important difference to $LiFeSiO_4$. Furthermore, this study has shown the effect of strain effects in the materials properties such as Li – ion conduction and Li / Mn antisite defect formation. Furthermore, tavorites such as $LiFePO_4F$ and $LiVPO_4F$ present similar characteristics with the olivines whereas their limitations in applicability are linked with their low power density. Additionally, it is reported that the introduction of Fluorine in the olivine structure leads to the transition of $Li^+$ diffusivity from 1D to multidimensional pathways. $LiVPO_4F$ has been reported to have excellent cycling performance and structural stability whereas $LiFePO_4F$ presents a limited $Li^+$ extraction mainly due to the high redox potential of $Fe^{3+}/Fe^{4+}$. Borates of the $BO_3$ polyanion group (TM = Mn, Co, Fe) are considered to present higher energy densities than other cathode materials, however much work has to be done in synthesis optimization and the understanding of kinetics in the atomic scale[53]. Recently, rocksalt-type structures $Li_3MO_4$ (Ru, Nb, Sb, Ta) have gained lots of interest and are being investigated as good ionic conductors[56] as they present anionic redox activity towards Li. Notably, the associated research and literature is still limited. Mn-doped $Li_3NbO_4$ exhibits high reversible capacity[57] while the Ni-doped material is able to present higher $Li^+$ - ion conductivity[58]. Furthermore $Li_3SbO_4$ presents good cyclability, however its low capacity is a crucial factor that should be addresed in future works. The structural diversity due to electrostatic interactions and Janh – Teller distortions on these systems is also reported. Lithium Zirconates such as $Li_2ZrO_3$ and $Li_6Zr_2O_7$ are good ionic conductors and piezoelectric crystals present attractive electrochemical properties and performance[59]. Specifically, $Li_2ZrO_3$ has been proposed as a battery material and a fussile material for nuclear applications investigated through experimental (Nuclear Magnetic Resonance, X – Ray Diffraction, Neutron diffraction) and also computational methods[60]. Electrochemical characterisation tests point to the excellent cycle performance and rate capability mainly attributed to the structural stability of the material[61], whereas fast $Li^+$-ion diffusion is also exhibited. Recently, the bottle-neck ionic transport in $Li_2ZrO_3$ has been reported as expanding interest in the intrinsic processes[62]. As these materials have been also investigated for $CO_2$ chemisorption, $Li_2CuO_2$ is an interesting structural system for both types of applications. As a potential candidate for $Li^+$ – ion batteries[63] and as a

$CO_2$ absorbent[64], it has recently attracted considerable interest. Despite its attractive properties such as its high theoretical capacity as well as Cu abundancy and low cost, the low structural stability and capacity loss has limited its potential. This was mainly attributed to the phase transitions during charging. It is characterised by the orthorhombic crystal structure that often falls into a close-packed layered atomic configuration. Controlling on the phase transitions is a fundamental strategy to preserve its capacity and cyclablility as required for a reliable cathode component. $Li_2SnO_3$ has been experimentally investigated as showing an attractive electrochemical performance with good cycling stability and high capacity[65]. Also layered $Li_2RuO_3$ is considered as a potential cathode due to the potential accommodation of both $Li^+$ and $Na^+$ ions in its structure. This will enhance the material's applicability in hybrid batteries[66] based on cation mixing. Interestingly, recent studies point to the limitations as both $Li^+$ – ions per formula can be extracted but only one is able to participate in the cycling process. However, good reversible intercalation processes have been reported combined with a good structural stability[67].

Sodium batteries[68] have also been considered as promising alternatives to $Li^+$ - ion battteries[69] initially focusing on $Na_{0.44}MnO_2$[70] that despite high capacity and cycling properties, presents limited applicability due to unstable intermediate phases during the extraction mechanisms in electrochemical cycles. Specifically, $Na_xMnO_2$ where x is in the range of 0.19 - 0.66 has been tested and capacity fading is attibuted to the biphasic region between 0.44 - 0.55 at low potential operation due to slower sodium diffusion in the intermediate phases. Furthermore, surface reactions and volume change occuring through assymetric evolution of the lattice parameters due to Jahn-Teller effects should be addresed as important factors to cycle performance.

It is an emerging approach to investigate and compare the same formula as a $Li^+$ and $Na^+$ ion battery compound[71]. An analogue of $NaMPO_4$ (M=Fe, Mn)[72] and its comparison with $Na_2FePO_4F$ showed that $Na^+$ ions in $NaFePO_4$ correspond to a lower activation energy of migration compared to $Li^+$ in $LiFePO_4$. In addition, these studies point to the importance of volume expansion during de-intercalation as this is connected to capacity fade. Synthesis of $NaMn_2O_4$ under high pressure has been recently considered[73] as a cathode material due to its stable cycle performance at room and high temperatures, however its overall capacity has to be improved. Specifically, despite its high theoretical capacity calculated to be 136.18 $mA \cdot h\ g^{-1}$, the discharge value is far below, at 65 $mA \cdot h\ g^{-1}$. This may be attributed to the large particle size that affects the overall electrochemical performance. To overcome this limitation, the Jahn – Teller effect should be minimized whereas the size of the cathode will also act beneficially to reduce the capacity fading.

Recent investigations on anode[74] materials have been fruitful based on the introduction of metals such as Si, Sn, Sb and Ge as well as metal oxides[75] such as $Fe_2O_3$, $Co_3O_4$ and $CuO_2$ as they provide capacities that are almost doubled when compared to graphite[43]. The aforementioned different approaches have been categorized as alloy / de-alloy and conversion materials respectively. Silicon based structures exhibit a high theoretical capacity despite their close-packed lattice configuration, where the $Li^+$ accommodation is often accompanied by a very high volume expansion. As an alternative to Si, Ge, Sb and Sn based materials have also attracted considerable interest due to their high theoretical capacities, however the volume expansion due to the lithiation / delithiation processes is among their major limitations[37]. Recent work[76] considers spinel-type titanates $LiMTiO_4$ (M=Mn, Fe, Co) as potential candidates for anode materials, where $LiCoTiO_4$ is reported to be the most promising. However, more experimental and theoretical work is demanded as $LiMnTiO_4$ has been also proposed as a cathode[77].

Furthermore, anodes must overcome the short circuiting that may lead to increased risks of flammability. Intercalation of $Li^+$ through graphite layers is occurred promoting mechanical stability, electrical and ionic conductivity[29]. Carbon presents high gravimetric capacity. However, the volumetric capacity of graphite electrodes is limited. Titanium dioxide $TiO_2$ is also considered as a very promising material for anodes that has already attracted a lot of interest due to its chemical stability, where it is suitable for mass production in a safe and cost-effective way. Fluorine doping may not drastically affect the total performance of the optical absorption however the electronic structure will be changed through the formation of surface oxygen vacancies. Among the advantages of $TiO_2$ is its high photocatalytic activity and oxidation capability. It has been investigated as a potential electrode for $Li^+$ and $Na^+$ batteries as well. Investigation for new electrolyte materials has also presented considerable progress. Disordered structures such as $LnBaCo_2O_{5.5}$[78] and lithium lanthanum titanates ($La_{2/3-x}Li_{3x}TiO_3$ - LLTO)[79] have attracted a lot of attention due to their high ionic conductivities and non-Arrhenius behaviour. LLTO is a perovskite, illustrated in **Figure 2.4**. Perovskites are oxide materials with the general formula of $ABO_3$. They exhibit an approximately cubic atomic configuration where the A ion is surrounded by eight $BO_6$ corner-sharing octahedra.

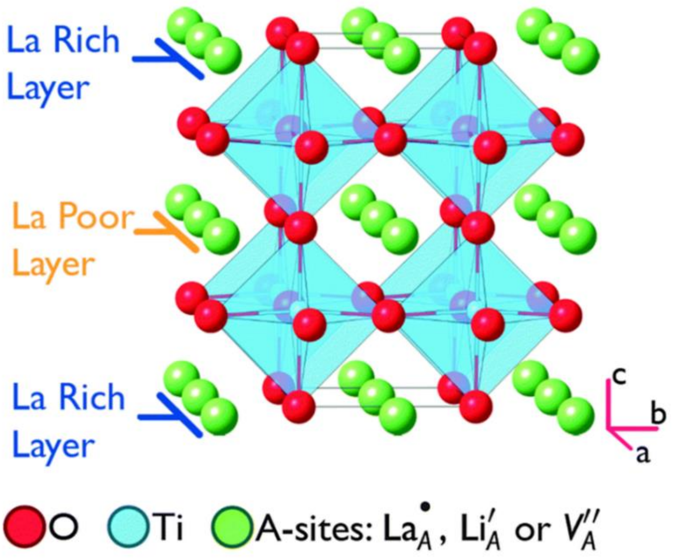

**Figure 2.4** The structure of $La_{2/3-x}Li_{3x}TiO_3$[79]

The materials $Li^+$ diffusivity has occurred through vacancy hopping in the lattice, being homogeneous and isotropic. Additionally, the diffusion pathways exhibit a 3D network in various directions. Notably, this work has also pointed out the potential predictive role of atomistic simulations in materials chemistry. Recently, monoclinic $LiMnBO_3$ has been investigated[80] with respect to the $Li^+$ ion diffusion channels adressing the mechanism to the atomic scale using both computational and experimental methods. Here, cation disorder strongly affects the intercalation kinetics processes in the material. The species transport follows a single dimensional pattern whereas the particle size has a major impact as well. Furthermore, the Li / Mn antisite formation leads to the pathways blocking, limiting the Li – ion extraction. In addition, the ionic conductivity in alkali nitrides $MNO_2$ ($M=Li^+$, $Na^+$, $K^+$, $Rb^+$ and $Cs^+$) as potential electrolyte materials has been also reported[81] mainly due to their stability at elevated temperatures. Overall, the systems defect processes and intrinsic mechanisms are linked as a function to the M cation size, therefore $CsNO_2$ exhibits the highest ionic conductivity among them. $Li^+$ ionic conductivity enhancement in $Li_{4\pm x}Si_{1-x}X_xO_4$ (X = P, Al or Ge) through substitution on Si sites has been also recently reported[82] to identify the relation of the ionic transport and the local host structure through theoretical and experimental techniques.

Notably, the formation of solid electrolyte interface (SEI)[83] is among the most important features in electrochemical cells. SEI is formed at the interface of anode and electrolyte during the first cycle of charge / discharge affecting the charge “loss”, rate capability and cyclability. Furthermore, it prevents the graphite anode exfoliation and blocks the electron transport through the electrolyte while allowing the ions to travel from cathode to anode. In other words, SEI should be ionically conductive but electronically insulating. This is among the most important of considerations, as SEI drastically affects the chemical reactions in a potential application. Notably, SEI is of great significance for safety issues as its possible decomposition (due to overheating of physical abuse)[84] will lead to combustion and finally expolsion of the battery[38].

## 2.4 Conduction Mechanisms – Electrochemistry

The electrochemical reactions of energy applications have been extensively investigated. The $Li^+$ intercalation / deintercalation in cathodes is strongly connected with electrical and ionic conductivity. Optimizing the capacity and overall performance is linked with the mechanisms of ionic and electronic conduction in positive (cathode) and negative (anode) electrodes[85]. Notably, the instrinsic mechanisms are linked to the chemical bonding of atoms. **Figure 2.5** illustrates the conduction phenomena in a cathode olivine particle during charge.

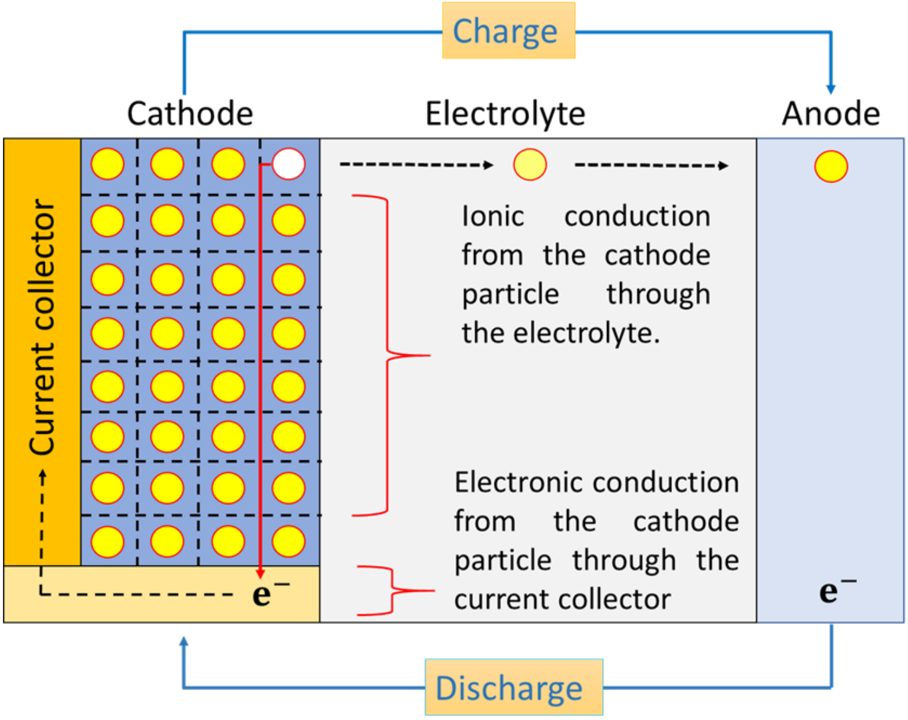

**Figure 2.5** Electronic and ionic conduction phenomena during charge / discharge

When a Li-ion diffuses from the cathode through the electrolyte (ionic coduction), it causes a valence state charge for the transition metal ion (electronic conduction) or alternatively the $Fe^{2+}$ ion is oxidized to $Fe^{3+}$. The diffusivity of cations within the electrolyte from cathode and anode and vice-versa corresponds to the maximum charging and discharging rates (power density) as well as being a measuring factor of the cells tolerance in repeated charging cycles. From the condensed matter approach, ion transport will occur through the path that corresponds to the minimum potential energy, or the lowest activation energy of migration. Thus, higher diffusivity corresponds to higher charge / discharge rates. Electronic conduction in battery materials is also important for the intercalation processes, however the exact relation with ionic conduction is not yet clarified. Notably, diffusion in the solid state is an intrinsically atomic process, governed by the transport of species leading to a position exchange with neighbours, from one side of an electrochemical cell to another.[24] Ionic crystals with a high Frenkel defect concentration correspond to low activation energies of migration and higher ionic conductivities. Among the most important aspects considered in energy materials such as LiBs are the properties of the host structure, the mechanisms of $Li^+$ insertion / extraction (transport properties), electronic conductivity and $Li^+$ diffusion, as well as synthesis and electrochemical properties[43]. In addition the intrinsic defect chemistry of electrode materials affect the performance of an electrochemical cell (high concentration of antisite defects block vacancy diffusion mechanisms of $Li^+$ - ion). The dimensionality of ionic diffusion is crucial for the charge / discharge rate capabilities. Layered series / rocksalt compounds exhibit 2D diffusion whereas olivines are expected to present a 1D diffusion. Additionaly, the insertion / extraction of $Li^+$ ions should not affect the host structure stability whereas any phase transformations due to high temperature in operation conditions, must be fully reversed. Among other techniques, applied mechanical strain is reported as beneficial in the materials behavior.

### 2.5 Summary

Understanding defect processes in energy materials is not only important for battery applications but also for solid-oxide fuel cells (SOFCs), photocatalytic and nuclear applications. This section provided a brief description of the research challenges based on previous works as well as future perspectives on the approach to the materials design and the links with their defect chemistry and associated mechanisms, such as diffusion and electronic conduction. Despite the accurate descriptions of the materials’ behaviour through experimental techniques (X-ray Diffraction and Nuclear Magnetic Resonance among others), the importance of atomic scale simulations required to determine in detail the intrinsic defect processes and diffusivity mechanisms is particularly highlighted. A greater insight into the defect properties of energy materials is crucial to a full understanding of their electrochemical behaviour in potential applications. Theoretical modelling can complement and interpret experimental results such as cation mixing by providing detailed information on the defect chemistry and dynamics. In the present thesis, the defect processes of specific structures are investigated, originating from the energy materials research agenda whilst highlighting their properties with respect to potential energy applications.

## REFERENCES

---

[1] Y.-G. Guo J.-S. Hu and L.-J. Wan, Nanostructured Materials for Electrochemical Energy Conversion and Storage Devices. *Advanced Materials*, **20**, 2878, (2008).

[2] H. Li, Z. Wang, L. Chen and X. Huan, Research on Advanced Materials for Li-ion Batteries. *Advanced Materials*, **21**, 4593, (2009).

[3] A. S. Aricò, P. Bruce, B. Scrosati, J.-M. Tarascon and W. V. Schalkwijk, Nanostructured materials for advanced energy conversion and storage devices. *Nature Materials*, **4**, 366. (2005).

[4] C. Liu, F. Li, L.-P. Ma and H.-M. Cheng, Advanced Materials for Energy Storage. *Advanced Materials*, **22**, 28, (2010).

[5] Q. Wang, B. Jiang, B. Li and Y. Yan, A critical review of thermal management models and solutions of lithium-ion batteries for the development of pure electric vehicles. *Renewable and Sustainable Energy Reviews*, **64**, 106, (2016).

[6] L. Lu, X. Han, J. Li, J. Hua and M. Ouyang, A review on the key issues for lithium-ion battery management in electric vehicles. *Journal of Power Sources*, **226**, 272, (2013).

[7] J. B. Goodenough and Y. Kim, Challenges for Rechargeable Li Batteries. *Chemistry of Materials*, **22**, 587, (2010)

[8] A. N. Jansen, A. J. Kahaian, K. D. Kepler, P. A. Nelson, K. Amine, D.W. Dees, D. R. Vissers and M. M. Thackeray, Development of a high-power lithium-ion battery. *Journal of Power Sources*, **81**, 092, (1999)

[9] J.-M. Tarascon, and M. Armand, Issues and challenges facing rechargeable lithium batteries. *Nature*, **414**, 359, (2001).

[10] M. Armand and J.-M. Tarascon, Building better batteries. *Nature*, **451**, 652, (2001).

[11] C. A. J. Fisher, V. M. Hart Prieto and M. S. Islam, Lithium battery materials $LiMPO_4$ (M = Mn, Fe, Co, and Ni): Insights into defect association, transport mechanisms, and doping behavior. *Chemistry of Materials*, **20**, 5907, (2008).

[12] P. G. Bruce, S. A. Freunberger, L. J. Hardwick and J.-M. Tarascon, Li-$O_2$ and Li-S batteries with high energy storage. *Nature Materials*, **11**, 19, (2012).

[13] N. Kamaya, K. Homma, Y. Yamakawa, M. Hirayama, R. Kanno, M. Yonemura, T. Kamiyama, Y. Kato, S. Hama, K. Kawamoto and A. Mitsui, A lithium superionic conductor. *Nature Materials*, **10**, 682, (2011).

[14] X. He, Y. Zhu and Y. Mo, Origin of fast ion diffusion in super-ionic conductors. *Nature Communications*, **8**, 15893, (2017).

---

[15] S. Chu, Y. Cui and N. Liu, The path towards sustainable energy. *Nature Materials*, **16**, 16, (2017).

[16] B. C. Steele and A. Heinzel, Materials for fuel-cell technologies. *Nature*, **414**, 345, (2001).

[17] K. Kang, Y. S. Meng, J. Bréger, C. P. Grey and G. Ceder Electrodes with high power and high capacity for rechargeable lithium batteries. *Science*, **311**, 977, (2006).

[18] I. Bloom, S. A. Jones, V. S. Battaglia, G. L. Henriksen, J. P. Christophersen, R. B. Wright, C. D. Ho, J. R. Belt and C. G Motloch, Effect of cathode composition on capacity fade, impedance rise and power fade in high-power, lithium-ion cells. *Journal of Power Sources*, **124**, 538, (2003).

[19] Y. Itou and Y. Ukyo, Performance of $LiNiCoO_2$ materials for advanced lithium-ion batteries, *Journal of Power Sources*, **146**, 39, (2005).

[20] Z. P. Cano, D. Banham, S. Ye, A. Hintennach, J. Lu, M. Fowler and Z. Chen, Batteries and fuel cells for emerging electric vehicle markets, *Nature Energy*, **3**, 279, (2018).

[21] Y. Wang, W. Davidson Richards, S. P. Ong, L. J. Miara, J. C. Kim, Y. Mo and G. Ceder, Design principles for solid-state lithium superionic conductors. *Nature Materials*, **14**, 1026, (2015).

[22] J. C. Bachman, S. Muy, A. Grimaud, H.-H. Chang, Nir Pour S. F. Lux, O. Paschos, F. Maglia, S. Lupart, P. Lamp, L. Giordano and Y. Shao-Horn, Chemical Reviews Inorganic solid state Electrolytes for lithium batteries: Mechanisms and properties governing ion conduction. *Chemical Reviews*, **116**, 140, (2016).

[23] H. Ji, A. Urban, D. A. Kitchaev, D.-H. Kwon, N. Artrith, C. Ophus, W. Huang, Z. Cai, T. Shi, J. Chul Kim, H. Kim and G. Ceder, Hidden structural and chemical order controls lithium transport in cation-disordered oxides for rechargeable batteries. *Nature Communications*, **10**, 592, (2019).

[24] D. Parfitt, A. Kordatos, P.P. Filippatos and A. Chroneos, Diffusion in energy materials: Governing dynamics from atomistic modelling. *Applied Physics Reviews*, **4**, 031305, (2017).

[25] Z. Wang, Z. Wang, W. Peng, H. Guo, X, Li, J, Wang and A. Qi, Structure and electrochemical performance of $LiCoO_2$ cathode material in different voltage ranges. *Ionics*, **20**, 11, 1525, (2014).

[26] National Institute for Occupational Safety and Health

[27] H. J. Bang, H. Joachin, H, Yang, K. Amine and J. Prakash, Contribution of the Structural Changes of $LiNi_{0.8}Co_{0.15}Al_{0.05}O_2$ Cathodes on the Exothermic Reactions in Li-Ion Cells. *Journal of The Electrochemical* Society, **153**, A 731, (2006).

---

[28] B. Andriyevsky, K. Doll and T. Jacob Electronic and Transport properties in $LiCoO_2$. *Physical Chemistry Chemical* Physics, **16,** 23412, (2014).

[29] N. Nitta, F. Wu, J. T. Lee and G. Yushin, Li – ion battery materials: present and future. *Materials Today*, **18**, 252, (2015).

[30] S. Patoux, L. Daniel, C. Bourbon, H. Lignier, C. Pagano, F. L. Cras, S. Jouanneau and S. Martinet, High voltage spinel oxides for Li – ion batteries: From the material research to the application. *Journal of Power Sources*, **189,** 344, (2009).

[31] W.-J. Zhang, Structure and performance of $LiFePO_4$ cathode materials: A review. *Journal of Power Sources*, **196**, 6, 2962, (2011).

[32] K. S. Nanjundaswamy, A. K. Padhi, J. B. Goodenough, S. Okada, H. Ohtsuka, H. Arai and J. Yamaki, Synthesis, redox potential evaluation and electrochemical characteristics of NASICON-related-3D framework compounds. *Solid State Ionics*, **92,** 1, (1996).

[33] M. Saiful Islam and Peter R. Slater Solid State Materials for Clean Energy: Insights from Atomic-scale Modelling. *MRS Bulletin* **34**, 935 (2009).

[34] H. Liu, M.-J. Choe, R. A. Enrique, B. Orvañanos, L. Zhou, T. Liu, K. Thornton and C P. Grey, Effects of Antisite Defects on Li Diffusion in $LiFePO_4$. *The Journal of Physical Chemistry C*, **121**, 12025, (2017).

[35] A. Swiderska – Mocek and A. Lewandowski Kinetics of Li-ion transfer reaction at $LiMn_2O_4$, $LiCoO_2$, and $LiFePO_4$ cathodes. *Journal of Solid State Electrochemistry*, **21**, 1365, (2017).

[36] S. Goriparti, E. Miele, F. D. Angelis, E D. Fabrizio, R. P. Zaccaria and C. Capiglia Review on recent progress of nanostructured anode materials for Li-ion batteries. *Journal of Power sources*, **257**, 421, (2014).

[37] A. Eftekhari, Low-voltage materials for lithium-ion batteries. *Energy Storage materials*, **7,** 157, (2017).

[38] K. Liu, Y. Liu, D. Lin, A. Pei and Yi Cui, Materials for lithium-ion battery safety. *Science Advances*, **4,** (2018).

[39] T. M. Bandhauer, S. Garimella, and T. F. Fuller, A Critical Review of Thermal Issues in Lithium-Ion Batteries. *Journal of The Electrochemical Society*, **158**, 3, 1, (2011).

[40] J. Wen, Y. Yu, and C. Chen, A Review on Lithium-Ion Batteries Safety Issues: Existing Problems and Possible Solutions. *Materials Express*, **2**, 3, (2012).

[41] G. Balakrishnan, R. Ramesh and T. Prem Kumar, Safety mechanisms in lithium-ion batteries. *Journal of Power Sources*, **155**, 401, (2006).

---

[42] Q. Wang, P. Ping, X. Zhao, G. Chu, J. Sun and C. Chen, Thermal runaway caused fire and explosion of lithium ion battery. *Journal of Power Sources*, **208**, 210, (2012).

[43] X. Rui, Q. Yan, M, Skyllas-Kazacos and T. M. Lim $Li_3V_2(PO_4)_3$ cathode materials for lithium-ion batteries: A review. *Journal of Power sources*, **258,** 19, (2014).

[44] Z. Gong and Y. Yang, Recent advances in the research of polyanion-type cathode materials for Li-ion batteries. *Energy & Environmental* Science, **4**, 3223, (2011).

[45] J. S. Yun, S. Kim, B.-W. Cho, K.-Y. Lee, K. Y. Chung, and W. Chang, Synthesis and Electrochemical Properties of $Li_3V_2(PO_4)_3$-$LiMnPO_4$ Composite Cathode Material for Lithium-ion Batteries. *Bulletin of the Korean Chemical Society*, **34**, 433, (2013).

[46] Zhu X., Yan Z., Wu W., Zeng W., Du Y., Zhong Y., Zhai H., Ji H., and Zhu Y., Manipulating size of $Li_3V_2(PO_4)_3$ with reduced graphene oxide: towards high-performance composite cathode for lithium ion batteries. *Scientific Reports*, **4**, 5768, (2014).

[47] S. Lee and S.S. Park, Atomistic Simulation Study of Monoclinic $Li_3V_2(PO_4)_3$ as a Cathode Material for Lithium Ion Battery: Structure, Defect Chemistry, Lithium Ion Transport Pathway, and Dynamics. *The Journal of Physical Chemistry C*, **116**, 25190, (2012).

[48] M. Hu, X. Pang and Z. Zhou, Recent progress in high-voltage lithium ion batteries. *Journal of Power Sources*, **237**, 229, (2013).

[49] L. Wang, J. Xu, C. Wang, X. Cui, J. Li, Y.-N. Zhou, A better understanding of the capacity fading mechanisms of $Li_3V_2(PO_4)_3$. *RSC Advances*, **5**, 71684, (2015).

[50] M. Sato, H. Ohkawa, K. Yoshida, M. Saito, K. Uematsu and K. Toda, Enhancement of discharge capacity of $Li_3V_2(PO_4)_3$ by stabilizing the orthorhombic phase at room temperature. *Solid State Ionics*, **135**, 137, (2000).

[51] J. Lee, A. Urban, X. Li, D. Su, G. Hautier and G. Seder, Unlocking the Potential of Cation-Disordered Oxides for Rechargeable Lithium Batteries. *Science*, **343,** 519, (2014).

[52] M. S. Islam and C. A. J. Fischer Lithium and Sodium battery cathode materials: computational insights into voltage, diffusion and nanostructural properties. *Chemical Society Reviews*, **43**, 185, (2014).

[53] B. Xu, D. Qian, Z, Wang and Y. S. Meng, Recent progress in cathode materials research for advanced lithium ion batteries. *Materials Science and Engineering: R: Reports*, **73,** 51, (2012).

[54] A. R. Armstrong, N. Kuganathan, M. S. Islam and P. G. Bruce, Structure and lithium transport pathways in $Li_2FeSiO_4$ Cathodes for Lithium Batteries. *Journal of the American Chemical* Society, **133**, 13031, (2011).

---

[55] M. Jia, H. Wang, Z. Sun, Y. Chen, C. Guo and L. Gan Exploring ion migration in $Li_2MnSiO_4$ for Li- ion batteries through strain effects. *RSC Advances*, **7,** 26089, (2017).

[56] Q. Jacquet, G. Rousse, A. Iadecola, M. Saubanere, M. – L. Doublet and J. – M. Tarascon Electrostatic interactions versus Second Order Jahn – Teller Distortion as the source of structural diversity in $Li_3MO_4$ compounds (M=Ru, Nb, Sb and Ta). *Chemistry of Materials*, **30**, 2, (2017).

[57] N. Yabuuchi, M. Takeuchi, M. Nakayama, H. Shiiba, M. Ogawa, K. Nakayama, T. Ohta, D. Endo, T. Ozaki, T. Inamasu, K. Sato and Shinichi Komaba, High-capacity electrode materials for rechargeable lithium batteries: $Li_3NbO_4$-based system with cation-disordered rocksalt structure. *Proceedings of the National Academy of Sciences of the United States of America*, **112**, 7650, (2015).

[58] V. L. Mc Laren, C. A. Kirk, M. Poisot, M. Castellanos and A. R. West, $Li^+$ ion conductivity in rock salt-structured nickel-doped $Li_3NbO_4$. *Dalton Transactions*, **19,** (2004).

[59] Y. Duan, Electronic Structural and Phonon Properties of Lithium Zirconates and Their Capabilities of $CO_2$ Capture: A First-Principle Density Functional Approach. *Journal of Renewable and sustainable energy,* **3**, 013102, (2011)

[60] A. R. Ferreira, K. Reuter and C. Scheurer, DFT simulations of $^7Li$ solid state NMR spectral parameters and $Li^+$ ion migration barriers in $Li_2ZrO_3$. *RSC Advances*, **6**, 41015, (2016).

[61] Y. Dong, Y. Zhao, H. Duan and J. Huang, Electrochemical performance and lithium-ion insertion/extraction mechanism studies of the novel $Li_2ZrO_3$ anode materials *Eletrochimica Acta*, **161,** 219, (2015).

[62] E. A. Sherstobitova, A. F. Gubkin, I. A. Bobrikov, A. V. Kalashnova and M. I. Pantyukhina, Bottle-necked ionic transport in $Li_2ZrO_3$: high temperature neutron diffraction and impedance spectroscopy. *Electrochimica Acta*, **209,** (2016).

[63] G. Ramos-Sanchez, I. C. Romero-Ibarra, J. Vasquez-Arenas, C. Tapia, N. Aguilar-Eseiza and I. Gonzales, Controlling $Li_2CuO_2$ single phase transition to preserve cathode capacity and cyclability in Li-ion batteries. *Solid State Ionics*, **303,** 89, (2017).

[64] K. Oh-ishi, Y. Matsukura, T. Okumura, Y. Matsunaga and R. Kobayashi, Fundamental research on gas–solid reaction between $CO_2$ and $Li_2CuO_2$ linking application for solid $CO_2$ absorbent. *Journal of Solid State Chemistry*, **211,** 162, (2011).

[65] Q. Wang, Y. Huang, Y. Zhao, W. Zhang and Y. Wang, Preparation of $Li_2SnO_3$ and its application in lithium-ion batteries. *Surface and Interface Analysis*, **45**, 1297, (2013).

[66] Y. Yao, P. Yang, X. Bie, C. Wang, Y. Wei, G. Chena and F. Du, High capacity and rate capability of a layered Li2RuO3 cathode utilized in hybrid $Na^+$/$Li^+$ batteries. *Journal of Materials Chemistry A*, **3**, 18273, (2015).

---

[67] M. -S. Park, Y. -G. Lim, J. -W. Park, J.-S. Kim, J.-W. Lee, J. H. Kim, S. X. Dou and Y.-J. Kim $Li_2RuO_3$ as an Additive for High-Energy Lithium-Ion Capacitors. *The Journal of Physical Chemistry C*, **117**, 11471, (2013).

[68] Jang-Yeon Hwang, Seung-Taek Myung and Yang-Kook Sun, Sodium-ion batteries: present and future. *Chemical Society Reviews*, **46**, 3529, (2017).

[69] P. K. Nayak, L. Yang, W. Brehm and P. Adelhelm, From Lithium-Ion to Sodium Ion Batteries: Advantages, Challenges and Surprises. *Angewandte Chemie International Edition*, **57**, 102, (2017).

[70] H. Kim, D. J. Kim, D. – H. Seo, M. S. Yeom, K. Kang, D. K. Kim and Y. Jung, Ab Initio Study of the Sodium Intercalation and Intermediate Phases in $Na_{0.44}MnO_2$ for Sodium-Ion Battery. *Chemistry of Materials*, **24**, 1205 (2012).

[71] C. Tealdi, J. Heath and M. S. Islam Feeling the strain: enhancing ionic transport in olivine phosphate cathodes for Li- and Na-ion batteries through strain effects. *Journal of Materials Chemistry A*, **4**, 6998, (2016).

[72] R. Tripathi, S. M. Wood, M. S. Islam and L. F. Nazar, Na-ion mobility in layered $Na_2FePO_4F$ and olivine Na [Fe, Mn] $PO_4$. *Energy and Environmental Science,* **6**, 2257, (2013).

[73] X. Liu, X. Wang, A. Iyo, H. Yu, D. Li and H. Zhou High stable post-spinel $NaMn_2O_4$ cathode for sodium ion battery. *Journal of Materials Chemistry* A, **2**, 14822, (2014).

[75] H. Li, X. Huang and L. Chen, Anodes based on oxide materials for lithium rechargeable batteries. *Solid State Ionics*, **123**, 189, (1999).

[76] M. Luo, H. Yu, H. Lan, L. Yan, S. Qian, W. Ye, M. Shui, N. Long and J. Shu, Synthesis and electrochemical characteristics of isostructural $LiMTiO_4$ (M = Mn, Fe, Co). *Ceramics International* **43**, 7, 5728, (2017).

[77] Y. Bao, X. Zhang, X, Zhang, L, Yang, X, Zhang, H, Chen, M, Yanga and D. Fang Free-standing and flexible $LiMnTiO_4$/carbon nanotube cathodes for high performance lithium ion batteries. *Journal of Power Sources,* **321**, 120 (2016).

[78] I. D. Seymour, A. Chroneos, J. A. Kilner and R. W. Grimes, Defect processes in orthorhombic $LnBaCo_2O_{5.5}$ double perovskites. *Physical Chemistry Chemical Physics*, **13**, 15305, (2011).

[79] E. E. Jay, M. J. D. Rushton, A. Chroneos, R.W. Grimes and J. A. Kilner, Genetics of superionic conductivity in lithium lanthanum titanates. *Physical Chemistry Chemical Physics*, **17**, 178, (2015).

---

[80] J. C. Kim, D.-H. Seo, H. Chen and G. Ceder, The effect of Antisite Disorder and particle size on Li intercalation kinetics in monoclinic $LiMnBO_3$ *Advanced Energy Materials*, **5**, 1401916, (2015).

[81] Y. Mateyshina and N. Uvarov Ionic conductivity of alkali nitrides *Solid State Ionics* **302,** 77, (2017).

[82] Y. Deng, C. Eames, B. Fleutot, R. David, J.-N. Chotard, E. Suard, C. Masquelier and M. Saiful Islam Enhancing the Lithium Ion Conductivity in Lithium Superionic Conductor (LISICON) Solid Electrolytes through a Mixed Polyanion Effect. *ACS Applied Materials & Interfaces*, **9**, 7050 (2017).

[83] P. Verma, P. Maire and P. Novak, A review of features and analyses of the solid electrolyte interphase in Li-ion batteries, *Electrochimica Acta*, **55,** 6332, (2010).

[84] F. Larsson, P. Andersson and B.-E. Mellander, Lithium-Ion Battery Aspects on Fires in Electrified Vehicles on the Basis of Experimental Abuse Tests. *Batteries*, **2**, 9, (2016)

[85] M. Park, X. Zhang, M. Chung, G. B. Less and A. M. Sastry, A review of conduction phenomena in Li-ion batteries, *Journal of Power Sources*, **195**, 7904, (2010).

# CHAPTER 3

# Point Defect Processes

## 3.1 Introduction

In this chapter the theoretical background of point defects, intrinsic processes in crystalline solids and diffusion mechanisms of ions is described with respect to the fields of condensed matter physics whereas the connection with the atomistic simulations' methodology employed for the thesis is highlighted. In crystalline structures, a major category of structural imperfections is the point defects. Intrinsic point defects correspond to disordered states in an atomic configuration in space or the lattice of system, often described by the anion and cation sublattices. The number, nature and concentration of point defects can be described by the temperature, pressure, composition and crystallographic information of the host lattice as well as the external conditions / environment. This category may include vacancies (missing atoms), interstitials (atoms that are in in-between sites and not in a lattice site of the solid), antisites (atoms that may occupy another atom position and vice versa) and dopants (foreign atoms introduced in the crystal as lattice sites or as interstitial.

**Figure 3.1** illustrates the vacancy, interstitial, Schottky and antisite defects in comparison with the perfect lattice formed by two different types of atoms. Point defects can be described as isolated species or through the formation of defect clusters[1]. Understanding the structures, energies, concentration of point defects as well as their interactions is crucial to interpret the mechanical and electronic properties of solids. Additionally, extrinsic defects such as dopants and their interaction with the host lattice is of crucial significance as they can modify its properties[2].

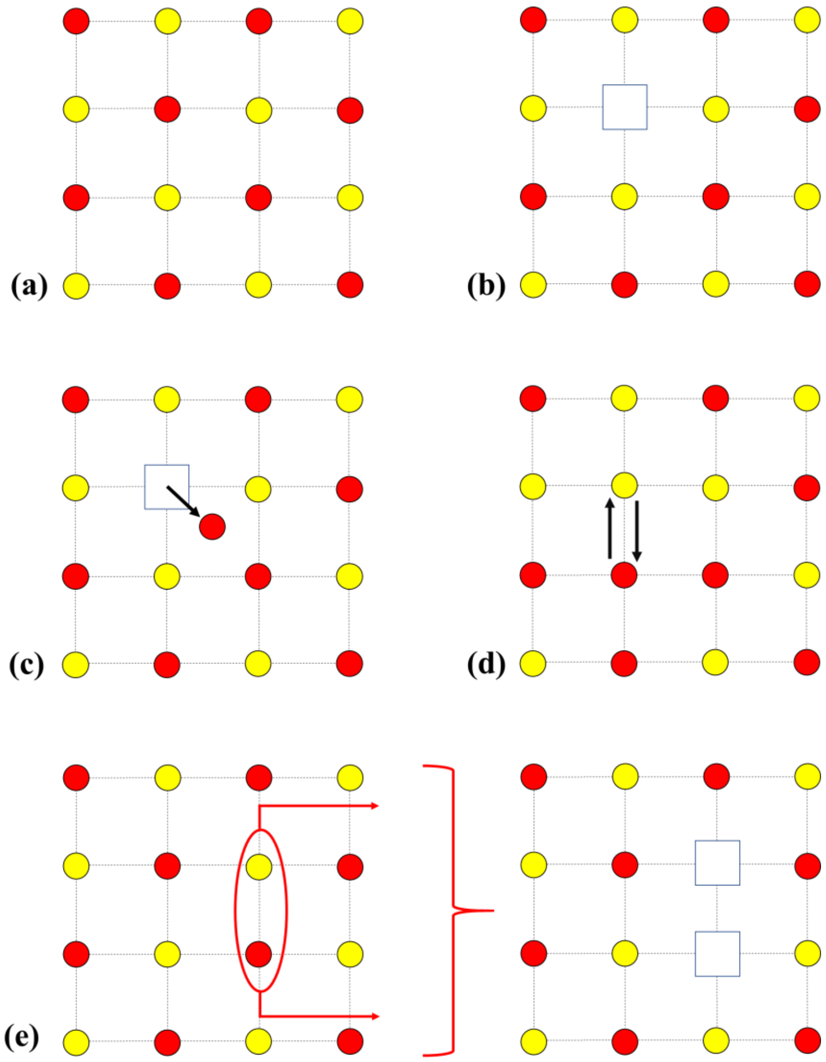

**Figure 3.1** Schematic representation of (a) The perfect lattice including 2 different types of atoms (b) The defect of a vacant site in the crystal (c) The movement of the atom from its initial position to an interstitial site (Frenkel mechanism) (d) The antisite defect of two neighbouring atoms (e) The Schottky mechanism.

The vacancy defect corresponds to the process where an atom of the host lattice leaves its initial position of equilibrium and lead to the creation of a vacant site in the crystal. This mechanism is strongly combined with the presence of occupied interstitial sites in the crystal as a consequence of the atom movement in the empty space in between the fixed crystallographic positions. This corresponds to the Frenkel mechanism. In addition, the defect chemistry investigation is affected by the general representation of the system in the atomic level that depends on the configurational factors such as the space group, structure type (perovskite, spinel etc) and crystallographic arrangement. Those defects are the most important for the mass transport approach and the dependence with the temperature and pressure justifies the characterization of thermodynamically reversible defects. Notably, different types of defects in the crystal are correlated and expected to affect its intrinsic properties and mechanisms in various ways. As a general principle, the energy that is demanded for the formation of each type of disorder in the system varies. Therefore, only one type of intrinsic structural disorder is dominant in the crystal as compared to the others. This is the characteristic type of disorder in the material and in order to target it, one has to examine every single possibility of intrinsic defects separately. The concentration of point defects can be described through the assumption that for a given set of ions, their crystal structure corresponds to the most stable and energetically favoured arrangement in the space. Thus, there is an energy barrier for the defects to be formed[3]. Defects form by balancing the increase of the enthalpy of the system by increasing the configurational entropy, thus point defects are entropically stabilized.

The Gibbs free energy $\Delta G_f$ (J) is associated with the entropy $\Delta S_f$ (J/K) and enthalpy $\Delta H_f$ (J) where T(K) is the temperature, as follows:

$$\Delta G_f = \Delta H_f - T\Delta S_f \quad \textbf{(3.1)}$$

For our reference, 1 J = $6.24150913 \times 10^{18}$ electron volts (eV). It is important to highlight that the defect formation is a complex procedure not only dependent to the potential energy for a configuration of atoms but also on the vibrational energy, electronic and vibrational entropy, the external chemical potential and the difference in volume between the defective and the perfect crystal[4].

## 3.2. Kröger–Vink Notation

Point defects in crystalline solids are usually represented through the Kröger-Vink notation [5]. The description is according to the nondefective structure chemical formula as well as the defect's effective charge. In addition, the symbolism is in agreement with the position of the defect in the crystal. At first, every atom in the perfect non – defective crystal with a given oxidation number is described as $\boldsymbol{A_A^X}$**.** A vacant site is assigned as 'V' by referring to the associated atom while an interstitial site is described by 'i'. An X substitutional at a Y site (or antisite) is described as $X_Y$ (or $Y_X$ respectively). **Figure 3.2** represents the overview of Kröger-Vink notation.

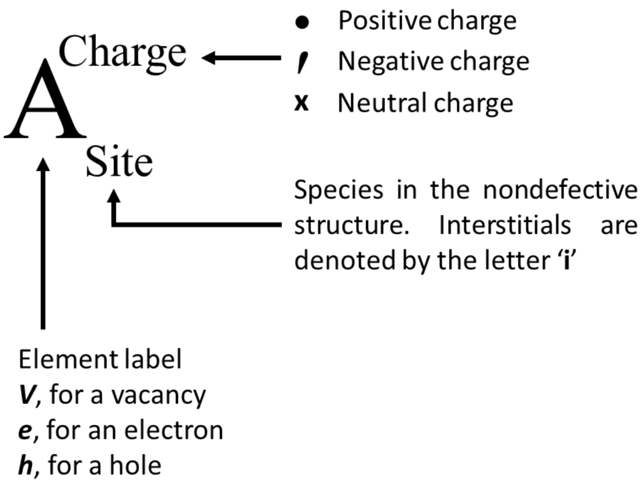

**Figure 3.2** Overview of Kröger–Vink notation.

**Table 3.1** Examples of the Kröger–Vink notation.

| Notation | Description | Effective Charge |
|---|---|---|
| $V_M^X$ | Vacancy of a neutral charge element | **0** |
| $V_O^{\cdot\cdot}$ | Oxygen vacancy | **2+** |
| $O_i''$ | Oxygen interstitial | **2-** |
| $Li_{Zr}'''$ | **Li**$^+$ occupying a **Zr**$^{4+}$ site | **-3**<br>$\begin{bmatrix} Li : 1+ \\ Zr : 4+ \end{bmatrix}$ |
| $\{Fe^{\cdot}_{Mg} : Na'_{Mg}\}^{x}$ | Neutral defect cluster: Fe on Mg site and Na on Mg site | **0**<br>$\begin{bmatrix} Fe^{\cdot}_{Mg} : 1+ \\ Mg'_{Fe} : 1- \end{bmatrix}$ |

The defect chemistry reactions considered throughout the thesis are also represented similarly. For example, a $Li^+$ Frenkel reaction in $Li_2CuO_2$ is described as follows:

$$Li_{Li}^{X} \rightarrow V_{Li}' + Li_i^{\bullet} \quad \textbf{(3.2)}$$

An antisite formation between two different species, (for example $Li^+$ and $Cu^{2+}$ in $Li_2CuO_2$) in the crystal is represented though the following reaction:

$$Li_{Li}^{X} + Cu_{Cu}^{X} \rightarrow Li_{Cu}' + Cu_{Li}^{\bullet} \quad \textbf{(3.3)}$$

Additionally, the charge of an ion is described with respect to the crystallographic site of occupation. For a vacancy or antisite defect, both of the ions occupation contributes to the complete effective charge of the structure. To represent a defect pair or cluster, one has to indicate them by the use of brackets pointing to the total cluster charge. Examples on the Kröger–Vink notation are shown in Table 3.1.

### 3.3. Defect Concentrations and thermodynamics

The concentration of defects is determined by the law of mass action and the defect formation energy[1]. Originating from the thermodynamics point of view, point defects in a solid can be described as a solution where the solid is the solvent and the defects are the solute. The thermodynamic concentration of point defects in equilibrium is given by the following relation:

$$\mathrm{C_r} = \mathrm{C_0} \exp\left(- \frac{\Delta \mathrm{G_f}}{\mathrm{k_B T}}\right) \quad \textbf{(3.4)}$$

Where $C_0$ is the concentration of defects at absolute zero temperature (T = 0 K), $\Delta G_f$ is the free Gibbs energy (J) and $k_B$ is the Boltzmann constant ($1.38064852 \times 10^{-23}$ $m^2$ kg $s^{-2}$ $K^{-1}$). The defect formation in the crystal, leads to the general increase of the internal energy and the entropy. It is attributed to the various possible configurations for the defect distribution in the available lattice positions. Overall, a number of *n* defects can be arranged in *N* sites though Ω available ways as:

$$\Omega = \frac{N\,(N-1)(N-2)\ldots(N-n+2)(N-n+1)}{n!} \quad \textbf{(3.5)}$$

And multiplying with $\frac{(N-n)!}{(N-n)!}$ will lead to:

$$\Omega = \frac{N!}{(N-n)!n!} \quad \textbf{(3.6)}$$

The configurational entropy is connected with the Ω microscopic configurations of the thermodynamic system as follows:

$$S = k_B \ln\Omega = k_B \ln\frac{N!}{(N-n)!n!} \quad \textbf{(3.7)}$$

A thermodynamic system with n point defects has a free energy F

$$F = n\,E_f - TS \quad \textbf{(3.8)}$$

Where $E_f$ is the defect formation energy and T is the temperature of the system. Minimizing $E_f$ will lead to the equilibrium number of defects. Thus, derivation with respect to *n* will give:

$$\frac{\partial F}{\partial n} = 0 \quad \textbf{(3.9)}$$

$$E_f - k_B T \left( ln \frac{N-n}{n} \right) = 0 \tag{3.10}$$

Considering the system is at the dilute limit (i.e. the defects are at low concentrations and practically do not interact) it can be assumed that the amount of point defects is significantly lower than the available lattice sites in the crystal (or $N - n \sim N$).

$$\frac{n}{N} = \exp\left( -\frac{E_f}{k_B T} \right) \tag{3.11}$$

Overall, the defect concentration (n / N) in a crystalline solid is governed by the temperature.

### 3.4. Diffusion

Diffusion in energy materials is a process strongly dependent to the structural disorder of the host lattice and the overall concentration of point defects[3]. It is the main transport mechanism caused by the Brownian motion of random species and leads to an associated increase in disorder or entropy. In the terms of mass action law, diffusion in condensed matter is represented as an ensemble of microscopic jumps and quasichemical interactions of atoms and defects.[6]

In most materials the ion mobilities are restricted to a system of pathways, these may be between identical starting and ending points or not. However, the preferential route will correspond to the lowest energy barrier.

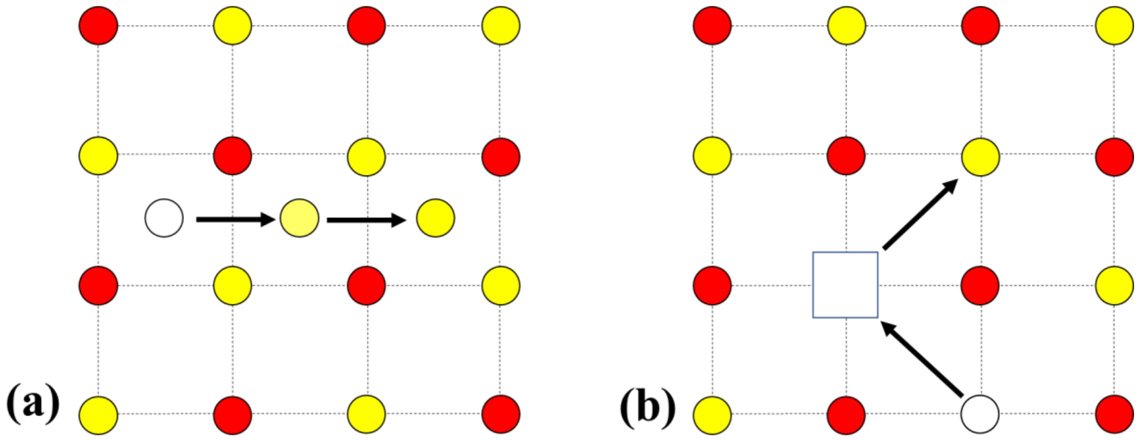

**Figure 3.3** Representation of (a) Interstitial diffusion mechanism (b) Vacancy diffusion mechanism.

The ionic transport in solids[7] is described by the movement of atoms from their initial positions of equilibrium within the empty space / lattice over an energy barrier of migration. The interstitial mechanism does not require the presence of additional defects while in the vacancy mechanism the atom jumps to the empty space by creating a vacancy that may be filled by another atom. The last case is the intersticialcy (the case where an interstitial atom disperses another atom from its formal lattice site to an interstitial site). The mechanism demands low values for the migration energy as well as low formation energies for the associate defects. Based on the fact that there are energy barriers that control the movement of ions in the lattice, the jump frequency of defect is described as follows[8]:

$$\omega = \nu \exp\left(- \frac{\Delta G_m}{\kappa_B T}\right) \qquad \textbf{(3.12)}$$

where ν is the vibrational frequency and $\Delta G_m$ is the free Gibbs energy that is required for the transport of the ion from the initial position to a saddle point. The diffusion coefficient as a function of temperature has an Arrhenius form as:

$$D = D_0 \exp\left(-\frac{H_\alpha}{\kappa_B T}\right) \tag{3.13}$$

Where $H_\alpha$ is the activation enthalpy of diffusion (activation energy of migration) and $D_0$ contain the entropy contributions related to the attempt migration frequency.

It is crucial to note that from the various possible routes that an atom can take advantage to move in a crystal, the one that actually mater corresponds to the one with the lowest migration energy. The presence of dopants in the crystal can affect the bulk diffusivity and the overall performance of the material, this means that a complex network may be formed driving the atoms to and away from the dopants. This leads us to the introduction of the activation energy / enthalpy of diffusion that is the sum of two contributions, the migration energy $\mathbf{E_m}$ and the formation energy $\mathbf{E_b}$. The last is associated with the amount of energy that is required to separate the point defect from the dopant ion. The formation energy of the defect is described as follows:

$$E_f\,(defect) = E\,(\text{defect}) + q\mu_\varepsilon - \sum_j n_j \mu_j \tag{3.14}$$

Where $E_f$ is the total energy of the supercell including the defect, q is the charge state of the defect, $\mu_\varepsilon$ is the electron chemical potential, $n_j$ is the type j number of atoms and $\mu_j$is the type j chemical potential respectively.

The migration energy $\mathbf{E_m}$ is described by the energy barrier between two different crystallographic positions that contribute to the diffusion mechanism. In many cases, the activation energy barrier as well as the total vibrational frequencies is dependent on the direction of the ionic transport. Thus, the diffusion coefficients may be anisotropic. Regarding the long-range diffusion for a particular system, it is vital to gain insights on the dimensionality as well as the preferential pathways (for example 1D ionic transport can be blocked by different types of defects)[9] The binding energies between different intrinsic defects are expressed as follows:

$$\mathrm{E_{binding}} = \mathrm{E_{defect\text{-}cluster}} - \left(\sum\nolimits_{\mathrm{components}} E_{\mathrm{isolated-defects}}\right) \qquad \mathbf{(3.15)}$$

As already mentioned the volume of the crystal structure is considered as an important factor in ion mobility[10]. This is directly connected to the potential change of the lattice parameters of the crystal under external compressive or tensile stress. The diffusivity is affected by the changes in the crystal as the empty space that benefits the ion transport may be increased or decreased respectively. In addition, the crystal may be distorted by different approaches such as hydrostatic, biaxial and uniaxial applied stress. The defective crystal demands an extra amount of energy in comparison with the perfect cell and it varies with the presence of other types of defects as well. The variations of the atom configurations may also affect the electronic conductivity in semiconductors or mixed ionic – electronic conductors.

## 3.5 Doping

It is unsurprising that in non-ideal systems in nature, an amount of intrinsic impurities of various elements may be trapped in the host crystal as substitutionals or interstitial defects in the perfect crystal. In addition, the materials performance is in direct connection with the doping processes and properties such as the band gap in semiconductors and migration barriers in ionic conductors are extensively investigated. Introduction of dopants is interpreted as the solution enthalpy in the solid. Considering isovalent doping **AO** in a host lattice **BO**, this will be described as:

$$\mathrm{AO} \rightarrow A_B^X + O_O^X + \mathrm{BO} \qquad \textbf{(3.16)}$$

$$K_{Solution} = \frac{[A_A^X]\,[O_O^X]}{[BO]} \approx \exp\left(-\frac{\Delta h_{sol}}{kT}\right) \qquad \textbf{(3.17)}$$

where $\Delta h_{sol}$ is the solution enthalpy and $K_{Solution}$ is the solution equilibrium constant. In essence, the rate of a chemical reaction depends on the reactants concentration or the process products according to the Mass Action law described as:

$$A\alpha + bB \leftrightarrow cC + dD \qquad \textbf{(3.18)}$$

$$K_{reaction} = \frac{[C]^c\,[D]^d}{[A]^a[B]^b} = \exp\left(-\frac{\Delta G}{kT}\right) \qquad \textbf{(3.19)}$$

For example, the solution enthalpy of $Al_2O_3$ in $Li_2CuO_2$ is given through the following reaction:

$$Al_2O_3 + 2Cu_{Cu}^X + 2Li_{Li}^X \rightarrow\ 2\,Al_{Cu}^{\bullet} + 2\,V_{Li}' +\ 2CuO + 2Li_2O \qquad \textbf{(3.20)}$$

Dopants may remain as isolated defects or interact with each other forming defect clusters. These may migrate through different positions in the host lattice or bind with other types of defects such as vacancies. Therefore, the introduction of extrinsic defects is in direct connection with different defects concentration.

### 3.6 Summary

In the present chapter the theoretical background of point defect processes has been described. The different disorder mechanisms have been introduced and their representation in Kröger–Vink notation used for this thesis is explained. The defect concentrations based on thermodynamic analysis have been discussed through the defects' formation energy $E_f$. Furthermore, diffusion of atoms as a fundamental mechanism in materials and its connection with the structural disorder of the lattice is presented. The activation energy of migration, the diffusion coefficient and the impact of doping processes are discussed.

## REFERENCES

---

[1] D. Parfitt, A. Kordatos, P.P. Filippatos and A. Chroneos, Diffusion in energy materials: Governing dynamics from atomistic modelling. *Applied Physics Reviews*, **4**, 031305, (2017).

[2] W. D. Callister, JR Materials Science and Engineering, An introduction, Wiley (2000).

[3] A. Chroneos, M. J. D. Rushton and R. W. Grimes, Fundamental point defect properties in ceramics. In: Konings R.J.M., (ed.) *Comprehensive Nuclear Materials*, **1**, 47, Amsterdam: Elsevier (2012).

[4] I. D. Faux and A. B. Lidiard, The volume of formation of Schottky defects in ionic crystals. *Philosophical Magazine A*. **43**, 291, (1981).

[5] F. A. Kröger and H. J. Vink, Relations between the Concentrations of Imperfections in Crystalline Solids. *Solid State Physics*, **3**, 307, (1956).

[6] A. N. Gorban, H. P. Sargsyan and H. A. Wahab, Quasichemical Models of Multicomponent Nonlinear Diffusion. *Mathematical Modelling of Natural Phenomena*, **6**, 184, (2011).

[7] P. Heitjans and S. Indris, Diffusion and ionic conduction in nanocrystalline ceramics. *Journal of Physics: Condensed Matter*, **15**, 30 (2003).

[8] C. Kittel, Introduction to Solid State Physics, *Wiley*, New York (1996).

[9] M. Saiful Islam and C. A. J. Fisher, Lithium and sodium battery cathode materials: computational insights into voltage, diffusion and nanostructural properties. *Chemical Society Reviews*, **43**, 185, (2014).

[10] Y. Wang, W. Davidson Richards, S. P. Ong, L. J. Miara, J. C. Kim, Y. Mo and G. Ceder, Design principles for solid state lithium superionic conductors. *Nature materials*, **14**, 1026 (2015).

# CHAPTER 4

# Methodology

## 4.1 Introduction

Density Functional Theory (DFT) is a method emerging from the Solid State Physics principles considered as very promising and famous for calculations since the 1970s. It derives the physical properties of an atomic system based on the density of electrons in it. In this section we will describe the key ideas of DFT. The main fundamental aspects of this method are related to the actual characteristics of the atoms unlike the standard mathematical pattern such as wavefunctions. On a basic approach, if we consider a set of atoms we need to know how their energy changes if they move from their initial positions. Defining an atom corresponds to its nuclei as well as the electron configuration and a configuration of atoms in space is considered as a system or crystallographic structure.

## 4.2 Theoretical background

One of the most important scientific advances of the 20th century was the development of quantum mechanics and the validation of this condensed matter theory through repeated experimental observations with high accuracy[1]. The quantum mechanical formulation offers the most complete description of the atomic interactions in the solid state. Quantum mechanically, the electronic structure of condensed matter can be described through the non – relativistic time independent Schrodinger equation for the many – electrons wavefunction $\Psi$[2].

$$\widehat{H}\ \Psi = [\widehat{T} + \widehat{V} + \widehat{U}]\ \Psi = \left[\sum_i^N \left(-\frac{\hbar^2}{2m}\right) + \sum_i^N V(\vec{r_i}) + \sum_{i<j}^N U(\vec{r_i} + \vec{r_j})\right] = E\Psi \qquad \textbf{(4.1)}$$

Where $\widehat{H}$ is the Hamiltonian, E is the total energy (ground state energy) of the electrons, $\widehat{T}$ is the kinetic energy of each electron, $\hat{V}$ is the potential energy from the external field due to positively charged nuclei (the interaction energy between each electron and the collection of atomic nuclei), and $\hat{U}$ is the electron–electron interaction energy. Importantly, atomic nuclei are much heavier than individual electrons. Considering that, the lighter electrons move considerably faster compared to the much heavier nuclei. Therefore, the nuclei are considered to be in fixed positions in space. However, the analytical or direct numerical solution of Schrödinger's equation for a large amount of atoms is intractable due to the correlations of multiple electrons. Density Functional Theory is based in two fundamental mathematical theorems proved by Kohn and Honenberg as well as the derivation of a set of equations by Kohn and Sham. The two K-H theorems are:

- **Ground State Density:** The total energy E[n(r)] (or any ground state property) of a system of electrons is expressed as a unique functional of the total electron density n(r)[3]
- **Variational Principle:** The variation minimum of this total energy is exactly equivalent to the true ground state energy. In other words, the n(r) that minimizes the E[n(r)] corresponds to the electron density of the full solution of Schrödinger's equation

DFT overcomes the problem of Schrödinger's equation for many interacting electrons and nuclei to a single particle Kohn-Sham expression[4], throughout the correct electron density is expressed involving a set of equations referring only to one single electron. The equations have the form:

$$\left[\frac{\hbar^2}{2m}\,\nabla^2 + V(\vec{r}) + V_H\,(\vec{r}) + \,V_{XC}\,(\vec{r})\right]\psi_i(\vec{r}) = \;\varepsilon_i\,\psi_i(\vec{r}) \qquad \textbf{(4.2)}$$

As shown in relation **4.2**, the solution of the Kohn–Sham equations depend on only three spatial variables, $\psi_i(\vec{r})$. The $V(\vec{r})$ potential defines the interaction of an electron and a set of atomic nuclei, whilst $V_H\,(\vec{r})$ is the Hartree potential defined as:

$$V_H\,(\vec{r}) = e^2 \int \frac{n(r')}{|\,r - r'|}\, d^3 r' \qquad \textbf{(4.3)}$$

$V_H\,(\vec{r})$ describes the repulsion between an electron and the total electron density $n(r')$. In addition, the $V_{XC}\,(\vec{r})$ potential is the functional derivative of the exchange correlation energy $E_{XC}$ defined as:

$$V_{XC}\,(\vec{r}) = \frac{\delta\;E_{XC}\,(r)}{\delta\,n(r)} \qquad \textbf{(4.4)}$$

Overall the electrons will respond more rapidly to changes in the surroundings than nuclei. The approach can be described roughly through two different processes. First, we solve the equations that describe motion for fixed positions of the atomic nuclei. Then, for a given set of electrons moving in the field of a set of nuclei we find the lowest energy configuration, or state, for the electrons. This lowest energy will be the ground state of the electrons (or the most stable state of the system) and the separation of the nuclei and electrons in two different problems is the Born – Oppenheimer approximation. Overall the problem is managed through continuous iterations as employed through a relative algorithm till the system reach the ground state.

1. Initially, a trial value for the electron density n (r) has to be defined.
2. Solve the K-S equations using the trial density and find the single particle wave functions $\psi_i(r)$.
3. Calculate the electron density $n_{KS}(r) = 2\sum_i \psi_i^* (\vec{r})\, \psi_i(\vec{r})$ by the K-S single particle wave functions.
4. Compare the calculated and trial densities. If the two densities are the same, then the true ground state electron density is reached, and the calculation of the ground state energy is eligible to proceed.

Shortcomings in DFT have attracted considerable interest[5] due to occasional underestimation of complex systems. The inability to predict dispersion interactions with good accuracy is often referred within the non-covalent interactions problem. For example, if we consider the interaction between two molecules, additional forces along with dispersion occur in their non-covalent attraction. Furthermore, the functionals' errors are connected to the non-covalent binding as it is weaker than covalent binding. However, recent progress in dispersion – corrected DFT methods provide a better agreement for a variety of systems.

DFT Limitations[6] to overcome should be also addressed through:

1. Delocalization Error: Responsible for non-precise estimation of migration energy barriers, electronic band gaps, incorrect long-range interactions among others.
2. Static correlation error: Responsible for dissociation of chemical bonds, issues with magnetic systems.

Overall, the delocalization error originates through the linearity breaking of the energy described as a function of fractional charge whilst static correlation error is connected with the energy constancy deviation with respect to the fractional spins of the system. Furthermore, the semiempirical DFT+U approach is an effective technique used for of highly correlated systems, which otherwise may lead to delocalized valence electrons[7].

### 4.2.1 The exchange – correlation Functional

Despite the introduction of the Kohn–Honenberg theorems in DFT, the true form of the exchange-correlation functional energy is not known and therefore different approximations have to be described.

The simplest approximation is the local density approximation (LDA). In this case there is a functional that can be exactly derived: the uniform electron gas. Here the electron density is constant at all points in space, n($\vec{r}$) = constant. Thus, the exchange – correlation energy for a density n($\vec{r}$) at a point r can be approximated through the electron gas:

$$E_{XC}^{LDA}\,[\vec{r}] = \int n\,\varepsilon_{XC}^{unif}[\mathrm{n}(\vec{r})]\mathrm{d}\vec{r} \qquad \textbf{(4.5)}$$

where $\varepsilon_{XC}^{unif}$ is the exchange – correlation energy per particle at each position of a uniform electron gas density n($\vec{r}$).

Notably, as in any real system there are variations in electron density that define chemical bonding as well as the charge density around atomic cores is highly non-uniform this approach is often considered of limited value, however it works for a huge variety of systems.

Despite the fact that LDA defines completely the Kohn – Sham equations, the Schrodinger's equation is not exactly solved. An alternative approximation to overcome those limitations that has been used in the present thesis is the general gradient approximation (GGA). Here a charge gradient is introduced as follows:

$$E_{XC}^{GGA}\,[\vec{r}] = \int f(n,\ \nabla n)\,\mathrm{d}\vec{r} \tag{4.6}$$

where $f(n,\ \nabla n)$ is the function of the charge density $n$ and its derivative. Considering the popularity of LDA / GGA approximations in computational physics and chemistry, it is among the biggest challenges to develop functionals that will be applicable and accurate.

### 4.2.2 Plane wave basis and k-Points

As DFT is applied in an arrangement of atoms that periodically arranged in space, expressing the wavefunction as a summation of plane waves will simplify the calculation. The solution of Schrödinger's equation for a periodic system must satisfy Bloch's theorem[8]

$$\Psi_{n,k}\,(\vec{r}) = u_n(\vec{r})e^{(ik\vec{r})} \tag{4.7}$$

where $u_n(\vec{r})$ is a function that possesses the periodicity of the supercell / potential and the wavefactor k corresponds to the position in the Brillouin zone (reciprocal space). Functions $e^{(ik\vec{r})}$ are called plane –waves and the complete wavefunction for state n is described as:

$$\Psi_{n,k}\,(\vec{r}) = \sum_k \Psi_{n,k}\,(\vec{r}) \tag{4.8}$$

Additionally, the $u_n(\vec{r})$ function is expanded for a periodic system in a plane-wave basis as follows:

$$u_n(\mathrm{r}) = \sum_g c_g\, e^{[ig\vec{r}]} \quad \textbf{(4.9)}$$

Leading to the following expression:

$$\Psi_{i,k}(\mathrm{r}) = \sum_g c_{i,k+g}\, e^{[i(k+g)\vec{r}]} \quad \textbf{(4.10)}$$

Where g, corresponds to the reciprocal lattice vectors of the lattice considered. According to this expression, the summation over g could be over an infinite amount of values. However, it is logical to assume that solutions with low energies are more physically justified than energies of very high values, as the expression 4.10 includes the kinetic energies of the wavefunction.

$$\mathrm{E} = \frac{h^2}{2m} |k+g|^2 \quad \textbf{(4.11)}$$

Thus, the sum over $g$ is truncated to a cutoff value ($g_{\mathrm{cutoff}}$) to include solutions with low kinetic energies only. Eventually this will introduce the parameter of the equivalent energy $E_{\mathrm{cutoff}}$ expressed as follows:

$$E_{cutoff} = \frac{\hbar^2\, g_{cutoff}^2}{2m_e} \quad \textbf{(4.12)}$$

where ħ is Planck's constant divided by $2\pi$, and $m_e$ is the mass of the electron. Notably, $E_{cutoff}$ should efficiently describe the wavefunction and correspond to a sufficiently large value in order to include enough plane-waves $e^{[ikr]}$. This is among the main reasons to constantly confirm if the calculations are fully converged.

Among the main concerns has been also the balance between efficiency and computational resources of the calculations. The k factor of the plane-wave should be summed over the

Brillouin zone, defined as the primitive cell in *k* space. The approach by Monkhorst and Pack[9] successfully reduce the computational demands to a manageable way as the wavefunction is evaluated for a special set of high symmetry k-points. In the present thesis, this scheme is applied to form a uniform grid in k-space that will effectively represent the Brillouin zone of the crystallographic structures.

### 4.3 Density of States

In quantum mechanics, a system is characterized by wave-like particles that can occupy states with specific wavelengths and propagation directions. The electronic structure of a crystallographic configuration varies, depending on the available states for occupation at an energy level as well as the topological properties of the material. Notably, DOS is described as the number of electron states in an interval (E, E+dE):

$$\mathrm{D} = \int_{E}^{E+dE} P(E)dE \qquad \textbf{(4.13)}$$

Where D is the total amount of states per unit volume and P(E) is the density of states per unit energy per unit volume. In the present thesis the energy dispersion and electronic band structure is investigated with respect to the defect chemistry and doping processes. From the experimental viewpoint, the similar insights can be extracted using advance techniques such as Angle - Resolved Photoemission Spectroscopy (ARPES). For every chemical formula, the wave-like behaviour of electrons for an element is represented by the atomic orbitals. Thus, the electronic DOS is determined through the resulting electron density in $k$ –space. The probability for an orbital at energy E to be occupied by an electron in thermal equilibrium is represented by the Fermi – Dirac distribution[10]:

$$f_0(\mathrm{E}) = \frac{1}{e^{\frac{(E - E_F)}{k_B T}} + 1} \quad \textbf{(4.14)}$$

Notably, the valence band corresponds to the total of all occupied states while at T = 0 K the states in the conduction band are unoccupied. Additionally, the energy of the highest occupied electronic state (the largest Fermions such as electrons and holes in the ground state of the system) corresponds to the Fermi energy or the chemical potential. Introduction of extrinsic defects (dopants) in the pristine material is expected to introduce additional states in the DOS affecting the materials behaviour (e.g. electronic band gap reduction in doped semiconductors). **Figure 4.1** illustrates the DOS for different types of materials with respect to their electronic conduction. The systems investigated for this thesis are semiconductors and insulators.

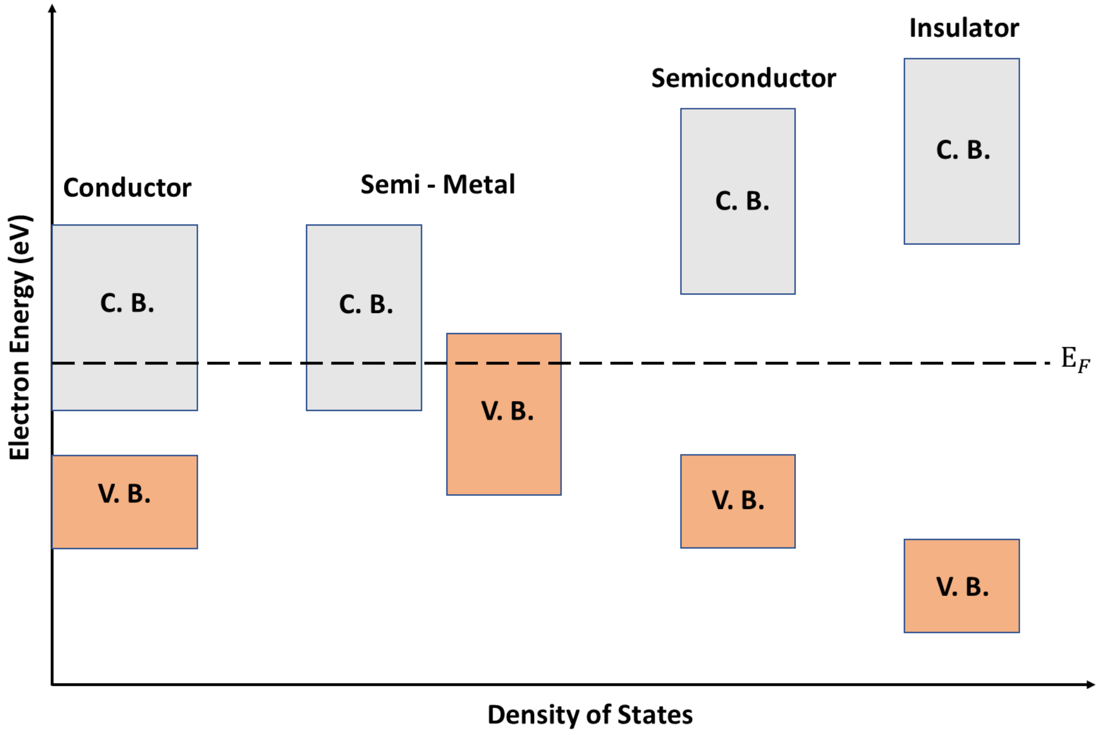

**Figure 4.1** Density of States for different types of materials.

### 4.4 CASTEP – Calculations

The calculations performed for this thesis were employed through the plane wave density functional theory code CASTEP[11, 12]. The atomic configurations for every structure within the general gradient approximation using the Perdew, Burke and Ernzerhof (PBE)[13] using ultrasoft pseudopotentials[14]. Conceptually, pseudopotentials represent the electron density from a chosen set of core electrons considering that chemical interatomic bonding is characterized mainly by valence (outer shell) electrons. Additionally, ultrasoft pseudopotentials as applied through CASTEP require fewer plane waves for a high computational accuracy. The atomic configurations of the systems have been tested in order to set the appropriate plane-wave basis set and k-points in the Brillouin zone. $E_{cutoff}$ is converged in the range of 100 eV to 800 eV using a step of 50 eV whereas the high symmetry k – points were chosen with respect to the supercell structure targeting the minimum divergence on the ground state energies. For all structural and electronic calculations, the cells were initially geometrically optimized. The cell parameters and atomic coordinates are allowed to relax using energy minimization under constant pressure conditions unless specified. In CASTEP code, the cell is optimized through the Broyden-Fletcher-Goldfarb-Shanno (BFGS) minimizer[15] geometry method[16]. Initially, the ionic positions may be specified in fractional coordinates as relative to the lattice vectors of the unit cell or through absolute coordinates. The scheme implementation uses a Hessian matrix which constantly updated until the optimization of the atomic coordinates and lattice parameters. The defect chemistry of the system is investigated through the different ground state energies of the perfect and defective structures, whereas the approach is based on charge–neutral defects. For the Density of States (DOS) investigation and visualization, the OPTADOS[17, 18] sub-code is employed. The electronic eigenvalues along the Monkhorst-Pack grid in the Brillouin zone are calculated non-self-consistently for both the valence and conduction bands, using electronic charge densities and potentials that are generated during the simulation. For every structure presented and investigated in the present thesis, a description of the calculation details is provided in the associated chapter.

# REFERENCES

---

[1] D. S. Sholl and J. A. Steckel, Density Functional Theory: A Practical Introduction, Wiley & Sons (2009).

[2] W. Kohn and A. E. Mattsson, Edge Electron Gas. *Physical Review Letters*, **81**, 3487 (1998).

[3] W. Kohn, Electronic structure of matter -wave functions and density functionals. *Reviews of Modern Physics*, **71**, 1253, (1998).

[4] W. Kohn and L. J. Sham, Self-Consistent Equations Including Exchange and Correlation Effects. *Physical Review*, **140,** A1133, (1965).

[5] G. A. DiLabio, Alberto Otero-de-la-Roza, Noncovalent Interactions in Density Functional Theory. *John Wiley & Sons, Inc.*, Reviews in Computational Chemistry, **29**, 1, (2016).

[6] A. J. Cohen, P. Mori-Sánchez, W. Yang, Insights into Current Limitations of Density Functional Theory. *Science*, **321**, 792, (2008).

[7] G. Ramos-Sanchez, I. C. Romero-Ibarra, J. Vasquez-Arenas, C. Tapia, N. Aguilar-Eseiza and I. Gonzales, Controlling $Li_2CuO_2$ single phase transition to preserve cathode capacity and cyclability in Li-ion batteries. Solid State Ionics, **303,** 89, (2017).

[8] C. Kittel, Introduction to Solid State Physics. New York: Wiley (1996).

[9] H. J. Monkhorst and J. D. Pack, Special points for Brillouin-zone integrations. *Physical Review* B, **13**, 5188, (1976).

[10] S.O. Kasap, Principles of Electronic Materials and Devices. Second Edition (2002).

[11] M. C. Payne, M. P. Teter, D. C. Allan, T. A. Arias and J. D. Joannopoulos, Iterative minimization techniques for ab initio total-energy calculations: molecular dynamics and conjugate gradients. *Reviews of Modern Physics*, **64**, 1045, (1992).

[12] M. D. Segall, P. J. D. Lindan, M. J. Probert, C. J. Pickard, P. J. Hasnip, S. J. Clark and M. C. Payne First-principles simulation: ideas, illustrations and the CASTEP code. *Journal of Physics: Condensed Matter*, **14**, 2717, (2002).

[13] J. P. Perdew, K. Burke and M. Ernzerhof, Generalized Gradient Approximation Made Simple. *Physical Review Lett*ers, **77**, 3865, (1996).

[14] D. Vanderbilt, Soft self-consistent pseudopotentials in a generalized eigenvalue formalism. *Physical Review*, B **41**, 7892, (1990).

---

[15] B. G. Pfrommer, M. Cote, S. G. Louie,  M. L. Cohen, Relaxation of Crystals with the Quasi-Newton Method. *Journal of Computational Physics*, **131**, 233, (1997).

[16] T. H. Fischer and J. Almlof, General methods for geometry and wave function optimization. *The Journal of Physical Chem*istry, **96**, 9768, (1992).

[17] R. J. Nicholls, A. J. Morris, C. J. Pickard and J. R. Yates, OptaDOS - a new tool for EELS calculations. *Journal of Physics: Conference Series*, **371**, 012062, (2012).

[18] A. J. Morris, R. Nicholls, C. J. Pickard and J. R.  Yates, OptaDOS: A tool for obtaining density of states, core-level and optical spectra from electronic structure codes. *Computer Physics Communications*, **185**, 1477, (2014).

# CHAPTER 5

## Intrinsic defect processes in lithium zirconate

Part of the results presented here has been published in the *Journal of Materials Science: Materials in Electronics* **28**, 11789 -11793 (2017)

### 5.1 Introduction

Lithium zirconate, $Li_2ZrO_3$, is presently being considered as a material in energy storage applications such as a solid sorbent for the reversible capture of $CO_2$, as a ceramic breeder for helium-cooled pebble bed blankets in reactors, as an anode in lithium batteries[1] as well as a coating for anodes and cathodes. Controlling the potential formation of defects[2] such as vacancies is very important and the introduction of dopants with respect to oxidation characteristics can effectively maintain the charge balance in the crystal. In this chapter, the intrinsic defect processes and doping in $Li_2ZrO_3$ through Density Functional Theory (DFT) are investigated. Atomistic simulation is an efficient way to gain understanding of the point defect energetics as well as further insights into the materials performance. There are only limited DFT studies in $Li_2ZrO_3$ wherein the recent study by Ferreira *et al.*[3] focused on the diffusion of $Li^+$ ions, in conjunction with experimental technique (Nuclear Magnetic Resonance (NMR)) to determine the pathways of the $Li^+$ ion conduction. Specifically, the calculation of $Li^+$ ions migration energy barriers as well as the relevance of $Li^+$ vacancies in the host lattice of the pristine material is reported, whilst the demand for a deeper understanding on the material's defect chemistry is highlighted. In this chapter, DFT is applied to investigate the defect mechanisms, electronic structure and doping processes in $Li_2ZrO_3$.

## 5.2 Intrinsic Defects

### 5.2.1 Methodology

In the atomistic simulation approach, the plane DFT code CASTEP[4, 5] is employed. The exchange and correlation interactions were formulated with the corrected density functional of Perdew, Burke and Ernzerhof (PBE)[6] within the generalized gradient approximation (GGA) in conjunction with ultrasoft pseudopotentials[7]. The plane wave basis set was tested with respect to convergence criteria and has been set to a cut-off of 400 eV. A 4 x 2 x 4 Monkhorst-Pack (MP)[8] K-point grid was used with a 96-atomic site supercell. All the calculations were under constant pressure conditions, which is an established way to perform DFT calculations in defective lattices. Under constant pressure conditions the crystal structure relaxes to the most energetically favourable configuration. Applying the same criteria to all calculations ensure the validity of outputs. Convergence was tested by increasing the cut-off up to 800 eV, the MP grid to 2x2x2 and by considering up to 4x2x4. These resulted in energy changes of less than 0.01 eV. This deviation is within the high levels of accuracy providing the ability to use less dense K-Point grid whilst not affecting the ground state energies and trends. Furthermore, the selected cut-off is the optimum point of convergence since 100-350 eV is not realistic when it comes to the ground state energies whereas no considerable deviations are evident over 500 eV. Notably, higher cut-off will demand additional computational resources and require much more time to complete the calculations with no meaningful contribution to the overall accuracy. All supercells have been relaxed from the ideal configurations in order to effectively represent the interatomic forces of attraction and repulsion within the different types of atoms in the $Li_2ZrO_3$ structure.

### 5.2.2 Crystallography

$Li_2ZrO_3$ considered in the present study is monoclinic within the C2/c space group (space group number 15). The calculated lattice parameters a = 5.4264 Å, b = 9.0258Å and c = 5.4211 Å (unit cell volume 244.9 Å$^3$) are in good agreement with the experimental results[9].

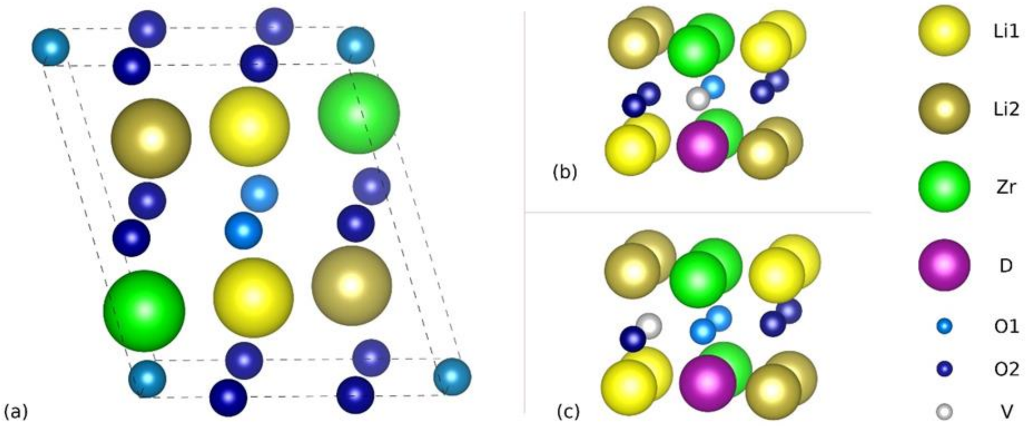

**Figure 5.1** A schematic representation of (a) the monoclinic $Li_2ZrO_3$ unit cell (lattice parameters a = 5.4218 Å, b = 9.0216 Å and c = 5.4187 Å), (b) the Dopant $(D) - V_O^{\cdot\cdot}$ defect cluster for a $V_O^{\cdot\cdot}$ at the $O_1$ site and (c) the Dopant $(D) - V_O^{\cdot\cdot}$ defect cluster for a $V_O^{\cdot\cdot}$ at the $O_2$ site.

The unit cell contains 24 atomic sites (refer to Figure 5.1 (a)). There are two non-equivalent $Li^+$ ions and two $Zr^{4+}$ residing at the Oc and 4e Wyckoff positions. The $O^{2-}$ ions reside in the 4d and 8f positions. In addition, the representation of the dopant (D) occupation in the lattice is shown in Figure 5.1 (b)-(c).

### 5.2.3 Point defects

The associated energetics of Frenkel defects, are important in the consideration of point defect related processes in energy materials (e.g. diffusion mechanism). Furthermore, in terms of nuclear applications, low formation energies can be associated with an increased concentration of point defects that can eventually lead to the distortion of the material crystal structure (e.g. phase transformation). In this respect, radiation damage can be described as an accumulation of defects formed by displacement sources[10, 11]. The three key Frenkel reactions in Kröger–Vink notation[12] are

$$\mathrm{Zr_{Zr}^{x}} \rightarrow \mathrm{V_{Zr}^{''''}} + \mathrm{Zr_{i}^{\bullet\bullet\bullet\bullet}} \tag{5.1}$$

$$\mathrm{Li_{Li}^{x}} \rightarrow \mathrm{V_{Li}^{'}} + \mathrm{Li_{i}^{\bullet}} \tag{5.2}$$

$$\mathrm{O_{O}^{x}} \rightarrow \mathrm{V_{O}^{\bullet\bullet}} + \mathrm{O_{i}^{''}} \tag{5.3}$$

The oxygen Frenkel energy (Eq. 5.3) was calculated to be 7.35 eV, which corresponds to a high value. In addition, concerning the cation Frenkel energies it is calculated that the $\mathrm{Li^+}$ Frenkel energy is significantly lower (5.77 eV) as compared to the $\mathrm{Zr^{4+}}$ Frenkel energy (19.56 eV). In essence, these Frenkel defect formation energies reflect that it would be energetically unfavourable to introduce highly charged defects (e.g. such as $Zr_i^{\bullet\bullet\bullet\bullet}$) in the $\mathrm{Li_2ZrO_3}$ lattice. Overall, these defects will be not beneficial for the host structure when it comes to the good structural stability under radiation damage or good charge / discharge cycle ratio. The lattice may experience phase transformations that may not be reversible, thus the high $\mathrm{Zr^{4+}}$ Frenkel energy shows that $\mathrm{Li_2ZrO_3}$ is a stable material appropriate for energy applications, even in high temperatures.

This is also the case when we refer to the formation of Schottky and antisite defects in the crystallographic structure. The formation of Schottky defects in $Li_2ZrO_3$ is given by:

$$2\mathrm{Li}_{\mathrm{Li}}^{\mathrm{x}} + \mathrm{Zr}_{\mathrm{Zr}}^{\mathrm{x}} + 3\mathrm{O}_{\mathrm{O}}^{\mathrm{x}} \rightarrow 2\mathrm{V}_{\mathrm{Li}}^{\prime} + \mathrm{V}_{\mathrm{Zr}}^{\prime\prime\prime\prime} + 3\mathrm{V}_{\mathrm{O}}^{\bullet\bullet} \qquad (5.4)$$

The Schottky defect formation is calculated to be 28.55 eV.

Considering the process of radiation damage, the point defects can recombine or occupy an alternative lattice site and form an antisite defect. Low antisite formation energies in the lattice imply that a concentration of residual defects will be present in the material[12]. The antisite formation mechanisms are given by:

$$\mathrm{Zr}_{\mathrm{Zr}}^{\mathrm{x}} + \mathrm{Li}_{\mathrm{Li}}^{\mathrm{x}} \rightarrow \mathrm{Zr}_{\mathrm{Li}}^{\bullet\bullet\bullet} + \mathrm{Li}_{\mathrm{Zr}}^{\prime\prime\prime} \qquad (5.5)$$

$$\mathrm{Zr}_{\mathrm{Zr}}^{\mathrm{x}} + \mathrm{O}_{\mathrm{O}}^{\mathrm{x}} \rightarrow \mathrm{Zr}_{\mathrm{O}}^{\bullet\bullet\bullet\bullet\bullet\bullet} + \mathrm{O}_{\mathrm{Zr}}^{\prime\prime\prime\prime\prime\prime} \qquad (5.6)$$

$$\mathrm{Li}_{\mathrm{Li}}^{\mathrm{x}} + \mathrm{O}_{\mathrm{O}}^{\mathrm{x}} \rightarrow \mathrm{Li}_{\mathrm{O}}^{\bullet\bullet\bullet} + \mathrm{O}_{\mathrm{Li}}^{\prime\prime\prime} \qquad (5.7)$$

It is calculated here that the antisite defect energies are 12.88 eV for Eq. 5.5, 23.35 eV for Eq. 5.6 and 12.59 eV for Eq. 5.7. Defects such as $Zr^{4+}$ at a $Zr^{4+}$ site and $O^{-2}$ at a $O^{2-}$ site are neutrally charged. Here we consider for completeness the highly unlikely case of having a cation at an anion site. Overall, it is logical that Eq. 5.6 is the most energetically unfavourable as it displays the highest difference in effective charges of elements (i.e. the $Zr^{4+}$ atom will not be accommodated in the $O^{2-}$ site and vice versa). Additionally, the energies from Eq. 5.5 and Eq. 5.6 (above 12 eV) lead to very high formation values and this in turn implies that the total concentration of antisite defects in $Li_2ZrO_3$ will be very limited.

## 5.3 Doping – Binding Energies

### 5.3.1 Divalent Dopants

Here the doping effect in $Li_2ZrO_3$ with divalent dopants (M = $Mg^{2+}$, $Zn^{2+}$, $Ca^{2+}$, $Cd^{2+}$, $Sr^{2+}$, and $Ba^{2+}$) is considered via the relation:

$$\mathrm{MO} \xrightarrow{\mathrm{Li_2ZrO_3}} \mathrm{M}''_{\mathrm{Zr}} + \mathrm{V}_{\mathrm{O}}^{\cdot\cdot} + \mathrm{O}_{\mathrm{O}}^{\mathrm{x}} \tag{5.8}$$

It can be observed through relation 5.8, that the introduction of divalent dopants as substitutionals in $Zr^{4+}$ sites leads to the formation of oxygen vacancies.

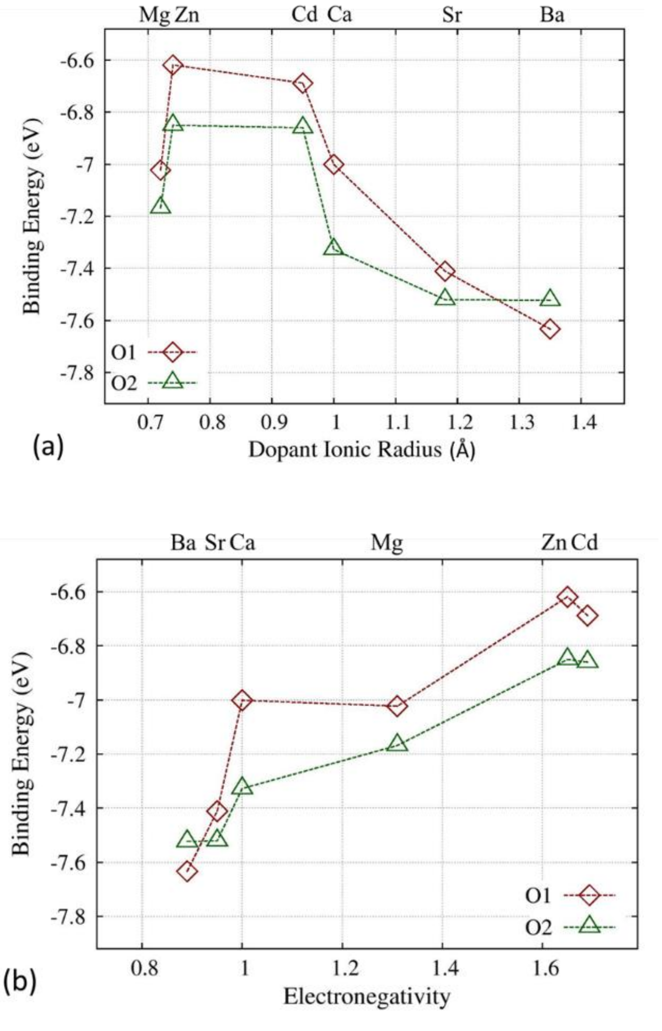

**Figure 5.2** The binding energies of the $\mathrm{Dopant} - \mathrm{V}_{\mathrm{O}}^{\cdot\cdot}$ defect clusters with respect to (a) the divalent dopant ionic radii and (b) the electronegativity of the divalent dopant.

**Figure 5.2** (a) represents the dependence of the binding energies with respect to the divalent dopant ionic radius. From a physical point of view, this is to charge balance the divalent dopant substitutional at a $Zr^{4+}$ site ($M_{Zr}''$) of an effective double negative charge with an oxygen vacancy ($V_O^{\cdot\cdot}$) that corresponds to an effective double positive charge. Here the association of $M_{Zr}''$ with the nearest neighbour oxygen vacancies at the $O_1$ and $O_2$ sites (refer to Figure 5.1(b)-(c) for the configurations) is considered. Next nearest neighbour configurations or defect clusters where the two defects are formed further apart, were calculated to be less energetically favourable. Irrespective of the oxygen vacancy site, a similar trend is observed. The binding energies decrease with the increase of the dopant ionic radius (except for $Mg^{2+}$) is observed. The binding energy difference between the highest and lowest points is about 1.01 eV. Figure 5.2 (b) represents the dependence of the binding energies with respect to the electronegativities of the divalent dopants. Furthermore, it is observed that there is an increase in the binding energies as the electronegativity of the substitutional divalent dopants is increased (with the exception of $Cd^{2+}$). Overall the increasing / decreasing behavior for trivalent dopants is not followed by $Mg^{2+}$ and $Cd^{2+}$ with respect to dopant ionic radius and electronegativity. Binding energies in oxides depend upon the relaxation of the substitutional dopant in the $O^{2-}$ vacant site and coulombic attraction as well since the substitutional dopant has an effective double negative charge and the oxygen vacancy has an effective double positive charge. These two contributions result in non-linear trends as it has been previously demonstrated in other oxides[13, 14].

### 5.3.2 Trivalent Dopants

In order to extend our investigation, the doping process of $Li_2ZrO_3$ with trivalent dopants ($Al^{3+}$, $Ga^{3+}$, $Sc^{3+}$, $In^{3+}$, $Y^{3+}$) is investigated. This will lead to the formation of one oxygen vacancy for every two trivalent atoms substituting for $Zr^{4+}$ atoms. The associated reaction can be described as follows:

$$R_2O_3 \xrightarrow{Li_2ZrO_3} 2R'_{Zr} + V_O^{\cdot\cdot} + 3O_O^x \tag{5.9}$$

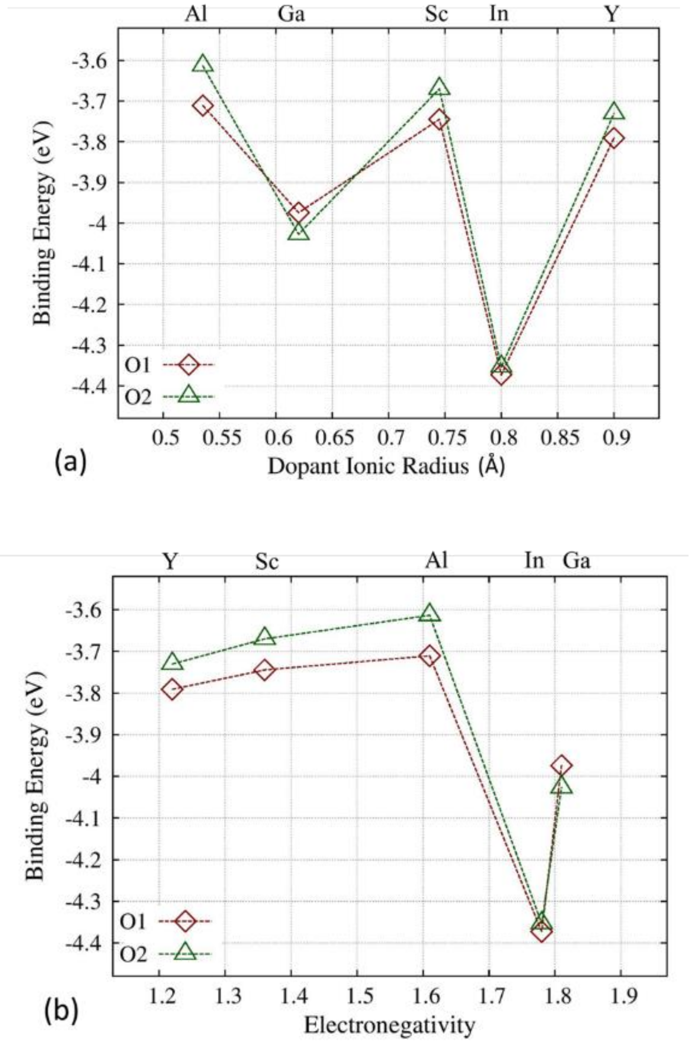

**Figure 5.3** Binding energies of the $\mathrm{Dopant} - V_O^{\cdot\cdot}$ defect clusters with respect to (a) the trivalent dopant ionic radii and (b) the electronegativity of the trivalent dopant.

Here, the binding energies between $O^{2-}$ vacancies and trivalent dopants that substitute $Zr^{4+}$ sites correspond to lower values as compared to divalent dopants. One should consider that introduction of two substitutional atoms to the $Li_2ZrO_3$ lattice will result to additional structural modifications. However trivalent dopants will strongly bind with oxygen vacancies and form defect clusters in the material, this should be considered as crucial when considering energy materials and should be further investigated. **Figure 5.3** shows the binding energies of the $\mathrm{Dopant} - V_O^{\cdot\cdot}$ defect clusters exhibiting lower values than divalent dopants. Interestingly, the defect clusters with $Al^{3+}$ and $Y^{3+}$ correspond to similar binding energies despite their ionic radius difference of about 0.35 Å (refer to Figure 5.3(a)). Figure 5.3(b) corresponds to the dependence of the binding energies with the substitutional trivalent dopant electronegativity. No clear trend is observed as in the case of the divalent ions.

### 5.3.3 Tetravalent Dopants

The $Li_2ZrO_3$ doping with tetravalent dopants (D = $Si^{4+}$, $Ge^{4+}$, $Ti^{4+}$, $Sn^{4+}$, $Ce^{4+}$) can also lead to an association with oxygen vacancies, however in this case mainly due to the relaxation of the dopant near the oxygen vacancy.

As expected, the binding energy values are lower when compared to divalent and trivalent dopants, where there is an element of Coulombic attraction that leads to the increase of the binding energies. With the exception of Pb, it is observed that the binding energies exceed a maximum of 2.4 eV, a relatively low level that reveals the weaker interaction of the dopant as already reported in literature[13, 14]. However, for this particular category the dopants of maximum (Ce) and minimum (Si) ionic radius correspond to similar binding energies. Recent experimental work by Zhan *et al.*[15] investigated the role of oxygen vacancies in $Li_2ZrO_3$ and Li - ion transport whereas in consistency with our results, introduction of dopants will increase the concentration of oxygen vacancies. In addition, Chattaraj *et al.*[16] extend the investigation in the material by theoretical modelling referring to the doping processes as a way to control the formation of oxygen vacancies.

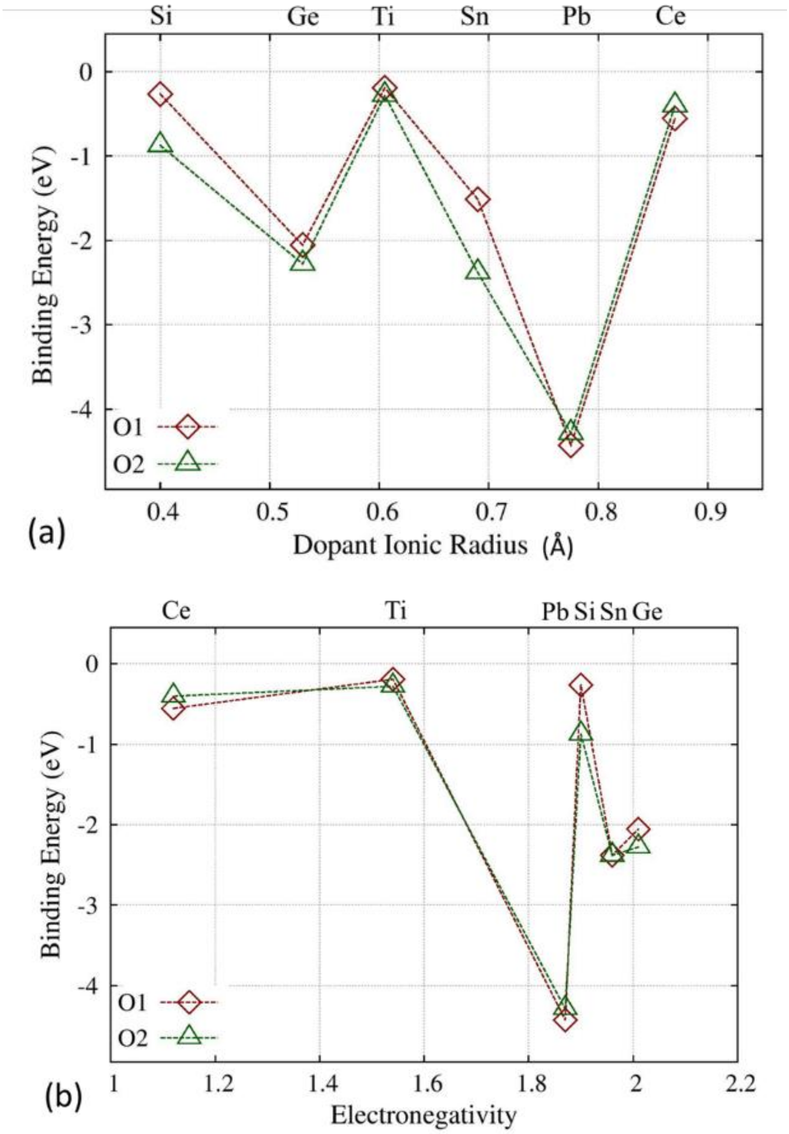

**Figure 5.4** Binding energies of the Dopant $- V_O^{\cdot\cdot}$ defect clusters with respect to (a) the tetravalent dopant ionic radii and (b) the electronegativity of the tetravalent dopant.

## 5.4 Dopant Vacancy Interactions – Density of States

In this section, DFT is employed to systematically investigate the impact of doping in the electronic structure of $Li_2ZrO_3$. In particular, the impact of divalent (Mg, Ca, Sr) and trivalent (Al, In, Y) substitutionals and their association with oxygen vacancies on the electronic properties of $Li_2ZrO_3$ is considered, mainly by calculating their density of states (DOS). The densities of states of the undoped $Li_2ZrO_3$ are shown in **Figure 5.5**. All elements contribute significantly in the valence and the conduction band. The p-orbitals of oxygen correspond to the dominant DOS in the valence band, whereas the d-orbital of zirconium and the s and p orbitals of lithium dominate the conduction band. For the exact contribution of the orbitals, refer to **Figure 5.6**. The band gap is 3.85 eV, in agreement with the 3.9 eV value that has been previously calculated with DFT.[17] Notably, no experimental value of the $Li_2ZrO_3$ band gap has yet been reported.

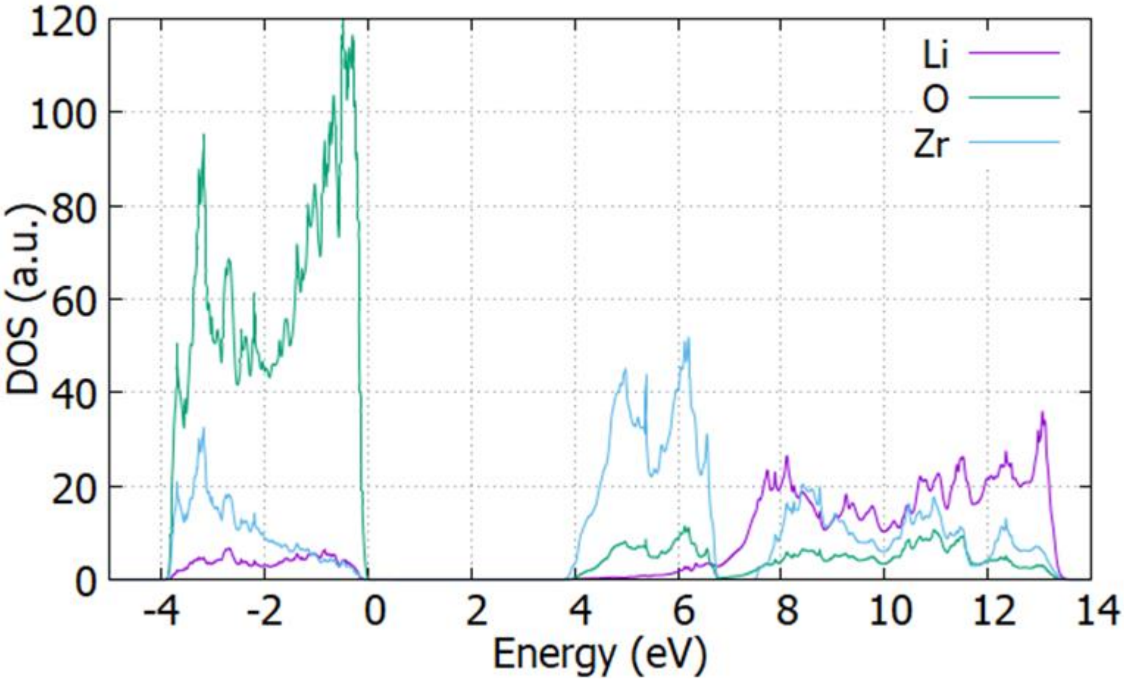

**Figure 5.5** Densities of states in undoped $Li_2ZrO_3$.

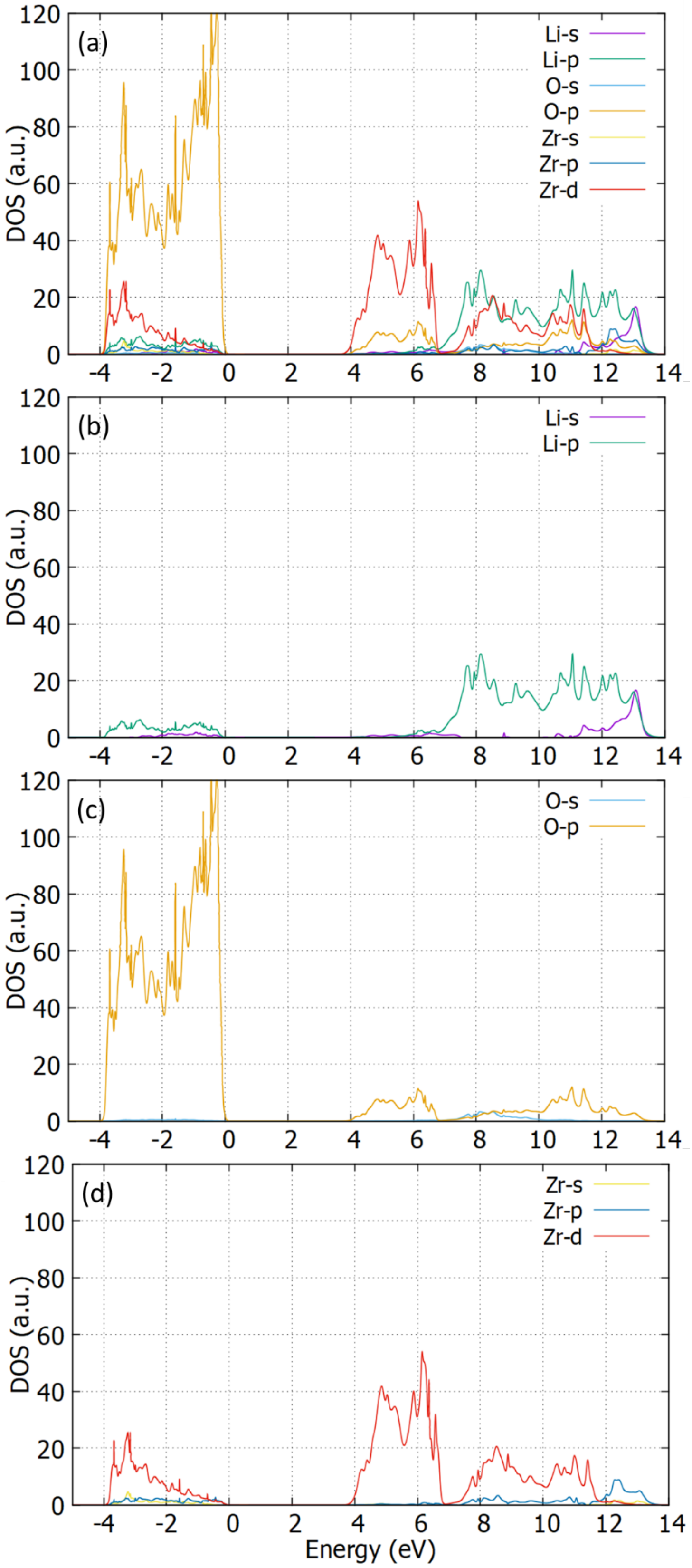

**Figure 5.6** $Li_2ZrO_3$ density of states for (a) All orbitals (b) $Li^+$ orbitals (c) $O^{2-}$ orbitals (d) $Zr^{4+}$ orbitals.

**Figure 5.7** represents the densities of states of substitutional dopants in $Li_2ZrO_3$ (refer to Figure 5.1 (b) for the structure). The DOS of the divalent dopants examined (Ca, Mg, Sr) are shown in Figure 5.7 (a)-(c) while the DOS of the trivalent dopants (Al, In, Y) are shown in Figure 5.7 (d)-(f). These calculations show that the dopants in the substitutional position do not introduce energy levels in the band gap, nor do they significantly alter the DOS of the material. In these cases, the DOS of $Li^+$ are similar, implying that the substitution of $Zr^{4+}$ with these dopants does not introduce midgap levels. **Figure 5.8** represents the densities of states of substitutional dopants-oxygen vacancy pairs in $Li_2ZrO_3$. Again, in Figure 5.7 (a)-(c) the DOS of the $M''_{Zr}V_O^{\cdot\cdot}$ pairs (where M = Ca, Mg, Sr) are shown whereas in Figure 5.7 (d)-(f) the DOS of the $R'_{Zr}V_O^{\cdot\cdot}$ pairs (where R = Al, In, Y) are shown. Doping in this case introduces energy levels in the bandgap (deep levels).

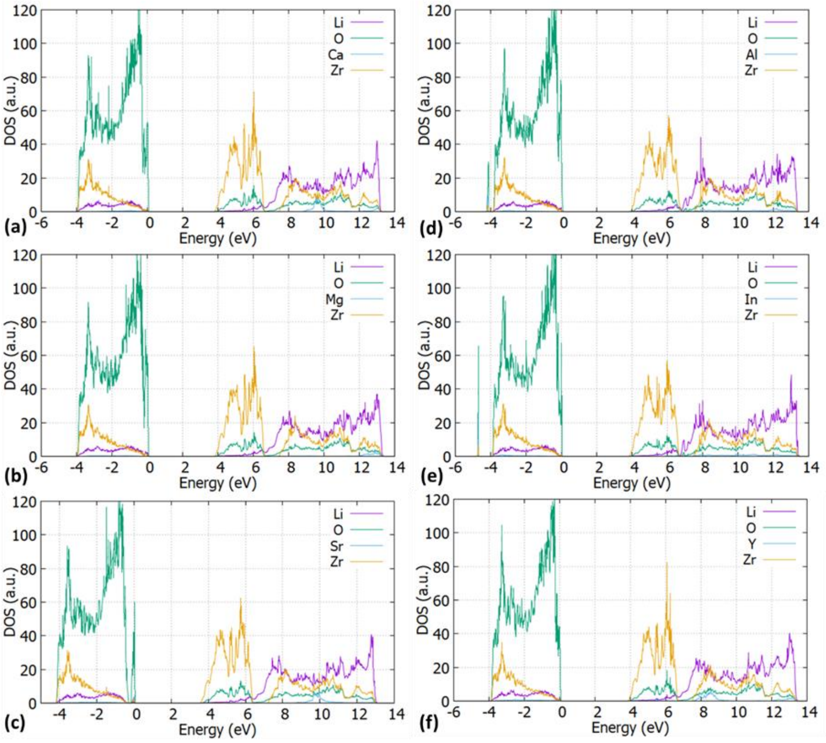

**Figure. 5.7** Densities of states of substitutional dopants in $Li_2ZrO_3$ (a)-(c) divalent dopants Ca, Mg, Sr (d)-(e) trivalent dopants, Al, In, Y.

The effect of the $\mathrm{M}_{\mathrm{Zr}}''\mathrm{V}_{\mathrm{O}}^{\bullet\bullet}$ pairs is pronounced in the case of divalent atoms. The calculated energy bandgap decreased to 2.75eV for $\mathrm{Ca}_{\mathrm{Zr}}''\mathrm{V}_{\mathrm{O}}^{\bullet\bullet}$, 2.85eV for $\mathrm{MgV}_{\mathrm{O}}^{\bullet\bullet}$ and 3.2 eV for $\mathrm{Sr}_{\mathrm{Zr}}''\mathrm{V}_{\mathrm{O}}^{\bullet\bullet}$ owing to a wide tail at the conduction band edge which is related to the Zr and O contribution. Midgap states attributed mainly to Zr are present at approximately 0.8 eV, 2.15 eV and 2.3 eV above the Fermi level for the $\mathrm{Ca}_{\mathrm{Zr}}''\mathrm{V}_{\mathrm{O}}^{\bullet\bullet}$ pairs, similar to the case of $\mathrm{MgV}_{\mathrm{O}}^{\bullet\bullet}$ pairs that exhibit states at 0.85 eV, 2.3 eV and 2.4 eV. In the case of $\mathrm{Sr}_{\mathrm{Zr}}''\mathrm{V}_{\mathrm{O}}^{\bullet\bullet}$ pairs, additional energy levels that can be attributed to O are present at 0.7 eV, 0.85 eV and 1.45 eV above the valence band, whereas the energy levels at 2.7eV and 2.8 eV can be attributed mainly to Zr (refer to Figure 5.8(a)-(c)). In the case of $\mathrm{R}_{\mathrm{Zr}}'\mathrm{V}_{\mathrm{O}}^{\bullet\bullet}$ pairs, a single deep level is introduced near the middle of the bandgap, at around 1.8 eV above the Fermi level (refer to Figure 5.8(d)-(f)). The $Li_2ZrO_3$ band gap for the $\mathrm{R}_{\mathrm{Zr}}'\mathrm{V}_{\mathrm{O}}^{\bullet\bullet}$ pairs, is calculated at 3.4 eV for $\mathrm{Al}_{\mathrm{Zr}}'\mathrm{V}_{\mathrm{O}}^{\bullet\bullet}$, 3.3 eV for $\mathrm{In}_{\mathrm{Zr}}'\mathrm{V}_{\mathrm{O}}^{\bullet\bullet}$ and 3.45 eV for $\mathrm{Y}_{\mathrm{Zr}}'\mathrm{V}_{\mathrm{O}}^{\bullet\bullet}$.

Consequently, in the case of the dopant-oxygen vacancy pairs, there is a significant effect on the electronic structure of the $Li_2ZrO_3$ via the introduction of midgap states and the reduction of the band gap. The effect of doping and defects on the electrochemical behaviour of $Li_2ZrO_3$ (and similar Li-based materials) is strong as they significantly affect the ionic and electronic charge carriers and as a result, the conductivity of the material. The deep levels present when defects are paired with an oxygen vacancy will have an effect on the charge transfer and will therefore need to be taken into consideration when designing an application for $Li_2ZrO_3$.

Although in the case of batteries, the ionic conduction is the leading mechanism of conduction, the concentration of both ionic and electronic charge carriers will need to be further investigated. In essence, experimental work is needed to determine the electronic structure of $Li_2ZrO_3$. Finally, given the applications of $Li_2ZrO_3$, the influence of temperature and pressure on the physical and defect processes of the material should be studied. In this framework, thermodynamic modelling and mass action analysis can also be employed synergetically with computational modelling and experimental studies.

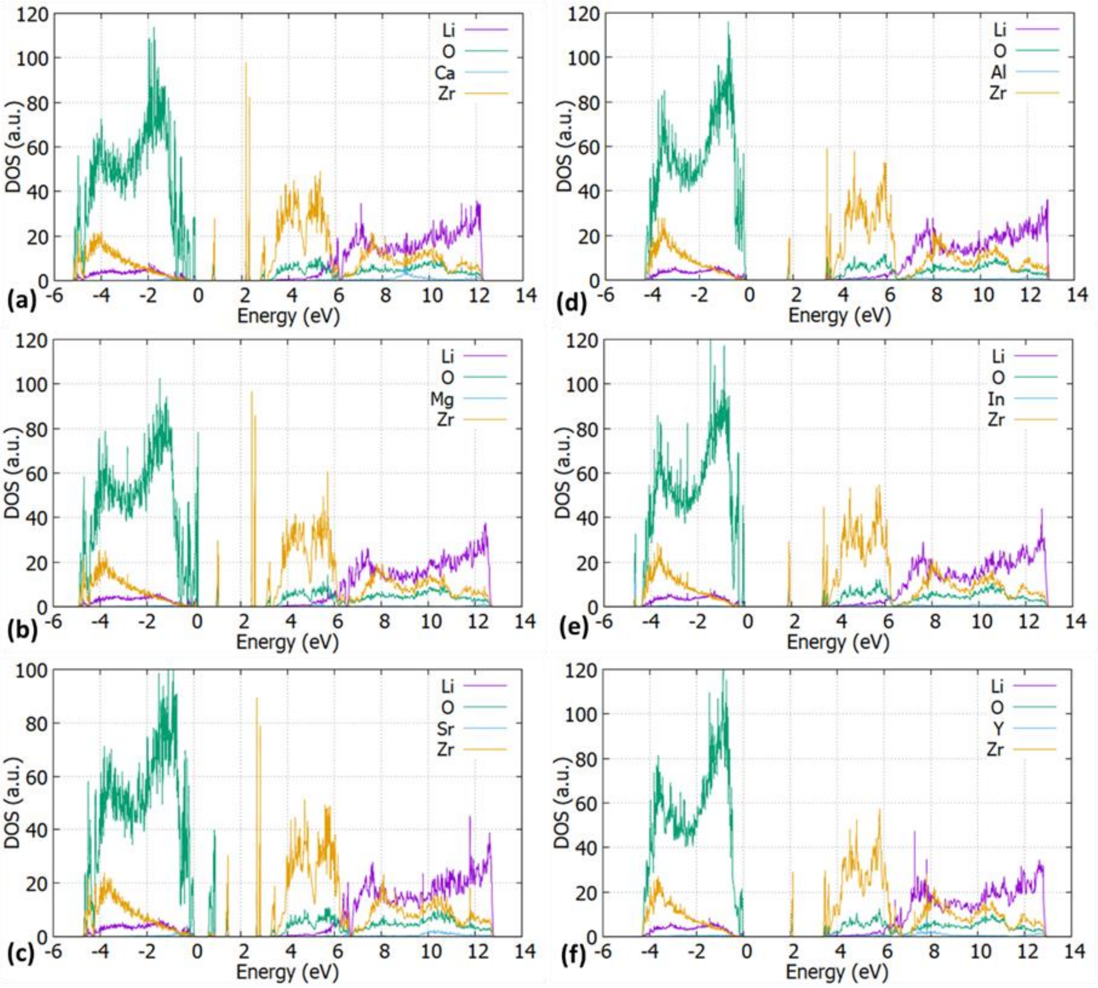

**Figure 5.8** Densities of states of substitutional dopants-oxygen vacancy pairs in $Li_2ZrO_3$ (a)-(c) divalent dopants (d)-(e) trivalent dopants.

## 5.5 Conclusions

In the present chapter, the intrinsic defect processes in $Li_2ZrO_3$ were investigated. It is calculated through the defect chemistry reactions that the $Li^+$ Frenkel corresponds to the lowest energy and thus, will be the dominant intrinsic defect process. Antisite defects formation were calculated to demand very high energies and therefore it is expected that under most conditions there will be only a very small concentration of antisites in the crystal. In $Li_2ZrO_3$, it is energetically costly to form oxygen vacancies via the Frenkel intrinsic defect process and an effective way to overcome this and form oxygen deficient structure is to dope with divalent or trivalent cations as these will substitute at $Zr^{4+}$ lattice sites. It is calculated that the dopant atoms will strongly bind with nearest neighbour oxygen vacancies. For the divalent dopants the strongest association is with dopants of the largest ionic radius (i.e. Ca, Sr, and Ba). This can be explained by the relaxation offered by the nearest neighbour vacancy. Tetravalent dopants will also associate with oxygen vacancies however, with lower binding energies. Doping with divalent and trivalent atoms can prove to be a defect engineering strategy to form oxygen vacancies, which can be controlled by the dopant concentration. The impact of dopant-oxygen vacancy pairs on the electronic structure of $Li_2ZrO_3$ has been also investigated. It was shown that dopant-oxygen vacancy pairs have a significant effect on the electronic structure of the $Li_2ZrO_3$ via the introduction of deep levels and a reduction of the band gap due to the appearance of wide band tails at the conduction band edge. As oxygen vacancies can have an impact on the diffusion mechanisms and the electronic properties of $Li_2ZrO_3$, this will need to be investigated in further experimental (using Secondary Ion Mass Spectrometry (SIMS), X-ray Photoelectron Spectroscopy (XPS), NMR) and computational work.

# REFERENCES

---

[1] Y. Dong, Y. Zhao, H. Duan and J. Huang, Electrochemical performance and lithium-ion insertion/extraction mechanism studies of the novel $Li_2ZrO_3$ anode materials, *Eletrochimica Acta*. **161** 219, (2015).

[2] E. A. Sherstobitova, A.F. Gubkin, I.A. Bobrikov, A. V. Kalashnova and M.I. Pantyukhina, Bottle-necked ionic transport in $Li_2ZrO_3$: high temperature neutron diffraction and impedance spectroscopy. *Electrochimica Acta*, **209**, (2016).

[3] A.R. Ferreira, K. Reuter and C. Scheurer, DFT simulations of $^7Li$ solid state NMR spectral parameters and $Li^+$ ion migration barriers in $Li_2ZrO_3$. *RSC Advances*, **6**, 41015, (2016).

[4] M. C. Payne, M. P. Teter, D. C. Allan, T. A. Arias and J. D. Joannopoulos, Iterative minimization techniques for ab initio total-energy calculations: molecular dynamics and conjugate gradients. *Reviews of Modern Physics*, **64**, 1045, (1992).

[5] M. D. Segall, P. J. D. Lindan, M. J. Probert, C. J. Pickard, P. J. Hasnip, S. J. Clark and M. C. Payne, First-principles simulation: ideas, illustrations and the CASTEP code. *Journal of Physics: Condensed Matter*, **14**, 2717 (2002).

[6] J. Perdew, K. Burke and M. Ernzerhof, Generalized Gradient Approximation Made Simple. *Physical Review Letters*, **77**, 3865, (1996).

[7] D. Vanderbilt, Soft self-consistent pseudopotentials in a generalized eigenvalue formalism. *Physical Review* B, **41**, 7892, (1990).

[8] H. J. Monkhorst and J. D. Pack, Special points for Brillouin-zone integrations. *Physical Review* B, **13**, 5188 (1976).

[9] J. Hodeau, M. Marezio, A. Santoro and R. Roth, Neutron profile refinement of the structures of $Li_2SnO_3$ and $Li_2ZrO_3$. *Journal of Solid State Chemistry*, **45**, 170, (1982).

[10] J. B. Gibson, A. N. Goland, M. Milgram and G. H. Vineyard, Dynamics of Radiation. Damage *Physical Review*, **120**, 1229, (1960).

[11] K. E. Sickafus, L. Minervini, R. W. Grimes, J. A. Valdez, M. Ishimaru, F. Li, K. J. McClellan and T. Hartmann, Radiation tolerance of complex oxides. *Science*, **289**, 748, (2000).

[12] F. A. Kröger and H. J. Vink, Relations between the Concentrations of Imperfections in Crystalline Solids. *Solid State Physics*, **3**, 307, (1956)

[13] L. Minervini, M. O. Zacate and R. W. Grimes Defect cluster formation in $M_2O_3$-doped $CeO_2$. *Solid State Ionics*, **116**, 339, (1999).

---

[14] I. D. Seymour, A. Chroneos, J. A. Kilner and R. W. Grimes, Defect processes in orthorhombic $LnBaCo_2O_{5.5}$ double perovskites. *Physical Chemistry Chemical Physics*, **13**, 15305, (2011).

[15] Xiaowen Zhan, Yang-Tse Cheng and Mona Shirpour, Nonstoichiometry and Li-ion transport in lithium zirconate: The role of oxygen vacancies. *Journal of the American Ceramic Society*, **101**, 4053, (2018).

[16] D. Chattaraj, Structural, electronic, elastic and thermodynamic properties of $Li_2ZrO_3$: A comprehensive study using DFT formalism. *Journal of Nuclear Materials*, **496**, 286, (2017).

[17] Y. Duan, J. Electronic Structural and Phonon Properties of Lithium Zirconates and Their Capabilities of $CO_2$ Capture: A First-Principle Density Functional Approach. *Renewable Sustainable Energy*, **3**, 013102, (2011).

# CHAPTER 6

# Intrinsic defect processes in $Li_2CuO_2$

Part of the results presented here has been published in *Scientific Reports* **8**, 6754 (2018)

## 6.1 Introduction

$Li_2CuO_2$ is considered as an important candidate material as a cathode in lithium ion batteries as it exhibits many interesting characteristics and has already been investigated for applications such as $CO_2$ chemisorption[1, 2]. In battery applications however, a phase transition during the first circle of charge / discharge has been confirmed and attributed to oxygen loss and partial delithiation. Ramos-Sanchez *et al.*[3], have recently reported on this phase transition control and proposed $Li_2CuO_2$ for future battery applications due to its high capacity in pre-charge conditions as well as its fast $Li^+$ ion mobility. The partial pressure chemisorption has been also investigated by Lara-Garcia and Pfeiffer[4]. In essence, it was reported that for low pressures the material's behaviour is not affected while for the increase of pressure combined with additional oxygen, the $CO_2$ chemisorption is enhanced. Furthermore, the $Li^+$ and $O^{2-}$ ion-diffusion can also affect the $CO_2$ chemisorption by means of an extra layer that forms on the surface and limits the process as the $CO_2$ cannot easily reach the bulk material. In this chapter, atomistic simulation methods are used to investigate the defect processes, electronic structure and lithium migration mechanisms in $Li_2CuO_2$. Overall, a detailed survey of the relative energetics of the formation of intrinsic defects, the solution of trivalent dopants ($Al^{3+}$, $Co^{3+}$, $Sc^{3+}$, $In^{3+}$, $Y^{3+}$, $Gd^{3+}$ and $La^{3+}$) is carried out, and the possible lithium ion migration pathways in $Li_2CuO_2$.

## 6.2. Defect chemistry and Dopants

### 6.2.1 Methodology

To calculate the defect processes and DOSs for pure and defective $Li_2CuO_2$, density functional theory simulations were employed using the plane wave code CASTEP[5, 6]. The exchange and correlation interactions were modelled by using the corrected density functional of Perdew, Burke and Ernzerhof (PBE)[7] in the generalised gradient approximation (GGA), with ultrasoft pseudopotentials[8]. The kinetic energy cut-off of the plane wave basis is 500 eV, in conjunction with a 3 x 2 x 3 Monkhorst-Pack (MP)[9] *k*-point grid and a 60-atomic site supercell. To consider correlation effects of localized electrons onsite Coulomb repulsions of 6 eV were set for the Cu 3d orbitals. This value has been tested to establish that the trends are not affected by the specific choice of U-parameter. The calculations were under constant pressure conditions. The system has been treated as spin polarized, in agreement with Ramos-Sanchez *et al.*[3], as an efficient way to correctly calculate the electronic structure of the material. Spin polarized DFT calculations are recommended for structures like transition metal oxides and metallic systems, indicating that different wavefunctions will be used for different spins. The ground state energies though, present minimum deviations as compared to the non-spin polarized system indicating that for $Li_2CuO_2$ the trends of the defect prosesses are not affected.

### 6.2.2 Crystallography

In order to investigate the materials defect chemistry, the structural configuration of the perfect cell is initially represented. **Figure 6.1** presents the crystallographic structure of $Li_2CuO_2$. As reported by Sapiña *et al.*[10], it is characterised by the body centered orthorombic (bcc) structure of the *Immm* space group (lattice parameters a = 3.6544 Å, b = 2.8602 Å and c = 9.3774 Å) whereas four $O^{-2}$ atoms reside around each $Cu^{+2}$ atom for the bc-plane, while for the square-shaped $CuO_2$, a shared edge on the b-axis is presented. The calculated crystallographic configurations are in good agreement with the experimental lattice parameters, angles and bond lengths to within 2.6% (refer to **Table 6.1**). All cells were modelled according to the convergence criteria and allowed to relax to the most energetically favoured atomic configuration.

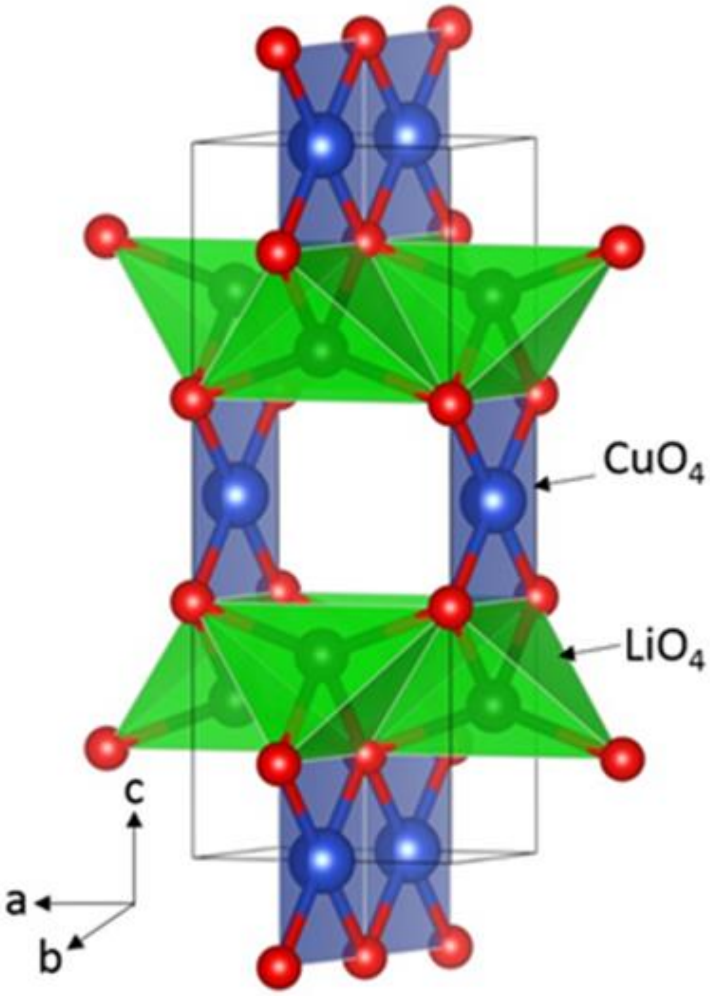

**Figure 6.1** The crystallographic structure of $Li_2CuO_2$ (space group *Immm*) showing $Li^+$ (green spheres), $Cu^{2+}$ (blue spheres), and $O^{2-}$ (red spheres).

As observed from Table 6.1, the divergence between the calculated and experimental lattice parameters is not negligible, however similar deviations are not uncommon for DFT studies (even well converged), when reproducing complicated crystal structures. The calculated lattice parameters are in good agreement with previous results however a deviation also reported in experimental previous studies[3, 11] is evident. Only limited theoretical work has been done in $Li_2CuO_2$ so far, where the calculated parameters are presenting a similar divergence[12, 13] whereas in the recent study of Johannes *et al.*[14] where the electronic structure in investigated, no discussion on the calculated lattice parameters is provided.

**Table 6.1.** Calculated and Experimental[10] Structural Parameters and Bond Distances.

| Parameter | Calc | Expt | \|Δ\|(%) |
|---|---|---|---|
| a (Å) | 3.654 | 3.6615 | 0.20 |
| b (Å) | 2.860 | 2.7887 | 2.56 |
| c (Å) | 9.377 | 9.5734 | 1.92 |
| $\alpha = \beta = \gamma$ (°) | 90.00 | 90.00 | 0.00 |
| Li – O (Å) | 1.944 | 1.9610 | 0.25 |
| Cu – O (Å) | 1.956 | 1.9577 | 2.12 |

### 6.2.3 Intrinsic Defects

Investigation of the intrinsic defect processes in energy materials is important to acquire insights into the atomic phenomena and understand their electrochemical behavior and their propensity to form intrinsic states of disorder. This is in direct connection with the material’s potential applications and performance. The intrinsic defect reactions in Kröger-Vink notation are described through the following relations:

$$Li\ Frenkel:\ Li_{Li}^{X} \rightarrow V_{Li}^{\prime} + Li_{i}^{\bullet} \tag{6.1}$$

$$O\ Frenkel:\ O_{O}^{X} \rightarrow V_{O}^{\bullet\bullet} + O_{i}^{\prime\prime} \tag{6.2}$$

$$Cu\ Frenkel:\ Cu_{Cu}^{X} \rightarrow V_{Cu}^{\prime\prime} + Cu_{i}^{\bullet\bullet} \tag{6.3}$$

$$Schottky:\ 2\ Li_{Li}^{X} + Cu_{Cu}^{X} + 2\ O_{O}^{X} \rightarrow 2\ V_{Li}^{\prime} + V_{Cu}^{\prime\prime} + 2\ V_{O}^{\bullet\bullet} + Li_{2}CuO_{2} \tag{6.4}$$

$$Li_{2}O\ Schottky:\ 2\ Li_{Li}^{X} + O_{O}^{X} \rightarrow 2\ V_{Li}^{\prime} + V_{O}^{\bullet\bullet} + Li_{2}O \tag{6.5}$$

$$Li/Cu\ antisite:\ Li_{Li}^{X} + Cu_{Cu}^{X} \rightarrow Li_{Cu}^{\prime} + Cu_{Li}^{\bullet} \tag{6.6}$$

$$Li/O\ antisite:\ Li_{Li}^{X} + O_{O}^{X} \rightarrow Li_{O}^{\bullet\bullet\bullet} + O_{Li}^{\prime\prime\prime} \tag{6.7}$$

$$Cu/O\ antisite:\ Cu_{Cu}^{X} + O_{O}^{X} \rightarrow Cu_{O}^{\bullet\bullet\bullet\bullet} + O_{Cu}^{\prime\prime\prime\prime} \tag{6.8}$$

The reaction energies for these intrinsic defect processes are reported in **Table 6.2**. These have been calculated based on the lowest ground state energies of the system. Typically, the formation of Frenkel and Schottky defects is unfavourable for most oxides. This in turn suggests that the formation of vacancies and interstitial defects will be limited at equilibrium conditions. Therefore, it is expected these intrinsic defects to be present only at low concentrations in undoped $Li_2CuO_2$. Overall, the lithium Frenkel mechanism is the lowest energy process compared to the other Frenkel and Schottky defects that have been considered. In addition, the formation enthalpy of $Li_2O$ via the $Li_2O$ Schottky-like reaction (relation 5) is a process that requires an amount of 1.75 eV per defect (refer to Table 6.2). This process can lead to the formation of additional $V_{Li}^{\prime}$ and $V_{O}^{\bullet}$, although at temperatures elevated far from room temperature. The formation of antisite defects ($Li_{Cu}^{\prime}$

and $Cu_{Li}^{\bullet}$) have also been considered corresponding to 0.07 eV, significantly lower than other intrinsic processes mainly due to the binding of the opposite charged defects and relaxation effects. The $Li_{O}^{\bullet\bullet\bullet}$ / $O_{Li}'''$ and $Cu_{O}^{\bullet\bullet\bullet\bullet}$ / $O_{Cu}''''$ antisite formations have been also considered through DFT. However, these correspond to even higher energies as compared to the Frenkel mechanisms as it is energetically unfavourable to let the $Cu^{2+}$ atoms be accommodated at $O^{2-}$ sites and vice-versa.

**Table 6.2.** Reaction energies for the intrinsic defect processes in $Li_2CuO_2$.

| Defect Process | Equation | Defect energy (eV) |
|---|---|---|
| Li Frenkel | 1 | 1.75 |
| O Frenkel | 2 | 2.33 |
| Cu Frenkel | 3 | 2.96 |
| Schottky | 4 | 3.9 |
| $Li_2O$ Schottky- like | 5 | 1.75 |
| Li/Cu antisite | 6 | 0.07 |
| Li/O antisite | 7 | 6.99 |
| O/Cu antisite | 8 | 6.14 |

### 6.3 Lithium self-diffusion.

It is noted that $Li_2CuO_2$ presents an attractive and fast $Li^+$ – ion mobility. This is a key component when designing battery materials as it corresponds to higher charge / discharge rates as well as better structural stability. Atomistic simulations have been used for the examination of possible $Li^+$ vacancy migration pathways as well as for the estimation of the corresponding activation energies of migration. Three different paths between adjacent $Li^+$ sites were investigated for the $Li^+$ vacancy migration mechanism (as shown in **Figure 6.2**).

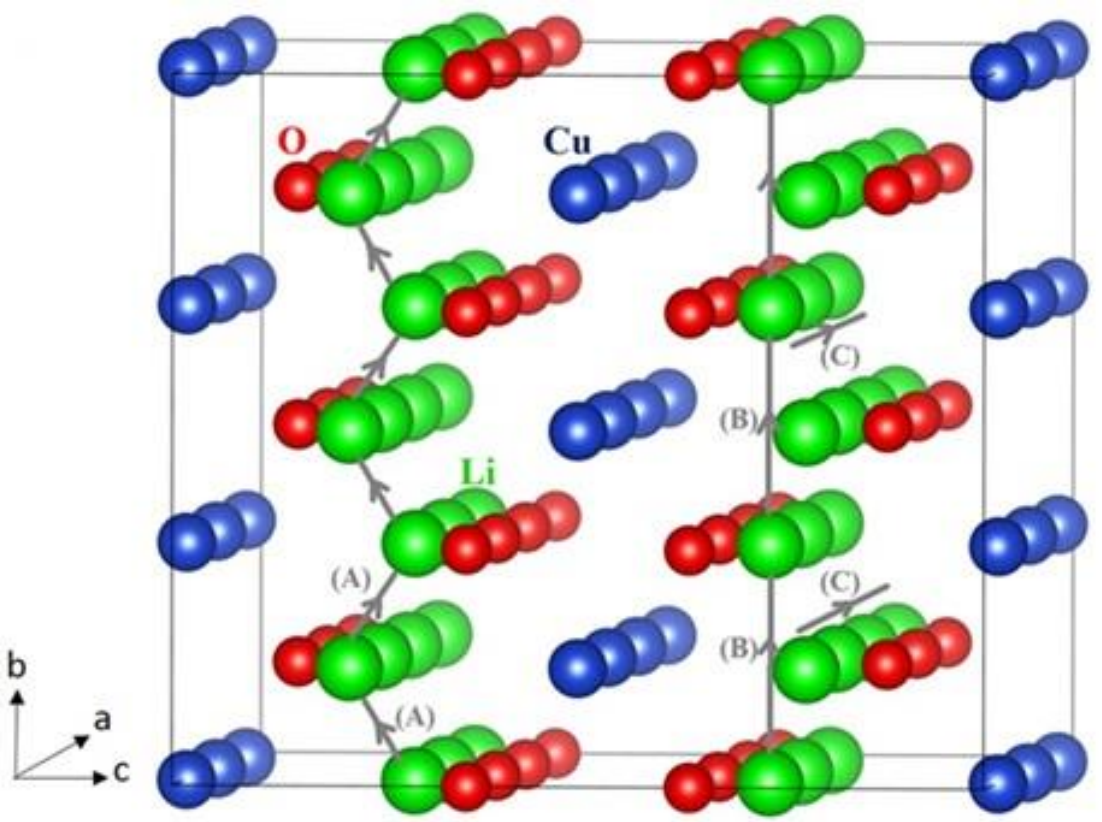

**Figure 6.2** The possible lithium ion migration paths considered. $Li^+$, $Cu^{2+}$, and $O^{2-}$ atoms are shown as green, blue and red spheres respectively.

The zig-zag $Li^+$ ion diffusion path (path A in **Figure 6.2**) in the ab-plane corresponds to the lowest energy process with an activation energy of migration of 0.11 eV. Here the activation energy of migration is defined as the position of the highest potential energy along the migration path and is calculated for a vacancy transfer of approximately 2.35 eV. The alternative $Li^+$ pathways (B and C) present higher activation energies of migration as shown in Figure 6.2 therefore they are not considered as favourable configurations of ion hopping.

**Table 6.3**. Three different energy profiles are shown in Figure 6.2 [for $Li^+$ diffusion paths (A, B and C)] of $Li^+$ vacancy hopping between two adjacent $Li^+$ sites in $Li_2CuO_2$. $E_{mig}$ corresponds to the activation energy for the $Li^+$ ion migration.

| Migration path | Li-Li separation (Å) | Activation energy (eV) |
|---|---|---|
| A | 2.35 | 0.11 |
| B | 2.79 | 1.43 |
| C | 3.58 | 4.58 |

## 6.4. Trivalent doping.

Despite the significantly low activation energy of migration for the lithium diffusion in $Li_2CuO_2$, this will be constrained mainly due to the high $Li^+$ Frenkel energies. This is because there will be a limited concentration of $V_{Li}'$ that will act as vehicles / accommodating sites and will mediate for Li self-diffusion via the vacancy mechanism. A defect engineering strategy is to introduce a high $V_{Li}'$ concentration through doping with trivalent ions. This process has been successfully employed in other energy materials[15] [16] and can be described in the Kröger-Vink notation as:

$$R_2O_3 + 2Cu_{Cu}^X + 2Li_{Li}^X \rightarrow 2\, R_{Cu}^{\bullet} + 2\, V_{Li}' + 2CuO + 2Li_2O \qquad (6.9)$$

To identify the oxide ($R_2O_3$,  R = Al, Sc, In, Y, Gd and La) of the minimum solution enthalpy in $Li_2CuO_2$, the solution enthalpy for every dopant versus the ionic radii is given in **Table 6.4**[17]. The solution energy of $Al_2O_3$ is the lowest energy process (0.97 eV/$Al^{3+}$) and therefore, doping $Li_2CuO_2$ with $Al^{3+}$ is a promising technique that will result in the $V_{Li}'$ formation, with energies significantly lower than those required by the $Li^+$ Frenkel reaction in the undoped material. This will eventually lead to a non-equilibrium $V_{Li}'$ concentration which in turn will provide additional dynamics for $Li^+$ self-diffusion increasing the total $Li^+$ diffusivity of the material.

**Table 6.4**. Solution enthalpy of $R_2O_3$ ($R$ = Al, Sc, In, Y, Gd and La) in $Li_2CuO_2$ using atomistic simulations[17].

| Dopant | Solution Enthalpy (eV) | Ionic Radii (A) |
|---|---|---|
| Al | 0.97 | 0.535 |
| Sc | 2.09 | 0.745 |
| In | 2.31 | 0.8 |
| Y | 3.14 | 0.9 |
| Gd | 3.54 | 0.938 |
| La | 4.00 | 1.032 |

It is shown that the $Al_2O_3$ solution enthalpy in $Li_2CuO_2$ is considerably lower than the enthalpies for the Schottky and Frenkel disorders. This in turn indicates that vacancy and interstitial concentrations will primarily be due to the extrinsic impurity compensation processes.

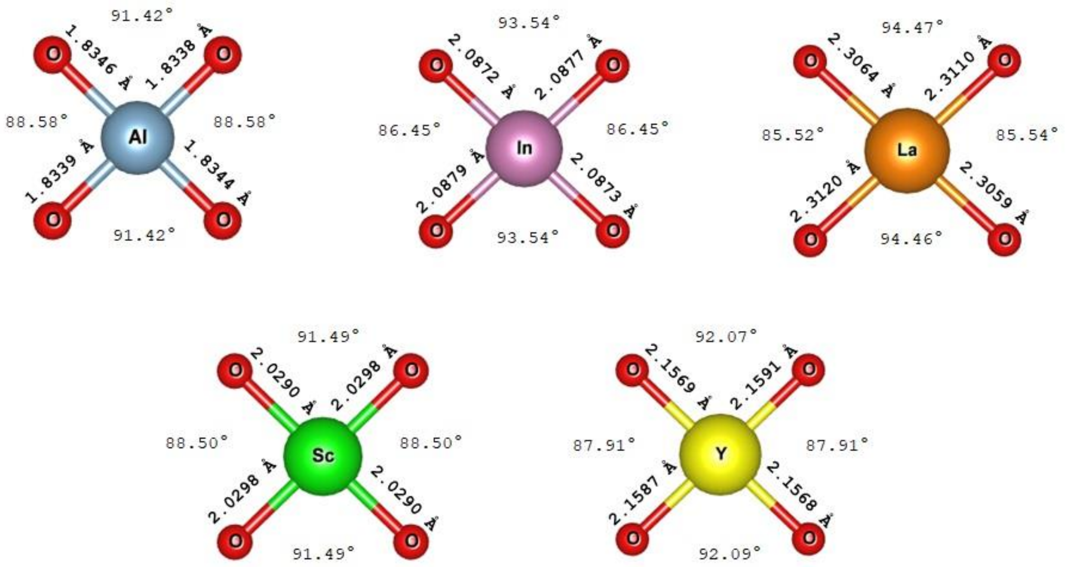

**Figure 6.3** The chemical bonding of the substitutional dopant with nearest oxygen atoms in $Li_2CuO_2$.

It is also expected that the introduction of substitutional dopants in the perfect lattice may also affect the activation energies of migration for lithium. The introduction of dopants in the vicinity of the migrating $V_{Li}'$ will result in the increase of the migration energy barriers from 0.22 eV (for the smallest dopant, Al) to 0.88 eV (for the largest dopant, La). In essence, it is observed that the largest increase of the migration energy barrier corresponds to the dopant of the largest ionic radii, in consistency with the stronger association (i.e. relaxation of the large dopant in the vacant space). Overall, these interactions will introduce an increase in the energetic barrier that needs to be overcome. **Figure 6.3** represents the chemical bonding of the substitutional trivalent dopants with the surrounding oxygen atoms.

## 6.5. Density of states

Here, density of states (DOS) calculations are performed whereas the individual contribution of each element (partial-DOS) is plotted in **Figure 6.4**, for the cases of (a) perfect cell (b) $V_{Li}'$ (c) $Al_{Cu}^{\bullet}$ and (d) $\{Al_{Cu}^{\bullet}:V_{Li}'\}^{X}$. The valence band maximum (VBM) is set at zero energy level. The perfect structure of $Li_2CuO_2$ is shown in Figure 6.4 (a), where the band gap is calculated at 1.05 eV. It is also shown that $Cu^{2+}$ and $O^{2-}$ mainly contribute to the DOS of the valence band, driven by the Cu-d and O-p orbitals, while $Li^{+}$ and $Cu^{2+}$ are the main contributors to the conduction band, driven by the Li-p and Cu-p orbitals as presented in **Figure 6.5**. It is also observed that the high states of $Cu^{2+}$ and $O^{2-}$ just below the VBM and the non-uniformity of the band as presented by two separated contributions. The effect on the DOS of the introduction of a lithium vacancy in the supercell is minimal (refer to Figure 6.4(b)) as no additional states are created into the band gap, whereas only a small increase is observed in the DOS in the conduction band due to Lithium.

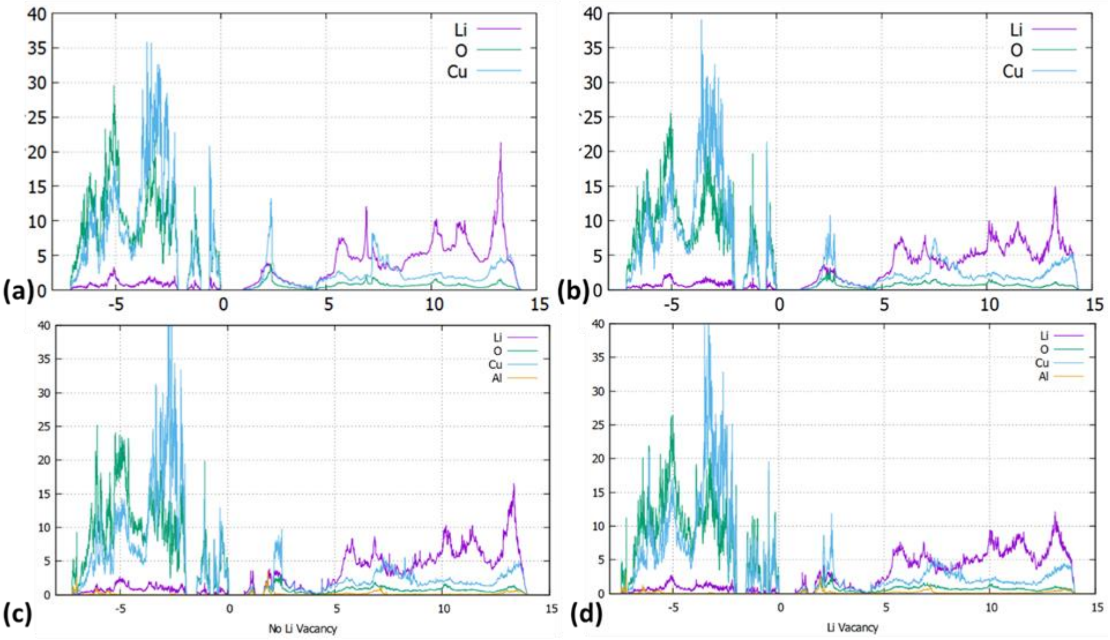

**Figure 6.4** The densities of states for $Li_2CuO_2$ (a) perfect cell (b) $V_{Li}'$ (c) $Al_{Cu}^{\bullet}$ (d) $\{Al_{Cu}^{\bullet}:V_{Li}'\}^{X}$.

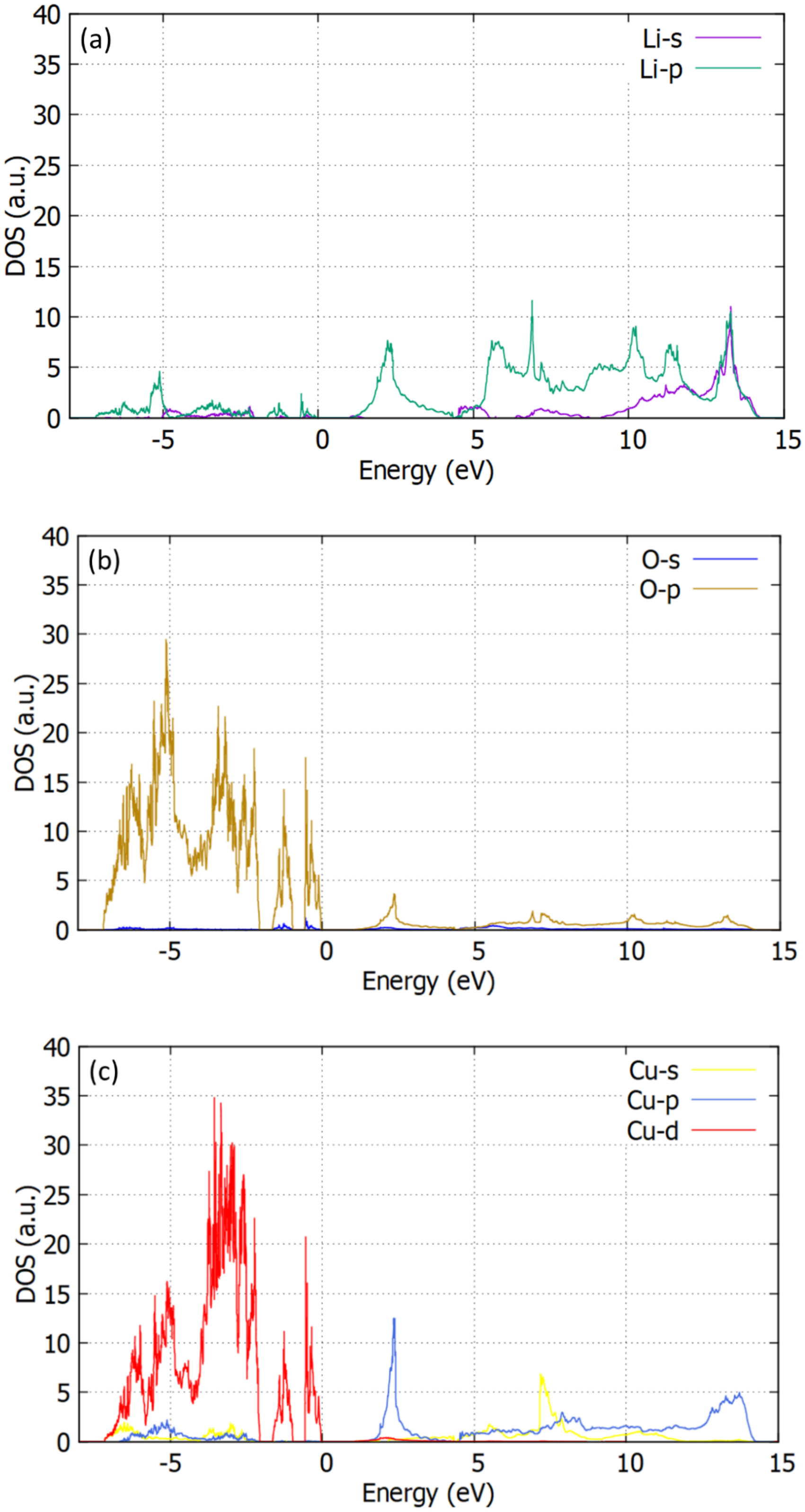

**Figure 6.5** The contribution of the atomic orbitals to the partial densities of states of the perfect $Li_2CuO_2$ supercell shown in Figure 6.4 (a).

The impact of the $Al_{Cu}^{\bullet}$ and $\{Al_{Cu}^{\bullet}\colon V_{Li}'\}^{X}$ pairs on the densities of states of $Li_2CuO_2$ was also considered and illustrated in Figure 6.6 (c) – (d). It is shown that the $Al_{Cu}^{\bullet}$ defect introduces a distribution of states in the band gap with a simultaneous minor narrowing of the gap itself to 0.80 eV. A similar picture is observed in Figure 6.4(d) for the $\{Al_{Cu}^{\bullet}\colon V_{Li}'\}^{X}$ case. The $R_{Cu}^{\bullet}$ and $\{R_{Cu}^{\bullet}\colon V_{Li}'\}^{X}$ doping configurations in $Li_2CuO_2$ are presented in **Figure 6.6**. Therefore, it is expected the introduction of $Al^{3+}$ (and other) dopants to have an effect on the electronic structure, mainly with the introduction of states in the band gap but also with a minor narrowing of the gap. Although the leading conduction mechanism for battery applications is ionic diffusion, the effect of the energy levels in the band gap has to be considered as well.

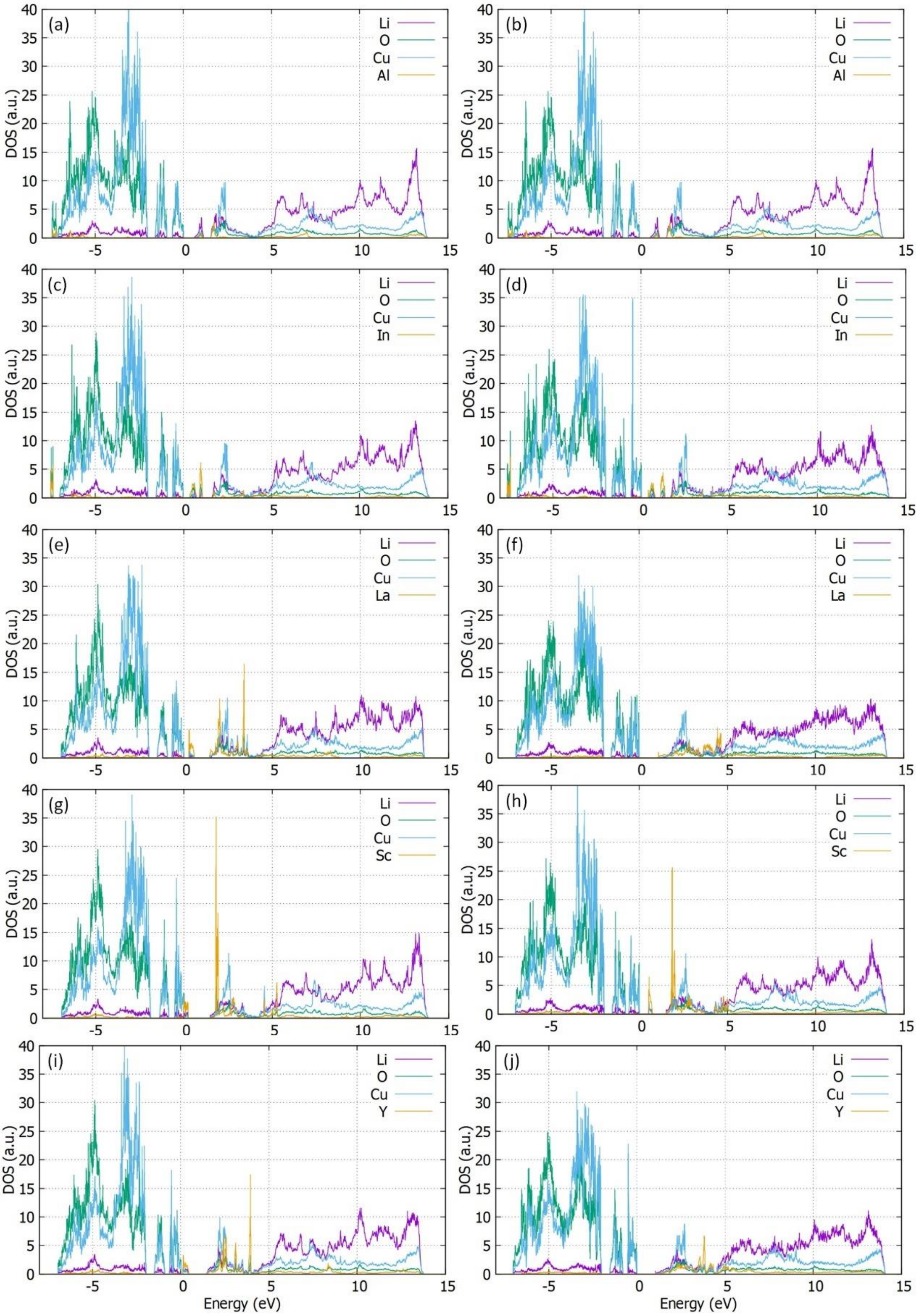

**Figure 6.6** The densities of states for (a) $Al^{\bullet}_{Cu}$ (b) $\{Al^{\bullet}_{\boldsymbol{Cu}}:V'_{\boldsymbol{Li}}\}^{x}$ (c) $In^{\bullet}_{Cu}$ (d) $\{In^{\bullet}_{\boldsymbol{Cu}}:V'_{\boldsymbol{Li}}\}^{x}$ (e) $La^{\bullet}_{Cu}$ (f) $\{La^{\bullet}_{\boldsymbol{Cu}}:V'_{\boldsymbol{Li}}\}^{x}$ (g) $Sc^{\bullet}_{Cu}$ (h) $\{Sc^{\bullet}_{\boldsymbol{Cu}}:V'_{\boldsymbol{Li}}\}^{x}$ (i) $Y^{\bullet}_{Cu}$ (j) $\{Y^{\bullet}_{\boldsymbol{Cu}}:V'_{\boldsymbol{Li}}\}^{x}$.

## 6.6 Conclusions

In the present chapter, the intrinsic defect processes and the $Li^+$ vacancy diffusion mechanisms in $Li_2CuO_2$ were investigated. Lithium vacancy diffusion presents a low migration energy barrier (0.11 eV) along zig-zag diffusion path in the ab-plane. However, in essence the relatively high lithium Frenkel energy implies a low concentration of lithium vacancies. Doping $Li_2CuO_2$ with aluminum is proposed to introduce a higher concentration of lithium vacancies in the lattice. The aluminum dopants will impact the activation energy of migration increasing the barrier to 0.22 eV. The combination of low solution enthalpy and low increase in the migration energy of lithium constitutes doping with aluminum to be the preferential doping strategy to increase the total lithium diffusivity in $Li_2CuO_2$, as compared to the intrinsic processes or the other considered dopants. Furthermore, the DOS analysis reveals that the introduction of aluminum will introduce electronic states into the energy band gap but with the lowest intensity when compared with alternative doping elements. So far, $Li_2CuO_2$ has been mainly considered as a promising material for $CO_2$ chemisorption and it is anticipated that the present investigation will motivate further experimental and theoretical work to determine the materials behaviour with respect to the diffusion properties of $Li_2CuO_2$ and its potential application in batteries. Additionally, it will generate further interest in lithium cuprate materials for energy storage applications. In the published version of the chapter[17], the defect chemistry and $Li^+$ – ion diffusion mechanisms and energetics are reported for the first time to my knowledge and should be further investigated through experimental techniques. This work has been recently cited by Aguilar-Eseiza *et al.*[18] showing the validity of theoretical modelling to complement with experimental methods.

# REFERENCES

---

[1] L. M. Palacios-Romero and H. Pfeiffer, Lithium cuprate ($Li_2CuO_2$): A new possible ceramic material for $CO_2$ chemisorption. *Chemistry Letters*, **37**, 862, (2008).

[2] K. Oh-ishi, Y. Matsukura, T. Okumura, Y. Matsunaga and R. Kobayashi, Fundamental research on gas–solid reaction between $CO_2$ and $Li_2CuO_2$ linking application for solid $CO_2$ absorbent. *Journal of Solid State Chemistry*, **211**, 162, (2014).

[3] G. Ramos-Sanchez, I.C. Romero-Ibarra, J. Vazquez-Arenas, C. Tapia, N. Aguilar-Eseiza and I. Gonzalez, Controlling $Li_2CuO_2$ single phase transition to preserve cathode capacity and cyclability in Li-ion batteries. *Solid State Ionics*, **303**, 89, (2017).

[4] H. A. Lara-Garcia and H. Pfeiffer, High and efficient $Li_2CuO_2$-$CO_2$ chemisorption using different partial pressures and enhancement produced by the oxygen addition. *Chemical Engineering Journal*, **313**, 1288, (2017).

[5] M. C. Payne, M. P. Teter, D. C. Allan, T. A. Arias and J. D. Joannopoulos, Iterative minimization techniques for ab initio total-energy calculations: molecular dynamics and conjugate gradients. *Reviews of Modern Physics*, **64**, 1045, (1992).

[6] M. D. Segall, P. J. D. Lindan, M. J. Probert, C. J. Pickard, P. J. Hasnip, S. J. Clark and M. C. Payne, First-principles simulation: ideas, illustrations and the CASTEP code. *Journal of Physics: Condensed Matter*, **14**, 2717, (2002).

[7] J. Perdew, K. Burke and M. Ernzerhof, Generalized Gradient Approximation Made Simple. *Physical Review Letters*, **77**, 3865, (1996).

[8] D. Vanderbilt, Soft self-consistent pseudopotentials in a generalized eigenvalue formalism. *Physical Review* B, **41**, 7892, (1990).

[9] H. J. Monkhorst and J. D. Pack, Special points for Brillouin-zone integrations. *Physical Review* B, **13**, 5188 (1976).

[10] F. Sapiña, J. Rodríguez-Carvajal, M.J. Sanchis, R. Ibáñez, A. Beltrán and D. Beltrán, Crystal and magnetic structure of $Li_2CuO_2$. *Solid State Communications*, **74**, 779, (1990).

[11] H. Arai, S. Okada, Y. Sakurai and J. Yamaki, Electrochemical and structural study of $Li_2CuO_2$, $LiCuO_2$ and $NaCuO_2$. *Solid State Ionics*, **106**, 45, (1998).

[12] H. Rosner, R. Hayn and S.-L. Drechsler, The electronic structure of $Li_2CuO_2$. *Physica B*, **259**, 1001, (1999).

[13] H. J. Xiang, C. Lee, and M.-H. Whangbo, Absence of a spiral magnetic order in $Li_2CuO_2$ containing one-dimensional $CuO_2$ ribbon chains. *Physical Review B*, **76**, (2007).

---

[14] M. D. Johannes, Karen Swider-Lyons and Corey T. Love, Oxygen character in the density of states as an indicator of the stability of Li-ion battery cathode materials. *Solid State Ionics,* **286**, 83, (2016).

[15] P. Dholabhai, J. B. Adams, P. Crozier and R. Sharma, A density functional study of defect migration in gadolinium doped ceria. *Physical Chemistry Chemical Physics*, **12**, 7904, (2010).

[16] M. J. D. Rushton and A. Chroneos, Impact of uniaxial strain and doping on oxygen diffusion in $CeO_2$. *Scientific Reports*, **4**, 6068 (2014).

[17] A. Kordatos, N. Kuganathan, N. Kelaidis, P. Iyngaran and A. Chroneos, Defects and lithium migration in $Li_2CuO_2$. *Scientific Reports*, **8**, 6754, (2018).

[18] N. Aguilar-Eseiza, G. Ramos-Sánchez, F. González and I. González, High voltage – Improved reversible capacity in $Ni^{+2/+3}$ modified copper-based cathodes for lithium ion batteries. *Electrochemistry Communications*, **96**, 32, (2018).

# CHAPTER 7

# $Li_2SnO_3$ and $Li_2RuO_3$ as battery materials: Intrinsic Defect Processes

Part of the results presented here has been published in *Scientific Reports* **8**, 12621 (2018) and *Scientific Reports*, **9**, 550, (2019).

## 7.1. Introduction

In this chapter, the defect processes in $Li_2SnO_3$ and $Li_2RuO_3$ are investigated, with respect to their potential application as $Li^+$ – ion battery components. A key feature of these materials is that in principle, the extraction of more than one lithium ion per formula unit is possible and thus, a greater insight into the defect properties is crucial to gain a better understanding of their electrochemical behaviour. Tin-based oxide $Li_2SnO_3$ has already attracted considerable interest as a promising cathode material for potential use in rechargeable $Li^+$- ion batteries due to its attractive high capacity (510.2 $mA{\cdot}h\,g^{-1}$)[1]. It has been proposed as an alternative to $Li_2MnO_3$, a material that despite its high capacity (>200 $mA{\cdot}h\,g^{-1}$) and energy density (934 $W{\cdot}h\,kg^{-1}$)[2, 3, 4, 5] is also characterized by poor structural stability during cycling as well as electronic conductivity. As both $Li_2MnO_3$ and $Li_2SnO_3$ crystallise in a monoclinic layered structure, it was suggested that the replacement of Mn by Sn could be a possible strategy to improve structural stability and thus cyclic performance and so consider $Li_2SnO_3$ as a viable cathode material for lithium ion batteries. Recently, Wang *et al.*[1, 6] have used X-ray diffraction to determine the structure of $Li_2SnO_3$ as well as a hydrothermal route to prepare $Li_2SnO_3$ where an electrochemical performance with high capacity and good cycling stability was observed. Additionally, layered $Li_2RuO_3$ is a promising candidate cathode material in rechargeable $Li^+$ – ion batteries due to its novel anionic redox process and high reversible capacity (230 $mA{\cdot}h\,g^{-1}$)[7]. A key feature of $Li_2RuO_3$ is that the lithium ion can be extracted with the concomitant oxidation of ruthenium from a tetravalent to hexavalent state. Moore *et al.*[8] have studied the electrochemical properties of $Li_2RuO_3$ whereas, a novel hybrid $Na^+/Li^+$ battery has recently been assembled using $Li_2RuO_3$ as a cathode material because of its unique structure accommodating both $Li^+$ and $Na^+$ ions[9]. $Li_2RuO_3$ was also suggested as an additive to improve the energy density in the high energy lithium-ion capacitors due to its high reversible characteristics for $Li^+$ ion intercalation/de-intercalation and structural stability[10]. In this chapter, the relative energetics of the formation of intrinsic defects in $Li_2SnO_3$ and $Li_2RuO_3$ are investigated, as well as the solution of trivalent dopants and the possible lithium ion migration pathways.

## 7.2 Defect chemistry

### 7.2.1 Methodology

The supercells were modelled though the plane wave density functional theory (DFT) code CASTEP[11, 12]. The plane wave basis set was set to a cut-off of 480 eV and a 2x2x2 Monkhorst-Pack (MP)[13] k-point grid was used with a 98-atomic site supercell. For the exchange and correlation interactions in the crystal, we use the formulation with the corrected density functional of Perdew, Burke and Ernzerhof (PBE)[14], within the generalized gradient approximation (GGA) with ultrasoft pseudopotentials [15]. All the calculations were under constant pressure conditions and the cells were relaxed in the minimum energy configuration before the investigation of the electronic structure. The Partial Density of States (PDOS) for the perfect and defective / doped structures was visualised through the OPTADOS tool[16, 17].

### 7.2.2 Crystallographic structure of $Li_2SnO_3$ and $Li_2RuO_3$

The structure of $Li_2SnO_3$ as presented in **Figure 7.1 (a)** exhibits a monoclinic crystallographic configuration with space group C2/c (lattice parameters a = 5.2900 Å, b = 9.1900 Å, c = 10.0300 Å, α = 90°, β = 100.1° and γ=90°) as reported by Lang[18]. where the $Sn^{4+}$ and $Li^{+}$ atoms tend to form octahedra with six $O^{2-}$ neighboring atoms.

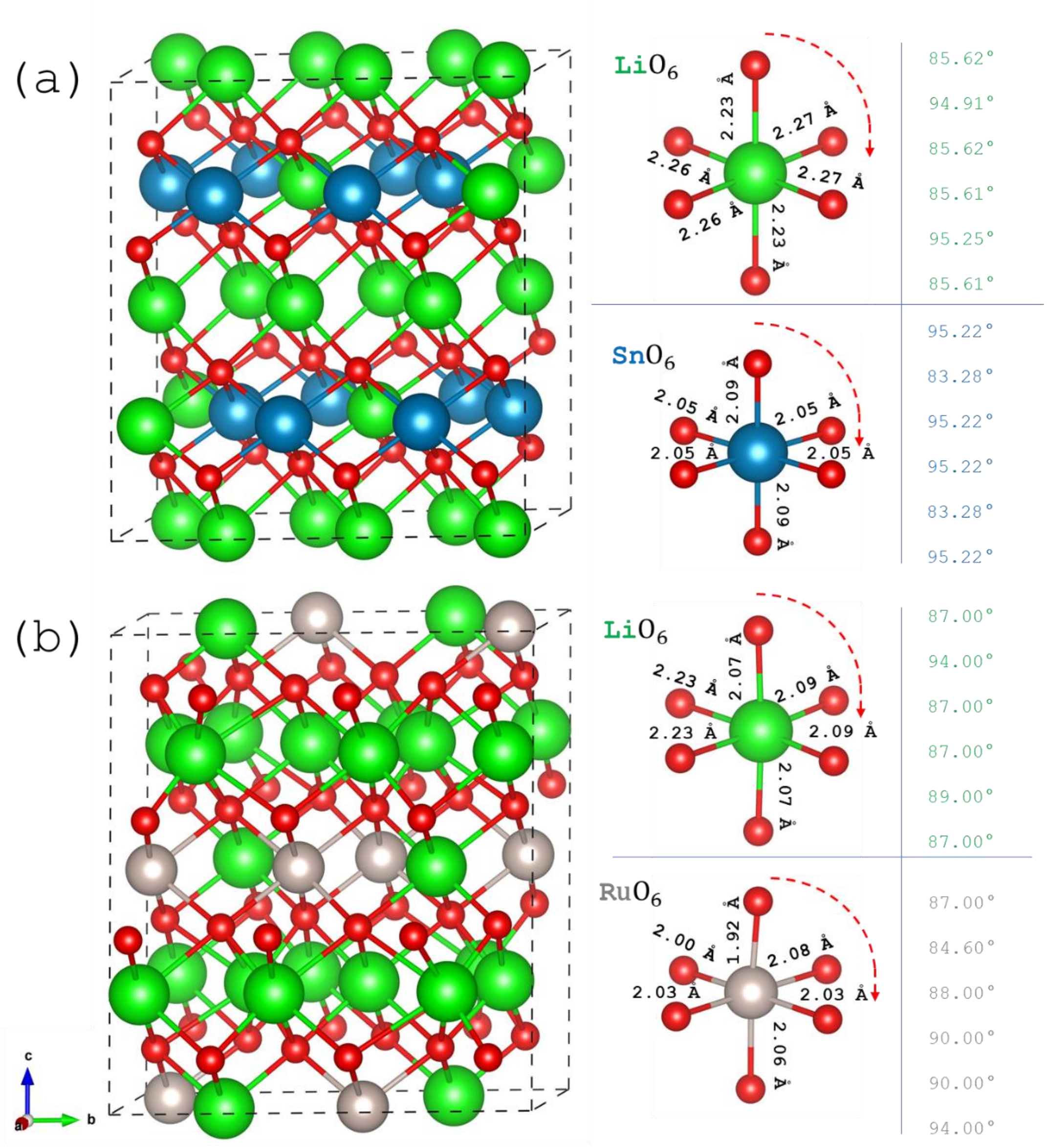

**Figure 7.1** The crystal structure (space group C2/c), atomic configuration and chemical environment of (a) $Li_2SnO_3$ and (b) $Li_2RuO_3$.

$Li_2RuO_3$ also crystallises in a monoclinic layered structure (**Figure 7.1 (b)**) with space group C2/c (lattice parameters a = 4.9230 Å, b = 8.7746 Å, c = 9.8776 Å, α = 90°, β = 100.073° and γ=90°) as reported by Kobayashi *et al.*[19] with the $Ru^{4+}$ and $Li^{+}$ atoms forming octahedra as well.

**Table 7.1** Calculated and Experimental Structural Parameters and Bond Distances for Monoclinic (c2/c) $Li_2SnO_3$ and $Li_2RuO_3$.

| **$Li_2SnO_3$** | Calc | Expt[18] | \|Δ\|(%) |
|---|---|---|---|
| a (Å) | 5.3029 | 5.2900 | 0.24 |
| b (Å) | 9.2563 | 9.1900 | 0.72 |
| c (Å) | 10.0598 | 10.0300 | 0.30 |
| α (°) | 90.0 | 90.0 | 0.00 |
| β (°) | 100.85 | 100.10 | 0.75 |
| γ (°) | 90.0 | 90.0 | 0.00 |
| **$Li_2RuO_3$** | Calc | Expt[19] | \|Δ\|(%) |
| a (Å) | 5.0622 | 4.9230 | 2.83 |
| b (Å) | 8.7521 | 8.7746 | 0.26 |
| c (Å) | 9.9749 | 9.8776 | 0.99 |
| α (°) | 90.0 | 90.0 | 0.00 |
| β (°) | 99.593 | 100.073 | 0.48 |
| γ (°) | 90.0 | 90.0 | 0.00 |

The modelled structural parameters of $Li_2RuO_3$ are in fair agreement with experiment[20, 21], particularly for a complicated crystal structure. The 3% difference in the volume is consistent with recent theoretical[22] work. The differences in the lattice parameters with this theoretical study are due to the different parameters used (pseudopotentials and exchange correlation conditions). The aim of the present thesis is to examine trends and as such these differences in the structural parameters will not have an impact.

### 7.2.3 Intrinsic Defect Processes

In order to gain insights into the electrochemical behavior of $Li_2SnO_3$ and $Li_2RuO_3$, a series of isolated point defect energies (vacancy, antisite and interstitial) are calculated and combined to assess the formation energies for Frenkel, Schottky and antisite defects. Here atomistic simulations were employed in $Li_2SnO_3$. The following equations represent the reactions involving these defects as written using Kröger-Vink notation[27].

$$\text{Li Frenkel: } \mathrm{Li}_{\mathrm{Li}}^{\mathrm{X}} \rightarrow V_{\mathrm{Li}}' + \mathrm{Li}_{\mathrm{i}}^{\bullet} \tag{7.1}$$

$$\text{O Frenkel: } \mathrm{O}_{\mathrm{O}}^{\mathrm{X}} \rightarrow V_{\mathrm{O}}^{\bullet\bullet} + \mathrm{O}_{\mathrm{i}}'' \tag{7.2}$$

$$\text{Sn Frenkel: } V_{\mathrm{Sn}}^{\mathrm{X}} \rightarrow V_{\mathrm{Sn}}'''' + \mathrm{V}_{\mathrm{i}}^{\bullet\bullet\bullet\bullet} \tag{7.3}$$

$$\text{Schottky: } 2\,\mathrm{Li}_{\mathrm{Li}}^{\mathrm{X}} + \mathrm{Sn}_{\mathrm{Sn}}^{\mathrm{X}} + 3\,\mathrm{O}_{\mathrm{O}}^{\mathrm{X}} \rightarrow 2\,V_{\mathrm{Li}}' + V_{\mathrm{Sn}}'''' + 3\,V_{\mathrm{O}}^{\bullet\bullet} + \mathrm{Li_2SnO_3} \tag{7.4}$$

$$\mathrm{Li_2O}\text{ Schottky: } 2\,\mathrm{Li}_{\mathrm{Li}}^{\mathrm{X}} + \mathrm{O}_{\mathrm{O}}^{\mathrm{X}} \rightarrow 2\,V_{\mathrm{Li}}' + V_{\mathrm{O}}^{\bullet\bullet} + \mathrm{Li_2O} \tag{7.5}$$

$$\text{Li/Sn antisite: } \mathrm{Li}_{\mathrm{Li}}^{\mathrm{X}} + V_{\mathrm{Sn}}^{\mathrm{X}} \rightarrow \mathrm{Li}_{\mathrm{Sn}}''' + \mathrm{Sn}_{\mathrm{Li}}^{\bullet\bullet\bullet} \tag{7.6}$$

Overall, the most favorable intrinsic disorder is $Li^+$ Frenkel whereas the formation of other Frenkel and Schottky defects corresponds to higher energies. This will result to high $Li^+$ – ion mobility rates within the crystal lattice, an important factor when investigating potential cathode materials. In addition, high $Sn^{4+}$ Frenkel energy indicates the material's good structural stability as a system for energy applications. Furthermore, the $Li^+/Sn^{4+}$ antisite defect process energy is calculated to be considerably high, indicating that a small percentage of Li on Sn sites ($\mathrm{Li}_{\mathrm{Sn}}'''$) and Sn on Li sites ($\mathrm{Sn}_{\mathrm{Li}}^{\bullet\bullet\bullet}$) is expected particularly at higher temperatures. This is in agreement with the intralayer intermixing between $Li^+$ and $Sn^{4+}$ found in the experiment[6]. Cation antisite defect formation in ionic conductors may limit or block $Li^+$ – ion diffusion and have been already observed in a variety of other $Li^+$ ion battery materials during cycling[23, 24]. Wang *et al*. highlights the demanded optimization of the cation site occupation during the material's synthesis. The defect processes' reaction energies are reported in **Table 7.2**.

**Table 7.2** Reaction energies for the intrinsic defect processes in $Li_2SnO_3$.

| Defect Process | Equation | Defect Energy (eV) |
|---|---|---|
| Li Frenkel | 1 | 4.74 |
| O Frenkel | 2 | 5.56 |
| Sn Frenkel | 3 | 15.46 |
| Schottky | 4 | 21.69 |
| $Li_2O$ Schottky- like | 5 | 8.17 |
| Li/Sn antisite | 6 | 10.41 |

Considering $Li_2RuO_3$, the associated defects through atomistic simulations[25] are represented through the following relations :

$$\text{Li Frenkel: } \mathrm{Li}_{\mathrm{Li}}^{\mathrm{X}} \rightarrow V_{\mathrm{Li}}^{\prime} + \mathrm{Li}_{\mathrm{i}}^{\bullet} \tag{7.7}$$

$$\text{O Frenkel: } \mathrm{O}_{\mathrm{O}}^{\mathrm{X}} \rightarrow V_{\mathrm{O}}^{\bullet\bullet} + \mathrm{O}_{\mathrm{i}}^{\prime\prime} \tag{7.8}$$

$$\text{Ru Frenkel: } V_{\mathrm{Ru}}^{\mathrm{X}} \rightarrow V_{\mathrm{Ru}}^{\prime\prime\prime\prime} + \mathrm{V}_{\mathrm{i}}^{\bullet\bullet\bullet\bullet} \tag{7.9}$$

$$\text{Schottky: } 2\ \mathrm{Li}_{\mathrm{Li}}^{\mathrm{X}} + \mathrm{Ru}_{\mathrm{Ru}}^{\mathrm{X}} + 3\ \mathrm{O}_{\mathrm{O}}^{\mathrm{X}} \rightarrow 2\ V_{\mathrm{Li}}^{\prime} + V_{\mathrm{Ru}}^{\prime\prime\prime\prime} + 3\ V_{\mathrm{O}}^{\bullet\bullet} + \mathrm{Li_2RuO_3} \tag{7.10}$$

$$\mathrm{Li_2O}\text{ Schottky: } 2\ \mathrm{Li}_{\mathrm{Li}}^{\mathrm{X}} + \mathrm{O}_{\mathrm{O}}^{\mathrm{X}} \rightarrow 2\ V_{\mathrm{Li}}^{\prime} + V_{\mathrm{O}}^{\bullet\bullet} + \mathrm{Li_2O} \tag{7.11}$$

$$\text{Li/Ru antisite: } \mathrm{Li}_{\mathrm{Li}}^{\mathrm{X}} + V_{\mathrm{Ru}}^{\mathrm{X}} \rightarrow \mathrm{Li}_{\mathrm{Ru}}^{\prime\prime\prime} + \mathrm{Ru}_{\mathrm{Li}}^{\bullet\bullet\bullet} \tag{7.12}$$

Here, the Li$^+$ Frenkel is the most favourable intrinsic disorder followed by Li$^+$ / Ru$^{4+}$ antisite defect whereas the formation of other Frenkel and Schottky defects is less favourable. The second most favorable defect process indicates that there will be a small percentage of Li on Ru sites ($\mathrm{Li}_{\mathrm{Ru}}^{\prime\prime\prime}$) and Ru on Li sites ($\mathrm{Ru}_{\mathrm{Li}}^{\bullet\bullet\bullet}$). The reaction energies for these intrinsic defect processes are reported in **Table 7.3**.

**Table 7.3** Reaction energies for the intrinsic defect processes in $Li_2RuO_3$.

| Defect Process | Equation | Defect Energy (eV) |
|---|---|---|
| Li Frenkel | 1 | 1.56 |
| O Frenkel | 2 | 7.86 |
| Ru Frenkel | 3 | 11.54 |
| Schottky | 4 | 5.80 |
| $Li_2O$ Schottky- like | 5 | 5.70 |
| Li/Ru antisite | 6 | 1.89 |

## 7.3 Lithium self-diffusion

High-rate cathode materials in lithium ion batteries require lithium ion diffusion with low activation energy, typically below 0.6 eV. Using atomistic simulations, it is possible to examine various possible diffusion paths for lithium ion diffusion and act synergetically with experiment providing complementary information. For the $Li^+$ vacancy migration mechanism, eight different local hopping routes in $Li_2SnO_3$ are investigated as represented in **Figure 7.2**.

Notably, the activation energy of migration is defined as the position of the highest potential energy along the migration path. Migration energies are reported in Table 7.4 together with the Li-Li separation. Long range paths have been also considered where the first path exhibits a zig-zag pattern (A→B→C→B→A) where the local $Li^+$ hopping corresponds to a calculated low activation energy of migration of 0.16 eV (local hop C). However, the complete mechanism exhibits an activation energy of 0.65 eV. Furthermore, the second pathway follows a straight line (X→Y) with an activation energy of 0.63 eV between two adjacent sites. Several different possible long-range $Li^+$ diffusion pathways have also been considered along the c-axis.

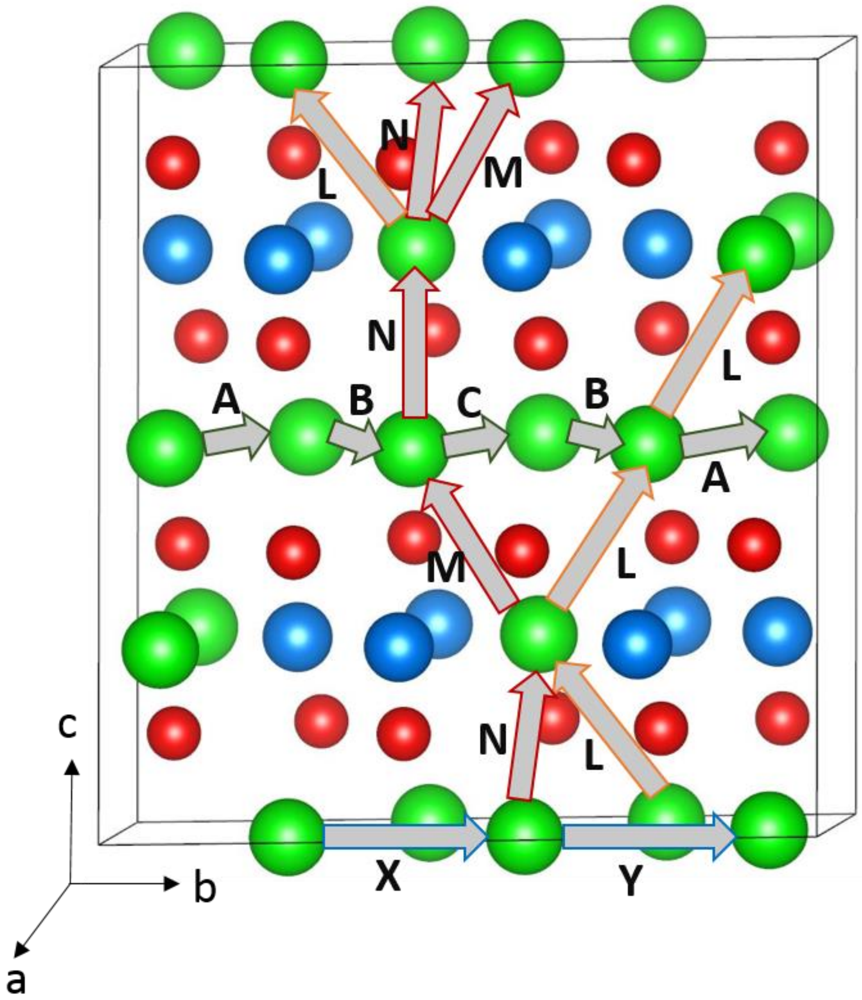

**Figure 7.2** Possible long-range lithium vacancy migration paths considered. Green, blue and red colors correspond to $Li^+$, $Sn^{4+}$, and $O^{2-}$ atoms respectively.

Overall, the lower activation energy long range path along the c-axis plane is L→L→L with the activation energy of migration to be 0.61 eV, very close to the ideal values as introduced earlier. Other long-range paths will exhibit activation energies higher than 0.61 eV in this direction indicating the local Li hops limitations along these pathways. The activation energy of Li-vacancy migration along the c axis has been reported to be 0.30 eV by Howard and Holzwarth[26], whereas here the calculated value is 0.61 eV. This divergence may be connected to the difference between their calculated *c*-lattice parameter (9.78 Å), and our estimated value (10.059 Å). The experimental *c*-lattice parameter is reported to be 10.03 Å[18].

**Table 7.4**. Eight different energy profiles (as shown in Figure 7.2) of $Li^+$ vacancy hopping between two adjacent Li sites in $Li_2SnO_3$.

| Migration path | Li-Li separation (Å) | Activation energy (eV) |
|---|---|---|
| A | 3.118 | 0.65 |
| B | 3.055 | 0.42 |
| C | 2.968 | 0.16 |
| L | 3.023 | 0.61 |
| M | 3.000 | 0.62 |
| N | 3.053 | 0.65 |
| X | 3.049 | 0.41 |
| Y | 3.159 | 0.63 |

Following on from our investigation of the $Li^+$ vacancy migration mechanisms, six different local $Li^+$ hopping configurations in $Li_2RuO_3$, have been considered as illustrated in **Figure 7.3**. As it can be observed from the figure these mechanisms cover all possible nearest neighboring hops of the lithium vacancy in the lattice. Overall, five long-range pathways of local $Li^+$ hops are constructed aiming for the lower activation energy of migration amongst them all. The first long range path exhibits a linear orientation (A→B→A→B) along the *b* axis including the local $Li^+$ hop with the lowest activation energy of migration of 0.65 eV (local hop B). However, the total activation energy for the complete transition will be 0.76 eV. Furthermore, the second pathway exhibits a zig-zag pattern (C→C→C→C) with an activation energy of 1.09 eV, while both the third and fourth migration routes [D→E→D→E and E→E→E→E] exhibit a linear path along *ab* plane with an activation energy of 0.73 eV. Finally, the fifth migration path (F→F→F→F) which is constructed along the *ac* plane corresponds to the highest activation energy of $Li^+$ migration, calculated to be 1.13 eV. Overall $Li_2RuO_3$ will exhibit similar activation energies of migration along the different pathways as compared to $Li_2SnO_3$.

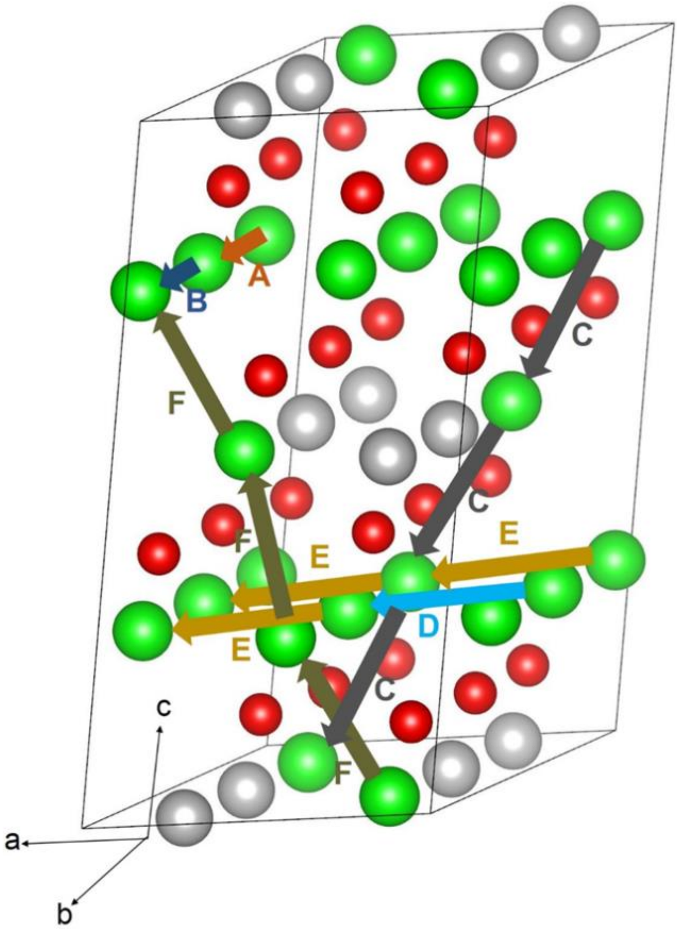

**Figure 7.3** Possible long-range lithium vacancy migration paths considered. Green, grey and red colors correspond to Li, Ru, and O atoms respectively.

**Table 7.5** Six different energy profiles as shown in Figure 7.3 of $Li^+$ vacancy hopping between two adjacent $Li^+$ sites in $Li_2RuO_3$.

| Migration path | Li-Li separation (Å) | Activation energy (eV) |
|---|---|---|
| A | 2.8978 | 0.76 |
| B | 2.9565 | 0.65 |
| C | 2.9786 | 1.09 |
| D | 2.9020 | 0.73 |
| E | 2.9312 | 0.73 |
| F | 2.9923 | 1.13 |

## 7.4 Doping

The incorporation of additional lithium into the as-prepared host material will enhance the capacity and thus, increase the applicability of $Li_2SnO_3$ and $Li_2RuO_3$ as component materials for rechargeable lithium batteries. A promising technique that has been already applied[27] to increase the amount of lithium is through doping with trivalent cations as substitutionals on Sn sites, which eventually leads to the creation of $Li^+$ interstitials. Here the solution of $R_2O_3$ ($R$ = Al, Sc, In, Y, Gd and La) in $Li_2SnO_3$ is considered via the following process (in Kröger-Vink notation):

$$\mathrm{R_2O_3 + 2Sn_{Sn}^{X} + Li_2O \rightarrow 2\,R'_{Sn} + 2\,Li_i^{\bullet} + 2\,SnO_2} \tag{7.13}$$

The calculated solution energies of $R_2O_3$ are shown in **Table 7.6** where it can be observed that the most favorable dopant solution energy (0.6 eV) is for $Al^{3+}$. This in turn is considered as a possible synthesis-doping strategy to introduce additional lithium into $Li_2SnO_3$. Although the exact amount of $Al^{3+}$ incorporation in the perfect lattice cannot be predicted in detail, an effective composition for Al-doped $Li_2SnO_3$ would be $Li_{2+x}Sn_{1-x}Al_xO_3$ (x= 0.0 – 1.0). Furthermore, the second most favorable doping process would be substituting the $Sn^{4+}$ site with $Sc^{3+,}$ where the solution energy would increase to 1.02 eV. Notably, the solution energy for alternative substitutional atoms will further increase in dependence with the dopant ionic radius.

**Table 7.6**. Enthalpy of solution of $R_2O_3$ (*R* = Al, Sc, In, Y, Gd and La) with respect to the $R^{3+}$ ionic radius in $Li_2SnO_3$.

| Dopant | Solution Enthalpy (eV) | Ionic Radii (A) |
|---|---|---|
| Al | 0.61 | 0.535 |
| Sc | 1.02 | 0.745 |
| In | 1.79 | 0.8 |
| Y | 2.00 | 0.9 |
| Gd | 2.27 | 0.938 |
| La | 2.81 | 1.032 |

**Figure 7.4** represents the local coordination (including bond lengths and angles) of oxygen atoms and dopants occupying the $Sn^{4+}$ site (Refer to Figure 1(a) for the octahedral $SnO_6$ unit in the relaxed structure of undoped $Li_2SnO_3$). The ionic radius of $Sn^{4+}$ in octahedral coordination is 0.69 Å while he ionic radius of $Al^{3+}$ corresponds to a smaller value of 0.16 Å. This will affect the coordination of the $AlO_6$ unit, as all of the six Al-O bonds will be shorter when compared to the Sn-O bonds presented in the undoped $Li_2SnO_3$ and the rest of the R-O bonding as well. It is mainly due to the smaller cation ionic radius of $Al^{3+}$ which will strongly polarise with the oxygen ions leading to a strong interatomic ionic bonding. The second lowest solution energy is for $Sc^{3+}$ whose ionic radius is 0.05 Å and 0.20 Å larger than those of $Sn^{4+}$ and $Al^{3+}$ respectively. Thus, the

bigger size of the $Sc^{3+}$ atom as compared to $Al^{3+}$ leads to a higher solution energy in doped $Li_2SnO_3$. For $In^{3+}$ to $La^{3+}$, the dopant-oxygen bond distance will increase while the bond angles will gradually decrease, indicating the generalised structural distortion that reflects on the solution energies. Notably, for the relaxed structure of $LaO_6$ unit, the La–O bond lengths are approximately equal, but ~0.30 Å longer than the Sn–O bonding in the $SnO_6$ unit. Furthermore, the ionic radius of $La^{3+}$ is 0.35 Å bigger than $Sn^{4+}$ leading to the highest solution energy of all cases. Thus, the solution energy values that correspond to the bigger substitutional atoms point out that they will drastically affect the structural configurations indicating that their introduction in $Li_2SnO_3$ and their accommodation to $Sn^{3+}$ sites will be unfavorable.

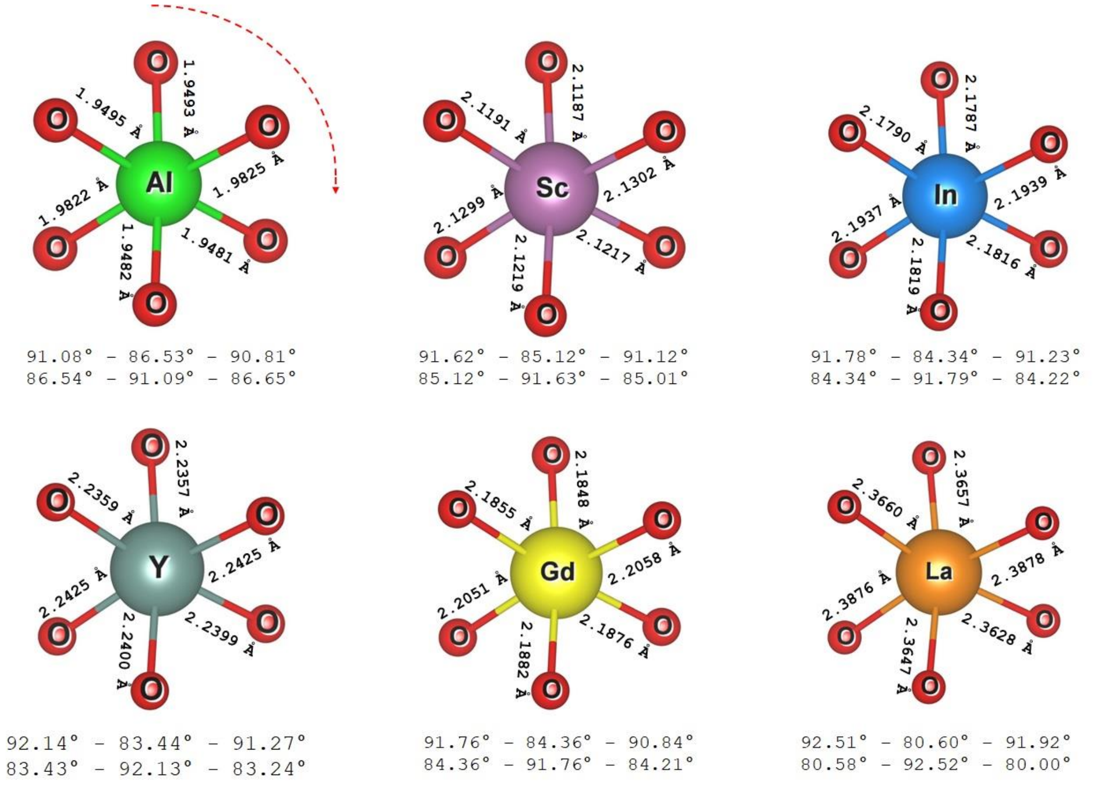

**Figure 7.4** Octahedral $SnO_6$ unit in the relaxed structure of doped $Li_2SnO_3$ and the coordination formed by the dopants on the $Sn^{4+}$ site with neighbor oxygen atoms.

A similar approach is also applied in $Li_2RuO_3$ to increase the amount of lithium by doping trivalent cations on $Ru^{4+}$ sites. This will lead to the formation of $Li^+$ interstitials as expected. Arunkumar's *et al.* [28] recent experimental study on $Co^{3+}$ doped $Li_2RuO_3$ reveals that the resultant $Li_{2.1}Ru_{0.9}Co_{0.1}O_3$ exhibits a significant reversible $Li^+$ extraction as compared to an undoped structure. Based on this mechanism, the solution of $R_2O_3$ ($R$ = Al, Co, Sc, In, Y, Gd and La) is considered via the following process (in Kröger-Vink notation):

$$\mathrm{R_2O_3} + 2\mathrm{Ru}_{\mathrm{Ru}}^{\mathrm{X}} + \mathrm{Li_2O} \rightarrow 2\,\mathrm{R}'_{\mathrm{Ru}} + 2\,\mathrm{Li}_{\mathrm{i}}^{\bullet} + 2\,\mathrm{RuO_2} \qquad (7.14)$$

**Table 7.7** presents the solution energies of $R_2O_3$ versus the substitutional ionic radius, where it is shown that doping with $Al^{3+}$ will be the most favorable process as it corresponds to the lowest solution energy amongst them all. Additionally, the solution energy for $Co_2O_3$ is slightly higher by only 0.05 eV suggesting that $Co^{3+}$ is also a promising candidate dopant to increase the $Li^+$ concentration in $Li_2RuO_3$. This investigation is in agreement with the experimental results reported for $Co^{3+}$ doping and suggests that substituting $Ru^{4+}$ with $Al^{3+}$ will be also a considerable process for introducing additional lithium into the host structure, although the exact amount of $Al^{3+}$ incorporation needs to be further explored. The calculated solution energies are positive for both $Al_2O_3$ and $Co_2O_3$ suggesting that these doping processes can be carried out only at high temperatures. The hypothesis is also supported by the higher temperature conditions (~1100°C for 12 hours) applied for the synthesis of Co-doped $Li_2RuO_3$.

**Table 7.7** Enthalpy of the solution of $R_2O_3$ (*R* = Al, Co, Sc, In, Y, Gd and La) with respect to the $R^{3+}$ ionic radius in $Li_2RuO_3$.

| **Dopant** | **Solution Enthalpy (eV)** | **Ionic Radii (A)** |
|---|---|---|
| Al | 2.8 | 0.535 |
| Co | 2.85 | 0.55 |
| Sc | 3.68 | 0.745 |
| In | 4.20 | 0.8 |
| Y | 5.24 | 0.9 |
| Gd | 5.80 | 0.938 |
| La | 6.90 | 1.032 |

The local coordination and bonding of R-O in $Li_2RuO_3$ are represented in **Figure 7.5**. Here, the ionic radius of $Ru^{4+}$ in octahedral coordination is 0.62 Å. whereas the ionic radius of $Al^{3+}$ is 0.08 Å smaller (0.54 Å). In the $AlO_6$ unit formation, all six Al-O bonds are slightly shorter as compared to the Ru-O bonds in the undoped atomic configuration. This is due to the smaller cation size of $Al^{3+}$ which strongly polarises with the oxygen ions forming strong ionic bonds. In addition, the ionic radius of $Co^{3+}$ (0.55 Å) is very close to that of $Al^{3+}$ as reflected in the similar bond lengths and angles. From $Sc^{3+}$ to $La^{3+}$, the dopant-oxygen interatomic distance gradually increases and the bond angles decrease leading to a structural distortion as well as higher solution energies. In the relaxed structure of the $LaO_6$ unit, the La–O bond lengths correspond to approximately similar values but are ~0.30 Å longer than the Ru–O bond lengths presented in $RuO_6$ unit. Furthermore, the ionic radius of $La^{3+}$ is 0.28 Å larger than $Ru^{4+}$ leading to extremely high solution energy.

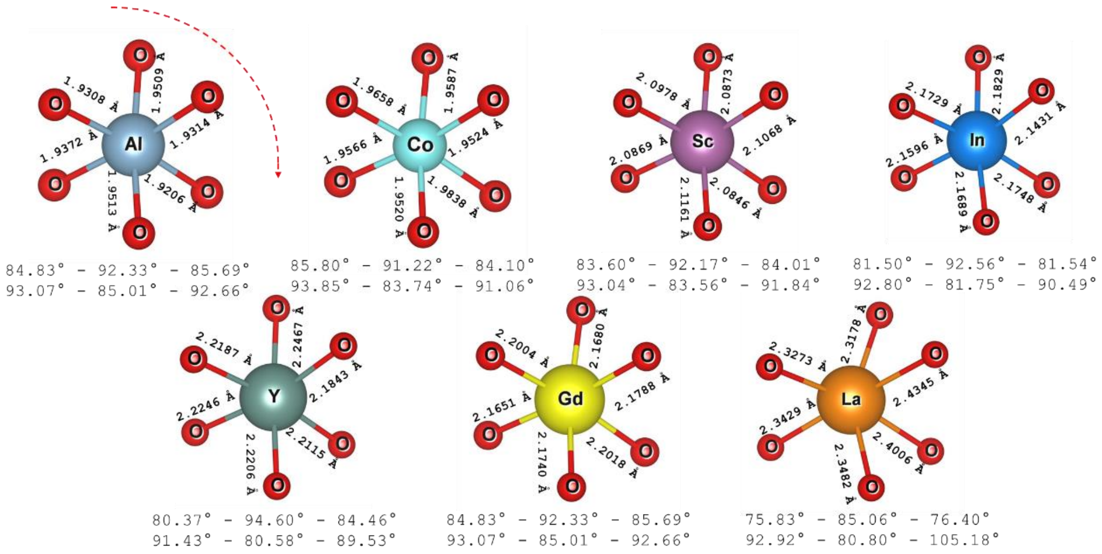

**Figure 7.5** Octahedral $RuO_6$ units of the relaxed structure in undoped $Li_2RuO_3$ and the coordination formed by dopants on the Ru site with neighbor oxygen atoms.

## 7.5. Density of States

### 7.5.1 $Li_2SnO_3$

For the considered trivalent dopants density of states (DOS) calculations have been performed plotting the individual contribution of each element (partial-DOS). In **Figure 7.6**, the PDOS for the cases of (a) perfect cell (b) $Li_i^{\bullet}$ (c) $Al'_{Sn}$ and (d) $\{Al'_{Sn}: Li_i^{\bullet}\}^X$ are reported with the valence band maximum (VBM) being set at zero energy level. The electronic structure is characterised by the dominant $O^{2-}$ p - states in the valence band near the Fermi level, where a band gap of approximately 3.1 eV is formed. The $Li^+$ p - states and $Sn^{4+}$ d-states are also contributing to the valence bands but with lower intensities compared to $O^{2-}$. On the edge of the conduction band, the main contributions in the total DOS are attributed to the $Li^+$ states and specifically to the $Li^+$ - s orbitals. The $O^{2-}$ p - states in the conduction band correspond to a similar profile as the $Li^+$ p – states, whereas the $Sn^{4+}$ orbitals are presented not to have a primary role in the total electronic structure of the material as shown in **Figure 7.7**

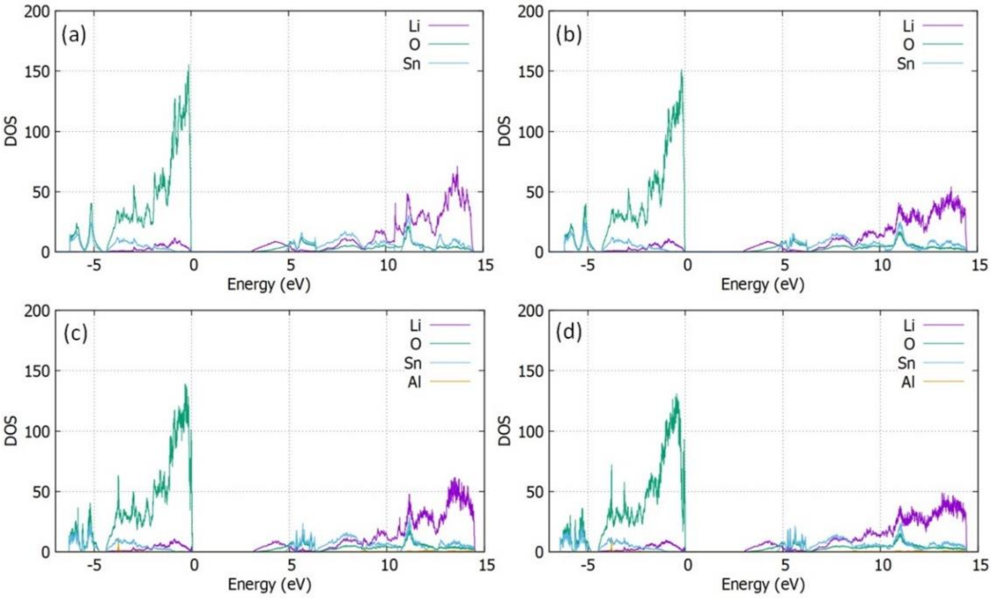

**Figure 7.6** The PDOS calculated using DFT for the (a) $Li_2SnO_3$ perfect cell (b) $Li_2SnO_3$ with $Li^+$ interstitial (c) Al – Doped $Li_2SnO_3$ and (d) Al - Doped $Li_2SnO_3$ with $Li^+$ interstitial.

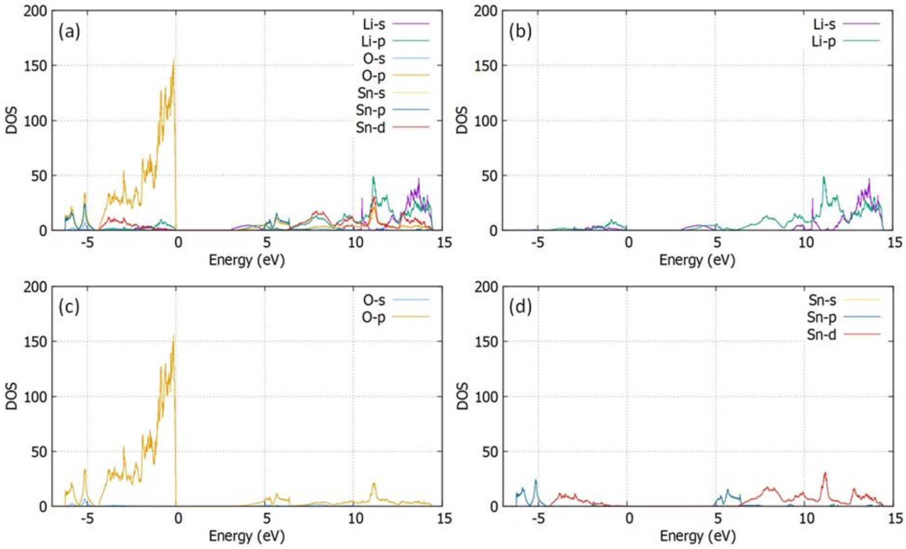

**Figure 7.7** (a) The complete contribution of the atomic orbitals in the Densities of States for the undoped $Li_2SnO_3$ (b) The contribution of $Li^+$ orbitals (c) The contribution of $O^{2-}$ orbitals and (d) The contribution of $Sn^{4+}$ orbitals.

In addition, the effect on the total DOS of the introduction of a lithium interstitial in the supercell is minimal. Specifically, no additional states are formed into the band gap, whereas the contribution of every element is not affected as shown in Figure 7.6 (b). The doping effect of trivalent dopants has been also considered and the impact of the $Al_{Sn}'$ and $\{Al_{Sn}'{:}\,Li_i^{\bullet}\}^X$ pairs on the densities of states on $Li_2SnO_3$ is presented in Figure 7.6 (c)-(d). Overall, the introduction of $Al^{3+}$ does not significantly impact the electronic structure as the Al – states contribution in the DOS is very weak. Furthermore, the cases of $Sc_{Sn}'$ and $\{Sc_{Sn}'{:}\,Li_i^{\bullet}\}^X$, $In_{Sn}'$ and $\{In_{Sn}'{:}\,Li_i^{\bullet}\}^X$, $Y_{Sn}'$ and $\{Y_{Sn}'{:}\,Li_i^{\bullet}\}^X$, $Gd_{Sn}'$ and $\{Gd_{Sn}'{:}\,Li_i^{\bullet}\}^X$ as well as $La_{Sn}'$ and $\{La_{Sn}'{:}\,Li_i^{\bullet}\}^X$ pairs have also been examined. Despite the dopants having stronger contributions compared with $Al^{3+}$, the electronic structure presents no considerable variations. However, for the $Gd_{Sn}'$ and $\{Gd_{Sn}'{:}\,Li_i^{\bullet}\}^X$ as well as the $La_{Sn}'$ and the $\{La_{Sn}'{:}\,Li_i^{\bullet}\}^X$ pairs that correspond to the dopants of a large ionic radius, the DOS includes in-gap states and a minor additional contribution next to the valence band. All DOS for the considered doping processes are shown in **Figure 7.8**.

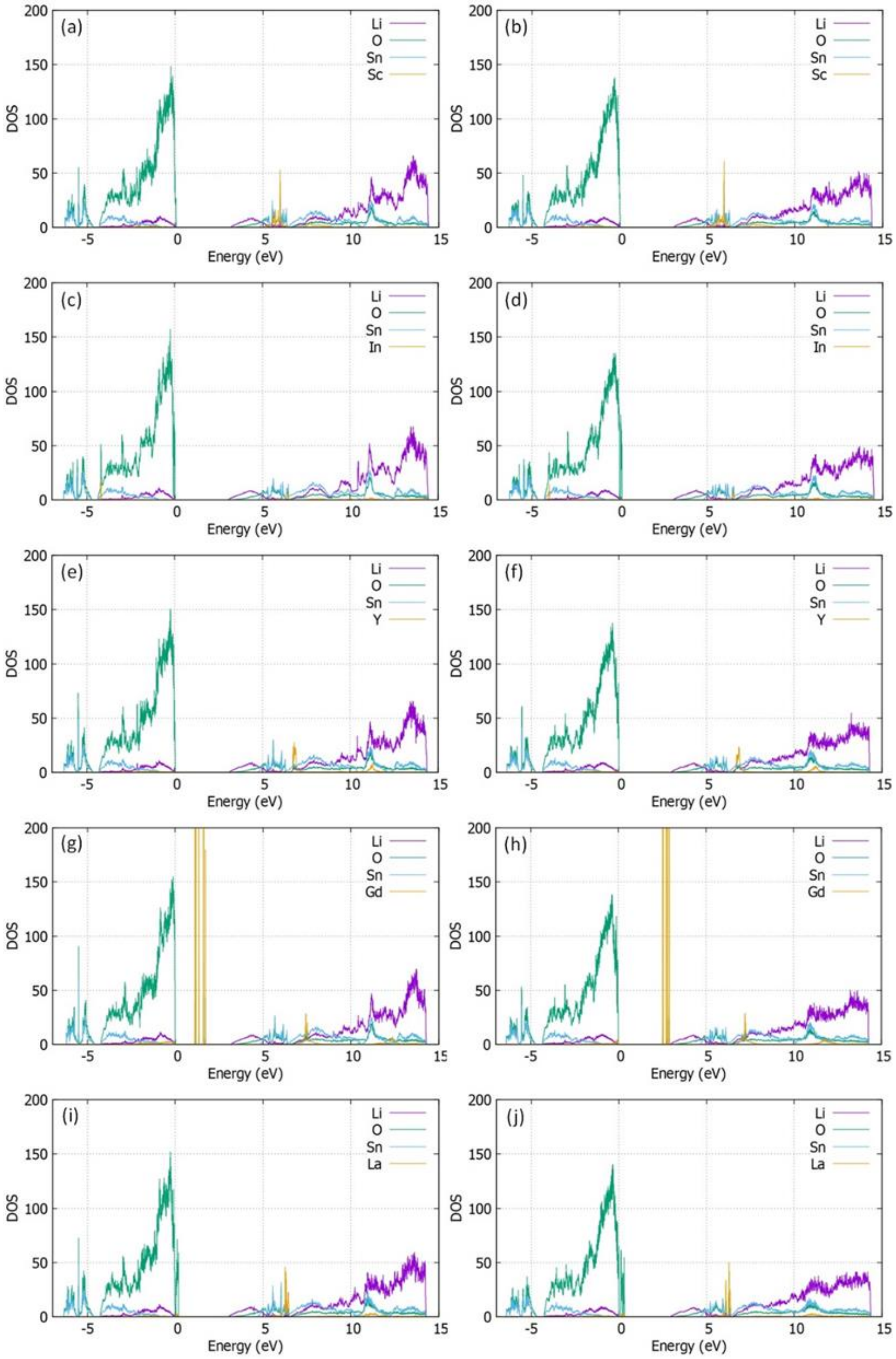

**Figure 7.8** The $Li_2SnO_3$ Densities of States for (a) Sc – doped supercell (b) Sc – doped supercell with one Li interstitial (c) In – doped supercell (d) In – doped supercell with one Li interstitial (e) Y – doped supercell (f) Y – doped supercell with one Li interstitial (g) Gd – doped supercell (h) Gd – doped supercell with one Li interstitial (i) La – doped supercell (j) La – doped supercell with one Li interstitial.

### 7.5.2 $Li_2RuO_3$

The electronic structure for the trivalent doping processes in $Li_2RuO_3$ has been also investigated using DFT. In particular, the contribution of every element in the Li2RuO3 crystal is visualised through the partial Density of States (PDOS). **Figure 7.9** presents the cases for (a) The non – defective structure (b) The $Li^+$ interstitial (c) The Al – doped supercell and (d) The Al – doped supercell with one $Li^+$ interstitial.

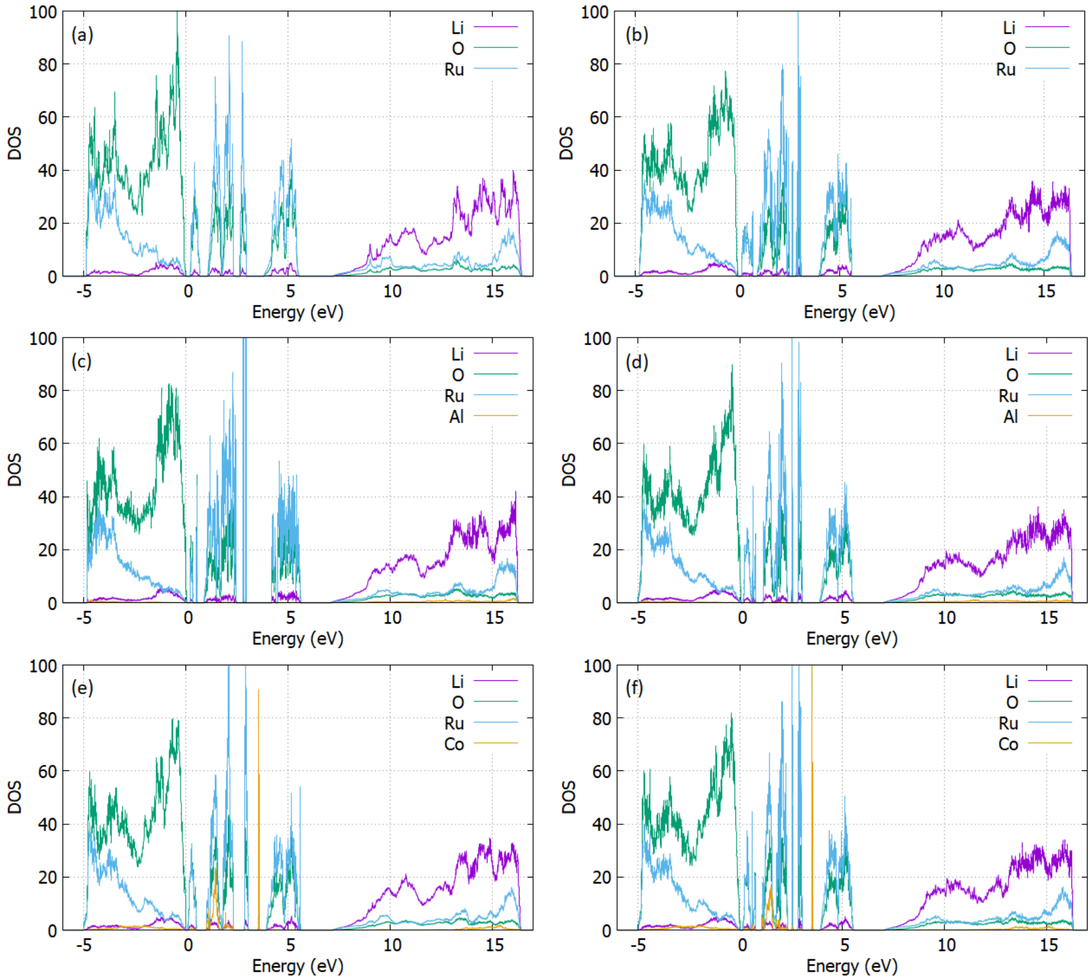

**Figure 7.9** $Li_2RuO_3$ PDOS for (a) The non – defective cell (d) The Li interstitial (c) The Al – doped cell (d) The Al – doped cell with one Li interstitial (e) The Co – doped cell (f) The Co – doped cell with one Li interstitial.

Overall, the material presents the formation of the valence band governed by the strong $O^{2-}$ p-states at the Fermi level which is set to 0.0 eV. Additionally, the conduction band is mainly characterised by the major contribution of $Li^{+}$ p-states leading to a band gap of approximately 7.2 eV. The exact contribution of orbitals for each element has been plotted separately in **Figure 7.10**.

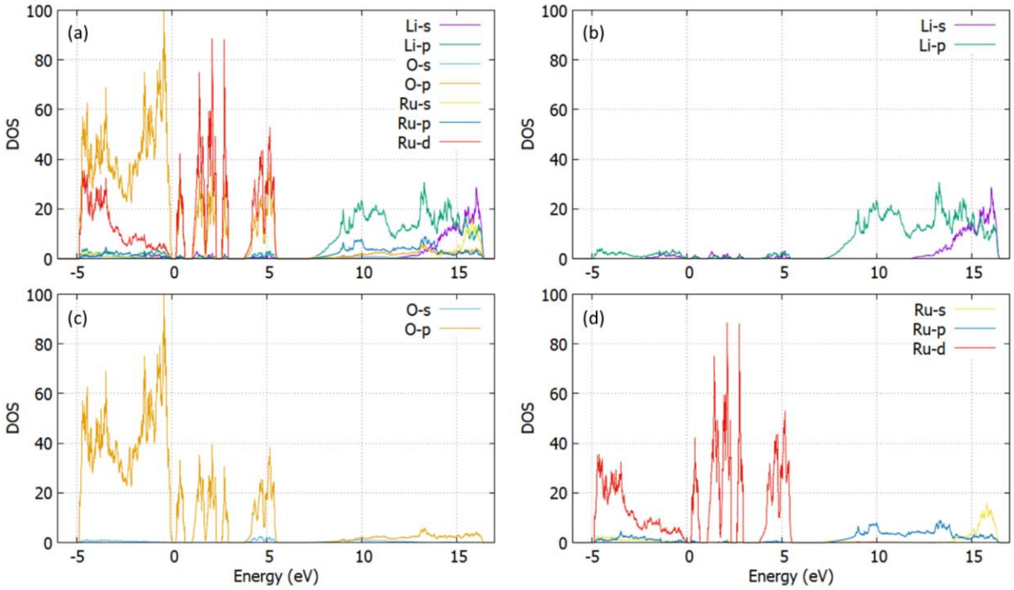

**Figure 7.10** $Li_2RuO_3$ PDOS for (a) The total contribution of orbitals in the non – defective cell (b) The contribution of $Li^{+}$ orbitals (c) The contribution of $O^{2-}$ orbitals (d) The contribution of $Ru^{4+}$ orbitals.

The presence of in gap states is mainly attributed to the $Ru^{4+}$ d-states and $O^{2-}$ p-states as well. This should be addressed and experimentally investigated as the properties of electronic conduction have to be controlled in terms of future energy applications. The last in-gap contribution is located at 1.66 from the valence band, however this non-uniformity points to an interesting behaviour that originates from electronic configuration parameters and must be considered for the oxidation and reduction reactions. The presence of a $Li^{+}$ interstitial does not affect the total DOS in a considerable way. Doping

$Li_2RuO_3$ with trivalent dopants that substitute the $Ru^{4+}$ site introduces additional contributions in the electronic structure. Regarding the lowest solution enthalpies, these correspond to the $Al^{3+}$ and $Co^{3+}$ doping processes. The dopant is initially introduced as substitutional in a $Ru^{4+}$ site presenting minor distortions in the crystal even combined with a $Li^{+}$ ion in an interstitial site. $Al^{3+}$ doping presents a low contribution at the conduction band with no additional states. However, additional contribution is observed for Co – doping, governed by the $Co^{3+}$ d – states and $O^{2-}$ p-states, whereas a weaker contribution due to the $Ru^{4+}$ d-states is also observed. The orbitals profile is illustrated in **Figure 7.11**. Furthermore, doping with elements of bigger radius introduce intense states in the electronic structure except for $In^{3+}$ as shown in **Figure 7.12**.

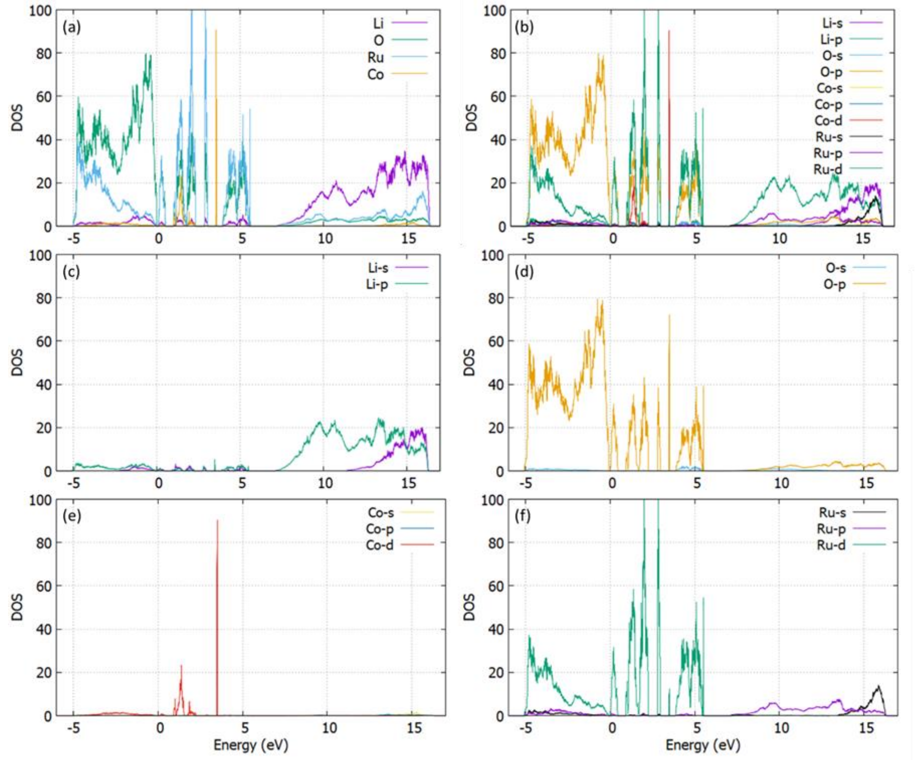

**Figure 7.11** The Co – doped $Li_2RuO_3$ PDOS for (a) The contribution of elements in the doped cell (b) The total contribution of orbitals (c) The contribution of $Li^{+}$ orbitals (d) The contribution of $O^{2-}$ orbitals (e) The contribution of $Co^{3+}$ orbitals (f) The contribution of $Ru^{4+}$ orbitals.

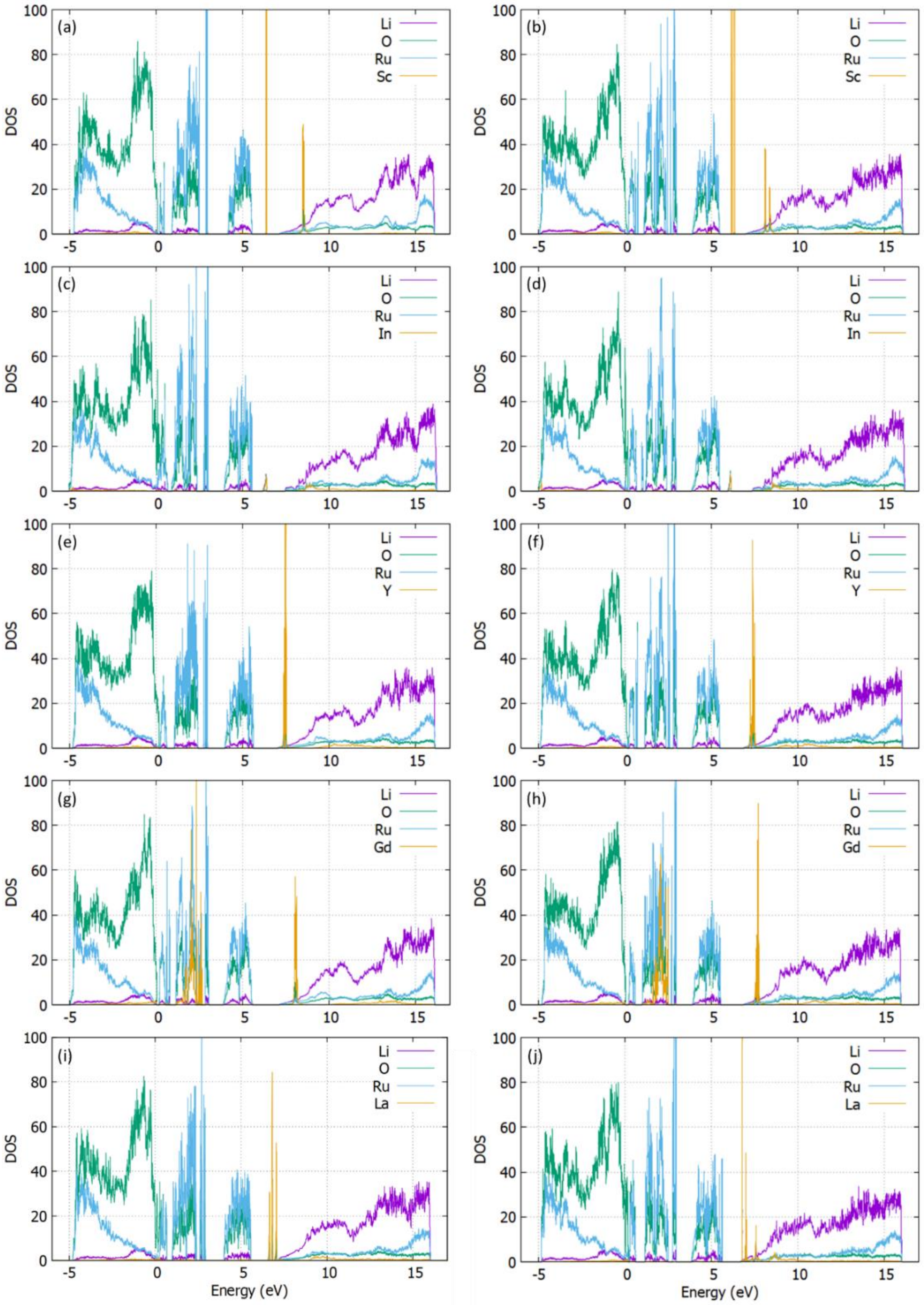

**Figure 7.12** The $Li_2RuO_3$ PDOS for (a) The Sc - doped supercell (d) The Sc - doped supercell with a Li interstitial (c) The In - doped supercell (d) The In - doped supercell with a Li interstitial (e) The Y - doped supercell (f) The Y - doped supercell with a Li interstitial (g) The Gd - doped supercell (h) The Gd - doped supercell with a Li interstitial (i) The La - doped supercell (j) The La - doped supercell with a Li interstitial.

## 7.6 Conclusions

In the present chapter, layered $Li_2SnO_3$ and $Li_2RuO_3$ have been investigated to provide detailed insights into intrinsic defects, lithium ion mobility and trivalent doping, which are relevant to their electrochemical behavior as lithium battery materials. The $Li^+$ Frenkel is the dominant defect process as it corresponds to the lowest energy for both $Li_2SnO_3$ and $Li_2RuO_3$. Antisite $Li^+/Sn^{4+}$ and $Li^+/Ru^{4+}$ disorder is slightly higher than $Li^+$ Frenkel in agreement with previous experimental work. Furthermore, $Li^+$ self-diffusion long range pathways correspond to an activation energy of migration of 0.61 eV and 0.73 eV for $Li_2SnO_3$ and $Li_2RuO_3$ respectively. The introduction of dopants is considered via the solution energy of $R_2O_3$ to increase lithium concentration in these systems. $Al_2O_3$ corresponds to the lowest solution energy for both materials whereas an increasing behaviour is reported for dopants of a larger ionic radius. Electronic structure calculations present an anisotropic behavior for both materials whereas the doping processes will introduce additional states in the DOS. This investigation should stimulate further theoretical and experimental work in order to expand the insights into the atomic scale phenomena and provide understanding of the intrinsic mechanisms of $Li_2SnO_3$ and $Li_2RuO_3$ as lithium ion battery materials.

# REFERENCES

---

[1] Q. Wang, Y. Huang, Y. Zhao, W. Zhang, and Y. Wang, Preparation of $Li_2SnO_3$ and its application in lithium-ion batteries. *Surface and Interface Analysis*, **45**, 1297, (2013).

[2] X. Dong, Y. Xu, S. Yan, S. Mao, L. Xiong and X. Sun, Towards low-cost, high energy density $Li_2MnO_3$ cathode materials. *Journal of Materials Chemistry A*, **3**, 670, (2015).

[3] M. M. Thackeray, S.-H. Kang, C. S. Johnson, J. T. Vaughey, R. Benedek and S. A. Hackney $Li_2MnO_3$-stabilized $LiMO_2$ (M = Mn, Ni, Co) electrodes for lithium-ion batteries. *Journal of Materials Chemistry*, **17**, 3112, (2007).

[4] J. R. Croy, D. Kim, M. Balasubramanian, K. Gallagher, S.-H. Kanga, and M. M. Thackeray, Countering the Voltage Decay in High Capacity $xLi_2MnO_3•(1–x)LiMO_2$ Electrodes (M=Mn, Ni, Co) for $Li^+$-Ion Batteries. *Journal of The Electrochemical Society*, **159**, A781, (2012).

[5] J. R. Croy, S. H. Kang, M. Balasubramanian, and M. M. Thackeray, $Li_2MnO_3$-based composite cathodes for lithium batteries: A novel synthesis approach and new structures. *Electrochemistry Communications*, **13**, 1063, (2011).

[6] Z. Wang, Y. Ren, T. Ma, W. Zhuang, S. Lu, G.-L. Xu, A. Abouimrane, K. Amine, Z. Chen, Probing cation intermixing in $Li_2SnO_3$. *RSC Advances*, **6**, 31559, (2016).

[7] M. Sathiya, G. Rousse, K. Ramesha, C. P. Laisa, H. Vezin, M. T. Sougrati, M-L. Doublet, D. Foix, D. Gonbeau, W. Walker, A. S. Prakash, M. Ben Hassine, L. Dupont and J-M. Tarascon Reversible anionic redox chemistry in high-capacity layered-oxide electrodes. *Nature Materials*, **12**, 827, (2013).

[8] G. J. Moore, C. S. Johnson and M. M. Thackeray, The electrochemical behaviour of $xLiNiO_2·(1−x) Li_2RuO_3$ and $Li_2Ru_{1−y}Zr_yO_3$ electrodes in lithium cells. *Journal of Power Sources*, **119-121**, 216, (2003).

[9] Y. Yao and P. Yang, X. Bie, C. Wang and Yingjin Wei and Gang Chen and Fei Du, High capacity and rate capability of a layered $Li_2RuO_3$ cathode utilized in hybrid $Na^+/Li^+$ batteries. *Journal of Materials Chemistry A*, **3**, 18273, (2015).

[10] M.-S.Park, Y.-G. Lim, J.-W. Park, J.-S. Kim, J.-W. Lee, J. H. Kim, S. X. Dou, Kim Young-Jun,. $Li_2RuO_3$ as an Additive for High-Energy Lithium-Ion Capacitors. *The Journal of Physical Chemistry C*, **117**, 11471, (2013).

[11] M. C. Payne, M. P. Teter, D. C. Allan, T. A. Arias and J. D. Joannopoulos, Iterative minimization techniques for ab initio total-energy calculations: molecular dynamics and conjugate gradients. *Reviews of Modern Physics*, **64**, 1045, (1992).

[12] M. D. Segall, P. J. D. Lindan, M. J. Probert, C. J. Pickard, P. J. Hasnip, S. J. Clark and M. C. Payne. First-principles simulation: ideas, illustrations and the CASTEP code. *Journal of Physics: Condensed Matter*, **14**, 2717 (2002).

---

[13] H. J. Monkhorst and J. D. Pack, Special points for Brillouin-zone integrations. *Physical Review B*, **13**, 5188, (1976).

[14] J. P. Perdew, K. Burke and M. Ernzerhof, Generalized Gradient Approximation Made Simple. *Physical Review Letters*, **77**, 3865, (1996).

[15] D. Vanderbilt, Soft self-consistent pseudopotentials in a generalized eigenvalue formalism. *Physical Review B,* **41**, 7892 (1990).

[16] R. J. Nicholls, A. J. Morris, C. J. Pickard and J. R. Yates, OptaDOS - a new tool for EELS calculations. *Journal of Physics: Conference* Series, **371**, 012062, (2012).

[17] A. J. Morris, R. Nicholls, C. J. Pickard and J. R. Yates, OptaDOS: A tool for obtaining density of states, core-level and optical spectra from electronic structure codes. *Computer Physics Communications*, **185**, 1477, (2014).

[18] G. Lang, Strukturvergleiche an ternaeren und quaternaeren Oxiden. *Zeitschrift für anorganische und allgemeine Chemie*, **348**, 246, (1950).

[19] H. Kobayashi, R. Kanno, Y. Kawamoto, M. Tabuchi, O. Nakamura, and M. Takano, Structure and lithium deintercalation of $Li_{2-x}RuO_3$. *Solid State Ionics*, **82**, 25, (1995).

[20] H. Kobayashi, R. Kanno, Y. Kawamoto and M. Tabuchi, O. Nakamura, Physical properties of the de-lithiated Li2 − xRuO3 with the layered structure, *Solid State Ionics*, **86**, 2, (1996).

[21] A.C.W.P. James and J.B. Goodenough, Structure and bonding in lithium ruthenate, $Li_2RuO_3$. *Journal of Solid State Chemistry*, **74**, 2, (1988).

[22] M. D. Johannes, A. M. Stux, and K. E. Swider-Lyons, Electronic structure and properties of Li-insertion materials: $Li_2RuO_3$ and $RuO_2$. *Physical Review B,* **77**, 075124 (2008).

[23] A. R. Armstrong, N. Kuganathan, M. S. Islam and P. G. Bruce, Structure and lithium transport pathways in $Li_2FeSiO_4$ Cathodes for Lithium Batteries. *Journal of the American Chemical* Society, **133**, 13031, (2011).

[24] H. Liu, M.-J. Choe, R. A. Enrique, B. Orvañanos, L. Zhou, T. Liu, K. Thornton and C P. Grey, Effects of Antisite Defects on Li Diffusion in $LiFePO_4$. *The Journal of Physical Chemistry C*, **121**, 12025, (2017).

[25] N. Kuganathan, A. Kordatos, and A. Chroneos, Defect Chemistry and Li-ion Diffusion in $Li_2RuO_3$. *Scientific Reports*, **9**, 550, (2019).

[26] J. Howard and N. A. W. Holzwarth, First-principles simulations of the porous layered calcogenides $Li_{2+x}SnO_3$ and $Li_{2+x}SnS_3$. *Physical Review B*, **94**, 064108, (2016).

---

[27] N. Kuganathan and M. S. Islam, $Li_2MnSiO_4$ Lithium Battery Material: Atomic-Scale Study of Defects, Lithium Mobility, and Trivalent Dopants. *Chemistry of Materials*, **21**, 5196, (2009).

[28] P. Arunkumar, W. J. Jeong, S. Won and W. B. Im, Improved electrochemical reversibility of over-lithiated layered $Li_2RuO_3$ cathodes: Understanding aliovalent $Co^{3+}$ substitution with excess lithium. *Journal of Power Sources*, **324**, 428, (2016).

# Chapter 8

# Defect Processes in $Li_3MO_4$ (M=Sb, Nb)

Part of the results presented here has been published in *Materials Chemistry and Physics*, **225**, 34, (2019) and *Scientific Reports*, **9**, 2192, (2019).

## 8.1. Introduction

"Li-rich" materials have been considered as anodes in $Li^+$ - ion batteries due to the potential high $Li^+$ ion concentration, low cost, lesser hazards and their constituent elements being highly abundant. Intrinsic defect processes are key factors to understand the electrochemical behaviour of an electrode material. $Li_3SbO_4$ has been suggested as an alternative anode material with high power density due to its excellent rate performance, cyclability and excellent Coulombic efficiency, although it has a low initial capacity[1]. Electrochemical studies were carried out by Kundu *et al.*[2] to improve its capacity by synthesising nanocrystalline composites ($Li_4Ti_5O_{12}$/$Li_3SbO_4$/C). However, limited experimental or theoretical studies are available in the literature. Additionally, $Li_3NbO_4$ has been examined as the host structure of a new class of high-capacity positive cathode materials for rechargeable $Li^+$ - ion batteries [3, 4, 5]. In the present study, the density of states in pristine and doped $Li_3SbO_4$ and $Li_3NbO_4$ is investigated. It is important to access whether these materials can be applicable as electrodes or electrolytes in solid state $Li^+$ – ion batteries.

## 8.2 Defect Chemistry

### 8.2.1 Methodology

The plane wave DFT code CASTEP[6, 7] is employed with the plane wave basis set to a cut-off of 450 eV. All of the $Li_3MO_4$ (M = Sb Nb) supercells were simulated using a 2x2x2 Monkhorst-Pack (MP)[8] k-point grid within a 128-atomic site supercell. Regarding the exchange and correlation interactions in the crystallographic structure of the material, the formulation with the corrected density functional of Perdew, Burke and Ernzerhof (PBE)[9] is applied in the generalised gradient approximation (GGA) with the use of ultrasoft pseudopotentials[10]. All supercells were optimized in the minimum energy according to the convergence criteria under constant pressure conditions. The obtained atomic configurations for the doped / undoped and defective supercells were used for the electronic structure calculations. The OPTADOS[11, 12] subcode is employed for the Density of States (DOS) investigation as well as the visualisation of outputs.

### 8.2.2 Crystallography

The crystal structure of $Li_3SbO_4$ (analogous with $Na_3BiO_4$) corresponds to a monoclinic crystallographic structure with space group P2/c (lattice parameters a = 5.1578 Å, b = 6.0923 Å, c = 5.1397 Å, α = 90°, β = 108.841° and γ=90°) as reported by Skakle *et al.*[13] **Figure 8.1 (a)** presents the structure and the chemical environments of $Sb^{5+}$ and $Li^+$ [both forming distorted $MO_6$ octahedra (M= Li or Sb)]. The starting point for the present study was to reproduce the experimentally observed monoclinic crystal structure and allow the ions to exhibit the lowest energy atomic configuration. Furthermore, $Li_3NbO_4$ is cubic with space group $I\bar{4}3m$ (lattice parameters a = b = c = 8.4150 Å, α = β = γ = 90°) as reported by Ukei *et al*.[14] **Figure 8.1 (b)** shows this structure and the chemical environments of cations with $Nb^{5+}$ forming edge-shared $NbO_6$ octahedra in the lattice. There is a good agreement between the calculated equilibrium lattice constants (tabulated in **Table 8.1**) and the lattice constants as observed in the experiment.

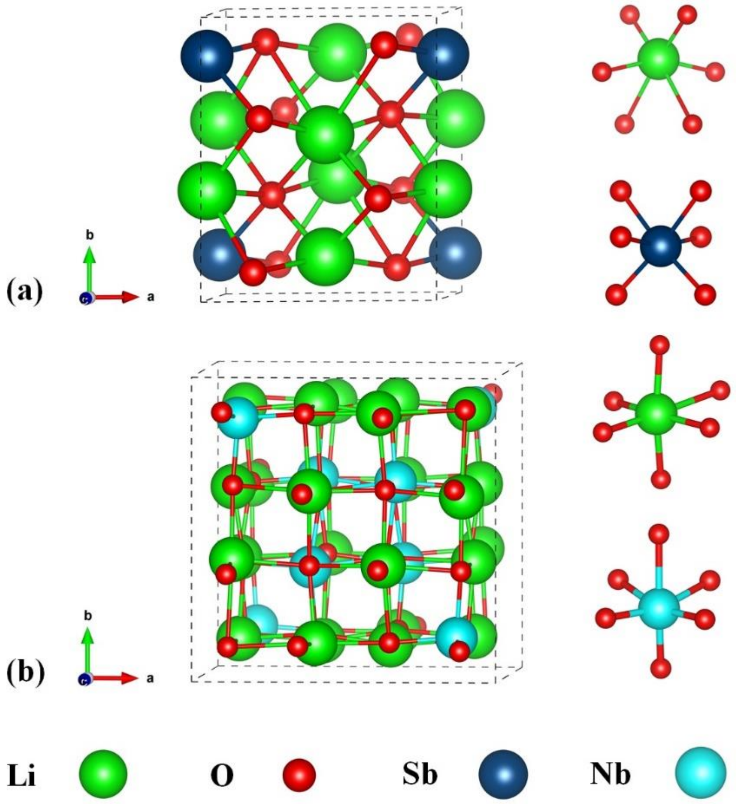

**Figure 8.1** The crystallographic structure for the **(a)** Monoclinic (P2/c) $Li_3SbO_4$ **(b)** Cubic ($I\bar{4}3m$) $Li_3NbO_4$.

Overall the calculated lattice parameters are in agreement with experimental studies, however a considerable deviation is observed for the $Li_3SbO_4$ structure also evident previously reported data[2, 15] although being very close to Sarke *et al*. Since there are no previous theoretical studies on this material to my knowledge, this should be further investigated. Notably, this should be connected with the electrostatic interactions and the Janh – Teller effect among other structural factors.

**Table 8.1.** Calculated and Experimental Structural Parameters for monoclinic (P2/c) $Li_3SbO_4$ and $Li_3NbO_4$.

| **$Li_3SbO_4$** Parameter | Calc | Expt[13] | \|Δ\|(%) |
|---|---|---|---|
| a (Å) | 5.1406 | 5.1578 | 0.33 |
| b (Å) | 6.0794 | 6.0923 | 0.21 |
| c (Å) | 5.1291 | 5.1397 | 0.20 |
| **$Li_3NbO_4$** Parameter | Calc | Expt[14] | \|Δ\|(%) |
| a (Å) | 8.4120 | 8.4150 | 0.03 |
| b (Å) | 8.4120 | 8.4150 | 0.03 |
| c (Å) | 8.4120 | 8.4150 | 0.03 |

### 8.2.3 Intrinsic defects

In recent atomistic simulation work, Kuganathan *et al.* [16, 17], calculated that the $Li^+$ Frenkel intrinsic disorder is prevalent in both materials corresponding to 1.18 eV for $Li_2SbO_4$ and 1.27 eV for $Li_3NbO_4$. For the latter material the Li / Nb antisite disorder has very low energy (0.39 eV) but only when the two antisites form a cluster, whereas the unassociated energy is very high (4.53 eV). Therefore, it is anticipated that this antisite reaction may play a role but at higher temperature or under non-equilibrium conditions. For completeness the $Li^+$ migration pathways are given in **Figure 8.2** and **Figure 8.3** respectively. The activation energies of the migrations are 0.19 eV (Pathway B) for $Li_3SbO_4$ and 0.48 eV (Pathway B) for $Li_3NbO_4$ respectively.

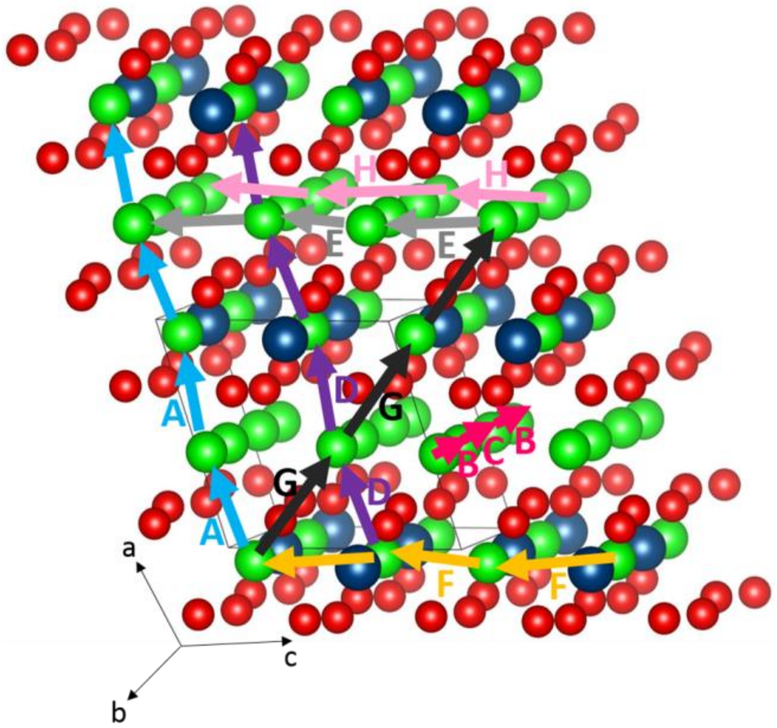

**Figure 8.2** Possible long-range lithium vacancy migration paths considered. Green, blue and red colours correspond to Li, Sb, and O atoms respectively.

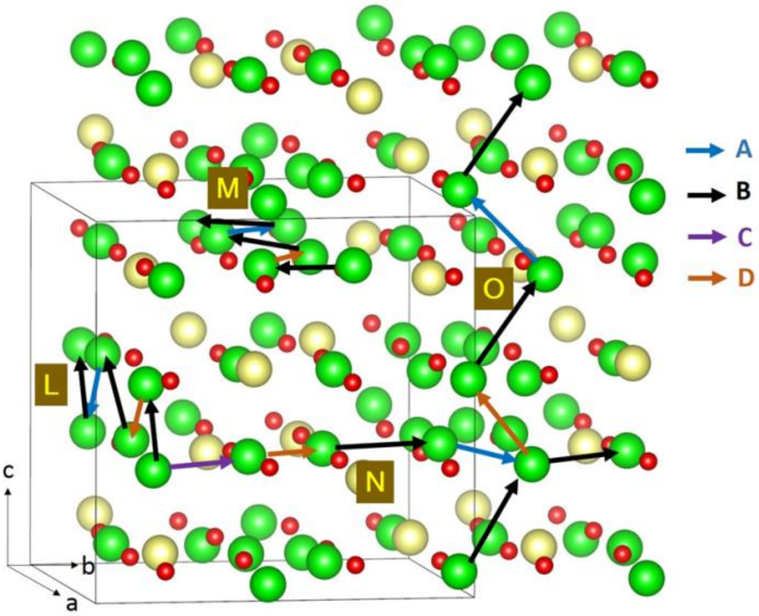

**Figure 8.3** Possible long-range lithium vacancy migration paths considered. Green, yellow and red colours correspond to Li, Nb, and O atoms respectively. Long range paths are labelled as L, M, N and O.

Very low migration energies are reported and constitute these materials as potential candidates for battery materials. Previous experimental work[1] has reported $Li_3SbO_4$ to be a potential electrode material (anode) where despite a low initial capacity, a good cycling performance is achieved. The electrostatic interactions have been investigated by Jacquet *et al.*[18], however limited theoretical work has been reported. This has motivated the electronic structure characterisation though Density of States (DOS) calculations and the doping processes investigation in the following sections.

## 8.3 Tetravalent Doping

Promising new cathode materials should exhibit high energy density (typically 250 to 620 $W\cdot h\ L^{-1}$)[19]. Introducing extra lithium into the as-prepared material will enhance the capacity and further increase the applicability of $Li_3MO_4$ (M=Sb, Nb) as materials for rechargeable lithium batteries. An engineering strategy to increase the concentration of lithium is by doping tetravalent cations into them, thus creating $Li^+$ interstitials. Here, the solution of $RO_2$ ($R$ = Si, Ge, Ti, Zr and Ce) via the following processes (in Kröger-Vink notation) is considered:

$$2\ RO_2 + 2Sb_{Sb}^{X} + Li_2O \rightarrow 2\ R'_{Sb} + 2\ Li_i^{\bullet} + Sb_2O_5 \tag{8.1}$$

$$2\ RO_2 + 2Nb_{Sb}^{X} + Li_2O \rightarrow 2\ R'_{Nb} + 2\ Li_i^{\bullet} + Nb_2O_5 \tag{8.2}$$

The solution energies of $RO_2$ are reported in **Table 8.6**. Overall, the most favorable dopant solution energy for $Li_3SbO_4$ is calculated for $SiO_2$ (0.15 eV). This suggests that a possible synthesis-doping strategy of introducing additional lithium into $Li_3SbO_4$ would be through accommodating $Si^{4+}$ on $Sb^{5+}$ sites, however the exact amount of $Si^{4+}$

incorporation cannot be predicted. The possible composition of Si-doped $Li_3SbO_4$ would be $Li_{3+x}Sb_{1-x}Si_xO_4$ (x= 0.0 – 1.0). The second most favourable dopant is $Ti^{4+}$ with the solution energy of 0.27 eV. The solution energy for $ZrO_2$ is only 0.09 eV higher than that of $TiO_2$ whereas the solution energy for $CeO_2$ is highly endothermic.

**Table 8.2**. Solution enthalpy of $RO_2$ (*R* = Si, Ge, Ti, Zr and Ce) in $Li_3SbO_4$ and $Li_3NbO_4$ using atomistic simulations[16 17].

| **Dopant** | **Solution Enthalpy (eV)** | **Ionic Radii (A)** |
|---|---|---|
| Si | 0.15 | 0.4 |
| Ge | 0.64 | 0.53 |
| Ti | 0.27 | 0.605 |
| Zr | 0.36 | 0.72 |
| Ce | 2.30 | 0.87 |
| **Dopant** | **Solution Enthalpy (eV)** | **Ionic Radii (A)** |
| Si | 1.29 | 0.4 |
| Ge | 0.98 | 0.53 |
| Ti | 2.20 | 0.605 |
| Zr | 2.03 | 0.72 |
| Ce | 4.69 | 0.87 |

The most favourable dopant solution energy (0.98 eV) is calculated for $GeO_2$. This suggests that a possible synthesis-doping strategy of introducing additional lithium into $Li_3NbO_4$ would be by doping $Ge^{4+}$ on the $Nb^{5+}$ site, although the exact amount of $Ge^{4+}$ incorporation cannot be predicted. The possible composition of Ge-doped $Li_3NbO_4$ would be $Li_{3+x}Nb_{1-x}Ge_xO_4$ (x= 0.0 – 1.0). The solution energy for $SiO_2$ is 1.29 eV suggests that Si is also a candidate dopant. Solution energies for $TiO_2$ and $ZrO_2$ are 2.20 eV and 2.03 eV respectively. Highly endothermic (4.69 eV) solution energy is calculated for $CeO_2$.

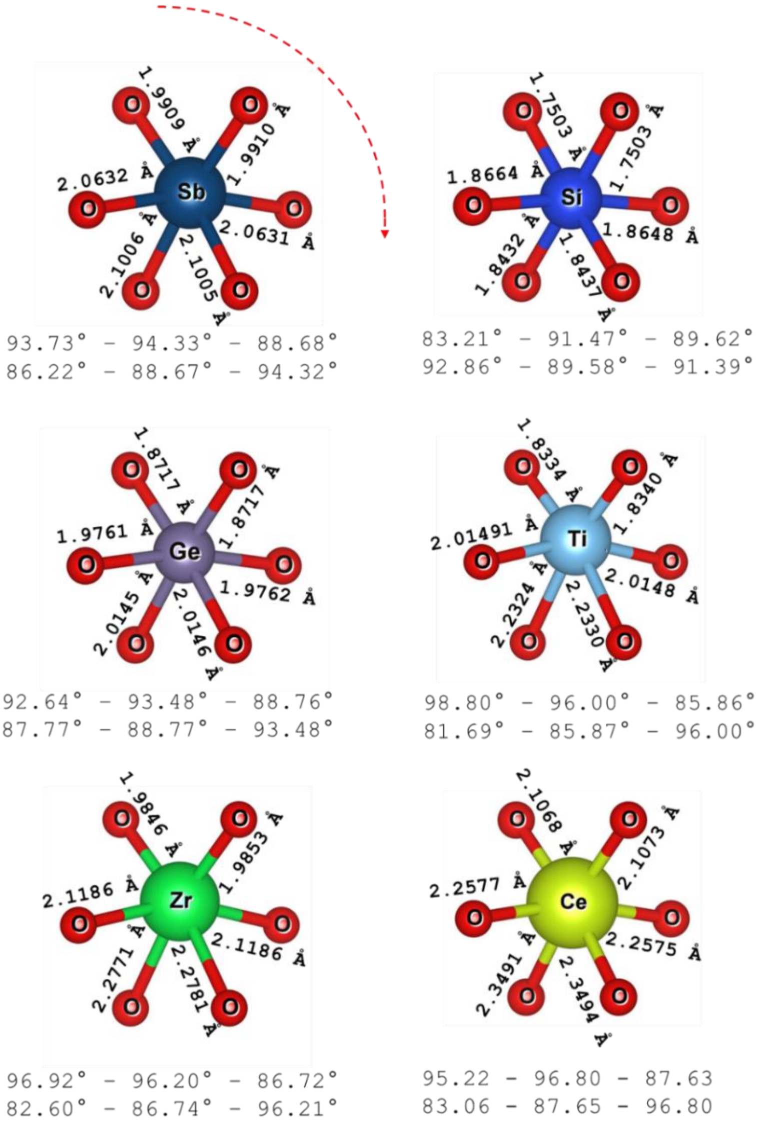

**Figure 8.4** Octahedral $SbO_6$ unit in the relaxed structure of undoped $Li_3SbO_4$ and the coordination formed by the dopants on the $Sb^{5+}$ site with neighbour oxygen atoms.

The local coordination of $Sb^{5+}$ with $O^{2-}$ atoms, bond lengths and angles in the relaxed structure of undoped $Li_3SbO_4$ and the doping elements occupying a $Sb^{5+}$ site are represented in **Figure 8.4**. The ionic radius of $Sb^{5+}$ in octahedral coordination is 0.60 Å whereas the ionic radius of $Si^{4+}$ is 0.40 Å smaller than $Sb^{5+}$. In the $SiO_6$ unit, the four Si-O bonds are shorter compared to the Sb-O bonds in the undoped structure as well as with the R-O bonds in the doped cell. This is due to its smaller cation size of $Si^{4+}$ which strongly polarises the oxygen ions forming strong bonds with O atoms. The second lowest solution energy (0.27 eV) is found for $Ti^{4+}$. Its ionic radius (0.605 Å) is very close to the radius of $Sb^{5+}$. However, due to its relatively smaller charge (+4), the solution energy increases slightly. The bigger size of the $Zr^{4+}$compared to that of $Si^{4+}$ shows a higher solution energy. This is reflected in the longer bond lengths of Zr-O and the shorter bond angles. There is a significant rise in the solution energy (2.30 ev) for $CeO_2$ due to its larger ionic radius reflecting in the longest bond lengths and shortest angles. The ionic radius of $Ge^{4+}$ (0.53 Å) is smaller than that of $Ti^{4+}$ or $Sb^{5+}$ and larger than that of $Si^{4+}$. The solution energy (0.64 eV) is higher than that of $Si^{4+}$, $Ti^{4+}$ and $Zr^{4+}$. Again, for $Li_3NbO_4$, the $RO_2$ ($R$ = Si, Ge, Ti, Zr and Ce) is considered. Local coordination of $Nb^{5+}$ with oxygen together with bond lengths and angles in the relaxed structure of undoped $Li_3NbO_4$ and the dopants occupying the $Nb^{5+}$ site are reported in **Figure 8.5**. The ionic radius of $Nb^{5+}$ in octahedral coordination is 0.64 Å. The ionic radius of $Ge^{4+}$ is 0.11 Å smaller than that of $Nb^{5+}$. In the $GeO_6$ unit, all six Ge-O bonds are shorter compared to the Nb-O bonds present in the undoped $Li_3NbO_4$. This is due to its smaller cation size of $Ge^{4+}$, which strongly polarises the oxygen ions forming strong bonds with O atoms. The second lowest solution energy is found for $Si^{4+}$. Its ionic radius (0.40 Å) is 0.24 Å shorther than that of $Nb^{5+}$. This is refelected in the shorter bond distances. However, due to its slightly larger cation mismatch, the solution energy increases slightly. In the $TiO_6$ unit, all six Ti-O bond lengths are shorter than those observed in the $NbO_6$ unit. However, the bond angles deviate significantly reflecting in the solutioin energy. In the $ZrO_6$ unit, three shorter and three longer Zr-O bonds are observed. However, the bond angles are shorter than the other octahedral units. The solution energy is slightly lower than that calculated for $Ti^{4+}$. The difference in the solution energies is also dependent on the electronic structure of the dopants. There is a significant rise in the solution energy (4.69 eV) for $CeO_2$ due to its larger ionic radius reflecting in the longest bond lengths and the shortest bond angles.

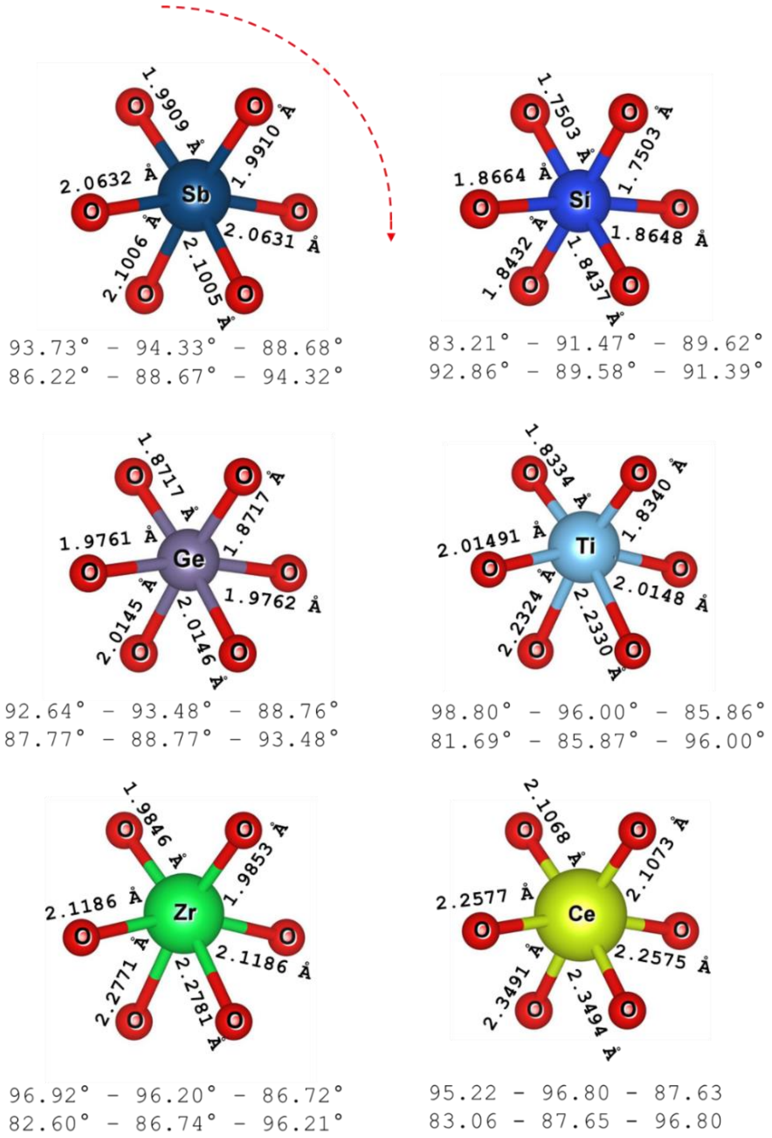

**Figure 8.5** Octahedral $NbO_6$ unit in the relaxed structure of undoped $Li_3NbO_4$ and the coordination formed by the dopants on the $Nb^{5+}$ site with neighbour oxygen atoms.

## 8.4. Density of States

### 8.4.1 $Li_3SbO_4$

For the tetravalent dopants considered in $Li_3SbO_4$ density of states (DOS) calculations are performed to consider the contribution of every element (partial-DOS) in the electronic structure. In **Figure 8.6** the PDOS for (a) the $Li_3SbO_4$ perfect cell (b) $Li_3SbO_4$ with a Li interstitial (c) Si – Doped $Li_3SbO_4$ and (d) Si- Doped $Li_3SbO_4$ with Li interstitial. Overall, the formation profile of the electronic structure indicates the ionic conduction to be the dominant mechanism compared to the electronic. The valence band maximum (VBM) is at zero energy level with the band gap being approximately 6 eV. However, an additional in – gap contribution is observed at 2.58 eV from the valence band with a width of 2.03 eV, as presented in Figure 8.6(a). Due to this non-continuation the intermediate contribution is not counted as a part of the conduction band.

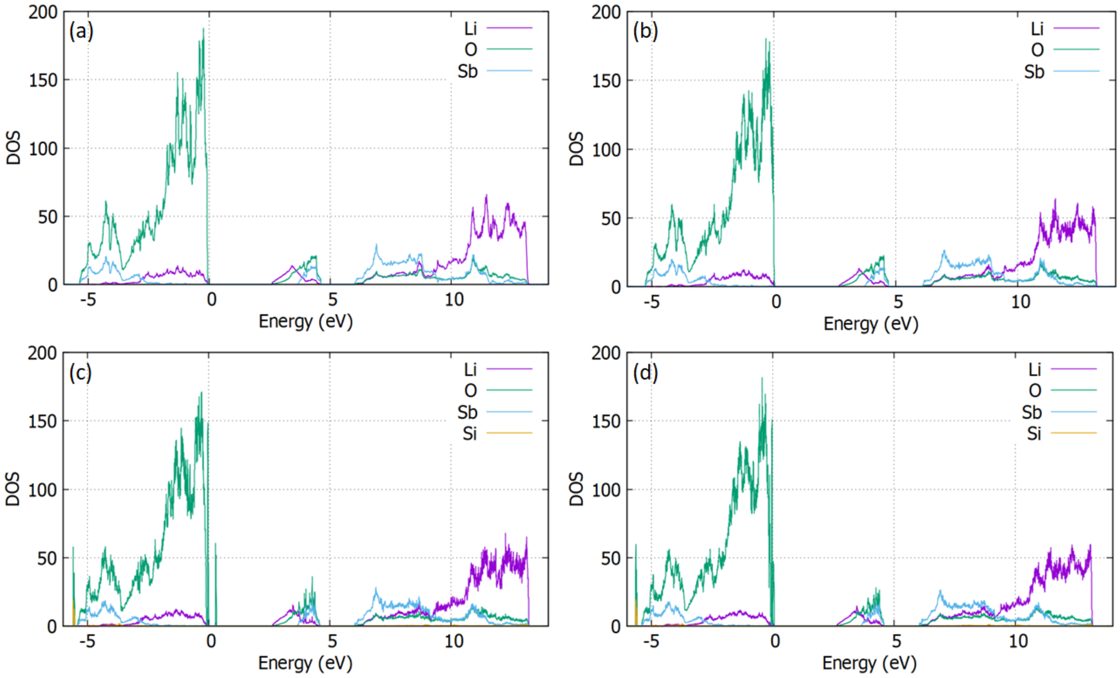

**Figure 8.6** The PDOS for the (a) $Li_3SbO_4$ perfect cell (b) $Li_3SbO_4$ with a $Li^+$ interstitial (c) $Si^{4+}$ – Doped $Li_3SbO_4$ and (d) $Si^{4+}$- Doped $Li_3SbO_4$ with $Li^+$ interstitial.

The electronic structure is characterised by the $O^{2-}$ p-states near the Fermi level whereas the edge of the conduction band is characterised by the $Sb^{5+}$ p-states and $Li^+$ p-states as well. (Refer to **Figure 8.7**) All elements are present in the in-gap contribution indicating a type of anisotropy for the electronic properties band. Furthermore, the presence of $Li^+$ interstitials in the crystal does not affect the PDOS profile, as shown in Figure 8.6 (b). In terms of the doping effect, additional states for all cases appear as a consequence of the substitutional atom that resides in the $Sb^{5+}$ site. Interestingly, the intensity as well as the quantity of these states increases with the ionic radius of the dopant (Refer to **Figure 8.8**). The $Si^{4+}$ case that corresponds to the lower radius and solution enthalpy of the system, presents the lowest contribution as shown in Figure 8.6 (c). In accordance with the un-doped supercell, no considerable changes are observed in the total DOS with the formation of a $Li^+$ interstitial. However, for bigger ions, there is an increasing amount of extra states with $Zr^{4+}$ and $Ce^{4+}$ being the most representative cases.

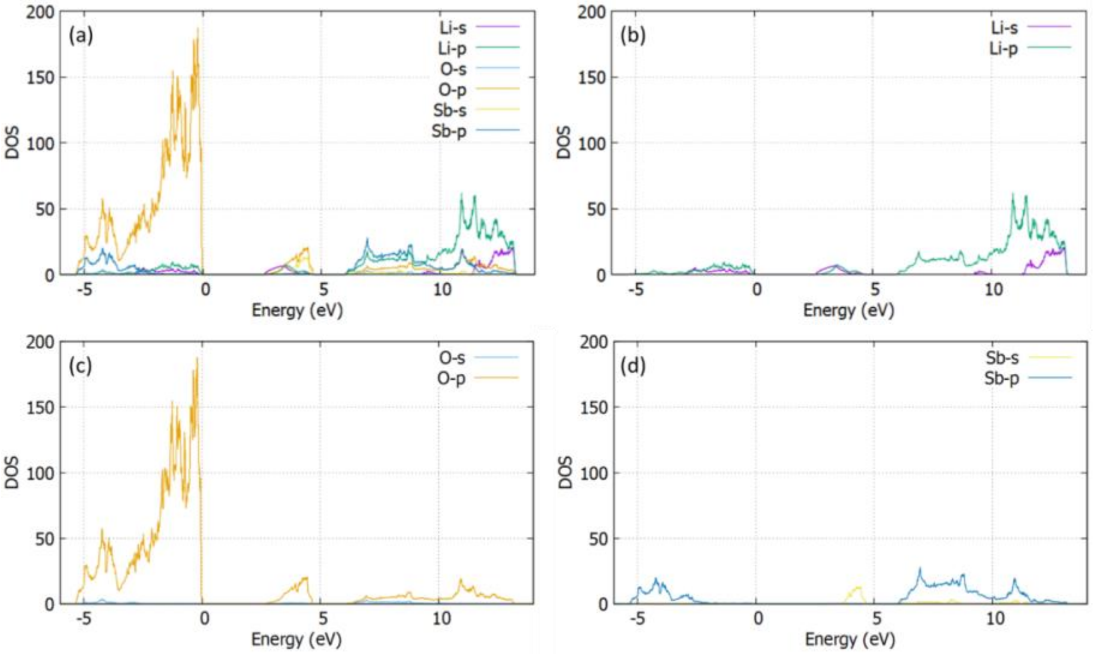

**Figure 8.7** The DOS for the undoped $Li_3SbO_4$ with respect to (a) The total contribution of orbitals (b) The $Li^+$ orbitals (c) The $O^{2-}$ orbitals (d) The $Sb^{5+}$ orbitals.

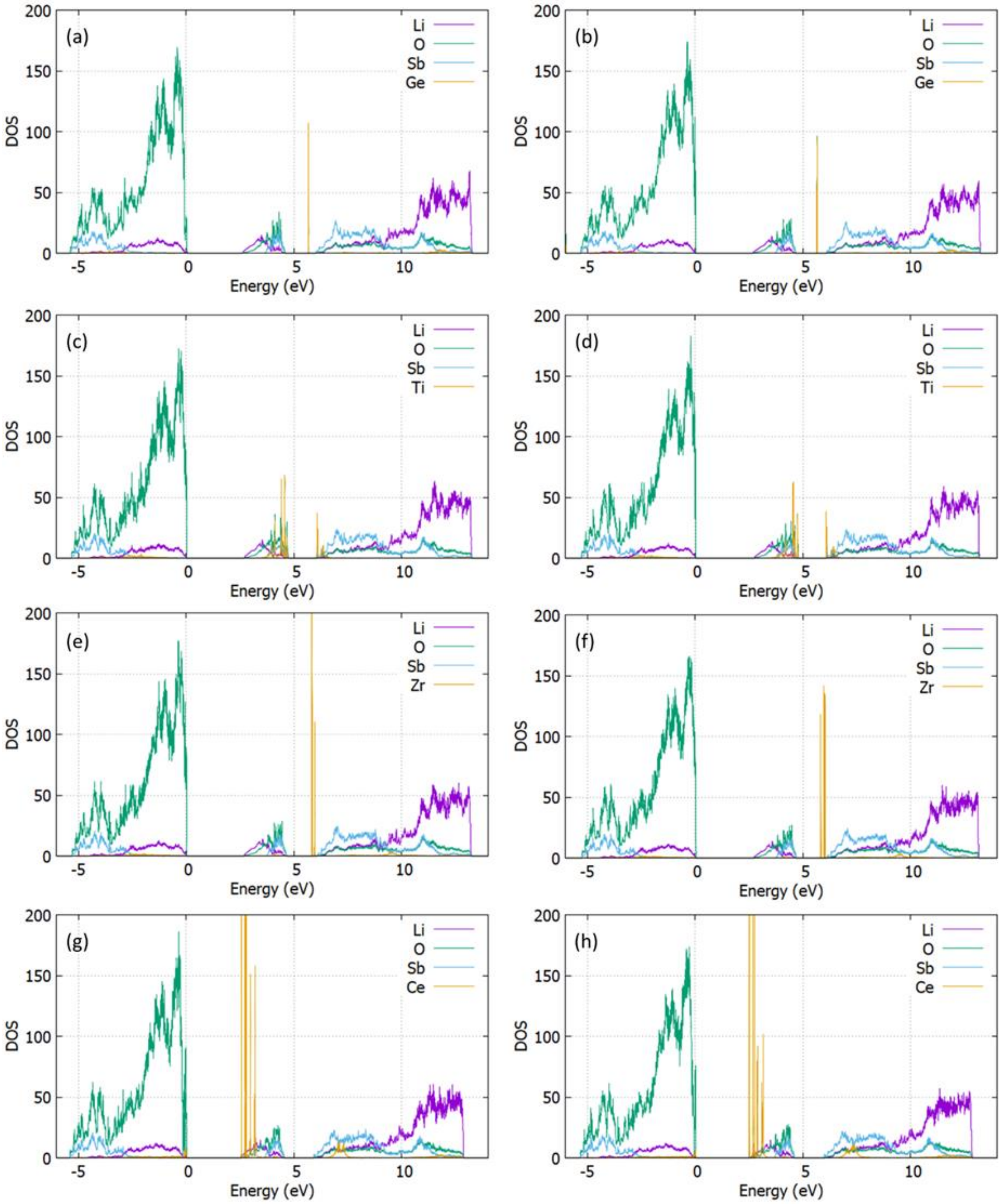

**Figure 8.8** The Density of States for the doped $Li_3SbO_4$ with respect to (a) $Ge^{4+}$ doping (b) $Ge^{4+}$ doping with a $Li^+$ interstitial (c) $Ti^{4+}$ doping (d) $Ti^{4+}$ doping with a $Li^+$ interstitial (e) $Zr^{4+}$ doping (f) $Zr^{4+}$ doping with a $Li^+$ interstitial (g) $Ce^{4+}$ doping (h) $Ce^{4+}$ doping with a $Li^+$ interstitial.

### 8.4.2 $Li_3NbO_4$

The electronic structure of $Li_3NbO_4$ is also investigated using DFT. **Figure 8.9** (a) presents the electronic structure with the $O^{2-}$ p-states set to the Fermi level forming a band gap of 6.95 eV where the $Nb^{5+}$ d-states dominate the conduction band (Refer to **Figure 8.10** for the exact contribution of the orbitals). In addition, a contribution of in-gap states is located at 4.0 eV from the valence band with a width of 1.15 eV, mainly attributed at the $O^{2-}$ p-states and the $Nb^{5+}$ d-states as well. Furthermore, $Li^+$ is calculated to have the strongest density in the conduction band. Overall, it is expected that the electronic conduction of $Li_3NbO_4$ is not the main conduction mechanism. Introducing $Li^+$ interstitials into the crystal does not significantly affect the profile of the total DOS, however a small tail of the valence band is observed in conjunction with additional $Nb^{5+}$ contribution close to the mid-gap state region.

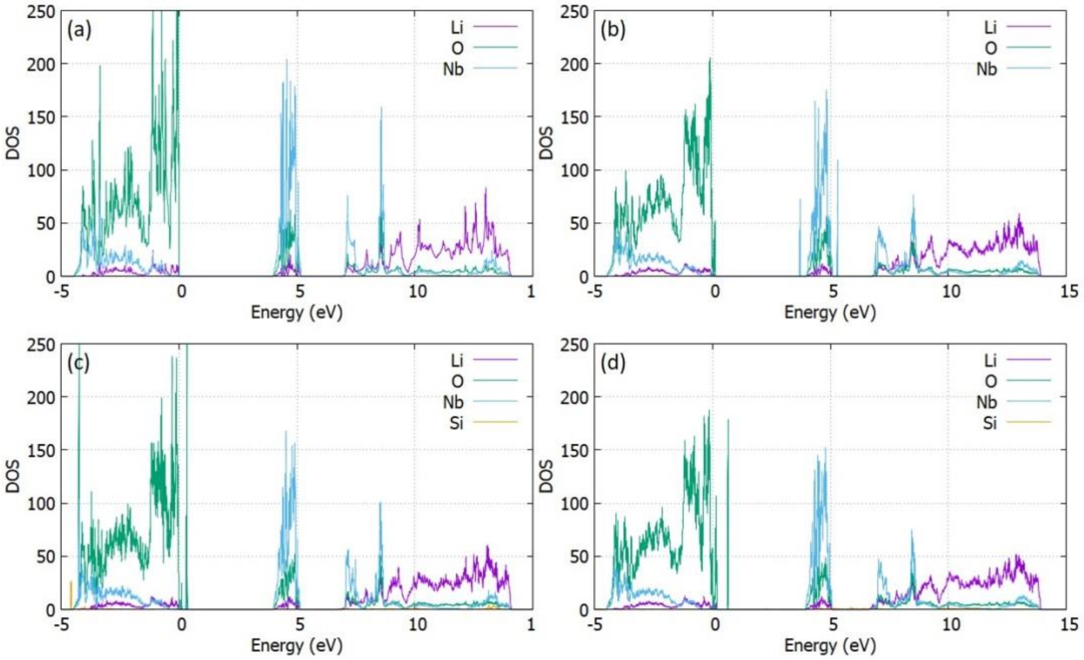

**Figure 8.9** The $Li_3NbO_4$ PDOS for the (a) Perfect cell (b) The $Li^+$ interstitial (c) The $Si^{4+}$ - doped cell (d) The $Si^{4+}$ - doped with a $Li^+$ interstitial.

Doping with tetravalent elements will increase the formation of $Li^+$ ion hosted in interstitial sites of the crystal. However, the increased $Li^+$ concentration in the crystal does not promote an increase in the total $Li^+$ contribution. The $Si^{4+}$ - doped $Li_3NbO_4$ corresponds to the lowest solution enthalpy while it is characterised by the smallest ionic radius of all the dopants examined. Figure 8.9 (c) – (d) shows the DOS for the $Si^{4+}$ doped supercell before and after the introduction of one $Li^+$ interstitial respectively. The formation of new states due to the dopant reaction with the host lattice is expected. This should be considered as both a structural distortion as well as a point of association with the electronic configuration between neighbouring atoms.

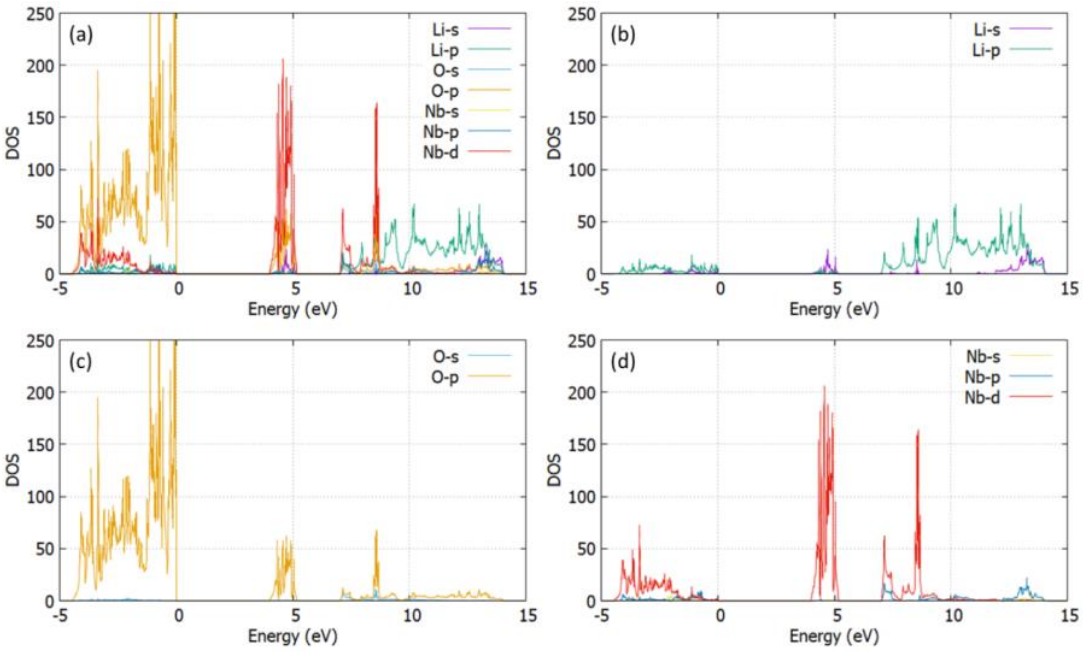

**Figure 8.10**. The PDOS for the non-defective $Li_3NbO_4$ structure with respect to (a) The complete contribution of orbitals (b) The $Li^+$ orbitals only (c) The $O^{2+}$ orbitals only (d) The $Nb^{5+}$ orbitals only.

The doping effect relates to additional contributions close to the conduction band as well as in the middle of the gap as well. The defect pairs of $Ge'_{Nb}$ and $\{Ge'_{Nb}: Li_i^{\bullet}\}^X$, $Ti'_{Nb}$ and $\{Ti'_{Nb}: Li_i^{\bullet}\}^X$, $Zr'_{Nb}$ and $\{Zr'_{Nb}: Li_i^{\bullet}\}^X$ and $Ce'_{Nb}$ and $\{Ce'_{Nb}: Li_i^{\bullet}\}^X$ have been also examined.

The minimum and maximum intensity corresponds to those of the smallest and biggest radius respectively (Refer to **Figure 8.11**, for the dopants considered).

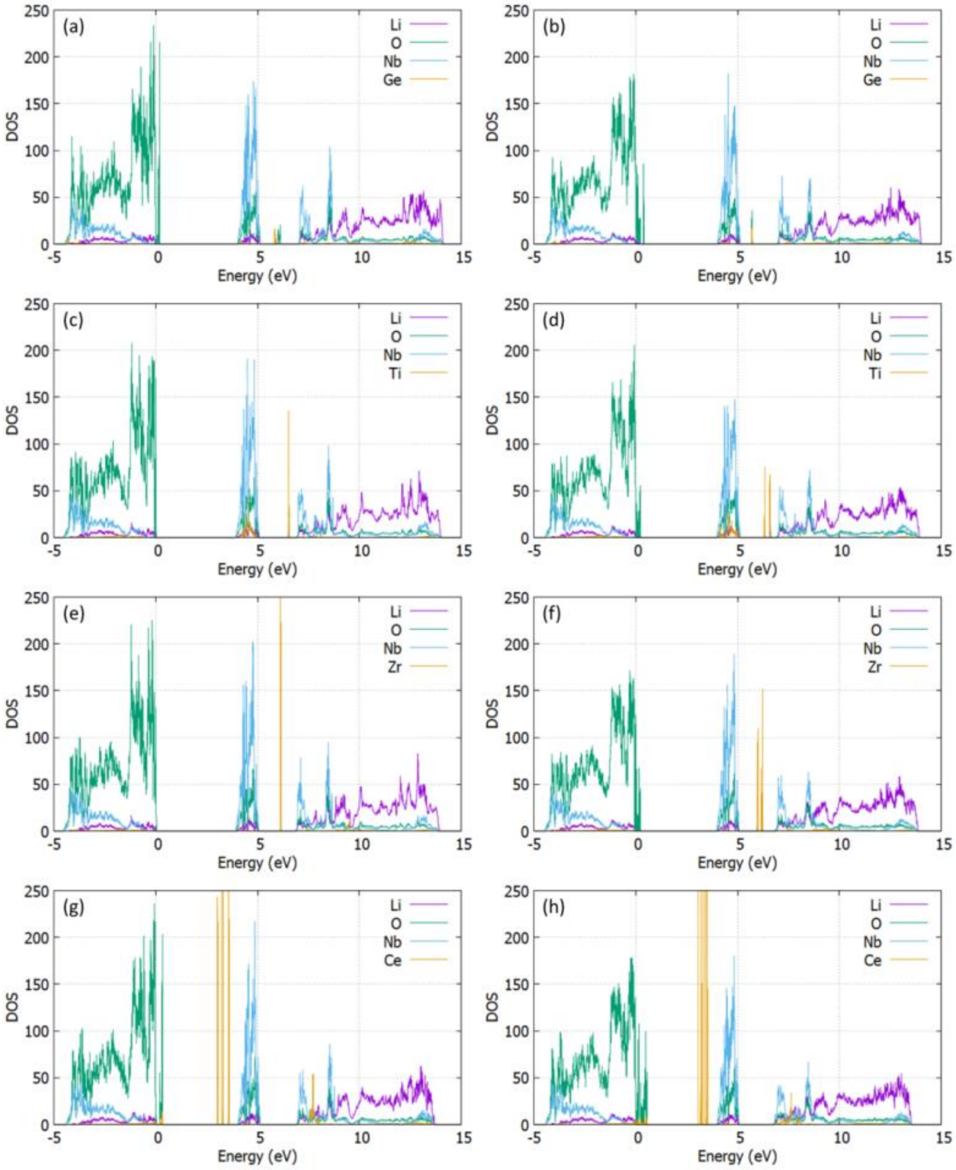

**Figure 8.11** The PDOS for the doped supercell with respect to (a) $Ge^{4+}$ doping (b) $Ge^{4+}$ doping with one $Li^{+}$ interstitial (c) $Ti^{4+}$ doping (d) $Ti^{4+}$ doping with one $Li^{+}$ interstitial (e) $Zr^{4+}$ doping (e) $Zr^{4+}$ doping with one $Li^{+}$ interstitial (g) $Ce^{4+}$ doping (h) $Ce^{4+}$ doping with one $Li^{+}$ interstitial.

Additionally, the interstitial mechanism tends to increase the dopant contribution whereas a slight non – uniformity of the valence band near the Fermi level with extra $O^{2-}$ states in the gap is observed. Figure 8.11 illustrates the DOS for the defect pairs of $Ge'_{Nb}$ and $\{Ge'_{Nb}\colon Li'_i\}''$, $Ti'_{Nb}$ and $\{Ti'_{Nb}\colon '\}''$, $Zr'_{Nb}$ and $\{Zr'_{Nb}\colon Li'_i\}''$and $Ce'_{Nb}$ and $\{Ce'_{Nb}\colon Li'_i\}''$. Overall, it is expected that the electronic structure with respect to the total Frenkel mechanism to remain unaffected, with the additional contributions to be attributed to the dopants.

## 8.5 Conclusions

The aim of the present chapter is to access whether $Li_3MO_4$ (M=Sb, Nb) can be used in solid oxide $Li^+$ batteries as electrodes or electrolyte materials. For completeness, recent atomistic simulation results have been reviewed. These revealed that the $Li^+$ migration via vacancy mechanism is a low energy process for $Li_3SbO_4$ but is considerably high for $Li_3NbO_4$. Atomistic simulations revealed that for $Li_3SbO_4$, the $Li^+$ Frenkel is the dominant intrinsic defect process, therefore there will be an adequate supply of $Li^+$ vacancies to mediate the $Li^+$ migration via the vacancy mechanism. Additionally, to enhance the $Li^+$ content, $Li_3SbO_4$ should be doped with $SiO_2$, $TiO_2$ or $ZrO_2$ to increase the concentration of $Li^+$ interstitials. Therefore, $Li_3SbO_4$ is an important material for Li – ion batteries but should it be considered as an electrolyte or an electrode? The present DFT electronic structure calculations revealed that $Li_3SbO_4$ is a promising material but only as an electrolyte. The DOS also proved that the material is unlikely to be an electrode material as $Sb^{5+}$ ions are more difficult to donate electrons. Additionally, the capacity of $Li_3SbO_4$ is reported to be limited by the redox potential and not the cycling rate. Here, $Li^+$ - ion mobility is not the only requirement for a cathode to offer reversible capacity. The material should be able to undergo a reversible oxidation process when $Li^+$ ions are extracted and reinserted.

# REFERENCES

---

[1] M. Kundu, S. Mahanty, R. N. Basu, $Li_3SbO_4$: A new high rate anode material for lithium-ion batteries. *Materials Letters*, **65**, 1105, (2011).

[2] M. Kundu, S. Mahanty, R. N. Basu, $Li_4Ti_5O_{12}/Li_3SbO_4/C$ composite anode for high rate lithium-ion batteries. *Materials Letters*, **65**, 3083, (2011).

[3] N. Yabuuchi, M. Takeuchi, M. Nakayama, H. Shiiba, M. Ogawa, K. Nakayama, T. Ohta, D. Endo, T. Ozaki, T. Inamasu, K.Sato, and S. Komaba, High-capacity electrode materials for rechargeable lithium batteries: $Li_3NbO_4$-based system with cation-disordered rocksalt structure. *Proceedings of the National Academy of Sciences of the United States of America*, **112**, 7650, (2015).

[4] N. Yabuuchi, M. Takeuchi, S. Komaba, S. Ichikawa, T. Ozaki and T. Inamasu, Synthesis and electrochemical properties of $Li_{1.3}Nb_{0.3}V_{0.4}O_2$ as a positive electrode material for rechargeable lithium batteries. *Chemical Communications*, **52**, 2051, (2016).

[5] V. L. McLaren, C. A. Kirk, M. Poisot, M. Castellanos and A. R. West, $Li^+$ ion conductivity in rock salt-structured nickel-doped $Li_3NbO_4$. *Dalton Transactions*, **0**, 3042, (2004).

[6] M. C. Payne, M. P. Teter, D. C. Allan, T. A. Arias and J. D. Joannopoulos, Iterative minimization techniques for ab initio total-energy calculations: molecular dynamics and conjugate gradients. *Reviews of Modern Physics*, **64**, 1045, (1992).

[7] M. D. Segall, P. J. D. Lindan, M. J. Probert, C. J. Pickard, P. J. Hasnip, S. J. Clark and M. C. Payne First-principles simulation: ideas, illustrations and the CASTEP code. *Journal of Physics: Condensed Matter*, **14**, 2717, (2002).

[8] H. J. Monkhorst and J. D. Pack, Special points for Brillouin-zone integrations. *Physical Rev*iew *B*, **13**, 5188, (1976).

[9] J. P. Perdew, K. Burke and M. Ernzerhof, Generalized Gradient Approximation Made Simple. *Physical Review Lett*ers, **77**, 3865, (1996).

[10] D. Vanderbilt, Soft self-consistent pseudopotentials in a generalized eigenvalue formalism. *Physical Review B*, **41**, 7892, (1990).

[11] R. J. Nicholls, A. J. Morris, C. J. Pickard and J. R. Yates, OptaDOS - a new tool for EELS calculations. *Journal of Physics: Conference Series*, **371**, 012062, (2012).

[12] A. J. Morris, R. Nicholls, C. J. Pickard and J. R. Yates, OptaDOS: A tool for obtaining density of states, core-level and optical spectra from electronic structure codes. *Computer Physics Communications*, **185**, 1477, (2014).

---

[13] J. M. S. Skakle, M. A. Castellanos R, S. T. Tovar, S. M. Fray and A. R. West, The crystal structure of $Li_3SbO_4$. *Journal of Materials Chemistry A*, **6**, 1939, (1996).

[14] K. Ukei, H. Suzuki, T. Shishido and T. Fukuda, $Li_3$NbO4. *Acta Crystallographica Section C: Crystal Structure Communications,* **50**, 655, (1994).

[15] S. Bernès, S.T.b Tovar, M.A Castellanos R, A comparison of the X-ray single-crystal structure of $Li_3SbO_4$ with the Rietveld refinement, *Acta Crystallographica Section C: Crystal Structure Communications,* **57**, 8, 883, (2001).

[16] N. Kuganathan, A. Kordatos, S. Anurakavan, P. Iyngaran and A. Chroneos, Li3SbO4 lithium-ion battery material: Defects, lithium ion diffusion and tetravalent dopants. *Materials Chemistry and Physics*, **225**, 34, (2019).

[17] N. Kuganathan, A. Kordatos, N. Kelaidis and Alexander Chroneos, Defects, Lithium Mobility and Tetravalent Dopants in the Li3NbO4 Cathode Material. *Scientific Reports,* **9**, 2192, (2019).

[18] Q. Jacquet, G. Rousse, A. Iadecola, M. Saubanère, M.-L. Doublet and Jean-Marie Tarascon Electrostatic Interactions versus Second Order Jahn-Teller Distortion as the Source of of Structural Diversity in $Li_3MO_4$ Compounds (M=Ru, Nb, Sb and Ta) *Chemistry of Materials*, **30**, (2017).

[19] "Panasonic Develops New Higher-Capacity 18650 Li-Ion Cells; Application of Silicon-based Alloy in Anode". greencarcongress.com. (2011).

# CHAPTER 9

## Defect processes in anatase $TiO_2$

Part of the results presented here has been published in *Solid State Ionics* **315**, 40-43 (2018), the *Journal of Applied Physics* **123**, 161510 (2018) and *Scientific Reports* **8**, 12790 (2018)

### 9.1 Introduction

Since its first investigation as a catalytic material[1], $TiO_2$ has attracted a lot of interest due to its high photocatalytic activity and chemical stability[2, 3, 4]. However, the limitation of a large band gap limits its properties to a small portion of the solar spectrum[5]. Anatase is a mineral form of $TiO_2$ along with rutile, ilmenite and brookite. Here, the anatase phase of $TiO_2$ is investigated as it is the most relevant for the applications considered. Specifically, the 3.2 eV gap of anatase corresponds to the ultraviolet range and its reduction is of crucial significance for applications in photocatalysis. Recently, titanium dioxide has been doped with lithium ($Li^+$) and sodium ($Na^+$) to consider its potential application in Li-ion and Na-ion batteries, respectively. The relative energetics of $Li^+$ and $Na^+$ in $TiO_2$ are important when considering this system as an anode in batteries. In the present chapter, Density Functional Theory (DFT) was employed to study the structure, electronic properties and migration of lithium and sodium interstitials in anatase as these can be important for battery applications. Furthermore, the defect pair formation / binding of $F^-$ and $N^+$ clusters in anatase is investigated and the most energetically favoured combinations as well as their influence on the materials behaviour is reported. The doping of the perfect crystal is an efficient technique to improve the material's photocatalytic properties. $N^+$ is a promising dopant for this approach in $TiO_2$ as it is able to reduce the band gap and lead to an enhanced photocatalytic activity through the visible light response[6, 7, 8]. It is considered that the band gap of the material should be approximately 2 eV. Fluorine doping may not drastically affect the total performance of the optical absorption however the electronic structure will be changed through the formation of surface oxygen vacancies[9, 10, 11, 12]. For this reason $F^-$ and $N^+$ codoped anatase is considered for a wide range of applications. Overall the electronic structure of anatase and the doping effect is investigated with respect to potential energy applications. The calculated results present a solid consistency with experimental studies, but more work has to be done in the future in order to gain further insights into the materials properties.

## 9.2 Methodology

For the calculations the plane wave DFT code CASTEP is used with the exchange and correlation interactions modelled using the corrected density functional of Perdew, Burke and Ernzerhof (PBE) in the generalised gradient approximation (GGA), with ultrasoft pseudopotentials. The kinetic energy cut-off of the plane wave basis is 480 eV, in conjunction with a 2 x 2 x 3 Monkhorst-Pack (MP) k-point grid and a 108-atomic site supercell. To consider the correlation effects of localised electrons onsite Coulomb repulsions of 8.2 eV are set for the Ti 3d orbitals. This value is tested to establish that the trends are not affected by the specific choice of U-parameter. The calculations were under constant pressure conditions. Note that in the present cell a dopant atom represents a 0.9% dopant concentration. Migration energy barriers were predicted using the linear synchronous transition (LST) and/or quadratic synchronous transition (QST) as implemented in CASTEP. The binding energies were defined here as the differences in energy between the defect cluster and its constituent defects being as far apart as possible in the supercell. Negative binding energies imply that the cluster is more energetically favourable compared to its relatively isolated constituent defects. For the DOS calculations, a denser mesh of 7 x 7 x 7 k-points was applied.

## 9.3 Results and discussion

### 9.3.1 $Li^+$ and $Na^+$ interstitial sites: Migration Mechanisms

Anatase is tetragonal with space group *I4/amd*[13, 14]. The lattice parameters of anatase $TiO_2$ are calculated at a = 3.806 Å and c = 9.724 Å in very good agreement with the experimental neutron diffraction results (a= 3.782 Å and c = 9.502 Å)[13] and theoretical results (a= 3.729–3.801 Å and c = 9.480–9.818 Å)[14, 15]. The crystallographic structure is shown in **Figure 9.1**.

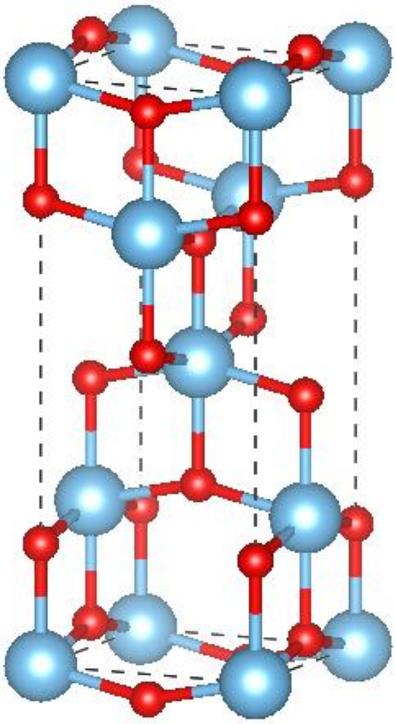

**Figure 9.1** The crystallographic structure of anatase $TiO_2$.

Understanding the diffusion mechanisms of $Li^+$ and $Na^+$ in oxides is technologically important to realise Li-ion batteries and more recently Na-ion batteries[16]. $Na^+$ is considered by the community as a promising alternative candidate as it is abundant and less expensive compared to $Li^+$. However, due to its larger atomic radius it typically requires more open host structures, in order to achieve the desired ionic diffusivity[17]. It has been previously reported that $TiO_2$ is an important candidate anode material for Li-ion batteries, as it is low cost, environmentally friendly, structurally and electrically stable[18]. In addition, the potential of $TiO_2$ for Na-ion batteries has been recently discussed[19]. $Li^+$ and $Na^+$ doping in anatase is achieved by taking advantage of the most energetically favourable interstitial sites in the crystal. The structure of the calculated minimum energy $Li_i$ and $Na_i$ defects in anatase is reported in **Figure 9.2**.

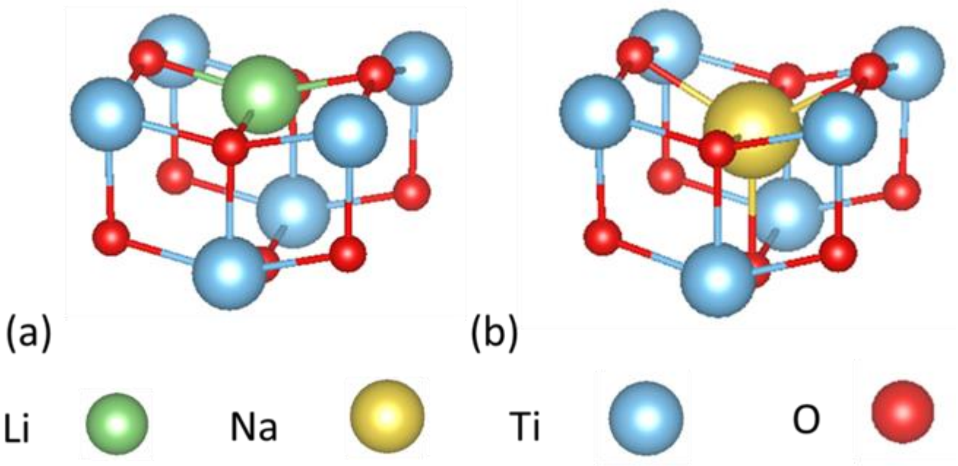

**Figure 9.2** The (a) $Li^+$ and (b) $Na^+$ interstitial sites in $TiO_2$.

These correspond to the lowest ground state energies among all considered. The calculations were under constant pressure conditions with the host oxide being allowed to relax to the most favourable configuration after the interstitial atom insertion. It is shown that the minimum energy interstitial sites are the distorted octahedral and not the tetrahedral sites in the lattice as confirmed also in previous literature[20]. In addition, the $Li_i$ and $Na_i$ defects reside 1.90 Å and 2.10-2.16 Å respectively from the nearest oxygen atom. Figure 9.2 (a) and (b) also reveals that the $Li_i$ and $Na_i$ ions are able to relax in a different geometry as would be expected by two ions of different size. Notably, the ionic radii of $Li^+$ and $Na^+$ are 0.59 Å and 0.99 Å, respectively). $Li^+$-ion solid-state conducting systems require high ionic conductivities (>1 mS $cm^{-1}$) at room temperature as well as low activation energies (< 0.6 eV)[21, 22]. If we consider a migration path between the initial and final state, the highest energy along this path is the activation energy of migration. A low activation energy of migration will typically correspond to high ionic diffusivity.

The diffusion mechanisms of the $Li_i$ and $Na_i$ in anatase are illustrated in **Figure 9.3**. Specifically, for the $Li_i$, the minimum energy migration path is along the b – axis corresponding to a migration energy barrier of 0.32 eV (refer to Figure 9.3 (a)). The distance for this transition is 3.78 Å). In this mechanism, the $Li^+$ ion preferential route is below the intermediate oxygen atom that interferes between the initial and final states. The most stable interstitial positions in the crystal accommodate the initial and final positions of the ions. For $Na_i$ the mechanism is very similar to $Li_i$, however higher migration energy (0.56 eV) is received. Typically, the lower migration energy pathways take advantage of the large channels (here the b-axis channel). Furthermore, it was previously proposed that the larger $Li_i$-Ti (or $Na_i$-Ti) interatomic distance at the saddle point can be linked to minimized migration energy barriers[23]. This is because Li diffusion in anatase is accelerated via the reduction of the electrostatic $Li_i$-Ti (or $Na_i$-Ti) repulsion. As it can be observed from **Table 1**, the presented results are consistent with the lowest energy migration energy being linked to the larger $Li_i$-Ti (or $Na_i$-Ti) distance in the lattice.

**Table 1**. The migration energy barriers (ME) and the distances of interstitial atoms to the nearest Ti atom at the saddle point. The numbering of the defect mechanisms corresponds to Figure 9.3.

| Mechanism | $\mathrm{Li_i}$ ME / eV | $\mathrm{Na_i}$ ME / eV | $\mathrm{Li_i}$-Ti / Å | $\mathrm{Na_i}$-Ti / Å |
|---|---|---|---|---|
| 3a | 0.32 | 0.56 | 2.83 | 2.83 |
| 3b | 0.58 | 0.78 | 2.57 | 2.79 |
| 3c | 0.75 | 0.81 | 2.55 | 2.60 |
| 3d | 0.74 | 0.75 | 2.55 | 2.57 |

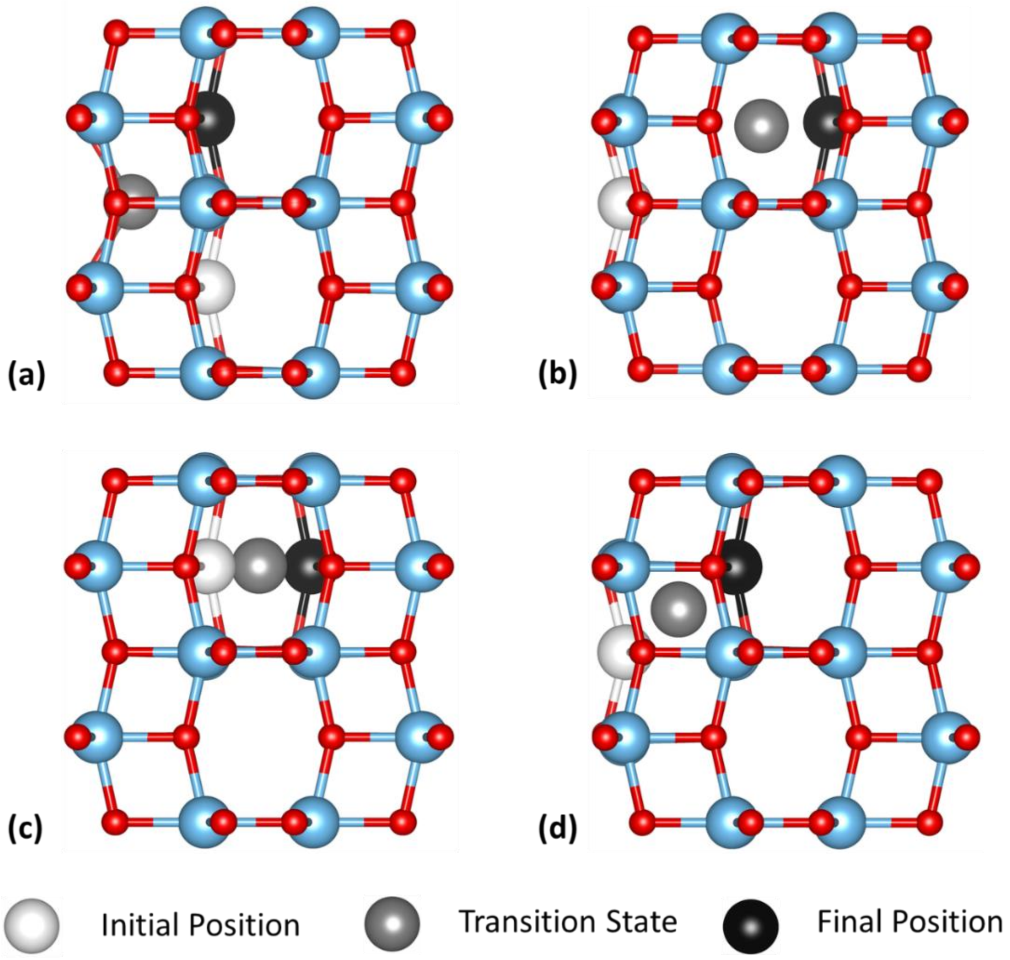

**Figure 9.3 (a)–(d)** The diffusion mechanisms of $\mathrm{Li_i}$ and $\mathrm{Na_i}$ in anatase.

Considering the associated $Li_i$ and $Na_i$ migration mechanisms along the other directions the movement of the interstitials to several nearest positions has been examined and the characteristic low energy mechanisms (refer to Figure 9.3 (b) – (d) and Table 1) have been reported. For all of these, higher migration energy barriers are reported when compared to the mechanism represented in Figure 9.3(a). In Figure 9.3(b) the $Li_i$ ion diffusion is characterised by a $Li_i$ migration energy barrier of 0.58 eV and 0.78 eV for $Na_i$ (distance of 5.45 Å) respectively. Overall, the migration energy barriers for $Na_i$ are higher compared to $Li_i$. Therefore, the mechanism along the b-axis is the dominant mechanism of migration in anatase. It is noted that at higher temperatures the mechanisms of higher energy may also lead to some limited diffusion along other directions.

### 9.3.2 Density of States for the $Li^+$ / $Na^+$ doped $TiO_2$

In order to investigate the Li and Na doping effect in anatase electronic structure, density of states calculations for the un-doped, $Li^+$ – doped and $Na^+$ - doped supercells have been performed. In **Figure 9.4** (a), the DOS of the perfect supercell is shown forming a band gap of ~ 3.1 eV. Additionally, in **Figure 9.4** (b) and (c) the effect of the $Li_i$ and $Na_i$ defects in the DOS of the supercell can be observed. The $Li_i$ introduces an energy level in the band gap at approximately 2 eV whereas a band tail is also observed extending 0.26 eV into the valence band. A similar deep level is introduced in the case of $Na_i$ as well, at approximately 1.9 eV above the valence band edge, along with a band tail, which protrudes 0.16 eV into the bandgap.

Although, it has previously been reported that the Local Density Approximation (LDA) and General Gradient Approximation (GGA) functionals fail to effectively reproduce the electronic properties of the material even with the inclusion of the Hubbard term, the present results are in agreement with previous work that makes use of the sX exchange – correlation functional to calculate the impact of the $Li_i$[20]. Therefore, the dopants ($Li_i$ and $Na_i$) introduce deep levels into the bandgap for both cases. Furthermore, even if the leading conduction mechanism is ionic diffusion, the effect of the deep levels should be considered when designing an energy storage application (batteries).

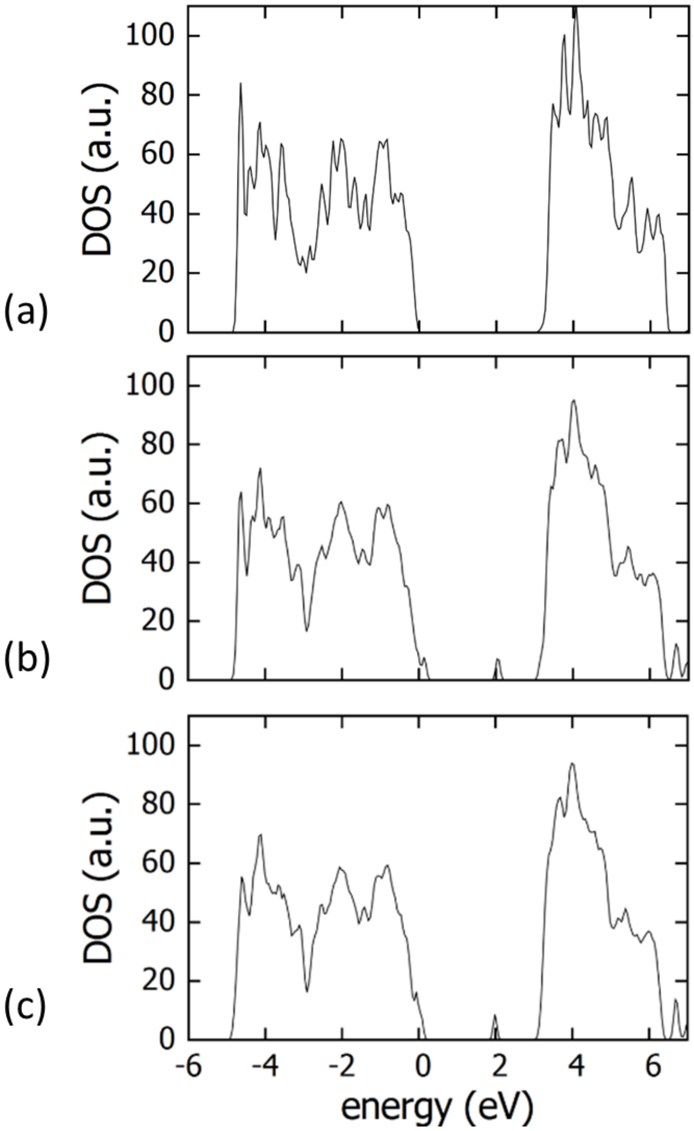

**Figure 9.4** The electronic structure of the (a) non – defective perfect supercell (b) defective supercell containing $Li_i$ and (c) defective supercell containing $Na_i$.

## 9.4 Defect pair formation in fluorine and nitrogen codoped $TiO_2$

### 9.4.1 Defect Pair Formation

In this section, investigation is reported in the defect pair formation / binding of $F^-$ and $N^+$ clusters in doped anatase throughout the most energetically favoured combinations as well as their influence in the materials behaviour. Different cases and configurations have been examined in order to gain insights into the most attractive defect configurations. The dopants have occupied various sites in the crystal either as an interstitial site, or a substitutional to an existing atom.

Based on DFT simulations, it is calculated that $F^-$ can actually substitute an oxygen site ($F_O$) or occupy an interstitial site in the crystal ($F_i$). The most interesting defect formations (isolated as well as pairs) are schematically represented in **Figure 9.5**. (minimum energy fluorine-nitrogen defects in anatase: (a) $F_i$, (b) the $N_i$, (c) $F_iN_i$ (d) $F_ON_i$ (e) $F_iN_{Ti}$ (f) $F_iN_i$_away and (g) $F_iF_i$ defects). It is calculated that $F_i$ resides 1.98 Å from the nearest oxygen atom (refer to Figure 9.5 (a)) and it is therefore considered as the binding processes of $F_i$ atoms to form a $F_iF_i$ pair. It is calculated that the $F_i$ present an attractive force behaviour, with approximately -0.10 eV.

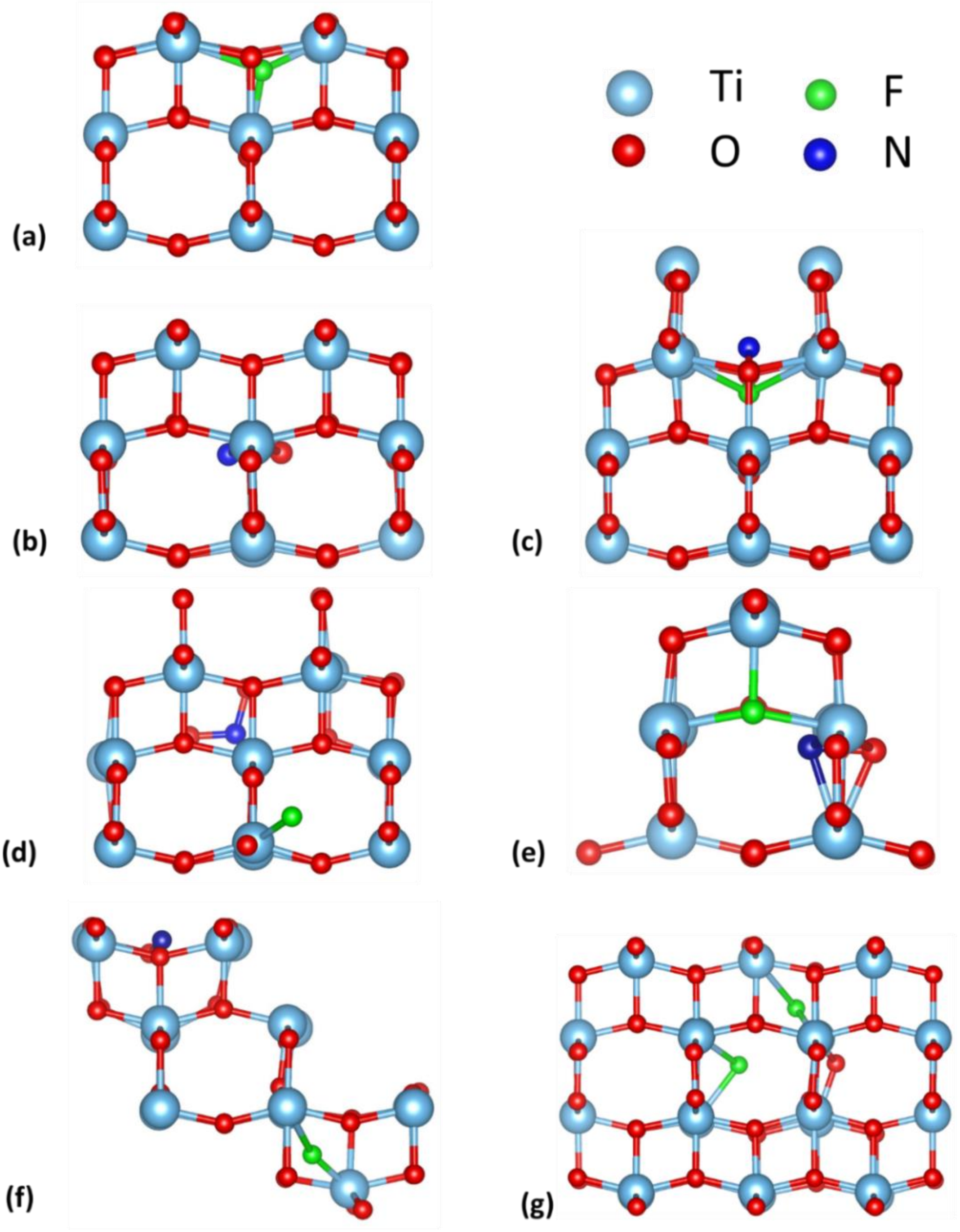

**Figure 9.5** The minimum energy fluorine-nitrogen defects in anatase $TiO_2$ (a) $F_i$ (b) $N_i$ (c) $F_iN_i$ (d) $F_ON_i$ (e) $F_iN_{Ti}$ (f) $F_iN_i$_away and (g) $F_iF_i$.

A different kind of performance is observed compared to already well-known semiconductors such as Si or Ge. These materials present repulsive forces for highly electronegative F interstitials, the opposite of what has been seen in anatase. Nitrogen was introduced at an interstitial site ($N_i$, refer to Figure 9.5 (b)) leading to the N 2-p states at 0.35 eV near the valence band that correspond to the band gap reduction at 2.57 eV in consistency with experimental works[24]. It is considered that in highly N and F codoped anatase, the isolated defects would possibly interact and lead to the formation of defect clusters. In addition, the low migration energy of $F_i$, infers that they will be mobile and therefore it will be very likely for a $F_i$ to encounter a N atom[25].

To account for this an extensive search is performed of the different possible associations of the interstitial and/or substitutional $F^-$ and $N^+$ defects. It is calculated that $F_iN_i$, $F_ON_i$ and $F_iN_{Ti}$ defects form with binding energies of -0.4 eV, -1.6 eV and -0.6 eV respectively. This implies that a $F_i$ would preferably bind to the $N_{Ti}$ (to form $F_iN_{Ti}$) rather than a $N_i$ (to form $F_iN_i$). Additionally, a $N_i$ would preferentially bind with FO (to form $F_ON_i$) rather than $F_i$ (to form $F_iN_i$).

### 9.4.2 Electronic structure

It is observed that the doping processes of anatase can affect the electronic structure. The band gap is again in agreement with previous theoretical and experimental results, ~ 3.1 eV. The valence and conduction bands are clearly formed with no gap in the states or deep levels. In **Figure 9.6 (a)** the effect of the $F_i$ on the DOS of the supercell is shown. In this case (supercell: $Ti_{36}O_{72}F_i$) the $F_i$ gives rise to a mid-gap state at 1.15eV above the valence band maximum (VBM) (mainly due to the Ti p-bands).

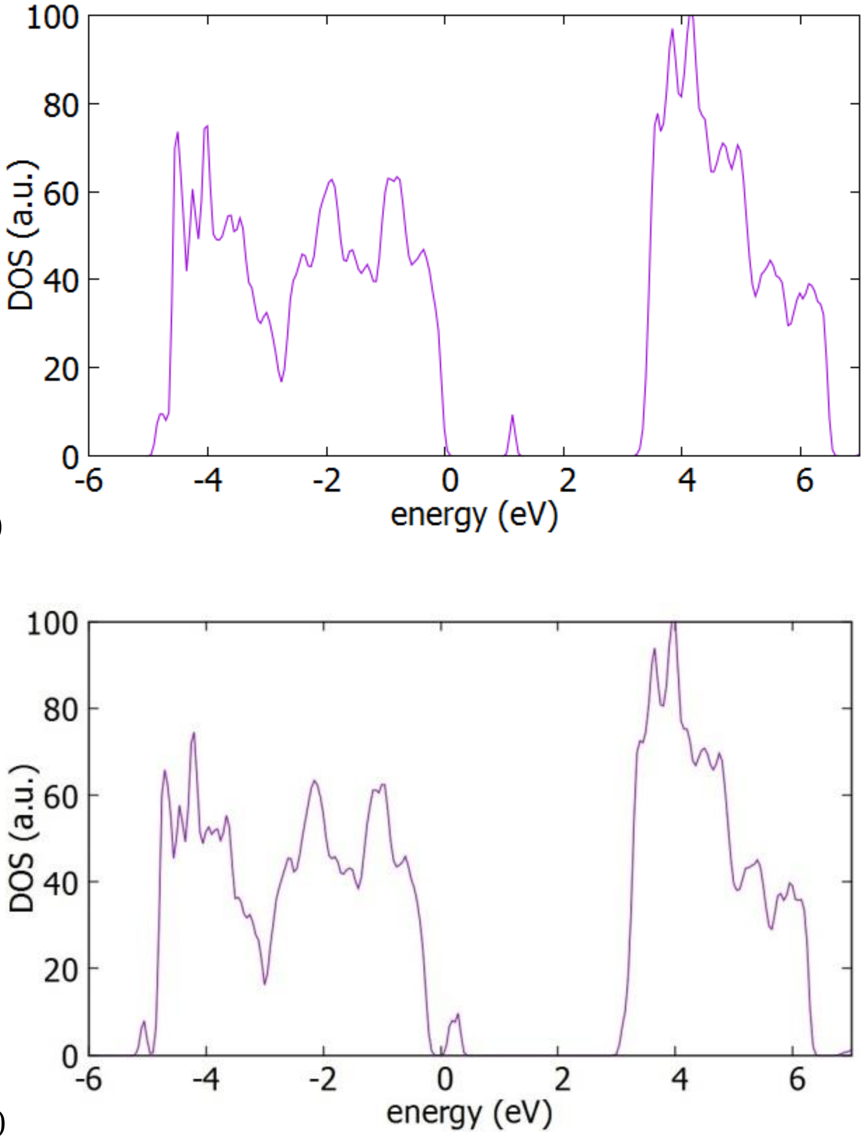

**Figure 9.6** Densities of States of the defective supercells containing (a) $F_i$ (b) $N_i$.

To acquire further understanding of the impact of the N-F defect clusters on the electronic structure of anatase density of states calculations were performed (refer to **Figure 9.7**). It was previously determined that F in $TiO_2$ can occupy oxygen sites. The introduction of $F^-$ in $O^{2-}$ lattice sites (i.e. FO) introduces the formation of $Ti^{3+}$ centers, which localize the extra electron required for charge compensation[25]. This is evident in the DOS of the $F_ON_i$ defect pair (refer to Figure 9.7 (b)) and the $Ti^{3+}$ states are just below the conduction band. The excitation of these occupied $Ti^{3+}$ states to the conduction band (CB) will result in a green colour[26]. Finally, the $F_iN_{Ti}$ defect will induce deep levels in the band gap at 2.03 eV and 2.27 eV below the conduction band (Figure 9.7 (c)). These will need to be investigated experimentally.

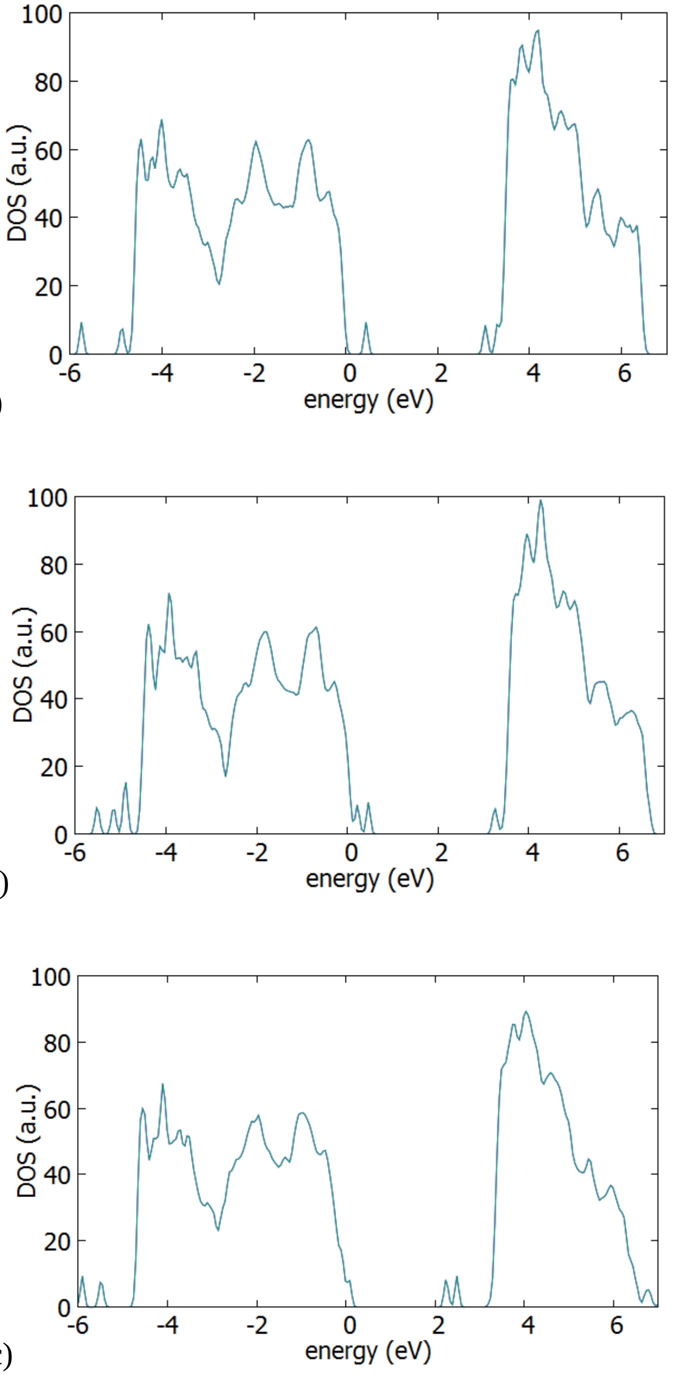

(a)

(b)

(c)

**Figure 9.7** Densities of States of the defective supercells containing (a) $F_iN_i$ (b) $F_ON_i$ (c) $F_iN_{Ti}$.

## 9.4 Strain effects in doped-anatase

Apart from the introduction of dopants in the host lattice, mechanical stress is another efficient way to affect the electronic properties and defect processes in metal oxides[27, 28, 29]. It is established that volume change through an external applied force can lead to changes in the band gap and the electronic structure of semiconductors and effectively modify their electrical properties[30, 31, 32, 33]. To assist in the interpretation of experimental results, but mainly to propose a pathway for better photocatalytic performance, the effect of mechanical strain along with the incorporation of structural defects needs to be examined. The effect of stress on the total unit cell volume is presented in **Figure 9.8**.

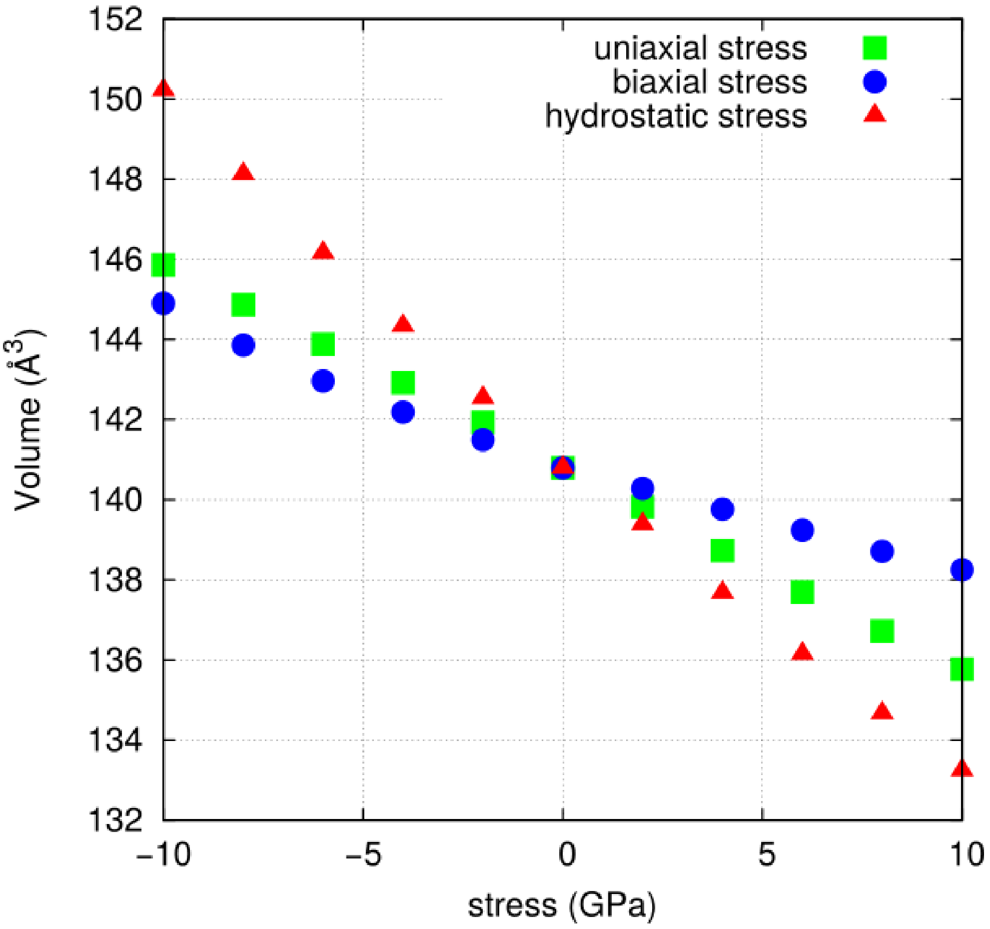

**Figure 9.8** The volume of $TiO_2$ primitive cell with respect to stress.

As expected, hydrostatic stress corresponds to the maximum effect on total volume. Additionally, biaxial stress on the (001) plane results in less volume change when compared to uniaxial stress along the [001] axis. As pointed out, this is because of the different compressibility of the axes as well as the different elastic constants of anatase ($c_{11}$= $c_{22}$ and $c_{33}$).

Numerous experimental studies have reported on the enhanced photocatalytic activity and band gap tuning through strain effects in anatase - $TiO_2$. Importantly, Arlt *et al.*[34] has investigated the $TiO_2$ polymorphs under external pressure showing the volume change whilst highlighting the agreement of experimental work with theoretical modelling. The results are consistent with the present thesis as well as with the study of Yin *et al.*[35] however this latter study does not clarify the type of applied pressure thus hydrostatic is considered following an almost linear trend. Biaxial strain is applicable through growth in substrates that will exhibit a lattice mismatch. Furthermore, Miyamura *et al*.[36] applied compressive / tensile stress on $TiO_2$ at very low values (< ± 0.22 GPa) far below compared to the present results. The published work of this chapter[37] has been recently cited by Magnan *et al*.[38] reporting on the epitaxial growth of anatase (001) and rutile (100)as well as the experimental characterization of electronic properties such as band gap and charge carriers. Thus, the reported results complement in the interpretation of experimental studies in order to tune anatase $TiO_2$ properties through strain.

Electronic structure calculations have been performed and have derived the band gap of anatase for each case under stress. The effect of stress on the band gap of $TiO_2$ for hydrostatic, biaxial and uniaxial stress is shown in **Figure 9.9**.

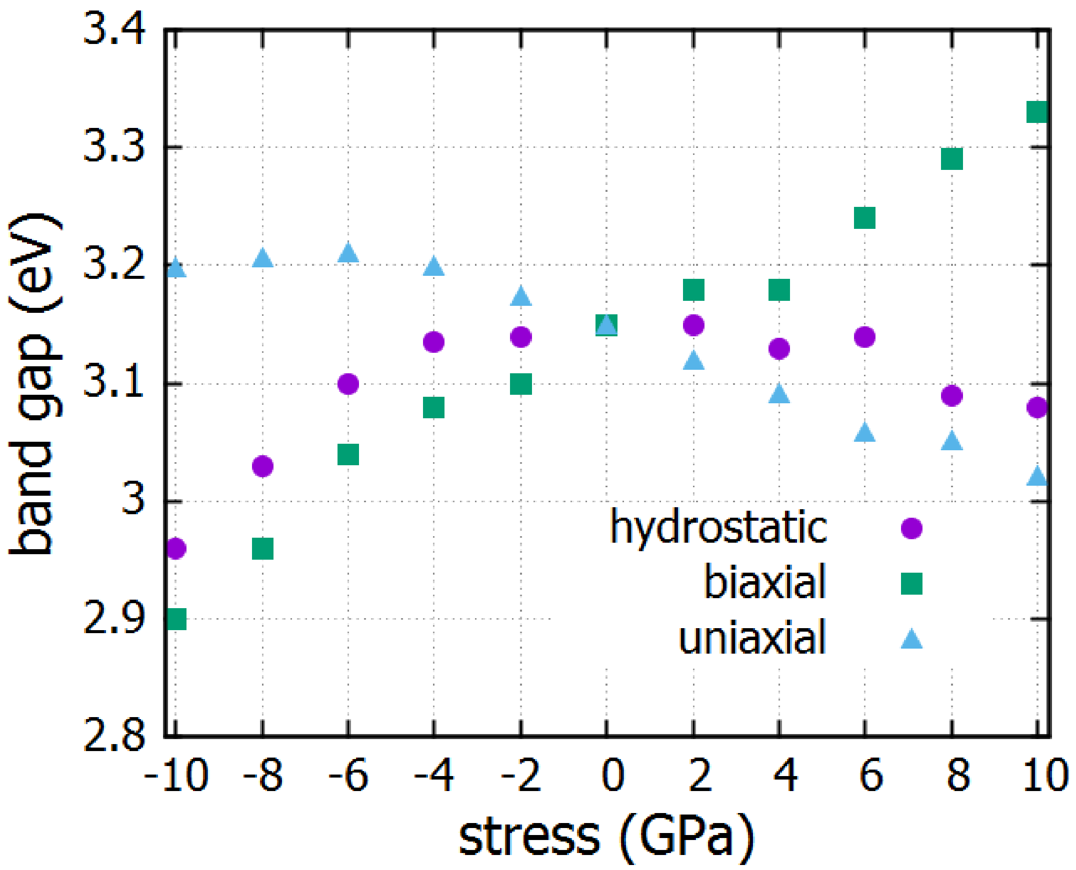

**Figure 9.9.** Band gap with respect to stress for undoped anatase for hydrostatic, biaxial and uniaxial stress.

As shown, the minimum band gap for anatase is obtained for the case of biaxial tensile stress, reaching 2.96 eV (close to the optimal gap of 2.0 eV) for the tensile stress of 8 GPa. Furthermore, the band gap as a function of stress is not linear as compared to a previous study (although similar trends are observed) where the PW91 GGA was applied, without the use of Hubbard +U correction[31]. The band gap versus biaxial stress when fitted with a second order polynomial, is approximately:

$$B.G.(eV) = 3.142eV + 19.8\frac{meV}{GPa}P - 0.265\frac{meV}{(GPa)^2}P^2 \qquad (9.1)$$

As presented in **Figure 9.10**, uniaxial compressive stress is an effective method to reduce the band gap. Compression in the z axis will lead to expansion in the xy plane, therefore the cases of uniaxial stress along the [001] axis and biaxial stress in the (001) plane are similar. Additionally, biaxial stress can be achieved by experimental growth methods and is a technological interest approach in order to introduce stress to a substrate.

## 9.5 Conclusions

In the present chapter, DFT calculations were used to investigate the $Li_i$ and $Na_i$ diffusion, the F / N defect clusters and strain effects in anatase. It was shown that the minimum energy $Li_i$ and $Na_i$ defects reside in similar distorted octahedral sites. The $Na_i$ defects are larger and distort the lattice more significantly as is reflected by the oxygen-defect distances. The DOS revealed that both $Li_i$ and $Na_i$ defects introduce deep levels into the band gap.  The preferential diffusion mechanism is along the b – axis for both $Li_i$ and $Na_i$ defects with the migration energy barrier for $Li_i$ being 0.24 eV lower compared to $Na_i$.

The information presented herein on the energy levels of the interfacial states existent in the bulk F-N codoped anatase can be useful for the interpretation of experimental results, or as input to possible Monte Carlo simulations. In general, it is expected that methods to increase the photocatalytic efficiency by doping may be weakened by recombination losses attributed to interface states, dependent on the application. In the present study about 1% nitrogen and/or 1% fluorine is considered. This concentration of nitrogen should be more than sufficient to reduce the band gap and increase the photocatalytic activity of anatase. It is expected that fluorine will mainly saturate dangling bonds.

It was revealed that the $F_iN_i$ $F_ON_i$ and $F_iN_{Ti}$ defects are bound and it is therefore expected that in codoped anatase there will be a significant concentration of these defects. Considering the impact of these defects on the electronic structure of anatase the DOS is examined. It was shown that for the $F_ON_i$ defect pair $Ti^{3+}$ states are just below the conduction band. Finally, the $F_iN_{Ti}$ defects introduce deep levels. It is therefore proposed here that anatase without oxygen vacancies and titanium vacancies will be a better material to codoped, as the deleterious $F_ON_i$ and $F_iN_{Ti}$ will not form.

At any rate the optimum concentration of N and F will need to be determined systematically to avoid the formation of the deleterious defects proposed here. Finally, experimental work will be required to determine the impact of temperature and other processing conditions on the interactions of N and F in $TiO_2$. In this respect thermodynamic modeling and mass action analysis can also be important and act synergetically with DFT and experiment.

# REFERENCES

---

[1] A. Fujishima and K. Honda, Electrochemical Photolysis of Water at a Semiconductor Electrode. *Nature*, **238**, 5358, (1972).

[2] M. Gratzel, Photoelectrochemical cells. *Nature*, **414**, 338, (2001).

[3] S. U. M. Khan, M. Al-Shahry and W. B. Ingler, Efficient photochemical water splitting by a chemically modified n-$TiO_2$. *Science*, **297**, 2243, (2002).

[4] S. P. Russo, I. E. Grey and N. C. Wilson, Nitrogen/Hydrogen Codoping of Anatase: A DFT Study. *The Journal of Physical Chemistry C*, **112**, 7653, (2008).

[5] Y. Gai, J. Li, S. -S. Li, J. -B., Xia and S. -H. Wei, Design of Narrow-Gap $TiO_2$ : A Passivated Codoping Approach for Enhanced Photoelectrochemical Activity. *Physical Review Letters*, **102**, 036402 (2009).

[6] R. Asahi, T. Morikawa, T. Ohwaki, K. Aoki and Y. Taga, Visible-Light Photocatalysis in Nitrogen-Doped Titanium Oxides. *Science*, **293**, 269, (2001).

[7] H. Pan, Y. -W. Zhang, V. B. Shenoy and H. Gao, Effects of H-, N-, and (H, N)-Doping on the Photocatalytic Activity of $TiO_2$. *The Journal of Physical Chemistry C*, **115**, 12224, (2011).

[8] X. Chen, L. Liu, P. Y. Yu and S. S. Mao, Increasing Solar Absorption for Photocatalysis with Black Hydrogenated Titanium Dioxide Nanocrystals. *Science*. **331**, 746. (2011).

[9] R. Zheng, Y. Guo, C. Jin, J. Xie, Y. Zhu and Y. Xie, Novel thermally stable phosphorus-doped $TiO_2$ photocatalyst synthesized by hydrolysis of $TiCl_4$. *Journal of Molecular Catalysis A: Chemical*, **319**, 46, (2010).

[10] R. Fagan, D. E. McCormack, S. Hinder and S. C. Pillai, Improved high temperature stability of anatase $TiO_2$ photocatalysts by N, F, P co-doping. *Materials & Design*, **96**, 44, (2016).

[11] Y. Xie, Y. Li and X. Zhao, Low-temperature preparation and visible-light-induced catalytic activity of anatase F–N-codoped $TiO_2$. *Journal of Molecular Catalysis A: Chemical*, **277**, 119 (2007).

[12] T. Yamada, Y. Gao and M. Nagai Hydrothermal synthesis and evaluation of visible-light-active photocatalyst of (N, F)-codoped anatase $TiO_2$ from an F-containing titanium chemical. *Journal of the Ceramic Society of Japan*, **116**, 614 (2008).

[13] J. K. Burdett, T. Hughbanks, G. J. Miller, J. W. Richardson and J. V. Smith, Structural-electronic relationships in inorganic solids: powder neutron diffraction studies of the rutile and anatase polymorphs of titanium dioxide at 15 and 295 K. *Journal of the American Chemical Society*, **109**, 3639, (1987).

---

[14] J. Muscat, V. Swamy and N. W. Harrison, First-principles calculations of the phase stability of $TiO_2$. *Physical Review B*, **65**, 224112, (2002).

[15] S. Tosoni, O. Lamiel-Garci, D. F. Hevia, J. S. Doña and F. Illas, Electronic Structure of F-Doped Bulk Rutile, Anatase, and Brookite Polymorphs of $TiO_2$. *The Journal of Physical Chemistry C*, **116**, 12738, (2012).

[16] D. Su, S. Dou and G. Wang, Anatase $TiO_2$: Better Anode Material Than Amorphous and Rutile Phases of $TiO_2$ for Na-Ion Batteries. *Chemistry of Materials*, **27**, 6022 (2015).

[17] J.-Y. Hwang, S.-T. Myung and Y.-K. Sun, Sodium-ion batteries: present and future. *Chemical Society Reviews*, **46**, 3529, (2017).

[18] J. Wei, J. X. Liu, Y. C. Dang, K. Xu and Y. Zhou, A Review of Nanostructured $TiO_2$ Application in Li-Ion Batteries. *Advanced Materials Research*, **750**, 301 (2013).

[19] H. Xiong, M. D. Slater, M. Balasubramanian, C. S. Johnson and T. Rajh, Amorphous $TiO_2$ Nanotube Anode for Rechargeable Sodium Ion Batteries. *The Journal of Physical Chemistry Letters*, **2**, 2560, (2011).

[20] J. A. Dawson and J. Robertson Improved Calculation of Li and Na Intercalation Properties in Anatase, Rutile, and $TiO_2$(B). *The Journal of Physical Chemistry C*, **120,** 22910, (2016).

[21] P. Knauth, Inorganic solid Li ion conductors: An overview. *Solid State Ionics*, **180**, 911, (2009).

[22] Yan Wang, William Davidson Richards, Shyue Ping Ong, Lincoln J. Miara, Jae Chul Kim, Yifei Mo and Gerbrand Ceder, Design principles for solid-state lithium superionic conductors. *Nature Materials*, **14**, 1026, (2015).

[23] Corinne Arrouvel, Stephen C. Parker and M. Saiful Islam, Lithium Insertion and Transport in the $TiO_2$−B Anode Material: A Computational Study. *Chemistry of Materials*, **21**, 4778, (2009).

[24] J. Cheng, J. Chen, W. Lin, Y. Liu and Y. Kong, Improved visible light photocatalytic activity of fluorine and nitrogen co-doped $TiO_2$ with tunable nanoparticle size. *Applied Surface Science*, **332**, 573, (2015).

[25] S. Tosoni, O. Lamiel-Garci, D. F. Hevia and F. Illas, Electronic Structure of F-Doped Bulk Rutile, Anatase, and Brookite Polymorphs of $TiO_2$. *The Journal of Physical Chemistry C*, **117**, 5855, (2013).

[26] H. A. Seibel II, P. Karen, T. R. Wagner and P. M. Woodward, Synthesis and characterization of color variants of nitrogen - and fluorine-substituted $TiO_2$. *Journal of Materials Chemistry*, **19**, 471, (2009).

---

[27] J. Garcia-Barriocanal, A. Rivera-Calzada, M. Varela, Z. Sefrioui, E. Iborra, C. Leon, S. J. Pennycook and J. Santamaria, Colossal ionic conductivity at interfaces of epitaxial $ZrO_2$:$Y_2O_3$/$SrTiO_3$ heterostructures. *Science,* **321**, 676, (2008).

[28] R. Darkins, M. L. Sushko, J. Liu and D. M. Duffy, Stress in titania nanoparticles: an atomistic study. *Physical Chemistry Chemical Physics*, **16**, 9441, (2014).

[29] A. Goyal, S. R. Phillpot, G. Subramanian, D. A. Andersson, C. R. Stanek, and B. P. Uberuaga, Impact of homogeneous strain on uranium vacancy diffusion in uranium dioxide. *Physical Review B,* **91**, 094103, (2015).

[30] L. Thulin and J. Guerra, Calculations of strain-modified anatase $TiO_2$ band structures. *Physical Review B*, **77**, 195112, (2008).

[31] W.-J. Yin, S. Chen, J.-H. Yang, X.-G. Gong, Y. Yan and S.-H. Wei, Effective band gap narrowing of anatase $TiO_2$ by strain along a soft crystal direction. *Applied Physics Letters*, **96**, 221901, (2010).

[32] L. Jia, D. J. Shu and M. Wang, Tuning the area percentage of reactive surface of $TiO_2$ by strain engineering. *Physical Review Letters*, **109**, 156104, (2012).

[33] W. Zhou and N. Umezawa, Viable approach toward efficient p-type conductivity in Al-doped anatase $TiO_2$ via strain engineering. *RSC Advances*, **7**, 20542, (2017).

[34] T. Arlt, M. Bermejo, M. A. Blanco, L. Gerward, J. Z. Jiang, J. Staun Olsen, and J. M. Recio, High-pressure polymorphs of anatase $TiO_2$. *Physical Review B,* **61**, 14414, (2000).

[35] Wan-Jian Yin, Shiyou Chen, Ji-Hui Yang, Xin-Gao Gong, Yanfa Yan, and Su-Huai Wei, Effective band gap narrowing of anatase $TiO_2$ by strain along a soft crystal direction. *Applied Physics Letters*, **96**, 221901, (2010).

[36] A. Miyamura, K. Kaneda, Y. Sato and Y. Shigesato, Effects of internal stress on photocatalytic properties of $TiO_2$ films, *Thin Solid Films*, **516**, 4603, (2008).

[37] N. Kelaidis, A. Kordatos, S.-R. G. Christopoulos, and A. Chroneos, A roadmap of strain in doped anatase $TiO_2$. *Scientific Reports*, **8**, 12790, (2018).

[38] H. Magnan, D. Stanescu, M. Rioult, E. Fonda and A. Barbier, Epitaxial $TiO_2$ Thin Film Photoanodes: Influence of Crystallographic Structure and Substrate Nature. *Journal of Physical Chemistry C*, **123**, 5240, (2019).

# CHAPTER 10

## Concluding remarks and future work

The aim of this thesis is the investigation of defect processes in materials for energy related applications such as Solid-Oxide Fuel Cells and Li – ion batteries. A number of materials are examined, while different issues are considered so as to improve their applicability and performance. Here, atomistic modelling[1] has been employed to investigate the defect processes and electronic structure in $Li_2ZrO_3$, $Li_2CuO_2$, $Li_2SnO_3$, $Li_2RuO_3$, $Li_3SbO_4$, $Li_3NbO_4$ and $TiO_2$. The calculations presented here are expected to act synergetically with experimental studies to improve the understanding on these materials. The defect processes are an efficient way to gain insights into the intrinsic mechanisms[2] such as diffusion and justify materials properties such as phase stability and electronic conduction[3]. Initially, the dominant defect mechanisms where reviewed followed by the investigation of each system's properties with respect to their potential applicability.

Firstly, $Li_2ZrO_3$ has been considered as it is an interesting system that needs to be further investigated. DFT calculations have been employed to investigate the defect processes, electronic structure and doping effects. The $Li^+$ Frenkel is the dominant mechanism, whereas the binding energies for different types of dopants with oxygen vacancies as well as the resulting electronic structure of the material are reported. The electronic band gap corresponds to 3.85 eV. The computational results should be further investigated and confirmed through experimental techniques.

$Li_2CuO_2$ has been investigated as a potential cathode due to the very low $Li^+$ - ions activation energy of migration through the vacancy mechanism. $Li^+$ Frenkel is identified as the dominant mechanism, whereas the doping processes via trivalent ions has been also considered as an efficient way to increase the $Li^+$ vacant sites in the material. Similarly, $Li_2SnO_3$ and $Li_2RuO_3$ defect processes, $Li^+$ self-diffusion, doping and electronic structure have been investigated as these systems have attracted considerable interest, however, further work has to be done in order to identify the key factors on the system performance. Furthermore, $Li_3SbO_4$ and $Li_3NbO_4$ exhibit an attractive set of properties and are proposed as potential candidates for Li – ion batteries. The defect chemistry and electronic structure have been investigated. Doping in these materials is considered as a promising technique to increase the $Li^+$ concentration and improve the cycling rates as well as to preserve the structural stability.

$TiO_2$ has been extensively investigated as it exhibits an outstanding chemical stability, however, the present results in doped anatase and strain effects expands the knowledge on the materials behaviour. The band gap dependence with respect to the applied external strain is reported. Additionally, the potential applicability as anode material in $Li^+$ and $Na^+$ has been investigated, where it is shown that $Li^+$ ions would migrate faster than $Na^+$ through interstitial sites. Furthermore, the defect cluster formation in $F^-$ / $N^+$ doped anatase is investigated as this is proposed to efficiently improve the materials photocatalytic activity.

Overall, the link between the defect chemistry and the potential performance of the materials in energy applications has been studied. Furthermore, the importance of future investigation through experimental techniques to establish their applicability in a low cost and safe environment is highlighted.

Future work will continue to focus on material for $Li^+$ - ion batteries, as well as $Na^+$ and $Mg^{2+}$ potential systems. The connection of point defects with the materials behaviour must be extensively investigated through advanced techniques. The investigation of different materials through DFT such as MAX phases and MX-enes[4] is also already under way. Furthermore, apart from DFT, methods such as static atomistic simulations and Molecular Dynamics will be also employed to complement the research goals and provide insights on the fundamental understanding of energy materials.

Additionally, mixed methods such as genetic algorithms and MD should be applied in promising disordered materials in order to provide a predictive role in the diffusion mechanisms and defect processes. Disordered ionic conductors such as cation disordered materials (for example LLTO – Lithium Lanthanum Titanate[5] or $LiMoCrO_2$[6]) offer new opportunities for further optimization of energy – related materials. These systems are difficult to examine using standard theoretical techniques as there are many difficult possible configurations. In that respect, a combination of genetic algorithms and atomistic simulations may yield results that are comparable to experiment and insights that are difficult to acquire using simpler techniques.

# REFERENCES

---

[1] D. Parfitt, A. Kordatos, P.P. Filippatos and A. Chroneos, Diffusion in energy materials: Governing dynamics from atomistic modelling. *Applied Physics Reviews*, **4**, 031305, (2017).

[2] M. S. Islam and C. A. J. Fischer Lithium and Sodium battery cathode materials: computational insights into voltage, diffusion and nanostructural properties. *Chemical Society Reviews*, **43**, 185 (2014).

[3] A. Eftekhari, Low-voltage materials for lithium-ion batteries. *Energy Storage materials*, **7**, 157, (2017).

[4] B. Anasori, M. R. Lukatskaya and Y. Gogotsi. 2D metal carbides and nitrides (MXenes) for energy storage. *Nature Reviews Materials*, **2**, 16098, (2017).

[5] E. E. Jay, M. J. D. Rushton, A. Chroneos, R.W. Grimes and J. A. Kilner Genetics of superionic conductivity in lithium lanthanum titanates. *Physical Chemistry Chemical Physics*, **17**, 178 (2015).

[6] J. Lee, A. Urban, X. Li, D. Su, G. Hautier and G. Seder, Unlocking the Potential of Cation-Disordered Oxides for Rechargeable Lithium Batteries. *Science*, **343** 519 (2014)

# APPENDIX A

## Journal Publications

**1.** S.-R. G. Christopoulos, A. Kordatos, M. W. D. Cooper, M. E. Fitzpatrick and A. Chroneos. Activation volumes of oxygen self-diffusion in fluorite structured oxides, *Materials Research Express,* **3,** 105504, (**2016**).

**2.** A. Kordatos, S.-R.G. Christopoulos, N. Kelaidis and A. Chroneos, Defect processes in $Li_2ZrO_3$: insights from atomistic modelling. *Journal of Materials Science: Materials in Electronics*, **28**, 11789, (**2017**).

**3.** D. Parfitt, A. Kordatos, P.P. Filippatos and A. Chroneos, Diffusion in energy materials: Governing dynamics from atomistic modelling. *Applied Physics Reviews*, **4**, 031305, (**2017**).

**4.** A. Kordatos, N. Kelaidis and A. Chroneos, Defect pair formation in fluorine and nitrogen codoped $TiO_2$, *Journal of Applied Physics*, **123**, 161510 (**2018**).

**5.** A. Kordatos, N. Kelaidis and A. Chroneos, Migration of sodium and lithium interstitials in anatase $TiO_2$, *Solid State Ionics,* **315**, 40, (**2018**).

**6.** A. Kordatos, N. Kuganathan, Nikolaos Kelaidis, P. Iyngaran and A. Chroneos, Defects and lithium migration in $Li_2CuO_2$. *Scientific Reports*, **8**, 6754, (**2018**).

**7.** N. Kuganathan, A. Kordatos, and A. Chroneos, $Li_2SnO_3$ as a Cathode Material for Lithium-ion Batteries: Defects, Lithium Ion Diffusion and Dopants. *Scientific Reports*, **8**, 12621, (**2018**).

**8.** N. Kelaidis, A. Kordatos, S.-R. G. Christopoulos, and A. Chroneos, A roadmap of strain in doped anatase $TiO_2$. *Scientific Reports*, **8**, 12790, (**2018**).

**9.** N. Kuganathan, A. Kordatos, M. E. Fitzpatrick, R.V. Vovk and A. Chroneos, Defect process and lithium diffusion in $Li_2TiO_3$. *Solid State Ionics*, **327**, 93, (**2018**).

**10.** N. Kuganathan, A. Kordatos, and A. Chroneos, Defect Chemistry and Li-ion Diffusion in $Li_2RuO_3$. *Scientific Reports*, **9**, 550, (**2019**).

**11.** N. Kuganathan, A. Kordatos, S. Anurakavan, P. Iyngaran and A. Chroneos, $Li_3SbO_4$ lithium-ion battery material: Defects, lithium ion diffusion and tetravalent dopants. *Materials Chemistry and Physics*, **225**, 34, (**2019**).

**12.** N. Kuganathan, A. Kordatos, N. Kelaidis and Alexander Chroneos, Defects, Lithium Mobility and Tetravalent Dopants in the $Li_3NbO_4$ Cathode Material. *Scientific Reports*, **9**, 2192, (**2019**).

# APPENDIX B

## Crystallography

Crystallography is the experimental science that investigates the types of atoms' arrangement in solids. In this section, the necessary information and background knowledge with respect to the crystallographic nomenclature used for the present thesis is provided.

### 1. The seven primitive crystal systems

The symmetry of each material is described by its space group. From the structural point of view, every system's primitive configuration should be categorized according to the associated crystallographic system[1] [2]. Overall solids are categorized as:

- *Crystalline*: The atoms are packed in a periodic configuration in space.
- *Non – crystalline*: Complex structures where atoms have no periodic packing. Often referred as amorphous phases.

Solids are described through the primitive cell as represented with respect to one of the seven crystallographic systems. Table 1 summarizes the crystallographic details as presented in Figure 1. These are:

- *Cubic:* All threes lattice parameters are equal in length and perpendicular to one another

- *Tetragonal:* Two of the three lattice parameters are equal in length and perpendicular to one another
- *Hexagonal:* Two of the three lattice parameters are equal in length, whereas two of the angles are equal $90^o$ and the third one is equal to $120^o$
- *Rhombohedral:* All threes lattice parameters are equal in length whereas all three angles are equal one to another but unequal to $90^o$
- *Orthorhombic:* The three lattice parameters are unequal in length and perpendicular to one another
- *Monoclinic:* The three lattice parameters are unequal in length, two of the angles are equal to $90^o$ whereas the third angle is unequal to $90^o$.
- *Triclinic:* The three lattice parameters are unequal in length, all angles are unequal to $90^o$.

**Table 1.** The crystallographic information for the seven crystal systems

| **System** | **Lattice** | **Angles** |
|---|---|---|
| Cubic | $a = b = c$ | $a = b = c = 90^o$ |
| Tetragonal | $a = b \neq c$ | $a = b = c = 90^o$ |
| Hexagonal | $a = b \neq c$ | $a = b = 90^o$, $c = 120^o$ |
| Rhombohedral | $a = b = c$ | $a = b = c \neq 90^o$ |
| Orthorhombic | $a \neq b \neq c$ | $a = b = c = 90^o$ |
| Monoclinic | $a \neq b \neq c$ | $a = b = 90^o$, $c \neq 90^o$ |
| Triclinic | $a \neq b \neq c$ | $a \neq b \neq c \neq 90^o$ |

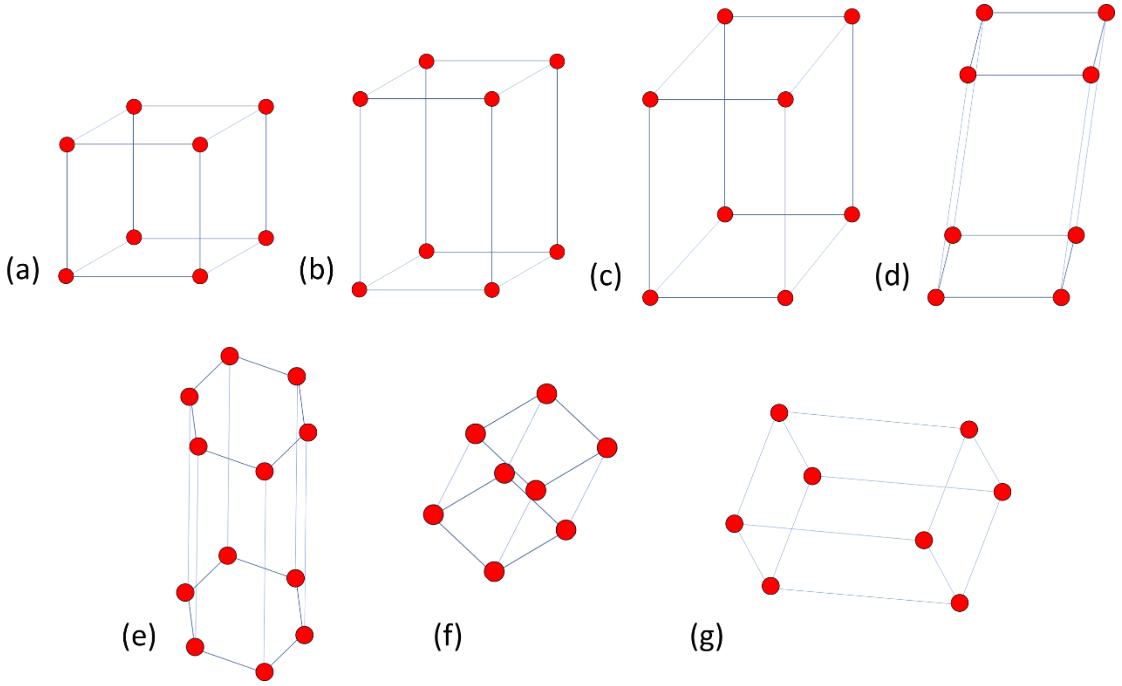

**Figure 1.** The crystal structure for (a) Cubic (b) Tetragonal (c) Monoclinic (e) Hexagonal (f) Rhombohedral and (g) Triclinic atomic configuration in solids

## 2. Bravais Lattices

Introduced by August Bravais[3] in 1850, Bravais lattices expanded the description of crystalline solids through the detailed analysis of arrangement in the unit cell. Figure 2 represents the different configurations of atom packing in the Cubic, Tetragonal, Rhombohedral and Monoclinic unit cells. The atom pacing can be described as:

- Body Centered: Atoms occupy sites on the cell corners with an additional point in the center of the cell.

- Face Centered: Atoms occupy sites on the cell corners with additional points in the center on all  of the cell sides.
- Base Centered: Atoms occupy sites on the cell corners with additional points in the center of one pair of parallel cell sides.

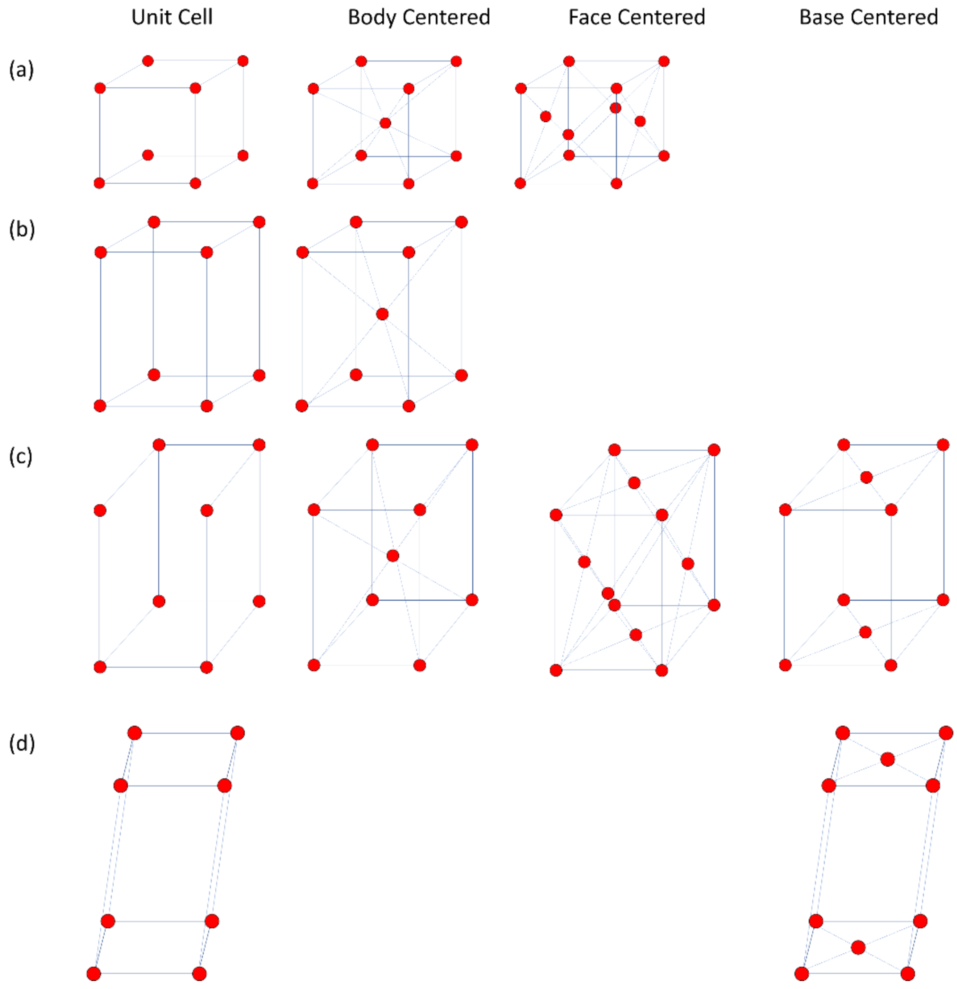

**Figure 2.** Representation of the Bravais lattices in (a) Cubic (b) Tetragonal (c) Rhombohedral (d) Monoclinic

# REFERENCES

---

[1] C. Kittel, Introduction to Solid State Physics, Wiley, New York (1996).

[2] W. D. Callister, JR Materials Science and Engineering, An introduction, Wiley (2000).

[3] Mois I. Aroyo, Ulrich Müller and Hans Wondratschek. *International Tables for Crystallography*, A1, 2, (2006).

# APPENDIX C

## Methodology Comments

In this section, a further description of the tools applied in terms of the methodology for the present thesis is provided. For the present thesis, the DFT code **CASTEP**[1] (Cambridge Serial Total Energy Package) is employed, a quantum mechanics program that is designed for solid-state physics and materials science. CASTEP is an open source academic and commercial package throughout structural, electronic and surface properties in crystalline solids are investigated from first principles.

## 1. CASTEP

CASTEP can be effectively used to investigate point defects such as vacancies or antisites as well as extended defects such as grain boundaries. The most common task in CASTEP is the Geometry Optimization where an arrangement of atoms is submitted to reach the most energetically favorable configuration is space. Other tasks can be:

- Single point calculation
- Electronic Spectroscopy
- Elastic constants calculation
- Transition state search

### 1.1 Input and output files

Initially the crystallographic data of the material is reached through a verified database in a ***Seed*.cif** file. The ***Seed*.cell** file is generated from the .cif file through the **cif2cell** subscript in

CASTEP. In the Seed.cell file, the lattice parameters, atomic positions, pseudopotentials as well as the Monkhorst-Pack (MP)$^2$ K-point grid are included. Pseudopotentials in CASTEP may be generated on-the-fly of be submitted as separate input files. **Figure 1** illustrates the structure of a ***Seed*.cell** file as an example. In the ***Seed*.param** file, all the necessary parameters for the run are provided. The task, plane wave basis and required output files are included. The CASTEP outputs are provided in the ***Seed*.castep** form. In this file, the process with all the iterations and the Hessian matrix throughout the ground state energy is reached are provided in detail.

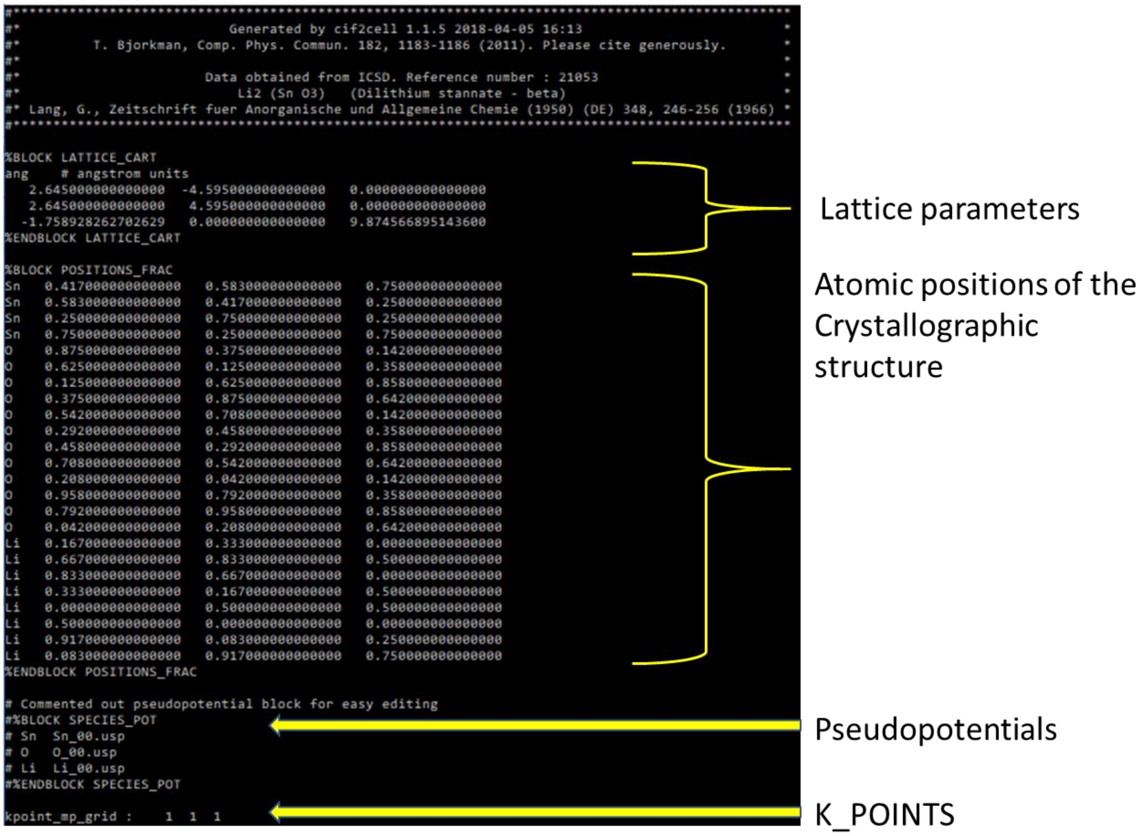

```
#*******************************************************************************
#*                         Generated by cif2cell 1.1.5 2018-04-05 16:13          *
#*          T. Bjorkman, Comp. Phys. Commun. 182, 1183-1186 (2011). Please cite generously.       *
#*                                                                               *
#*                       Data obtained from ICSD. Reference number : 21053       *
#*                           Li2 (Sn O3)   (Dilithium stannate - beta)           *
#* Lang, G., Zeitschrift fuer Anorganische und Allgemeine Chemie (1950) (DE) 348, 246-256 (1966) *
#*******************************************************************************

%BLOCK LATTICE_CART
ang    # angstrom units
   2.645000000000000  -4.595000000000000   0.000000000000000
   2.645000000000000   4.595000000000000   0.000000000000000
  -1.758928262702629   0.000000000000000   9.874566895143600
%ENDBLOCK LATTICE_CART

%BLOCK POSITIONS_FRAC
Sn   0.417000000000000   0.583000000000000   0.750000000000000
Sn   0.583000000000000   0.417000000000000   0.250000000000000
Sn   0.250000000000000   0.750000000000000   0.250000000000000
Sn   0.750000000000000   0.250000000000000   0.750000000000000
O    0.875000000000000   0.375000000000000   0.142000000000000
O    0.625000000000000   0.125000000000000   0.358000000000000
O    0.125000000000000   0.625000000000000   0.858000000000000
O    0.375000000000000   0.875000000000000   0.642000000000000
O    0.542000000000000   0.708000000000000   0.142000000000000
O    0.292000000000000   0.458000000000000   0.358000000000000
O    0.458000000000000   0.292000000000000   0.858000000000000
O    0.708000000000000   0.542000000000000   0.642000000000000
O    0.208000000000000   0.042000000000000   0.142000000000000
O    0.958000000000000   0.792000000000000   0.358000000000000
O    0.792000000000000   0.958000000000000   0.858000000000000
O    0.042000000000000   0.208000000000000   0.642000000000000
Li   0.167000000000000   0.333000000000000   0.000000000000000
Li   0.667000000000000   0.833000000000000   0.500000000000000
Li   0.833000000000000   0.667000000000000   0.000000000000000
Li   0.333000000000000   0.167000000000000   0.500000000000000
Li   0.000000000000000   0.500000000000000   0.500000000000000
Li   0.500000000000000   0.000000000000000   0.000000000000000
Li   0.917000000000000   0.083000000000000   0.250000000000000
Li   0.083000000000000   0.917000000000000   0.750000000000000
%ENDBLOCK POSITIONS_FRAC

# Commented out pseudopotential block for easy editing
#%BLOCK SPECIES_POT
# Sn  Sn_00.usp
# O   O_00.usp
# Li  Li_00.usp
#%ENDBLOCK SPECIES_POT

kpoint_mp_grid :    1  1  1
```

**Figure 1**. Example of ***Seed*.cell** file submitted as an input for a CASTEP job

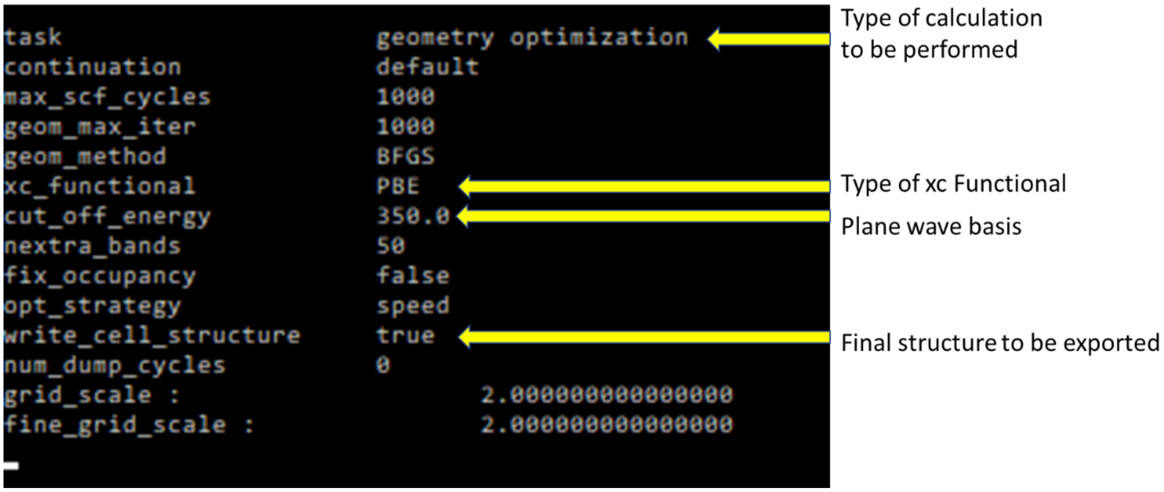

```
task                     geometry optimization
continuation             default
max_scf_cycles           1000
geom_max_iter            1000
geom_method              BFGS
xc_functional            PBE
cut_off_energy           350.0
nextra_bands             50
fix_occupancy            false
opt_strategy             speed
write_cell_structure     true
num_dump_cycles          0
grid_scale :                    2.000000000000000
fine_grid_scale :               2.000000000000000
```

**Figure 2.** Example of ***Seed*.param** file submitted as an input for a CASTEP job

In the Seed.param file, at first the type of calculation has to be defined as task. In addition, one has to specify the type of the exchange – correlation functional that will be applied on the calculation.

## 1.2 Convergence Testing

Among the most important concerns in DFT is whether the data are converged or not, thus the initial part of the investigation is the search of ideal plane wave basis cut-off and K-point grid criteria through the performance of convergence tests. This is equally important for the extraction of accurate outputs as well as balancing computational time with computational resources.

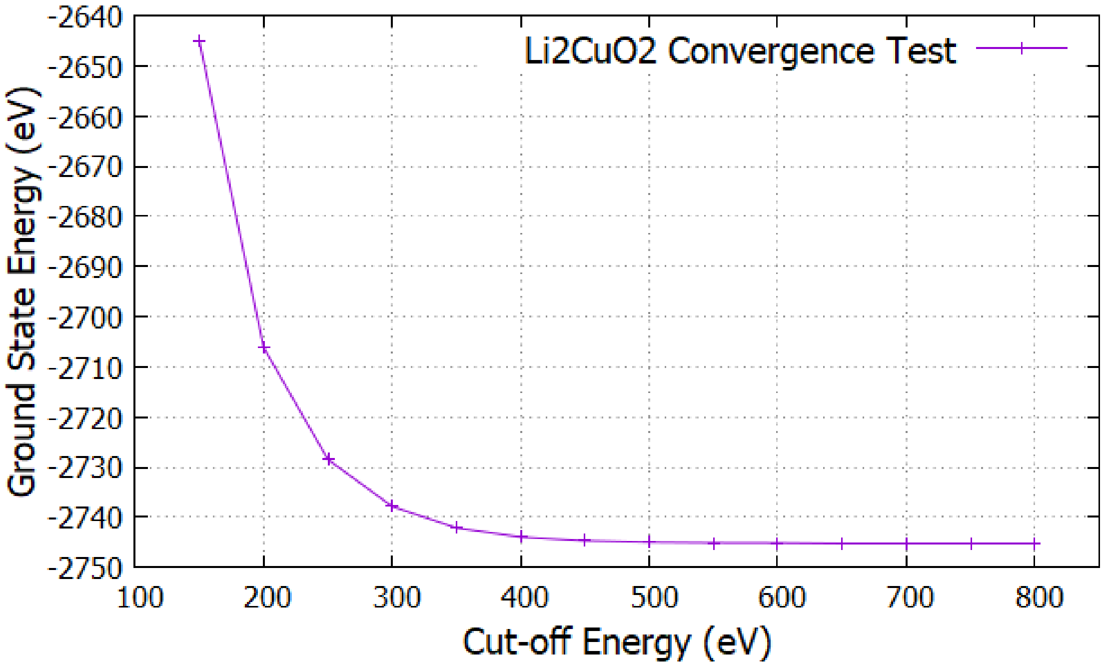

**Figure 3**. Convergence test for $Li_2CuO_2$

### 1.3 Migration barrier – Linear Synchronous Transition (LST)

Among the most important tasks in CASTEP is the search for transition states in the crystal. With this feature, one would be able to investigate the migration of atoms be defining its initial and final positions in the lattice. Available options are:

- LST Maximum
- LST/Optimization
- Halgren-Lipscomb
- Complete LST/QST

As an output, the activation energy of migration as well as the transition state point is provided in the ***Seed*.castep** file.

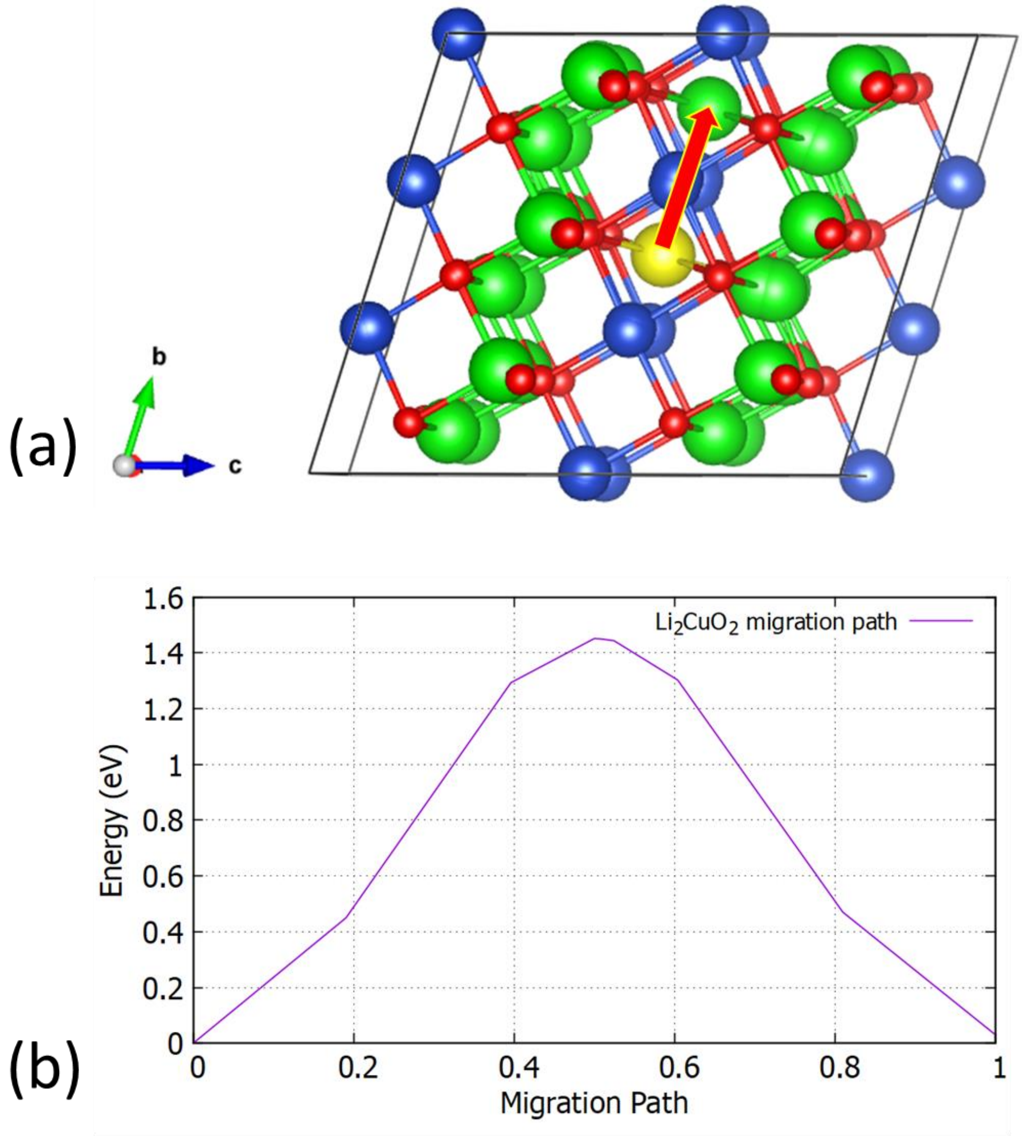

**Figure 4.** Complete LST/QST task showing (a) The initial and final positions of transition and (b) The activation energy of migration for the specific pathway

### 1.3 External Pressure

CASTEP provide the ability to apply compressive or tensile strain on a cell to investigate the intrinsic prosses under various conditions. The lattice parameters and volume or the new cell are extracted when the structure is optimized. Given this opportunity, the user is able to get insights into the materials properties under strain conditions in detail. The type of external pressure as applied to the cell structure should be added in the cell file as represented in Figure 5.

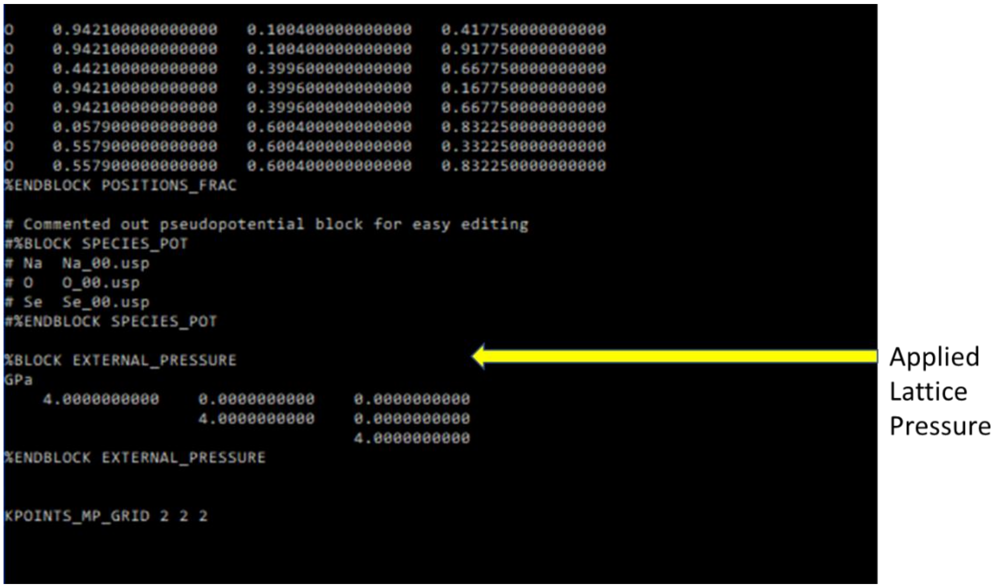

```
O    0.942100000000000   0.100400000000000   0.417750000000000
O    0.942100000000000   0.100400000000000   0.917750000000000
O    0.442100000000000   0.399600000000000   0.667750000000000
O    0.942100000000000   0.399600000000000   0.167750000000000
O    0.942100000000000   0.399600000000000   0.667750000000000
O    0.057900000000000   0.600400000000000   0.832250000000000
O    0.557900000000000   0.600400000000000   0.332250000000000
O    0.557900000000000   0.600400000000000   0.832250000000000
%ENDBLOCK POSITIONS_FRAC

# Commented out pseudopotential block for easy editing
#%BLOCK SPECIES_POT
# Na  Na_00.usp
# O   O_00.usp
# Se  Se_00.usp
#%ENDBLOCK SPECIES_POT

%BLOCK EXTERNAL_PRESSURE
GPa
    4.0000000000    0.0000000000    0.0000000000
                    4.0000000000    0.0000000000
                                    4.0000000000
%ENDBLOCK EXTERNAL_PRESSURE


KPOINTS_MP_GRID 2 2 2
```

Applied
Lattice
Pressure

**Figure 5.** Applied external pressure [4 GPa, Hydrostatic]

Overall the DFT calculations are straightforward and accurate, already confirmed by experimental studies. However, the method presents limitations that have to be considered when applying atomistic simulations. At first, DFT cannot deal with huge number of atoms, thus the cell has to be around 200 atoms to the maximum. For very complex structures, even smaller amounts (50 – 100) may not reach ground state of demand very high levels of time / power / resources. For this reason, we limit our approach of the defect chemistry in average cells  (2x2x2 or 3x3x3 for example) taking advantage of the structures' periodicity in space. An additional limitation of DFT is that all calculations are in zero temperature. An isolated cell is assumed based on the application of the same conditions to every calculation to ensure the validity of the systems' behavior. As reported, LDA / GGA approximations may not be effective on the investigation of specific features such as electronic structure and band gaps. Thus, hybrid exchange-correlation functionals such as HSE06 with norm-conserving pseudopotentials (not generated on-the-fly) have to be applied. Other methods such as Molecular Dynamics may deal better with these issues (Wide temperature range, thousands of atoms in cell), however this method is based in semiempirical pseudopotentials for the exchange correlation interactions using the Newton equations whereas quantum mechanics are more realistic and accurate. Validation of the results occurs in the realistic outputs and the comparison with experimental studies. Furthermore, duplication of specific outputs in different cells (1x2x2 and 3x4x3 for example) ensures that the materials properties are correctly investigated. The last technique is an efficient way to deal with long-range interactions too.

## 2. VESTA

VESTA[3] (Visualization for Electronic and Structural Analysis) is a 3D visualization program employed in the present thesis for the representation of structural models and investigation of atoms, bonds and interatomic distances. By submitting the crystallographic information as an input, it is possible to get a visual version of the various states of disorder through a detailed crystal model. Structural models may be represented as ball-and-stick, polyhedral, space-filling and wireframe among others. Among the most useful tools is the ability to measure angles and interatomic distances in a given arrangement of atoms as well as to transform unit cells to bigger structures. Visual representation of advanced structures like surface models is also possible.

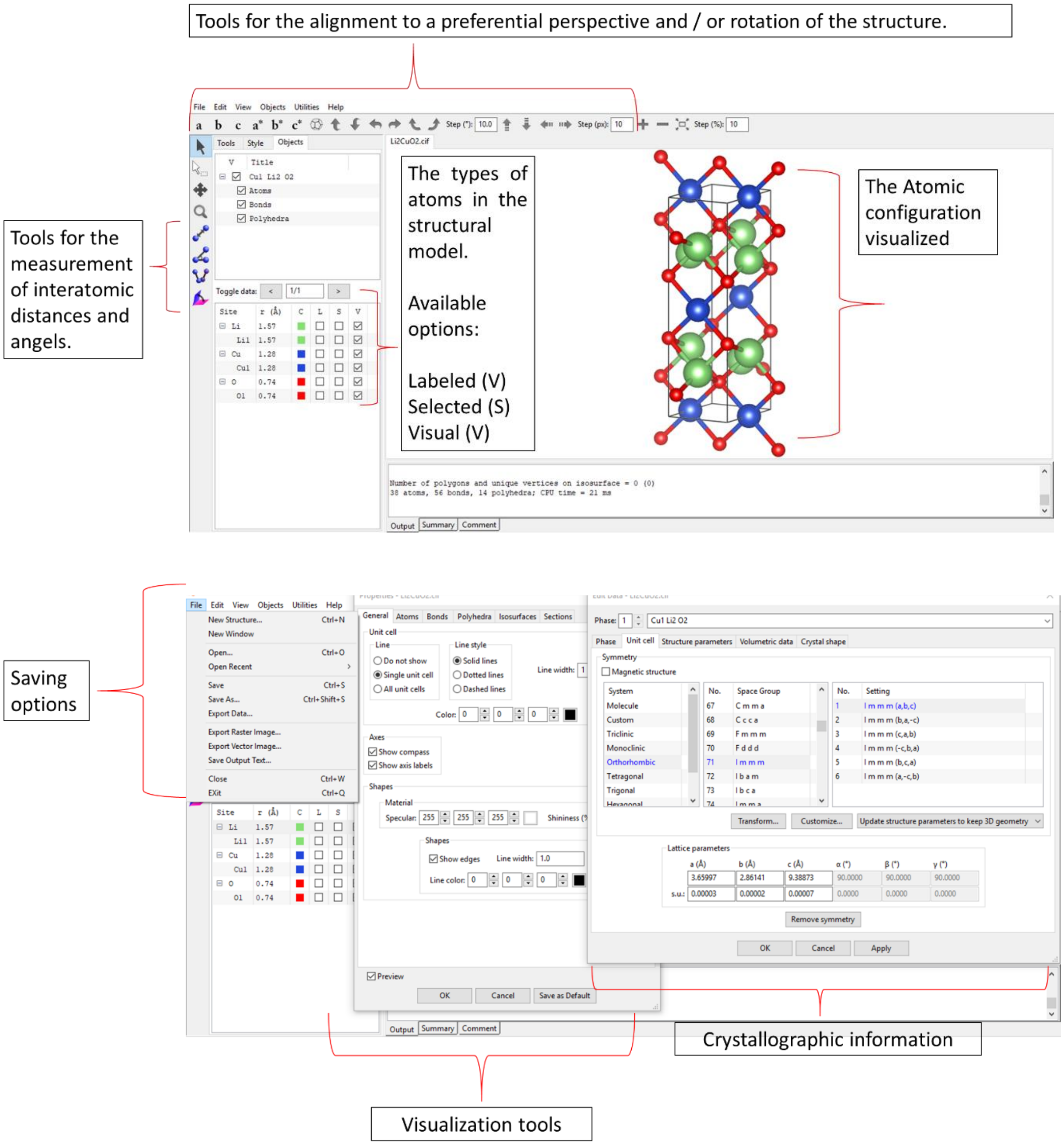

| Site | r (Å) | C | L | S | V |
|---|---|---|---|---|---|
| ⊟ Li | 1.57 | 🟩 | ☐ | ☐ | ☑ |
| Li1 | 1.57 | 🟩 | ☐ | ☐ | ☑ |
| ⊟ Cu | 1.28 | 🟦 | ☐ | ☐ | ☑ |
| Cu1 | 1.28 | 🟦 | ☐ | ☐ | ☑ |
| ⊟ O | 0.74 | 🟥 | ☐ | ☐ | ☑ |
| O1 | 0.74 | 🟥 | ☐ | ☐ | ☑ |

```
Number of polygons and unique vertices on isosurface = 0 (0)
38 atoms, 56 bonds, 14 polyhedra; CPU time = 21 ms
```

Phase: 1 Cu1 Li2 O2

Line: ○ Do not show ● Single unit cell ○ All unit cells

Line style: ● Solid lines ○ Dotted lines ○ Dashed lines

Axes: ☑ Show compass ☑ Show axis labels

Shapes: ☑ Show edges Line width: 1.0

Specular: 255 255 255

☑ Preview

Symmetry: ☐ Magnetic structure

| System | No. | Space Group | No. | Setting |
|---|---|---|---|---|
| Molecule | 67 | C m m a | 1 | I m m m (a,b,c) |
| Custom | 68 | C c c a | 2 | I m m m (b,a,-c) |
| Triclinic | 69 | F m m m | 3 | I m m m (c,a,b) |
| Monoclinic | 70 | F d d d | 4 | I m m m (-c,b,a) |
| Orthorhombic | 71 | I m m m | 5 | I m m m (b,c,a) |
| Tetragonal | 72 | I b a m | 6 | I m m m (a,-c,b) |
| Trigonal | 73 | I b c a | | |
| Hexagonal | 74 | I m m a | | |

Lattice parameters

| | a (Å) | b (Å) | c (Å) | α (°) | β (°) | γ (°) |
|---|---|---|---|---|---|---|
| | 3.65997 | 2.86141 | 9.38873 | 90.0000 | 90.0000 | 90.0000 |
| s.u.: | 0.00003 | 0.00002 | 0.00007 | 0.0000 | 0.0000 | 0.0000 |

**Figure 6.** Visualization options through VESTA

## 3. OptaDOS

OptaDOS[4] [5]is a freely available code for calculating optical, (core-level) excitation spectra as well as full and partial density of states. The code is applied in the present thesis for the visualization of electronic structure data. The available PDOS options we have worked so far are:

- Angular, where the DOS contributions are decomposed as atomic orbitals.
- Species where the DOS contributions are decomposed onto atomic species for each element.
- Species_ang, where the DOS contributions are decomposed onto angular channels for each element.

The total DOS of a given cell will represent the structure of the valence / conduction bands as total contributions of the whole crystal. OptaDOS provide us with better visualization of outputs and understanding of every different element contribution in the DOS through the PDOS option.

## 4. COMPARISON

Numerous DFT codes have been successfully employed to investigate the atomistic processes in the solid state. Among the most famous are: **VASP** (Vienna Ab-initio Simulation Package), **SIESTA** (Spanish Initiative for Electronic Simulations with Thousands of Atoms), **QUANTUMESPRESSO** and **NWChem**. As currently, most studies are based on CASTEP and VASP, one could compare the different features of these two. At first, the background theory is almost identical as both use pseudopotentials through a plane-wave basis in a range of exchange-correlation functionals. CASTEP uses norm-conserving ultra-soft pseudopotentials as well as Vanderbilt[6] ultrasoft pseudopotentials. VASP uses norm-conserving and ultra-soft pseudopotentials too but the latter were not in the Vanderbilt scheme and considered to be inaccurate in the past, however nowadays great progress has been done and both codes are on the same level. An effective technique of comparison of different codes is through the pseudopotential libraries. On the big picture, Lejaeghere *et al.*[7] have recently reported on the reproducibility of DFT results through different codes. This work is based on the DFT calculations through 40 different methods. Most of the codes tested present a very good agreement with each other pointing to the implementation and accuracy. It is important that throughout the growing field of computational methods, every new addition can be tested and verified. Furthermore, comparison of different DFT codes will result in improvements in the total methodology through the development of new functionals and pseudopotentials. This will result to the enhancement of accuracy and predictive efficiency of atomistic simulations.

# REFERENCES

---

[1] M. D. Segall, P. J. D. Lindan, M. J. Probert, C. J. Pickard, P. J. Hasnip, S. J. Clark and M. C. Payne, First-principles simulation: ideas, illustrations and the CASTEP code *Journal of Physics: Condensed Matter*, **14**, 2717, (2002).

[2] H. J. Monkhorst and J. D. Pack, Special points for Brillouin-zone integrations *Physical Review* B, **13**, 5188, (1976).

[3] K. Momma and F. Izumi, "VESTA 3 for three-dimensional visualization of crystal, volumetric and morphology data," *Journal of Applied Crystallography*, **44**, 1272, (2011).

[4] R. J. Nicholls, A. J. Morris, C. J. Pickard and J. R. Yates, OptaDOS - a new tool for EELS calculations. *Journal of Physics: Conference Series*, **371**, 012062, (2012).

[5] A. J. Morris, R. Nicholls, C. J. Pickard and J. R. Yates, OptaDOS: A tool for obtaining density of states, core-level and optical spectra from electronic structure codes. *Computer Physics Communications*, **185**, 1477, (2014).

[6] D. Vanderbilt, Soft self-consistent pseudopotentials in a generalized eigenvalue formalism, *Physical Review* B, **41**, 7892, (1990).

[7] K. Lejaeghere, G. Bihlmayer, T. Björkman, P. Blaha, S. Blügel, V. Blum, D. Caliste, I. E. Castelli, S. J. Clark, A. Dal Corso, S. de Gironcoli, T. Deutsch, J. K. Dewhurst, I. Di Marco, C. Draxl, M. Dułak, O. Eriksson, J. A. Flores-Livas, K. F. Garrity, L. Genovese, P. Giannozzi, M. Giantomassi, S. Goedecker, X. Gonze, O. Grånäs, E. K. U. Gross, A. Gulans, F. Gygi, D. R. Hamann, P. J. Hasnip, N. A. W. Holzwarth, D. Iuşan, D. B. Jochym, F. Jollet, D. l Jones, G. Kresse, K. Koepernik, E. Küçükbenli, Y. O. Kvashnin, I. L. M. Locht, S. Lubeck, M. Marsman, N. Marzari, U. Nitzsche, L. Nordström, T. Ozaki, L. Paulatto, C. J. Pickard, W. Poelmans, M. I. J. Probert, K. Refson, M. Richter, G.-M. Rignanese, S. Saha, M. Scheffler, M. Schlipf, K. Schwarz, S. Sharma, F. Tavazza, P. Thunström, A. Tkatchenko, M. Torrent, D. Vanderbilt, M. J. van Setten, V. Van Speybroeck, J. M. Wills, J. R. Yates, G.-X. Zhang and S. Cottenier, *Reproducibility in density functional theory calculations of solids*, Science, **351,** (6280), (2016).